

Formation and properties of ultrathin silicon dioxide films on Ru(0001): an in-situ spectro-microscopy study

vorgelegt von
Dipl.-Ing.
Hagen William Klemm
geb. in Erlabrunn

von der Fakultät III – Prozesswissenschaften
der Technischen Universität Berlin
zur Erlangung des akademischen Grades

Doktor der Ingenieurwissenschaften
- Dr.-Ing. -

genehmigte Dissertation

Promotionsausschuss:

Vorsitzender: Prof. Dr. Walter Reimers
Gutachter: Prof. Dr. Hans-Joachim Freund
Prof. Dr. Frank Behrendt

Tag der wissenschaftlichen Aussprache: 05. Januar 2018

Berlin 2018

Ich erkläre hiermit, dass ich die vorliegende Arbeit selbständig verfasst und keine anderen als die angegebenen Quellen und Hilfsmittel verwendet habe.

Berlin, den January 23, 2018

Contents

Acknowledgements	A
Zusammenfassung	C
Abstract	E
1 Introduction	1
2 Experimental setup and theory	3
2.1 The setup	3
2.2 LEEM, LEED and DF-LEEM	9
2.3 μ XPS	15
Overview of preparation and characterization of the investigated film structures	18
3 The clean Ru(0001) surface	21
4 The oxygen terminations of Ru(0001)	27
4.1 The oxygen covered ruthenium surface	27
4.2 1O Termination p(2x2) – 0.25 ML	35
4.3 2O Termination p(2x1) – 0.5 ML	38
4.4 3O Termination p(2x2) – 0.75 ML	42
4.5 4O Termination (1x1) – 1 ML	46
5 The silicon deposition	48
5.1 Calibration of deposition rate	48
5.2 Silicon deposition in oxygen at room temperature	56
5.2.1 After deposition of 1 ML	64
5.2.2 After deposition of 2 ML	66
5.2.3 The role of Ru as a catalyst during the deposition in oxygen .	68

6	The (2x2)R30° ML-phase	70
6.1	Preparation, and characterization of properties	70
6.2	Interpretation: Formation and morphology of the (2x2)R30°-phase . .	80
6.3	The adsorption site model	82
7	The p(2x2) ML-phase	89
7.1	Preparation, and characterization of properties	89
7.2	Interpretation: Formation, morphology and model of the p(2x2) ML-phase	97
8	The Xmas star BL-phase	99
8.1	The oxidation of the BL	99
8.1.1	Preparation, and characterization of properties	99
8.1.2	The morphology and chemical state of film pre-annealed in oxygen	103
8.2	Preparation in UHV, and characterization of properties	105
8.3	Preparation in oxygen, and characterization of properties	110
8.4	Interpretation: The formation, morphology and chemical state of the Xmas star BL-phase	114
9	The p(2x2) BL-phase and the vitreous BL-phase	119
9.1	The appearance of p(2x2)-BL-phase and vitreous BL-phase in oxygen	119
9.2	p(2x2) BL-phase: Preparation, and characterization of properties . .	122
9.3	Interpretation: The formation, morphology and chemical state of the p(2x2) BL-phase	127
9.4	Vitreous BL-phase: Preparation, and characterization of properties .	128
9.5	Interpretation: Formation, morphology and chemical state of the vitreous BL-phase	139
9.6	Controlling the oxygen amount at the Ru(0001)-surface by thermal annealing or oxygen intercalation	145
10	Summary and outlook	151
	References	171

List of Figures

2.1	Sideview foto of the SMART system	5
2.2	Scheme of the SMART microscope	6
2.3	Working principle of the Omega filter	8
2.4	The Bragg and the Laue condition, Ewald sphere	11
2.5	Principles of μ LEED, LEEM & DF-LEEM at the SMART microscope	12
2.6	Determination of energy scale in μ XPS	17
2.7	The four preparation steps of the silica films	18
2.8	Comparison of the LEEM(IV) curves for each preparation step of the silica films	19
3.1	LEEM and LEED images of a clean Ru(0001)	22
3.2	Model of the Ru(0001)	23
3.3	LEEM(IV) of clean Ru(0001)	24
3.4	LEED(IV) of clean Ru(0001)	25
3.5	XPS of Ru 3d region of the clean Ru(0001)	26
4.1	Models of the oxygen-terminations	29
4.2	DF-LEEM during oxygen exposure at RT	31
4.3	LEEM(IV) curves of the oxygen terminations	32
4.4	XPS of the O 1s region for the oxygen terminations of Ru(0001) . . .	33
4.5	XPS of the Ru 3d _{5/2} region for the oxygen terminations of Ru(0001) .	34
4.6	DF-images of 1O termination	35
4.7	DF-LEEM(IV) of the 1O termination	37
4.8	LEED(IV) of the 1O termination	37
4.9	DF-images of 2O termination	39
4.10	large scale DF-images of 2O termination	39

4.11 DF-LEEM(IV) of the 2O termination	40
4.12 LEED(IV) of the 2O termination	41
4.13 In-situ DF-LEEM - annealing the 2O termination in UHV	42
4.14 Formation of the 3O termination in LEED	43
4.15 DF-images of 3O termination	44
4.16 DF-LEEM(IV) of the 3O termination	45
4.17 LEED(IV) of the 3O termination	45
4.18 LEEM & LEED-images of 4O terminated	46
4.19 LEED(IV) of the 4O termination	47
5.1 Silicene on Ag(111)	49
5.2 LEEM & LEED snapshots of the Si-deposition in UHV at 520 K	50
5.3 LEEM(iV) after Si-deposition in UHV at 520 K	51
5.4 In-situ XPS of the Si 2p line during the Silicon deposition in UHV at 520 K onto Ru(0001)	53
5.5 LEEM intensity decay during the Silicon deposition in UHV at 520 K onto Ru(0001)	55
5.6 IRRAS measurements of mono- and bilayer silica on Ru(0001)	56
5.7 Cross section of LEED during Si-deposition at RT onto 3O terminated Ru(0001)	57
5.8 LEED during Si-deposition at RT onto 3O terminated Ru(0001)	58
5.9 Cross section of LEED during Si-deposition at RT onto 4O terminated Ru(0001)	60
5.10 In-situ XPS of the Si 2p line during Si-deposition in O ₂ onto 3O terminated Ru(0001)	63
5.11 LEEM & LEED, XPS after deposition of 1 ML Si in O ₂ at RT	64
5.12 LEEM/LEED, XPS after deposition of 1 ML Si in UHV at RT	65
5.13 LEEM/LEED, XPS after deposition of 2 ML Si in UHV at RT	66
5.14 LEEM(iV) curves after deposition of 1 ML and 2 ML silicon	67
6.1 In-situ LEED of ML annealing in UHV	71
6.2 In-situ LEED of ML annealing in UHV - moiré spots	73
6.3 DF-LEEM series of a ML annealed in UHV	74
6.4 Influence of different annealing conditions	75
6.5 LEEM(IV) of the (2x2)R30° phase	76

6.6	DF-LEEM(IV) of the (2x2)R30° ML phase	77
6.7	LEED(IV) of the (2x2)R30° ML phase	78
6.8	XPS of the (2x2)R30° ML phase	79
6.9	Illustration of adsorption site model	83
6.10	Cross section of a LEED image of (2x2)R30° silica in direction of <001> of Ru	84
6.11	Occupation of adsorption sites of stressed, relaxed and compressed rotated silica layers on Ru	85
6.12	Superimposition of defect pattern found in STM with adsorption site model	86
6.13	Superimposition of a LEED pattern of the (2x2)R30° silica and of a LEED pattern simulation	88
7.1	In-situ LEED of ML annealing in O ₂	90
7.2	LEEM and LEED images of p(2x2) ML phase	91
7.3	LEEM(IV) of the p(2x2) ML phase in O ₂	92
7.4	DF-LEEM(IV) of the p(2x2) ML phase in O ₂	93
7.5	LEEM(IV) of the p(2x2) ML phase after different final annealing tem- peratures in O ₂	94
7.6	LEED(IV) of the p(2x2) ML phase	95
7.7	XPS of the p(2x2) ML phase	96
7.8	Atomic model of the p(2x2) ML phase on Ru(0001)	98
8.1	In-situ LEED of BL during a pre-annealing to 605 K in O ₂	100
8.2	LEEM after the pre-annealing of the BL in O ₂	101
8.3	MEM to LEEM transitions of films after the pre-annealing with dif- ferent T of the BL in O ₂	101
8.4	XPS after a pre-annealing	102
8.5	Model of the processes during pre-annealing	104
8.6	In-situ LEED of BL template annealing in UHV	106
8.7	LEEM and LEED images of Xmas star BL phase prepared in UHV .	107
8.8	LEEM(IV) of Xmas star BL phase	108
8.9	DF-LEEM/DF-LEEM(IV) of Xmas star phase	109
8.10	XPS of the Xmas star phase	110
8.11	In-situ LEED of preparation of the Xmas star phase in O ₂	111

8.12	LEEM and LEED images of Xmas star BL phase prepared in O ₂	112
8.13	LEEM(IV) of the Xmas star phase prepared in O ₂	112
8.14	XPS of the Xmas star phase prepared in O ₂	113
8.15	LEED model of Xmas star phase	116
8.16	STM images of the Xmas star phase and structure model	117
9.1	In-situ LEED of BL prepared by low heating rate in O ₂	120
9.2	In-situ LEED during preparation of the p(2x2) BL-phase in O ₂	123
9.3	LEEM(IV) of the p(2x2) BL-phase prepared in O ₂	124
9.4	DF-LEEM(IV) of the p(2x2) BL-phase	125
9.5	LEED(IV) of the p(2x2) BL-phase	126
9.6	XPS of the p(2x2) BL-phase	127
9.7	In-situ LEED during preparation of the vitreous BL-phase in O ₂	129
9.8	In-situ LEEM & LEED during preparation of the vitreous BL-phase in O ₂	130
9.9	LEEM/LEED of a vitreous BL prepared in O ₂	131
9.10	LEEM(IV) of the vitreous BL-phase prepared in O ₂	132
9.11	DF-LEEM/DF-LEEM(IV) at different positions of the ring in recip- rocal space	133
9.12	DF-LEEM-probing of the ring in reciprocal space	135
9.13	LEED(IV) of vitreous BL at room temperature	136
9.14	XPS of the vitreous BL-phase prepared in oxygen	138
9.15	XPS of the vitreous BL-phase prepared in UHV	139
9.16	Fit of electronic structures found in LEED(IV)	140
9.17	Determination of the E _A of the p(2x2) to vitreous transition	143
9.18	Illustration of the Stone-Wales defect	145
9.19	XPS of vitreous BL after UHV annealings and subsequent O ₂ exposure	147
9.20	LEEM/LEEM(IV)/LEED of vitreous BL after UHV annealing and subsequent O ₂ exposure	149
9.21	Sketch of desorption and intercalation routes of O ₂ below BL	150
10.1	LEEM(IV) curves of the ML- and BL-phases	154
10.2	Intermediate states of the phase transitions of silica	155
10.3	Evaporation front for films with more than 4 ML silicon	156

List of Tables

10.1 Preparation conditions and the resulting LEED patterns and XPS results of the different silica phases	153
---	-----

Acronyms

AFM	Atomic force microscopy
BESSY II	Berlin Electron Storage Ring Society for Synchrotron Radiation, facility II
BL	Bilayer
DF-LEEM	Dark field-LEEM
DF-LEEM(IV)	Dark field-LEEM(IV)
DFT	Density functional theory
FTIR	Fourier-transform infrared spectroscopy
IRRAS	Infrarot-Reflexions-Absorptions-Spektroskopie, in english: reflection-absorption infrared spectroscopy
LEED	Low energy electron diffraction
LEED(IV)	Intensity vs. voltage LEED
LEEM	Low energy electron microscopy
LEEM(IV)	Intensity vs. voltage LEEM
MEM	Mirror electron microscopy
ML	Monolayer
PEEM	Photo emission electron microscopy
SMART	Spectro-microscopy with aberration correction for many relevant techniques
STM	Scanning tunneling microscope
UHV	Ultra-high vacuum
XPS	X-ray photoelectron spectroscopy

Acknowledgements

Most importantly, I want to thank Prof. Dr. Hans-Joachim Freund for the opportunity to do this work at the Fritz-Haber-Institute. His advice and support, and particular his trust in me and his great patience for a work that took unexpectedly long, made this work possible. The time at the chemical physics department has been an inspiration for me to realize what is possible to achieve with a large group of great scientists gathered and guided in one institute. I especially enjoyed the internationality of the department, which gave me the possibility to meet people from all over the world and to learn about their culture. Also, the department workshops and seminars with the participation of experts in their fields gave insights in various scientific topics and have been a valuable additional education for me.

I also want to thank Prof. Dr. Dietrich Menzel for all his support (professionally and personally) during all these years. His guidance, support and ideas have been of inestimable value and he was an exceptional mentor. I deeply thank him for believing in me and supporting me when my endurance was weakened!

Special thanks go to Prof. Dr. Frank Behrendt, who was willing to be my supervisor at the technical university Berlin after the tragic and unexpected death of my previous supervisor Prof. Dr. Helmut Schubert.

A lot of thanks go to Dr. Thomas Schmidt, the team leader of the spectro-microscopy-group. His overwhelming experience in spectro-microscopy, theoretically and practically, cannot be overrated. In all these years, he has not been only a great supervisor and mentor, but also became a friend. In the same way I want to thank the rest of the group: the two engineers, Marcel Springer and Stephan Pohl, who supported me technically and mentally during a lot of bake outs and repairs at the microscope; the other PhD-students, namely, Alessandro Sala, Francesca Genuzio, Gina Peschel, Alexander Fuhrich and Feng Xiong for their support during countless day- and nightshifts at the synchrotron; the post-docs, Giuseppe Rombola, Helder Marchetto, Daniel Gottlob and, especially, Mauricio Prieto and Ewa Madey who worked closely with me in the silica project.

During my time at the chemical physics department I got help from all the other work groups. The list of people is countless, here only a few people can be named: the structure and reactivity group led by Dr. Shamil Shaikhutdinov and his post-docs and PhD-students, Dr. Heloise Tissot and Dr. Emre Emmez; the scanning probe microscopy group led by Dr. Markus Heyde and his post-docs Dr. David Kuhness, Dr. Hyun Jin Yang and his former PhD-students, Dr. Christin Büchner, Dr. Stephanie Stuckenholtz and Dr. Leonid Lichtenstein; Dr. Helmut Kuhlenbeck,

head of the spectroscopy group. My thanks go to the other former team leaders and their colleagues as well.

For the provision of the DFT results to determine the atomic model of silica Xmas star (zig zag) BL phase I want to thank Dr. Denis Usvyat, Prof. Dr. Martin Schütz and Prof. Dr. Joachim Sauer.

I also want to thank the people working and supporting me at BESSY II, especially Dr. Willy Mahler, Robert Schulz, Francois-Xavier Talon, Dr. Antje Vollmer, all the people of the work shop and the guards at BESSY II. During my time at the synchrotron I have met a lot people and a lot of them became friends, thank you!

Special thanks go to my family: my parents, who supported me all these years and raised me to be the person I am and my brother, who died tragically this year and who was a big influence in so many, unimaginable aspects of my life. Maria Ekimova has always given strength to, when I needed it. All my new and very old friends, who had to live with all my scientific babblings in these years, but never let me down. Thank you all!

Zusammenfassung

In der vorliegenden Arbeit werden die Ergebnisse einer systematischen Untersuchung der Präparationsbedingungen von mono- (ML) und bilagendicken (BL) Siliziumdioxidschichten (SiO_2) auf einer Ru(0001) Einkristalloberfläche präsentiert. Jeder Präparationsschritt wurde detailliert analysiert: Angefangen bei der reinen Ru(0001)-Oberfläche und deren verschiedenen Sauerstoffterminierungen wurde die Abscheidung von Silizium bei geringem Sauerstoffpartialdruck auf eine mit Sauerstoff terminierte Rutheniumoberfläche untersucht und anschließend wurden die verschiedenen Silikaphasen präpariert, in dem die Proben im Ultrahochvakuum (UHV) oder in einer Sauerstoffatmosphäre hochgeheizt und abgekühlt wurden. Als Analysemethoden kamen niederenergetische Elektronenmikroskopie (englisch kurz: LEEM), Dunkelfeld-LEEM, niederenergetische Mikro-Punkt-Elektronenbeugung (englisch kurz: μ LEED) und Mikro-Fokus-Röntgenphotoelektronenspektroskopie (englisch kurz: μ XPS) zum Einsatz, wobei die einzigartige Möglichkeit von in-situ und Echtzeit-Messungen genutzt wurde, um ein tieferes Verständnis der ablaufenden Prozesse während der einzelnen Präparationsschritte zu erhalten. Die verschiedenen Sauerstoffterminierungen, 1O, 2O, 3O und 4O, wurden ausführlich mit den obigen Methoden charakterisiert und dienten später als Referenz, um Aussagen über das Interface zwischen Ruthenium und Silika zu treffen.

Die Untersuchung der Siliziumabscheidung zeigte, dass unter den gegebenen Bedingungen (Raumtemperatur, $p_{\text{O}_2} = 2.0 \times 10^{-7}$ mbar) Ruthenium als Katalysator für die Siliziumoxidierung fungiert. Ruthenium spaltet dabei an seiner Oberfläche molekularen Sauerstoff aus der Sauerstoffhintergrund-Atmosphäre zu atomarem Sauerstoff, der dann schon bei Raumtemperatur Silizium oxidiert. Es zeigte sich, dass ab der Bedeckung von einer ML diese katalytische Wirkung durch das Siliziumdioxid inhibiert wird und deshalb unvollständig oxidiertes Siliziumdioxid in der zweiten ML vorherrscht. Eine vollständige Oxidation der zweiten ML erfolgt durch Hochheizen in Sauerstoff auf 625 K; Sauerstoff diffundiert hierbei durch den amorphen Film und Ruthenium dient wieder als Katalysator. Siliziumdioxid liegt danach als vollständig oxidiertes, aber ungeordneter Film auf der Oberfläche vor.

Das ML Siliziumdioxid ordnet sich im UHV oberhalb einer Temperatur von 1000 K zu einer um 30° zu Ruthenium rotierten (2×2) Überstruktur ($(2 \times 2)\text{R}30^\circ$) und in $p_{\text{O}_2} = 5.0 \times 10^{-6}$ mbar Sauerstoff ab einer Temperatur von 900 K zu einer $p(2 \times 2)$ Überstruktur. Die $(2 \times 2)\text{R}30^\circ$ Silikaphase im UHV ist im Gegensatz zu der in Sauerstoff präparierten $p(2 \times 2)$, um 4.3 % relaxiert. Die atomare Struktur der rotierten Phasen wird mit Hilfe eines Modells erklärt, dass die Besetzung von Adsorptionssplätzen und deren resultierendes Moiré-Muster kombiniert. Im XPS-Spektrum wurde in der O 1s Linie kein zusätzlich adsorbierter Sauerstoff gefunden, es wurde

jedoch neben der Silizium-Sauerstoff (Si-O) Bindung noch eine weitere Komponente bei 529.8 eV gefunden und einer Ru-O-Si Bindungen zugeordnet. Nach der Präparation in einer Sauerstoffatmosphäre ist auf der Rutheniumoberfläche zusätzlicher Sauerstoff adsorbiert, der im XPS Spektrum der O 1s Linie als weitere Komponente bei 529.1 eV auftritt. Durch den Vergleich der Form der Ru 3d_{5/2} Linien der sauerstoffbedeckten Oberflächen mit denen der ML-Silika Phasen konnte auf die Bedeckung der Adsorptionsplätze auf dem Ruthenium zurückgeschlossen werden. So wurde gefunden, dass die (2x2)R30° Silikaphase einer 1O Bedeckung und die p(2x2) einer 3O Bedeckung entspricht. Es kann so geschlussfolgert werden, dass der Energiegewinn durch die Besetzung von zusätzlichen Adsorptionsplätzen auf dem Ruthenium den Energiebedarf für die Streckung des Siliziumdioxid-Gitters kompensiert bzw. überwiegt. Für beide Siliziumdioxid Phasen der ML wurden keine Rotationsdomänen gefunden.

Für das bilagen (BL) Siliziumdioxid wurden drei Strukturphasen auf Ruthenium untersucht, worunter eine bisher nicht in der Literatur erfasst wurde. Die neue Phase bildet sich oberhalb einer Temperatur von 1050 K entweder im UHV oder bei einer hohen Heizrate von mehr als 7.5 K/s in $p_{\text{O}_2} = 5.0 \times 10^{-6}$ mbar Sauerstoff. Wegen ihres auffälligen Beugungsbildes wird sie in dieser Arbeit als Weihnachtsstern-Phase (Xmas-star) bezeichnet. Sie besitzt 3 Rotationsdomänen im Gegensatz zu den anderen beiden Phasen, die keinerlei Rotationsdomänen besitzen. Bei einer niedrigen Heizrate von 1 K/s bildet sich ab 950 K in $p_{\text{O}_2} = 5.0 \times 10^{-6}$ mbar Sauerstoff zunächst eine kristalline p(2x2) Überstruktur, die sich bei weiter erhöhter Temperatur (>1075 K) in eine (zwei-dimensionale) glasartige Phase umwandelt. Die Phasenumwandlung von der p(2x2) zur glasartigen Phase beginnt im UHV hingegen schon bei 1025 K. Die Dauer der Phasenumwandlung wurde in UHV und Sauerstoff für verschiedene Temperaturen experimentell ermittelt und mit Hilfe einer Arrhenius-Auftragung die notwendige Aktivierungsenergie zu 4.2 eV bestimmt, was gut mit einem theoretisch ermittelten Wert für die Bildung eines Stone-Wales-Defekts in hexagonalen Silika Bilagen-Gittern übereinstimmt. Die Umwandlung von kristalliner zu glasartiger Phase findet dabei in Gebieten statt, deren Größe unter der Ortsauflösungsgrenze des Mikroskops liegt. Eine Analyse der Ru 3d_{5/2} Peakform in XPS für die verschiedenen Bilagen-Phasen zeigte, dass je nach Präparationsbedingungen unterschiedlich viel Sauerstoff auf der Rutheniumoberfläche unter dem Silika adsorbiert ist. Für die Xmas-star Phase wurde eine 1O ähnliche Bedeckung gefunden, für die kristalline p(2x2) eine 3O und für die glasartige eine 1O Bedeckung (bei Präparation in UHV) und eine 4O Bedeckung (bei Präparation in Sauerstoff). Des Weiteren wurde die Desorption und Adsorption von Sauerstoff unter der glasartigen Phase untersucht. Dabei wurde die Bildung von makroskopischen Löchern bei der Desorption von Sauerstoff im UHV bei einer Temperatur über 1125 K beobachtet.

Mit Hilfe der hier gefunden Ergebnisse ist es möglich, gezielt die verschiedenen Silika-Phasen zu präparieren und für weitere Untersuchungen zu nutzen.

Abstract

This work presents the results of a systematic study of the preparation conditions of silica mono- and bilayers on a single crystal ruthenium (0001) surface. Each preparation step was analysed in detail with different methods. Starting with the clean Ru(0001) surface and the different oxygen terminations on it, the deposition of silicon in a low oxygen atmosphere onto an oxygen-pre-covered ruthenium surface was investigated and the preparation of different silica phases by annealing and cooling of the deposited films under ultra-high vacuum (UHV) or oxygen atmosphere conditions was studied. As analysis methods Low energy electron microscopy (LEEM), dark-field LEEM, micro spot low energy electron diffraction (μ LEED) and micro spot photoelectron spectroscopy (μ XPS) were applied, where the unique possibility of in-situ and real-time measurements was used to gain a deeper understanding of the ongoing processes during the preparation steps. The different oxygen terminations, 1O, 2O, 3O and 4O were extensively characterized with these methods and were later used as reference to gain knowledge about the interface of ruthenium and silica.

The investigation of the silica deposition shows that under the used conditions (room temperature, $p_{\text{O}_2} = 2.0 \times 10^{-7}$ mbar) ruthenium acts as a catalyst for the silicon oxidation. At its surface ruthenium dissociates oxygen molecules to atomic oxygen, which is used to oxidize the silicon already at room temperature. It was found that upon reaching the amount of one ML the completed silicon dioxide film inhibits the catalytic properties of the ruthenium substrate and therefore only partially oxidized silicon exists in the second layer. A full oxidation of the second layer was achieved by a short annealing in $p_{\text{O}_2} = 5.0 \times 10^{-6}$ mbar oxygen at 625 K; oxygen diffuses through the amorphous film and ruthenium acts as a catalyst again. Afterwards the silicon dioxide film is fully oxidized but disordered.

The ML silicon dioxide formed two structures depending on the preparation condition: (a) annealed in UHV a 30° rotated (2x2) superstructure ((2x2)R 30°) is formed above temperatures of 1000 K and (b) annealing under an $p_{\text{O}_2} = 5.0 \times 10^{-6}$ mbar oxygen atmosphere led to a p(2x2) superstructure above a temperature of 900 K. The (2x2)R 30° ML-phase of silica in UHV is 4.3 % relaxed in comparison to the p(2x2) ML-phase produced in oxygen. The atomic structure of the rotated phase could be explained by a model, which combines the occupation of adsorption sites and their resulting moiré-pattern. In the XPS spectrum of the O 1s line no additional adsorbed oxygen was found. However, besides the silicon-oxygen bond an additional component at 529.8 eV was found and assigned to Ru-O-Si bonds. After the preparation under the oxygen atmosphere additional oxygen was adsorbed on the surface appearing as an additional component at 529.1 eV. By comparing the

Ru $3d_{5/2}$ XPS line shape of oxygen covered Ru surface as reference with the ones of the ML silica the occupation of adsorption sites on ruthenium could be concluded. It was found that the $(2 \times 2)R30^\circ$ ML-phase of silica matches a 1O termination and the $p(2 \times 2)$ ML-phase a 3O termination. With this it could be concluded that the energy gained by additional occupation of ruthenium adsorption sites compensated or even exceeded the energy need to stretch the silicon dioxide lattice. For both ML silicon dioxide phases no rotational domains were found.

Three phases of the bilayer (BL) silica on ruthenium were investigated and one of them has not been reported in literature so far. This new crystalline phase appears at a temperature of 1050 K in UHV or at a high annealing rate of more than 7.5 K/s in $p_{O_2} = 5.0 \times 10^{-6}$ mbar oxygen. Because of its specific diffraction pattern, it will be referred to as Xmas-star phase in this work. It consists of three rotational domains, contrary to the other two phases, which show no rotational domains. By annealing in oxygen at a low heating rate of 1 K/s a crystalline $p(2 \times 2)$ BL-phase was formed at about 950 K and subsequently transformed into a (two-dimensional) vitreous BL-phase at higher temperatures (>1100 K). The phase transition from the $p(2 \times 2)$ to the vitreous BL-phase started in UHV already at 1025 K. The duration of the phase transition was determined experimentally in oxygen atmosphere and in UHV, respectively, and from an Arrhenius plot, the activation energy for the transformation was estimated to be 4.2 eV, matching very well a theoretically calculated value for the Stone-Wales defect appearing in hexagonal silica bilayer lattices. The transformation from the crystalline to the vitreous phase occurred in very small areas with a domain size below the lateral resolution limit of the microscope, thus appearing as a homogeneous change on the whole surface. An analysis of the shape of the Ru $3d_{5/2}$ lines for the different bilayer phases showed that depending on the preparation conditions different amounts of oxygen were adsorbed on the ruthenium surface below the silica layer. For the Xmas star phase a coverage similar to a 1O termination was found, for the crystalline $p(2 \times 2)$ BL-phase a 3O termination and for the vitreous a 1O termination (after preparation in UHV) and a 4O termination (after the preparation under an oxygen atmosphere). Furthermore, the desorption and adsorption of oxygen below the vitreous phase were investigated. Here, the appearance of macroscopic holes in the layer during the desorption of oxygen at elevated temperatures of about 1125 K in UHV was found.

Based on the results reported in the present dissertation, it will be possible to prepare different target-oriented silica ML- and BL-phases for further investigations.

Introduction

Silicon dioxide, SiO_2 or silica, surrounds us in our daily life everywhere. It is found in nature as sand, rock, mountains, and in the earth mantle [1,2], even in meteorite craters [3], but also as basic material for many industry products. The easy processing and large availability make Silica irreplaceable nowadays. Glass, its amorphous phase, is its main application, for example for windows, cups or lenses. Moreover, silicon dioxide plays a major role in semiconductor industry [4], especially in the silicon planar technology, where it is used as insulator in metal-oxide-semiconductor-field-effect-transistors (MOSFETs) or in the chemical industry as basic component for catalytically active materials like zeolites or as support for heterogeneous catalysts [5].

A large variety of bulk crystalline silica phases is well known [6], for example quartz, cristobalite and tridymite. Their structure and formation have been studied down to the atomic level. The basic unit in the silicon-oxygen system is a tetrahedron, where one silicon atom is surrounded by four oxygen atoms. The tetrahedra are connected by corner-sharing oxygen atoms so that one-dimensional chains (inosilicates), two-dimensional sheets (phyllosilicates), or three-dimensional networks (tectosilicates) are formed. For glassy or vitreous silica, a two-dimensional model was proposed by Zachariasen in 1932 [7]. In the model, the tetrahedra build a network which has no long-range order. In the two-dimensional case a mesh-net is formed, where a mesh is a ring and each ring can consist of a variable number of silica tetrahedra as ring-members, for example 3, 4, 5, 6, 7 or more. The random distribution of these rings leads to the amorphousness of the silica. 80 years after the suggestion of Zachariasen, the model was experimentally verified by atomically resolved Atomic force microscopy (AFM) and Scanning tunneling microscope (STM) measurements at the Fritz-Haber-Institute [8]. This was possible through the finding, that a sil-

ica bilayer forms a two-dimensional sheet on ruthenium(0001), which is covalently bound in itself and only weakly coupling to the surface by van der Waals forces [9,10]. Therefore, it lifts off and floats on the surface in contrast to the silica monolayer, which is covalently bound via Ru-O-Si bonds to the substrate. Both systems, the monolayer (ML) and bilayer (BL) silica on ruthenium have been studied in detail in terms of their structure and properties [11–17]. These studies even evolved to the exploration of the chemistry in confined spaces, here between the BL and the ruthenium support, to model the basic properties of zeolites [18]. For the monolayer two different crystalline phases have been found, and for the bilayer two different phases, a crystalline and a vitreous. The crystalline phases consist exclusively of 6-member rings of silicon dioxide tetrahedra. In the monolayer of silica each tetrahedron has a covalent bond to ruthenium, while the other three bonds connect to other tetrahedra. In the case of the bilayer, only silicon-oxygen-silicon bonds exist. The transition from the crystalline to the vitreous phase is of special interest here, because its understanding could provide new insights for the transformations of silica-based or derived materials [19].

However, a detailed in-situ study of the formation of these phases and its dependency on parameters like temperature, oxygen pressure or heating rate, has not been done yet: it is the topic of this work. With the knowledge of the influence of the preparation conditions, it should be possible to prepare target-oriented samples to get later snapshots of the formation processes of these phases with ex-situ techniques. The spectro-microscope used in this work combines the investigation of macroscopic properties in microscopy like the morphology of the films on a larger scale than in AFM/STM (several tens of micrometres vs. hundreds of nanometer) with the local chemical environment and its structure than integral methods like IRRAS or conventional XPS and LEED (several hundreds of micrometres vs. tens of micrometers). The knowledge of the macroscopic properties is very important for already found applications like using the layer as molecular sieve [20] or transferring it [21].

Experimental setup and theory

2.1 The setup

The experiments of this work were done at the SMART system at Berlin Electron Storage Ring Society for Synchrotron Radiation, facility II (BESSY II). The SMART system is a unique spectro-microscope. Through its aberration correction and energy filtering system (with an energy resolution of 180 meV [22, 23]) it has up to now the best lateral resolution in LEEM of 2.6 nm [24] and in Photo emission electron microscopy (PEEM) of 18 nm [25] in the world. It is located at beam line UE49-PGM-c at the third-generation synchrotron source BESSY II at the Helmholtz Center Berlin in Germany [26].

Different kinds of measurements methods are possible with this spectro-microscope, e.g.:

- XPEEM (X-ray photoelectron emission microscopy)
- μ XPS (Micro spot photoelectron spectroscopy)
- NEXAFS-PEEM (Near edge X-ray absorption fine structure PEEM)
- XMCD (X-ray magnetic circular dichroism)
- PED (Photoelectron diffraction)
- Valence band structure mapping/ARUPS
- LEEM (Low energy electron microscopy)
- DF-LEEM (Dark field – LEEM)

- μ LEED (Micro spot low energy electron diffraction)
- LEED(IV), LEEM(IV) (Intensity vs. voltage LEED/LEEM)

In-situ and real-time experiments with x-rays are possible in a gas atmosphere up to about $p_{\text{O}_2} = 1 \times 10^{-7}$ mbar, limited by the interlock system of the beamline. However, using the electron gun, experiments are possible under a gas atmosphere up to about $p_{\text{O}_2} = 1 \times 10^{-4}$ mbar.

The microscope itself consists of several steel chambers, which are evacuated to ultra-high vacuum conditions ($\text{UHV} = p < 1 \times 10^{-9}$ mbar) by ion getter and turbo pumps. The base pressure of the whole system is $\times 10^{-10}$ mbar. This prevents contamination of the sample surface because in the pressure of 1×10^{-7} mbar at room temperature one can assume an adsorption of one layer per second of the residual gas molecules on the surface (corresponding to 15 min for one layer in the 10^{-10} mbar range). The mean free path length for electrons needed to travel through the microscope is sufficiently high for pressures better than 10^{-5} mbar. In the main experimental chamber, the sample can be exposed under controlled conditions to clean gases like oxygen, carbon monoxide or hydrogen, while the sample is heated or cooled. In an attached preparation chamber samples can be cleaned by argon ion sputtering if needed, and preparations under higher pressures up to about 5 mbar can be carried out. The sample temperature can be measured by a thermocouple spot-welded close to the sample on the sample holder or by an infrared pyrometer. Several e-beam evaporators (Focus GMBH, EFM 3s, address: Neukirchner Str. 2, 65510 Huenstetten, Germany, [27]) are attached to the main chamber, allowing the in-situ investigation of the deposition of e.g. silicon, iron or germanium on the sample surface. Through a port at the side of the main chamber, the microscope is connected to the beamline and x-rays from the synchrotron light source can illuminate the sample surface. A side view of the microscope with its main components is shown in figure 2.1.

The synchrotron, a particle accelerator, is used as light source, providing soft x-rays with a high flux, a very well-defined energy, and high brilliance. The main component of the synchrotron is the electron storage ring, a large scale UHV system (circumference 240 m), in which electrons are circling in a closed loop with an energy up to 1.7 GeV. In some ring segments undulators are located, which are periodic structures of dipole magnets that force the electrons to travel in an oscillating path while emitting energy in the form of photons. The photons leave the storage ring of the synchrotron tangentially in the ring plane. They are guided through tubes

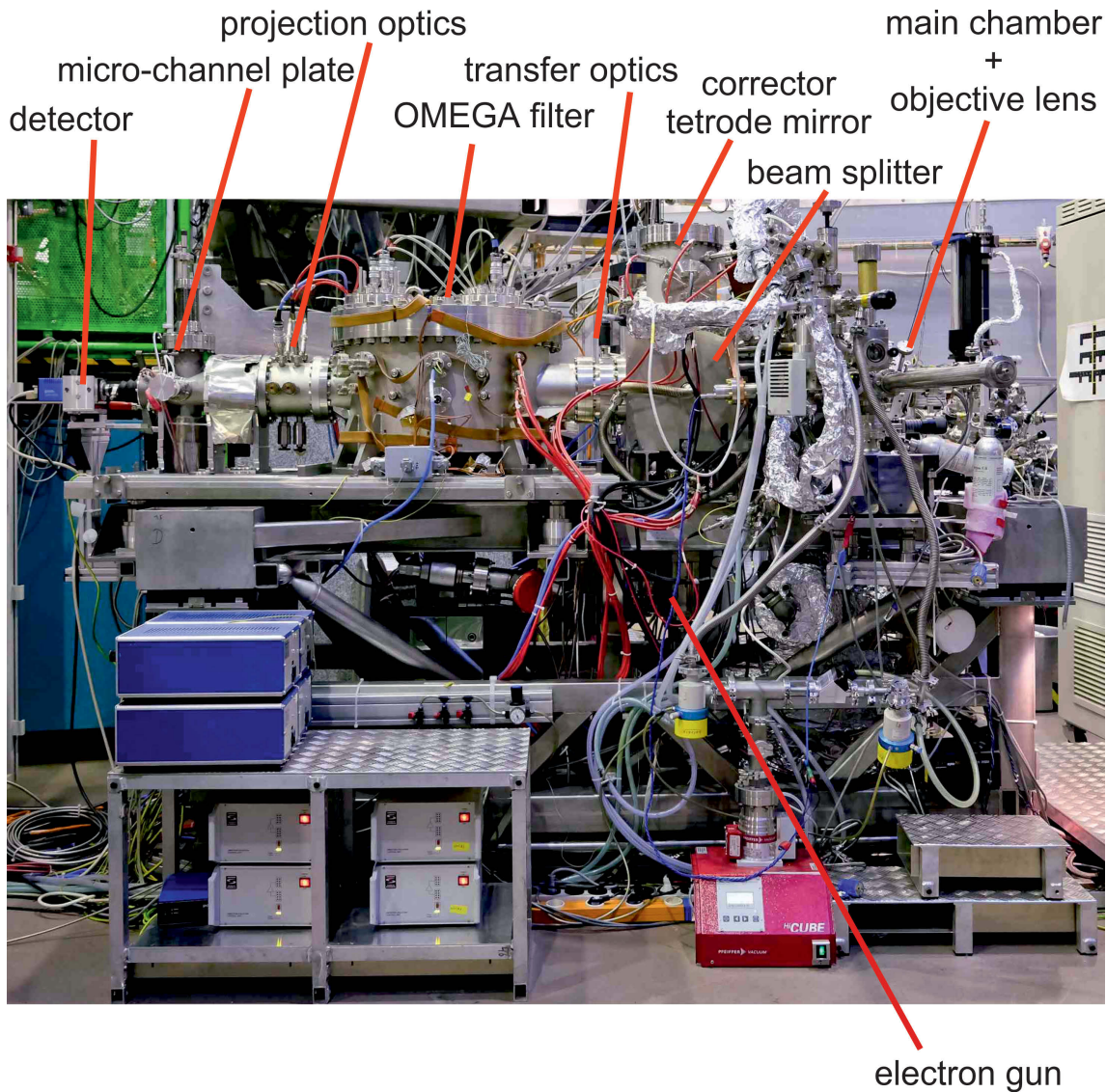


Figure 2.1: Sideview of the SMART system. The main components of the microscope are highlighted.

under UHV by plane and curved mirrors first to a grating monochromator and then to the end station. The segment between the undulator device and the end station is called beamline. The beamline for this experiment allows to use x-rays tuneable in an energy range from 90 eV to 1200 eV.

A short description of the working principle of the microscope will be given, for a more detailed description see reference [28] and the papers cited therein. A detailed description of the alignment procedure can be found in [29].

The microscope consists mainly of four parts: (i) the illumination column (light red), (ii) the beam splitter, (iii) the main chamber with the sample and the objective lens (light green), and (iv) the imaging column (light purple) (these transparent colours are used for assignment in figure 2.2).

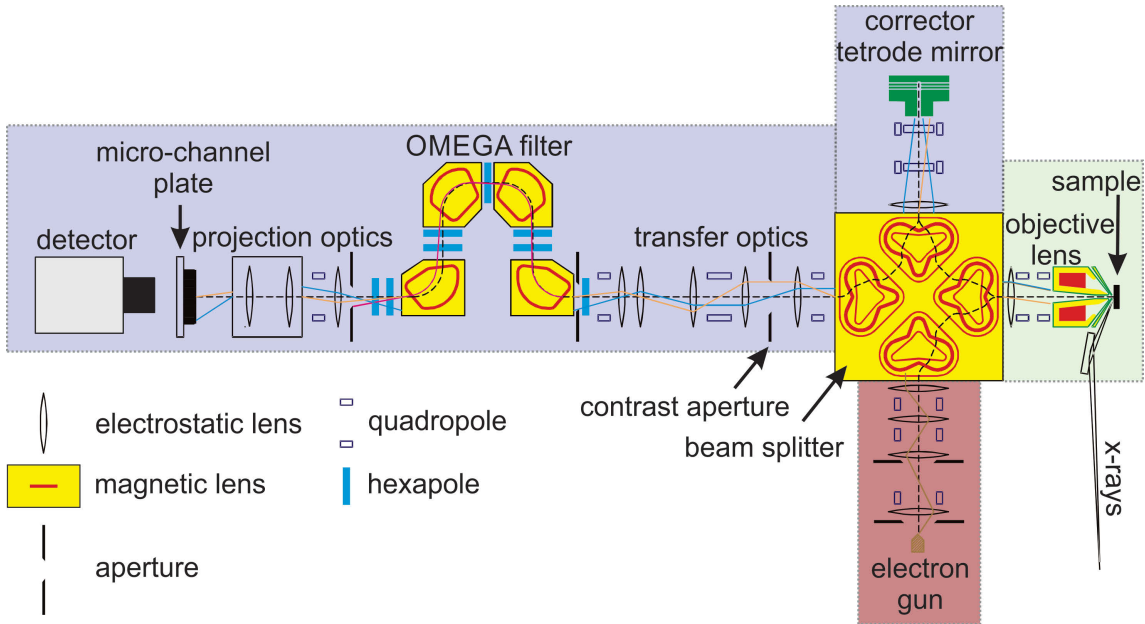


Figure 2.2: Scheme of the SMART. For details see text.

The illumination column consists of an electron gun and several condenser lenses. Electrons are emitted from a zirconium oxide coated tungsten field emitter tip in the electron gun and accelerated to 15 keV. The source of the electrons, in this case a Schottky field effect emitter, should ideally be point but is in reality a disc and is imaged via a condenser lens system into the image plane of the beam splitter. The potential of the electron emitter is set to -15 kV, therefore the electrons are accelerated to a kinetic energy E_{Kin} of 15 keV.

The beam splitter is a central part of the microscope. It is a dispersion-free magnetic beam separator [30] which connects the illumination column with the objective lens, the corrector tetrode mirror and the imaging column. It consists of four magnetic sector fields and has therefore a fourfold symmetry. It bends the incoming electron beam from the illumination column by an angle of 90° .

The electron beam of the gun is bent to the objective lens, which forms an immersion lens [31] with the sample, the so-called cathode lens. Apart from a small offset called start voltage (StV), the sample is at the potential -15 keV. The difference of the emitter and the sample potential is therefore just the StV (plus the difference of the workfunction), which means, the kinetic energy of the electrons at the sam-

ple surface corresponds to the StV value. If the sample potential is lower or equal -15 kV, then the electrons cannot reach the sample surface and are reflected in front of the surface. Because of the 100 % reflectivity of the electrons, this mode is called mirror electron microscopy (MEM). Here, one is sensitive to the local work function and the contrast is dominated by the vacuum potential.

If the sample potential is higher than -15 kV, then the electrons have a kinetic energy high enough to penetrate the sample and are reflected inside the bulk. The start voltage can be tuned between 0 V and +1000 V. Due to the small mean free path length the electrons probe the first few (up to 10) atomic layers of the sample surface and the measurement is therefore very surface sensitive. The electrons interacting with the surface atoms can be inelastically scattered, or elastically reflected or diffracted. The backscattered electrons leave the sample surface and are accelerated into the direction of the objective lens, where they reach a kinetic energy of 15 keV again and enter the beam splitter. The electron beam trajectory is then bent by 90°; however, because of the Lorentz law, into the direction of the corrector tetrode mirror.

The imaging column consists of a corrector tetrode mirror, transfer optics, an energy filter, projecting optics, a micro-channel plate, and a detector. The tetrode electron mirror induces spherical and chromatic aberrations of the opposite sign, compensating the aberrations of the objective lens [32–34]. The electrons entering the tetrode are slowed down and reflected by the electric field within it. Spherical aberrations for a fixed kinetic energy of the electrons are corrected by the shape of the equipotential surfaces in the electric field of the mirror; chromatic aberrations for lower or higher kinetic energies are corrected by the equipotential surfaces after or before the equipotential surfaces of the electric field for this fixed energy. In principle electrons with a higher kinetic energy penetrate deeper into the electric field, while electrons with a lower kinetic energy penetrate less. The reflected electron beam is then bent by the beam splitter again by 90° to the transfer lens optics, where the electrostatic lenses magnify the image and appropriately place the image and the back focal plane at the entrance of the energy filter. The contrast aperture is situated in the back focal plane and blocks diffracted electron beams; at the same time it is the entry slit of the energy filter. The energy filter consists of four magnetic sector fields. Electrons on the optical axis with the right kinetic energy pass the energy filter in a Ω -shape and therefore the energy filter is referred to as Omega filter [22, 35]. Electrons with lower or higher kinetic energies traverse the magnetic sector fields with different trajectories. In principle, the electrons with lower kinetic energy than the pass energy

(E_{pass}) will be strongly bent, the ones with higher energy less. The Omega filter generates a 1:1 image at its exit in an achromatic plane. In this plane, electrons with different kinetic energies will generate identical images, but the electrons cross the image point under an angle, i.e. here one has an angular energy dispersion in this plane. Behind the achromatic plane there is a (lateral) energy dispersive plane; different kinetic energies will be focussed with different horizontal displacements. With the help of a slit aperture inserted into the energy dispersive plane electrons with a certain kinetic energy can be selected (see figure 2.3). The projection optics behind the Omega filter magnifies the image further onto the 2d detector system. It consists of a micro-channel plate that multiplies the incoming electrons and projects them onto a phosphor screen, where the incoming electron signal is converted to photons. The light image at the back of the phosphor screen is imaged with a CCD-camera in real time. The overall magnification of the microscope ranges from $M = 500$ to 100000, corresponding to field of views between $\text{FoV} = 80 \mu\text{m}$ to 400 nm.

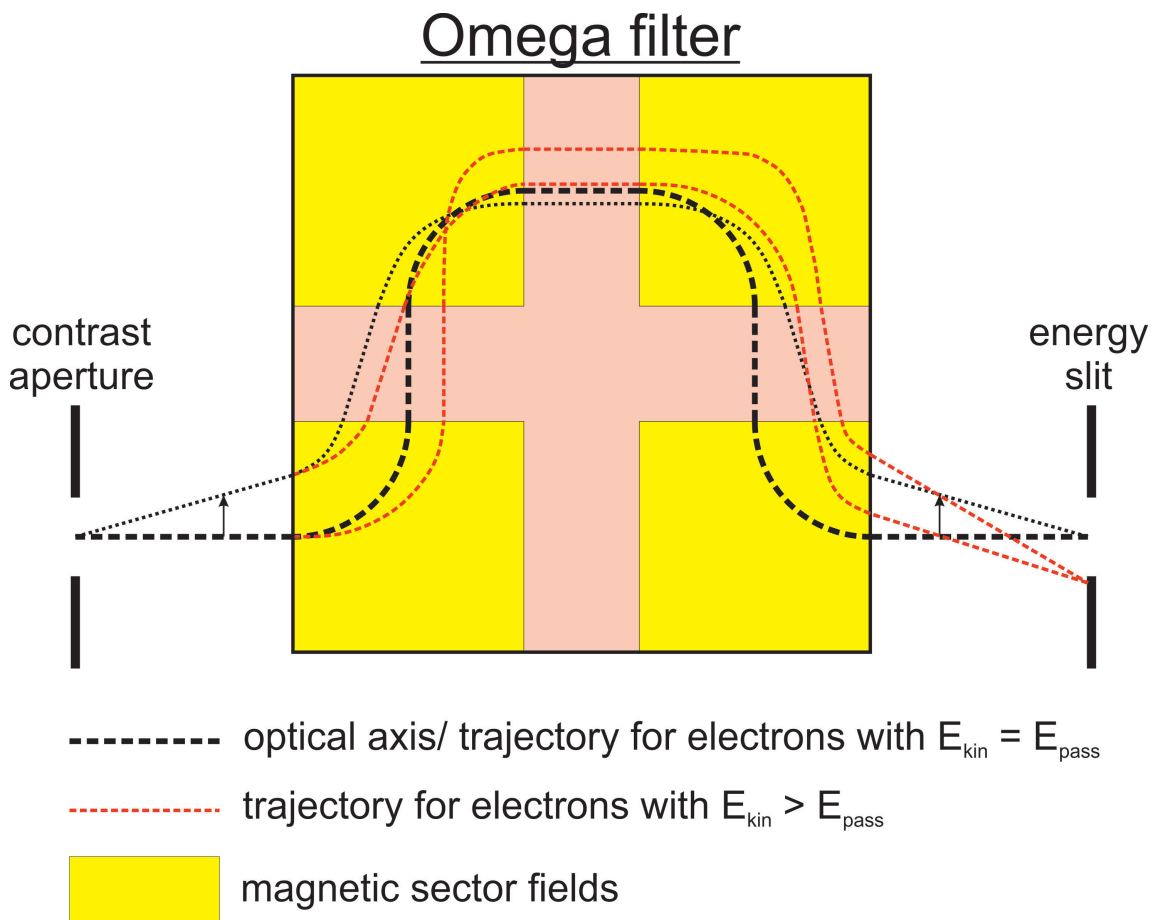


Figure 2.3: Illustration of the working principle of the Omega filter. The electrons enter the filter through the contrast aperture on the left side. The trajectories in this image are simplified and much more complex in reality.

2.2 LEEM, LEED and DF-LEEM

Of all the possible measurements that the microscope allows, the most important ones for this work, namely LEEM, DF-LEEM, μ LEED and μ XPS will be briefly discussed focusing on their operation principle and theory.

LEEM was developed by Ernst Bauer in the early nineteen sixties. It is a true imaging electron microscopy method where all image pixels are acquired simultaneously from an illuminated sample area on the surface [36]. To understand the principle of LEEM and DF-LEEM, the kinematic theory of Low energy electron diffraction (LEED) is a good base. Here, only the real basics of this theory will be addressed, for details see references [37, 38]. In contrast to the technical working principle, it is easier to use the wave-particle-dualism and to treat the electrons as waves [39]. Their energy at the surface is the start voltage StV plus an offset value (depending on the workfunction). The higher the StV applied to the electron the shorter its wave length and therefore the higher their kinetic energy.

As for all wave scattering events, a pattern is formed for waves passing an obstacle or slit. The atoms or molecules act as scattering centres for the electron waves and their arrangement leads to the typical pattern found in LEED.

In more detail, a crystal consists of a periodically repeated unit, the basis that is distributed in an ordered manner in space. The ordering could be described by lattices, which are built by different operations like translation, rotation, mirroring, inversion and their combination. For each crystal lattice in real space a corresponding lattice in the reciprocal space can be described and constructed by its basis vectors \vec{b}_1 , \vec{b}_2 and \vec{b}_3 :

$$\vec{b}_1 = 2\pi \frac{\vec{a}_2 \times \vec{a}_3}{\vec{a}_1(\vec{a}_2 \times \vec{a}_3)}, \quad \vec{b}_2 = 2\pi \frac{\vec{a}_3 \times \vec{a}_1}{\vec{a}_2(\vec{a}_3 \times \vec{a}_1)}, \quad \vec{b}_3 = 2\pi \frac{\vec{a}_1 \times \vec{a}_2}{\vec{a}_3(\vec{a}_1 \times \vec{a}_2)} \quad (2.1)$$

Here \vec{a}_1 , \vec{a}_2 and \vec{a}_3 are the basis vectors of the lattice in real space and define the unit cell in real space. The reciprocal basis vectors are perpendicular to the plane defined by the two vectors \vec{a}_1 and \vec{a}_2 and their unit is reciprocal to the one of the real space, thus defining the unit cell in reciprocal space. The unit cell itself is the smallest volume element of a lattice and contains exactly one lattice point.

The basis and lattice describe the crystal structure. It should be noted here, that the basis could be one atom, like in ruthenium, or multiple atoms like in SiO₂ or even large organic molecules like PTCDA [40] or proteins [41]. If the wave length of the electrons is comparable to the periodic length of the crystal structure, interference of the backscattered waves of the electrons occurs.

The Bragg condition describes the reflection at lattice planes of the crystal, where only lattice planes lead to a constructive reflection, which follow:

$$n\lambda = 2d \sin \theta = \Delta s \quad (2.2)$$

d is the distance between parallel lattice planes, λ the wave length, θ the angle between the incoming wave and the lattice plane, n a natural number and Δs the phase shift (see figure 2.4). So, for a known wave length and known diffraction geometry the distance of neighbouring planes can be calculated. This procedure is used in the Debye-Scherrer-method in x-ray diffraction.

The Laue equation describes the reflection due to identical objects (atoms, molecules) at points of the lattice: constructive interference appears, if the change of the wave vector during the scattering process corresponds to a vector of the reciprocal lattice:

$$\vec{k} - \vec{k}' = \Delta\vec{k} = \vec{g} \quad (2.3)$$

\vec{k} and \vec{k}' are the incoming and outgoing beam, $\delta\vec{k}$ is the change of them, \vec{g} a reciprocal lattice vector. For elastic scattering is $k = k' = \frac{2\pi}{\lambda}$.

A geometric interpretation of the Laue condition is the Ewald sphere (see figure 2.4). Its radius is the inverse of the electron wave length and its centre is the centre in real space. Points of the reciprocal space which are on the sphere are connected by reciprocal lattice vectors \vec{g} . Constructive interference occurs in the direction, where reciprocal points are on the sphere. As shown in figure 2.4, the image on the detector is only a gnomonic projection; therefore, a diffraction pattern is the two-dimensional projection of the three-dimensional surface of the Ewald sphere in reciprocal space.

For low energy electrons, the mean free path length in the sample is very small (about 1 nm) in comparison to the width of the probed sample surface (about 5 μm). So, the probed area is a disc, with only the topmost slice of the sample being probed. This transforms the lattice points to perpendicular streaks to the surface in reciprocal space.

The intensity of the diffraction spots I found in LEED can be described as a function of the combination of the diffracted intensities by the lattice $G(\vec{k}, \vec{k}')$ and by the basis $F(\vec{k}, \vec{k}')$:

$$I = G(\vec{k}, \vec{k}') \cdot F(\vec{k}, \vec{k}') \quad (2.4)$$

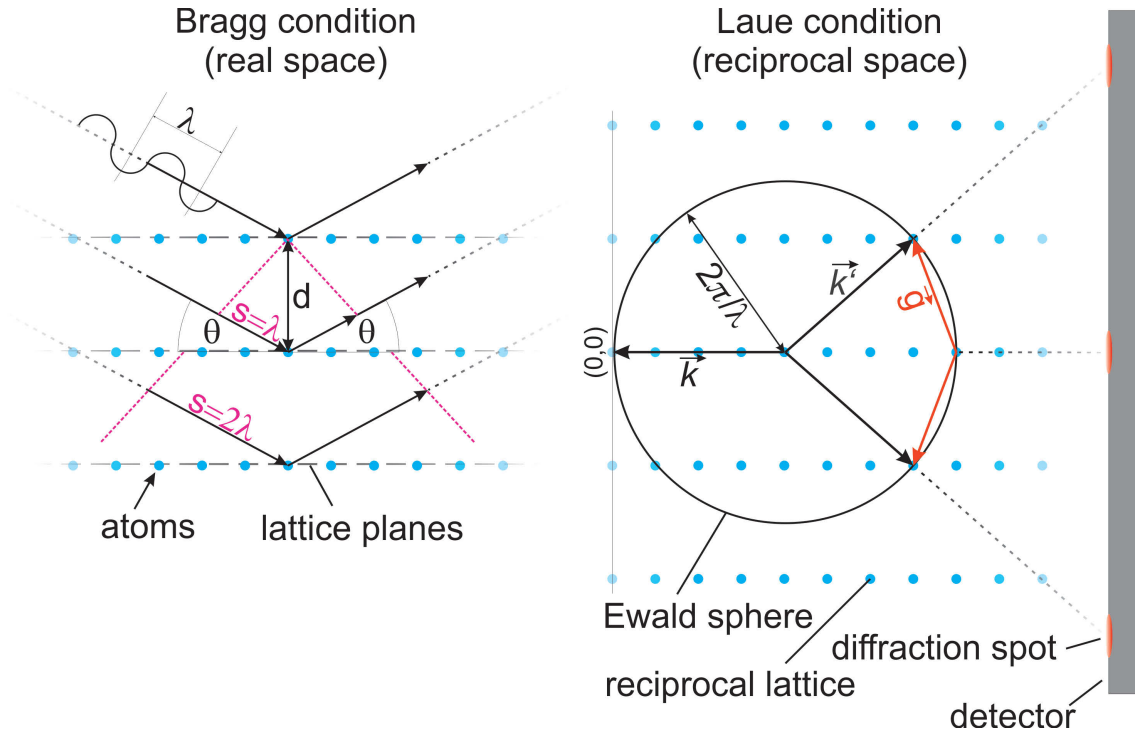


Figure 2.4: Illustration of the Bragg and Laue condition. For details see text.

$G(\vec{k}, \vec{k}')$ is the intensity lattice factor and $F(\vec{k}, \vec{k}')$ is the intensity structure factor. The intensity structure factor is the addition of the atomic form factor f_k , which describes the reflection of each atom k of the basis as function of the angle of the incoming electron beam. In general, the intensity lattice factor is strongly dependent on the lattice orientation relative to the incoming electron beam, while the intensity structure factor is more dependent on the kinetic energy of the electrons.

With increasing StV the radius of the Ewald sphere increases and the intensity dependence on the kinetic energy of the streaks in reciprocal space is probed.

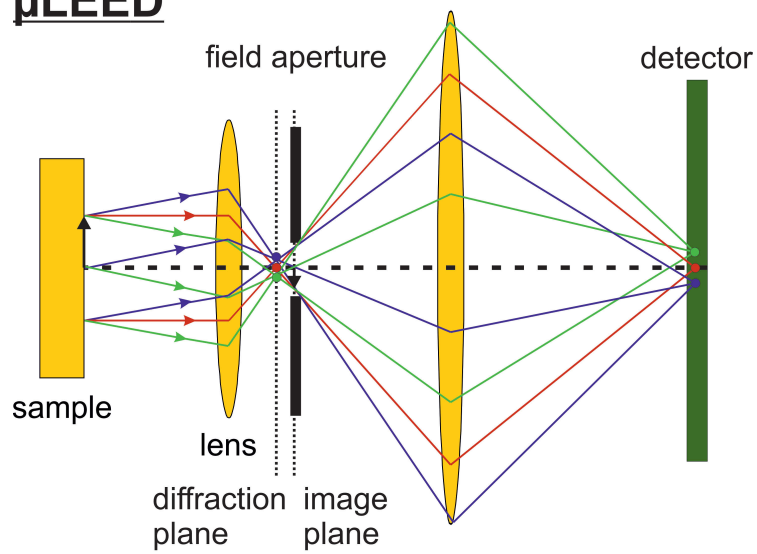
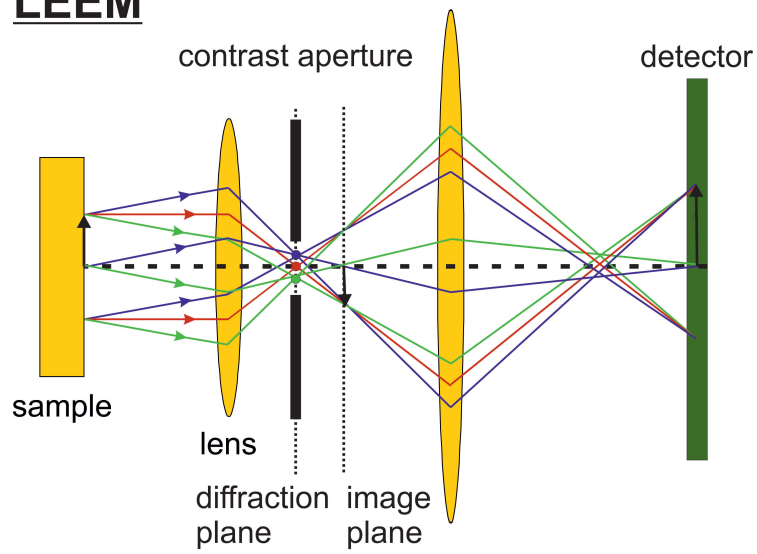
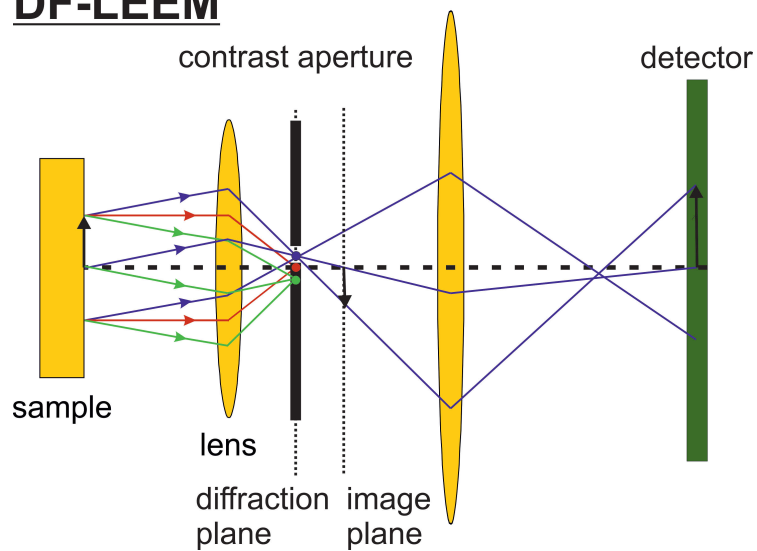
The objective lens focuses all diffracted beams in its back focal plane (diffraction plane). In the μ LEED mode at the SMART, the back focal plane of the objective lens is minimized by the excitation of the first transfer lens in front of the entrance slit (contrast aperture, in this case acting as a field aperture) of the Omega filter and therefore projected onto the phosphor screen (see figure 2.5). This enables the investigation of the crystal structure of a sample area of about $5 \mu\text{m}$. In LEEM, the back focal plane is magnified in the plane of the contrast aperture. Diffracted beams, which are far off the optical axis, cannot pass the contrast aperture and therefore are blocked (see figure 2.5). Electrons that mainly contribute to the (0,0) diffraction spot or that are in close angular range of it can pass the contrast aperture (purple and green in figure 2.5). This increases the contrast of the image. This mode is

called bright field mode. In contrast, in the dark field mode (DF) any of the other LEED spots than the (00) beam is used. In principle, one could mechanically move the contrast aperture in the LEED plane to select that spot, but that would cause large aberrations (with a related loss of resolution) due to off axis beams. Instead, in DF-LEEM the incoming electron beam is deflected. By the deflection with the appropriate angle, a diffracted beam is brought on the optical axis of the microscope and only electrons mainly contributing to a specific diffraction spot can pass through the contrast aperture, for example the violet beam in figure 2.5. In the DF-LEEM image only areas contributing to the selected diffraction spot are visible, so different phases, or rotated domains can be visualized.

The LEED image contains information of the crystal structure. So using it the two-dimensional basis perpendicular to the incoming beam and its atomic distances can be determined. Furthermore, Intensity vs. voltage LEED (LEED(IV)) measurements, which correspond to the intensity dependence of the diffraction spots when the StV is changed (known as LEED(IV) curves), are very sensitive to the atomic arrangement and therefore are good finger prints for different phases having a similar crystal lattice. With the help of the dynamic LEED theory, where multiple scattering is considered, the intensity dependence for a certain atomic arrangement can be simulated. However, these calculations are very complex and done in an iterative way until a good agreement with the experimental data is achieved, so they are a task in themselves which would transgress this work. The spot profiles contain information about the statistical distribution of distances or sizes of defects on the surface like islands, structural domains, terraces or steps.

On the other hand, the LEEM image contains information of the 2D surface morphology. In principle, three different kinds of contrast are possible: the phase contrast, the amplitude contrast and the diffraction contrast. The phase contrast depends on the kinetic energy of the electrons. A part of the wave is reflected on the upper part of the step, the other part on the lower side. After reflection the two partial waves interfere with each other. In case of the phase shift of π , corresponding to half wave length, destructive interference occurs. Moreover, the amplitude contrast takes the reflectivity of different atoms and their arrangement in the unit cell into account, especially in the atomic form factor. Additionally, the diffraction contrast

Figure 2.5 (facing page): *Illustration of the principles of μ LEED, LEEM and DF-LEEM at the SMART microscope. The primary electron beam is not shown, it is perpendicular to the surface like the red beam. For details see text.*

μ LEED**LEEM****DF-LEEM**

is enhanced by using a contrast aperture and blocking diffracted beams far off the axis (see bright field or dark field mode above and figure 2.5).

2.3 μ XPS

Here only the basics of photon electron spectroscopy will be addressed. For a more detailed explanation see [42].

Photoelectron spectroscopy is a widely used technique in surface science. Its early beginnings go back to the end of the 19th century, when it was noticed that light interacts with electric charge [43,44]. In 1900 P. Lenard managed to produce cathode rays by illuminating a cathode with UV light and determined the emittance of electrons as reason [45]. Moreover, he found a dependence of the frequency of the light on the kinetic energy of the electrons. Later, Einstein explained this behaviour by the photoelectric effect [46]. Basically, his theory describes electrons which are bound by a positive coulomb potential originating from the atom cores. A photon provides the energy E_{Photon} for an electron to overcome this potential barrier and to leave the atom or solid, respectively. A surplus of the photon energy is conserved as kinetic energy of the electron leaving the solid. The invention of electron spectrometers allowed to determine the spectrum of emitted photo-electrons depending on the kinetic energy [47,48]. It was found that each element has specific peaks in its electron spectrum and that chemical shifts of these peaks exist for differently bound atoms [48] in molecules or substances. The chemical shift of the electrons of an atom is very sensitive to the next neighbouring atoms, so that it allows to investigate the close chemical surrounding of an atom. So, photo-electron spectroscopy can be used for the chemical analysis of a substance. Each element emits electrons from states with a specific binding energy E_{Bin} , it can be determined through:

$$E_{Bin} = E_{Photon} - E_{Kin} - \Theta \quad (2.5)$$

where Θ is the work function (energy difference between the Fermi energy E_F and the vacuum energy E_{Vac}).

The photoemission process can be described by a one-step model [49] or by a three-step model [50]. In the one-step model, the wave function of an electron within a solid couples with a wave function in vacuum, whereby the electron executes the transition directly into the vacuum. The three-step model describes the photoemission of the electron by three partial steps: the excitation of an electron of an atom, its transport to the surface and its exit into vacuum.

As lab sources for x-rays magnesium or aluminium anodes are very common, however, their photon energy is fixed. Synchrotrons and their beamlines have the advantage of the tunability of the photon energy for x-rays. In BESSY II the x-ray

light is guided in a beamline to the SMART, focused and illuminates then a sample area of about $16 \mu\text{m}^2$ in grating incidence. For these measurements, the electron beam of the electron gun is deflected so it cannot pass through the beam splitter. The emitted photoelectrons are then accelerated into the direction of the objective lens, due to the electric field between the sample and the lens. The part of the kinetic energy spectrum of electrons which are to be recorded can be set by the start voltage. Only those electrons can pass the Omega filter. A field aperture can be introduced in the image plane before the Omega filter, allowing the probing of an area of typically $5 \mu\text{m}$ (minimum is 100 nm) to obtain localized spectra of the sample surface. The projection lens system is set such that the energy dispersive plane of the Omega filter is directly imaged onto the multi-channel plate and acquired as image. In the energy dispersive plane, the electrons are dispersive in the horizontal axis, while in the vertical axis the vertical lateral distribution at the sample surface is imaged. A raw image of the dispersive plane is shown at the left side in figure 2.6, with a size of 1600×1200 pixel. It is visible that the image of the energy dispersive plane is smaller than the image acquired by the CCD chip of the camera, it has a width of about 950 pixel corresponding to 17 eV. The kinetic energy of the electrons increases from right to left. The photoelectron spectra can be extracted by a cut along the horizontal plane of the image, which is shown in the right side of figure 2.6. The kinetic energy axis is then calculated by

$$E_{Kin} = StV + \frac{x_0 - x}{56} \quad (2.6)$$

Here x_0 is the position of the pixel, where the electrons with the exactly set start voltage arrive. Its value is determined by using the elastically backscattered electrons of the electron gun, because they produce a sharp peak in the energy dispersive plane. In the horizontal axis 56 pixel correspond to 1 eV, so it is possible to assign a kinetic energy to every pixel.

The kinetic energy of the electrons at the valence band edge representing the electrons with the Fermi energy $E_{(Kin,Fermi)}$ can be fitted for each measurement. Then the Fermi energy is arbitrarily set as the zero point for the binding energy scale. This was the procedure adopted throughout the whole set of measurements of this thesis because the photon energy could vary due to small changes in the beamline in the range of one eV or below. The Fermi energy is here more reliable, because of the small thickness of the silica, so that the Fermi level of bulk ruthenium is always measured and used as a reference between different measurements. The binding energy is then determined by

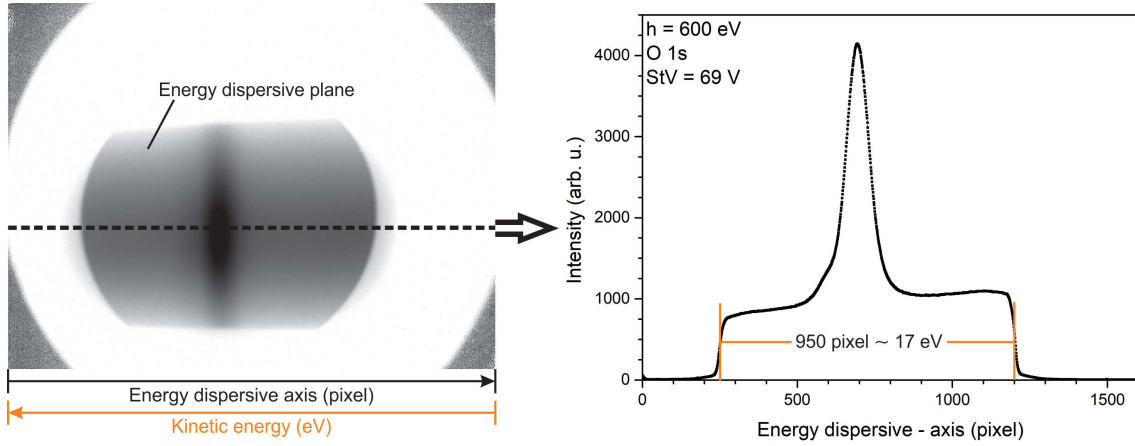


Figure 2.6: Inverse grey-scale image of the energy dispersive plane and the curve of the horizontal cross-section through it. The O 1s region of an electron spectrum is shown. For details see text.

$$E_{Bin} = E_{(Kin, Fermi)} - E_{Kin} \quad (2.7)$$

Due to the mean free path of electrons in a solid, the information depth is restricted to a few atomic layers and XPS is therefore surface sensitive. The mean free path depends on the kinetic energy of the electrons [51], so by choosing the right photon energy the same sample depth for different binding energies can be probed. In this work, the photon energy was always tuned in a way that the region of interest of the photoelectron spectrum had a kinetic energy of about 70 eV there the mean free path length has a minimum for most elements of about 0.4 nm. These photon energies are 175 eV for the Si 2p line, 360 eV for the Ru 3d line and 600 eV for the O 1s line.

Overview of preparation and characterization of the investigated film structures

The following chapters describe the method to prepare a (2x2) crystalline silica mono- or bilayer [8,9] and the preparation conditions for a yet unpublished crystalline structure found on Ru(0001). In the chapters, each preparation step is described and investigated in detail with LEEM, LEED and photoelectron spectroscopy measurements. A model of the oxidation of silicon on ruthenium surface with ruthenium acting as a catalyst is proposed.

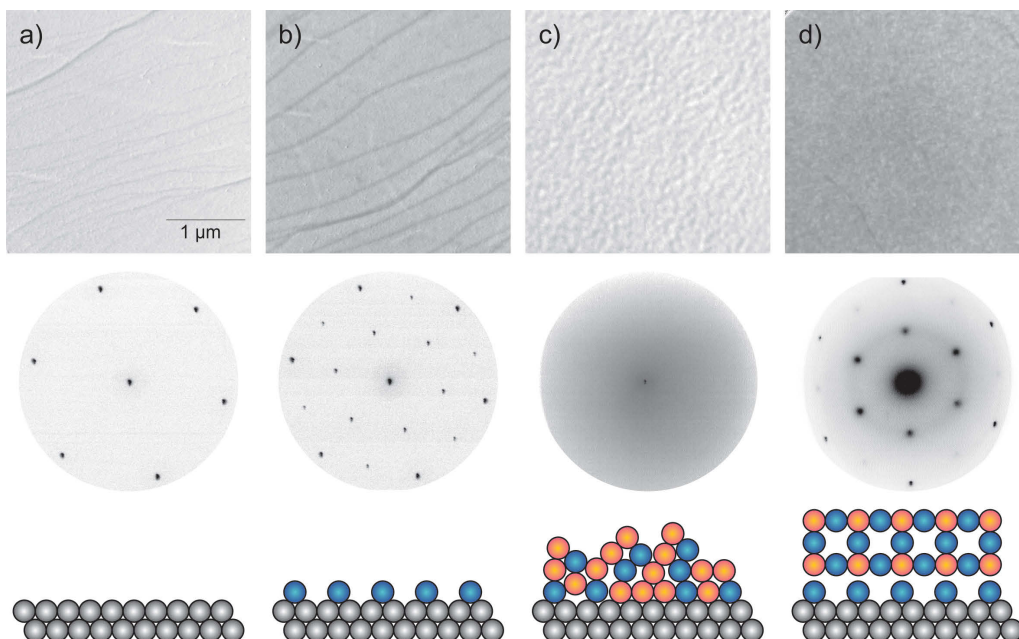


Figure 2.7: Upper row: LEEM images in linear contrast scaling, middle row: corresponding LEED images in inverted logarithmic contrast scaling, lowest row: ball model of surface; grey balls represent the Ru atoms, blue ones oxygen atoms, and orange ones Silicon atoms. Column a) clean Ru(0001), b) 3O terminated Ru(0001), c) after silicon deposition and d) after final oxidation and annealing.

As an introductory image, figure 2.7 contains in a) to d) the four main steps of the common (2x2) silica bilayer preparation: The clean Ruthenium surface, the oxygen terminated surface, after silicon deposition and after the final annealing in oxygen. Starting with clean Ru(0001) (figure 2.7a)): In the LEEM image thin black lines are single atomic steps on the surface, while thick black lines represent step bunches. The atomically flat terraces show no special contrast and are uniformly grey. The LEED shows a hexagonal (1x1) pattern with no extra spots. After an oxygen treatment to produce the 3O structure the surface shows in LEEM still the same features as for the clean Ruthenium, but the LEED shows an additional (2x2) superstructure (figure 2.7b)). Silicon deposition at RT leads to an unordered, not completely oxidized silica film on the surface. In contrast to figure 2.7a) and b) in c) atomic steps or step bunches are not visible anymore. The surface looks homogeneously rough. The (2x2) LEED pattern has vanished and only the (0,0) spot remains. After a final annealing step in oxygen in LEEM atomic steps and step bunches are visible again (figure 2.7d)). The roughness at the terraces is decreased, but they do not look as smooth and homogeneous as for clean or oxygen terminated ruthenium. The LEED pattern shows a (2x2) reconstruction again and a weak ring structure connecting the (2x2) spots.

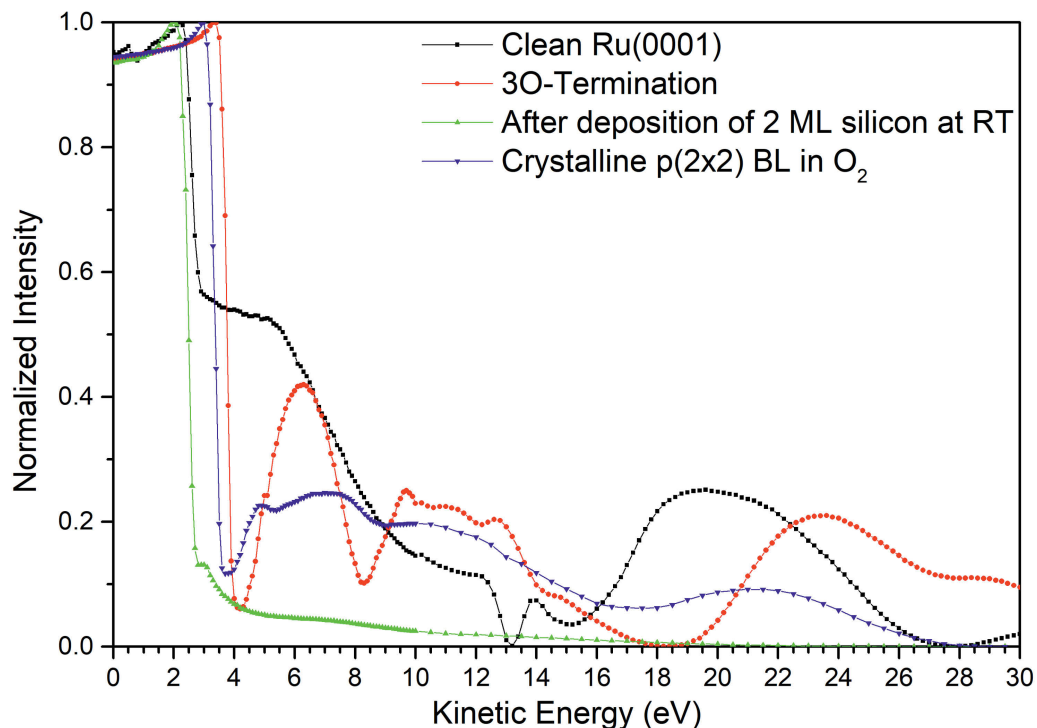


Figure 2.8: LEEM(IV) curves for each preparation step. The black curve represents the clean Ru(0001), the red one the oxygen terminated ruthenium surface, the green one that after silicon deposition and the blue one that for the silica film after the final oxidation. The curves were normalized using the maximum intensity of the MEM region.

As the surfaces show only small differences in LEEM between clean, oxygen terminated, and silica covered and the LEED mainly shows (2x2) spots, visual identification of the different silica phases is quite difficult. It turned out that for each preparation step a characteristic LEEM(IV) curve is found. Thus, these curves can be used as finger print for the various stages, despite the lack of a full understanding of all features at present. Moreover, the transition from MEM to LEEM changes for each step, showing also a dependence on the surface dipole, which turns out to be also dependent on the oxygen coverage (see figure 2.8) and therefore could lead to misinterpretations.

The clean Ru(0001) surface

Ruthenium is a noble metal belonging to platinum group metals and therefore a transition metal. Its atomic number is 44 and has an atomic weight of 101.07 u [52]. Its crystal structure is hcp with $a = 0.428$ nm and $c = 0.271$ nm [53]. At room temperature it appears silvery - white metallic. It is used as a catalyst in ammonia synthesis [54–56] and for the methanol decomposition in direct methanol fuel cells [57, 58], as organometallic catalyst [59], and plays an important role as an intermediate layer in hard disk drives [60, 61]. In science it is used as a model catalyst, for example for CO catalysis [62].

In this study a ruthenium single crystal with a diameter of 10 mm and a height of 3 mm was used. It has been cut, oriented and polished in the crystal lab of the Fritz-Haber-Institute from a boule purchased from MaTeck (Mateck GmbH, Im Langenbroich 20, 52428 Jülich).

To achieve a clean Ru(0001) surface the following cleaning steps were performed. They were based on the suggested cleaning steps of [63]:

1. Cleaning by Argon ion sputtering for at least 15 min with $I_s = 5 \mu\text{A}$ and $U_{\text{Acc}} = 1.2$ kV.
2. O_2 annealing in $p_{\text{O}_2} = 2.0 \times 10^{-6}$ mbar with 1 K/s up to 600 K, then fast increasing to 1100 K and holding for 5 min.
3. Closing O_2 valve and continuing annealing for 5 min with 1250 K at base pressure lower than 5.0×10^{-9} mbar.
4. Afterwards flash to 1350 K and holding for 1 min and fast cooling down with >5 K/s.

This leads to a stepped surface with an average terrace width of about 200 nm or larger (figure 3.1a) and b)) and the LEED shows a (1x1) pattern of the Ru(0001) surface (figure 3.1c)). In the LEEM image thin black lines are single atomic steps on the surface and the atomically flat terraces show no special contrast and are uniformly grey.

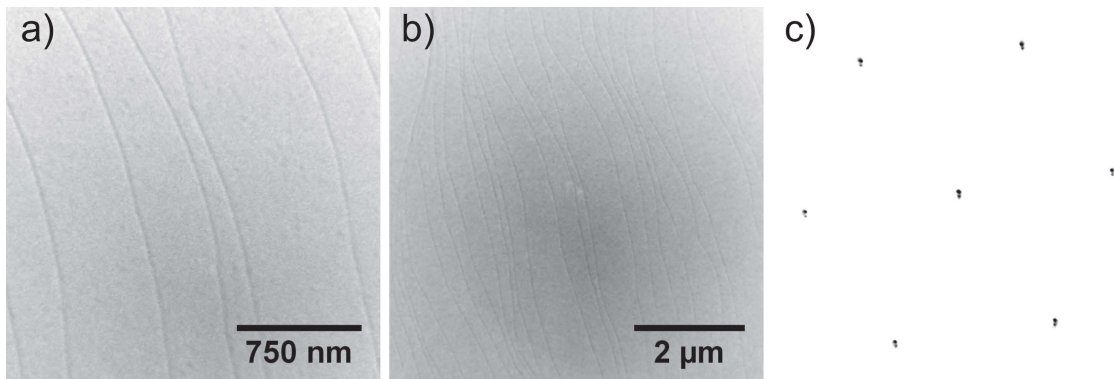


Figure 3.1: LEEM and LEED images of a clean Ru(0001). a) shows the large atomically flat terraces in detail on the surface, b) is an overview over several micrometres of the surface. c) (1x1) Diffraction pattern of the clean Ru(0001) surface in inverted logarithmic contrast scaling. All kinetic energies are 42 eV.

The hcp reconstruction has threefold symmetry, but the experimental LEED pattern is 6-fold symmetric. The reason for this is the stepped surface, where the atomic layers on the adjacent terraces are rotated by 180° [64] (see figure 3.2). Inside the unit cell four different adsorption sites are visible: The hcp site, where there is a ruthenium atom below, the fcc site, where there is no ruthenium atom below, the bridge site between two neighboring atoms and the top site - on top of an atom.

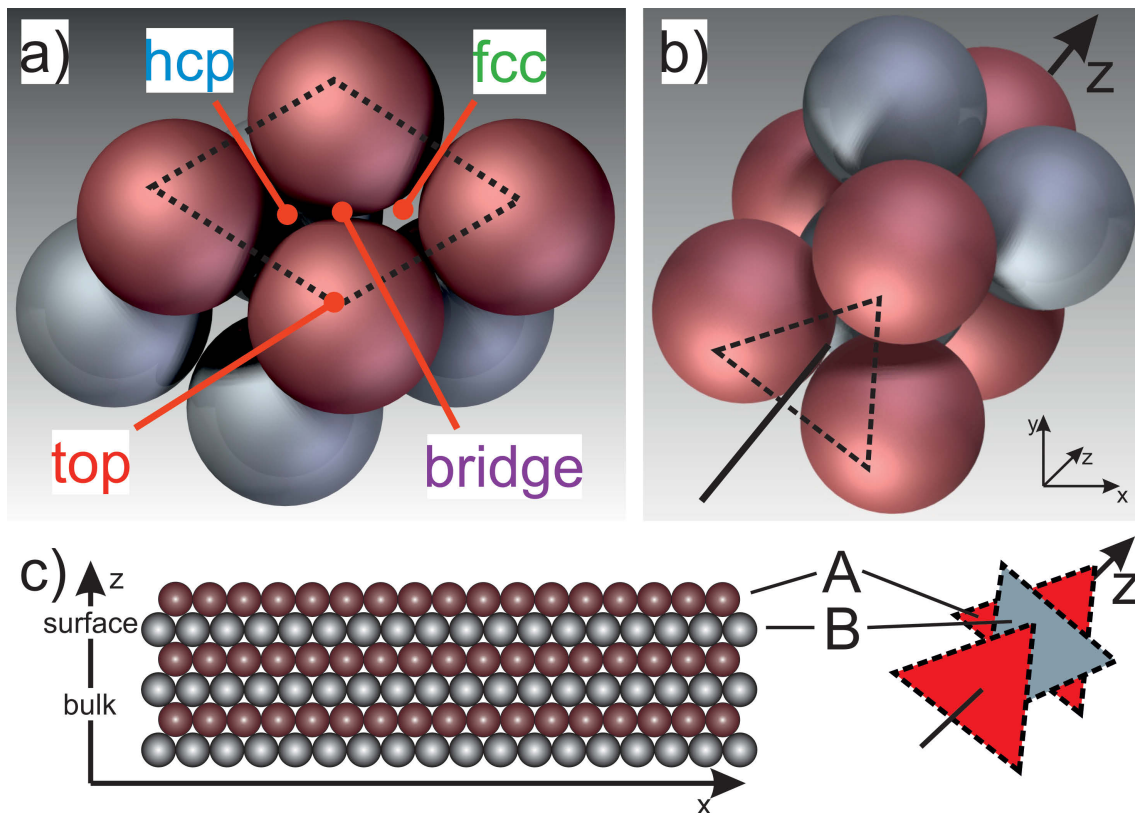


Figure 3.2: Models to explain the symmetry of ruthenium. a) is a top view of the Ru(0001) surface with its preferred adsorption sites. The red balls represent the first layer, grey ones the second, the dashed line marks the unit cell of Ruthenium. b) is a oblique projection of three ruthenium layers. c) sketches the situation in b) with the AB stacking by a side view of the ruthenium crystal and the 180° rotation of the layers to each other.

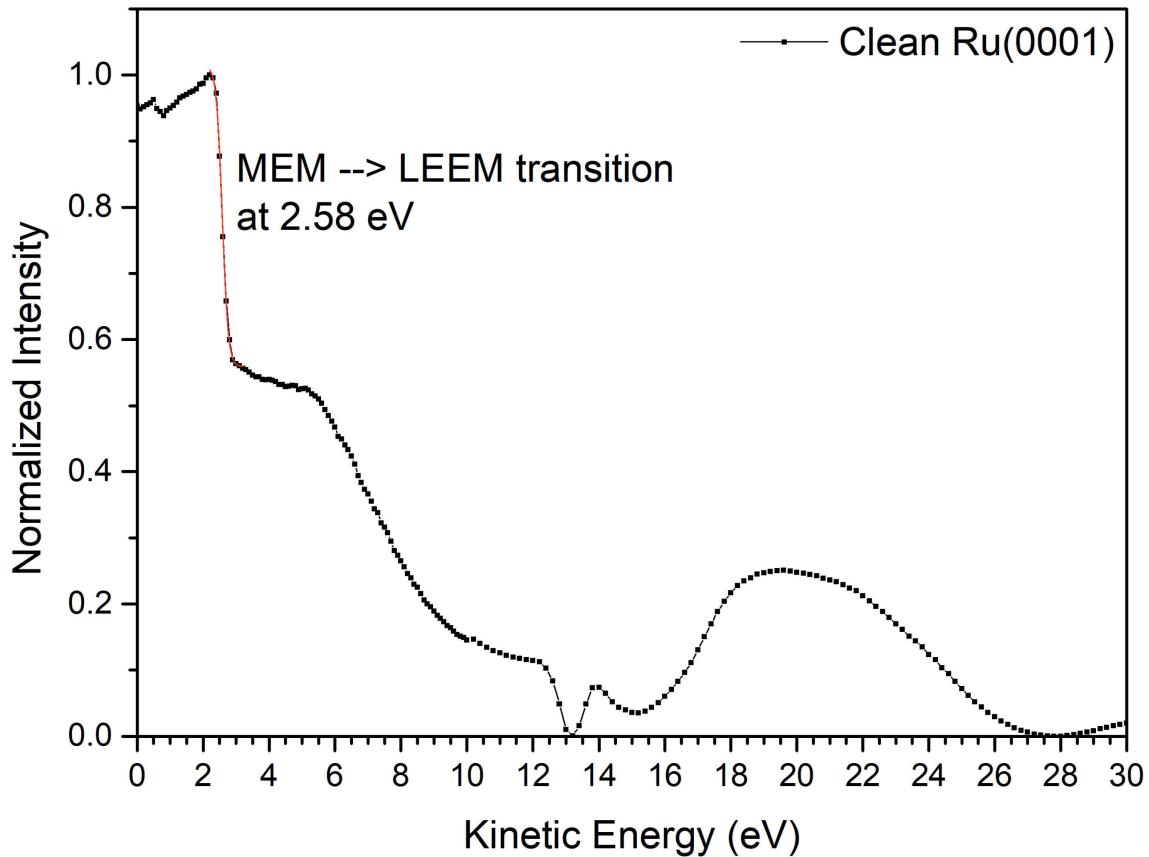


Figure 3.3: LEEM(IV) reflectivity curve of a clean Ru(0001) surface measured in bright field. The curve is normalized to the MEM region, where 100 % of the electrons are reflected.

The LEEM(iV) curve represents the energy dependent reflectivity in real space of the electrons contributing to the (0,0) spot in reciprocal space. For the clean surface it shows characteristic and remarkable features (figure 3.3). The MEM to LEEM transition for the used microscope (depending mainly on the electron emitter potential and the possible offset voltage of the voltage supplies) happens at 2.58 eV, then by a small plateau of nearly constant intensity with a width of 2 eV and followed by a strong loss of intensity. In the shown energy range there are two minima, assigned to an unoccupied f-band state of the surface (13.2 eV) and the bulk states (15 eV) discussed in detail in [65]. A newer publication suggests that this feature originate from a complicated multiBloch-wave structure of the LEED state [66]. The intensity has a broad maximum of 6 eV width at 20 eV and a following decrease.

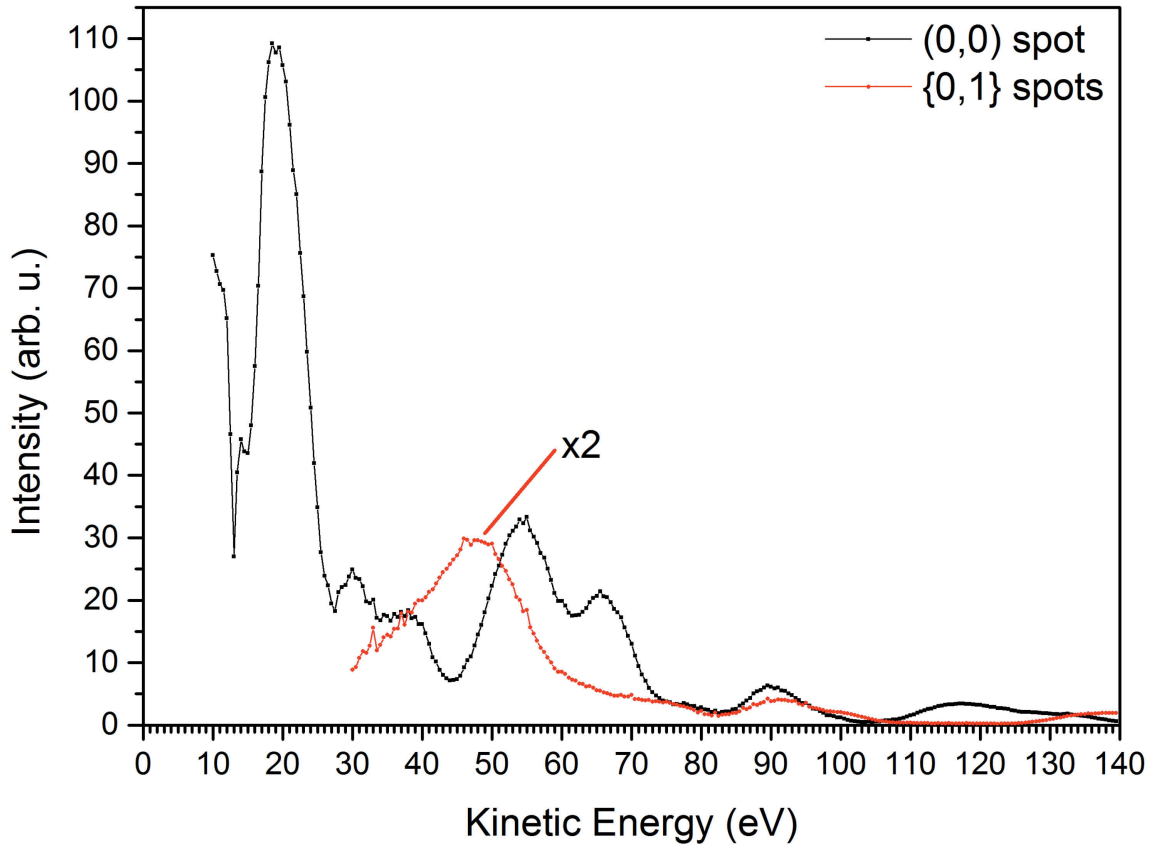


Figure 3.4: LEED(IV) curves of clean Ru(0001) of the (0,0) and {0,1} spots in the energy range between 10 to 140 eV.

While LEEM(IV) measurements give the opportunity to probe differences in the lateral reflectivity, LEED(IV) measurements allow to measure the reflectivity differences of the diffracted electrons. In comparison to LEEM(IV) measurements they can be performed much faster over a larger energy range. Figure 3.3 shows a LEED(IV) of a clean Ru(0001) surface for the (0,0) spot and {0,1} spots with a wider energy range. As already pointed out the reflectivity curve of the (0,0) spot shows the same features as the LEEM(IV) curve, comparing the energy range between 10 to 30 eV.

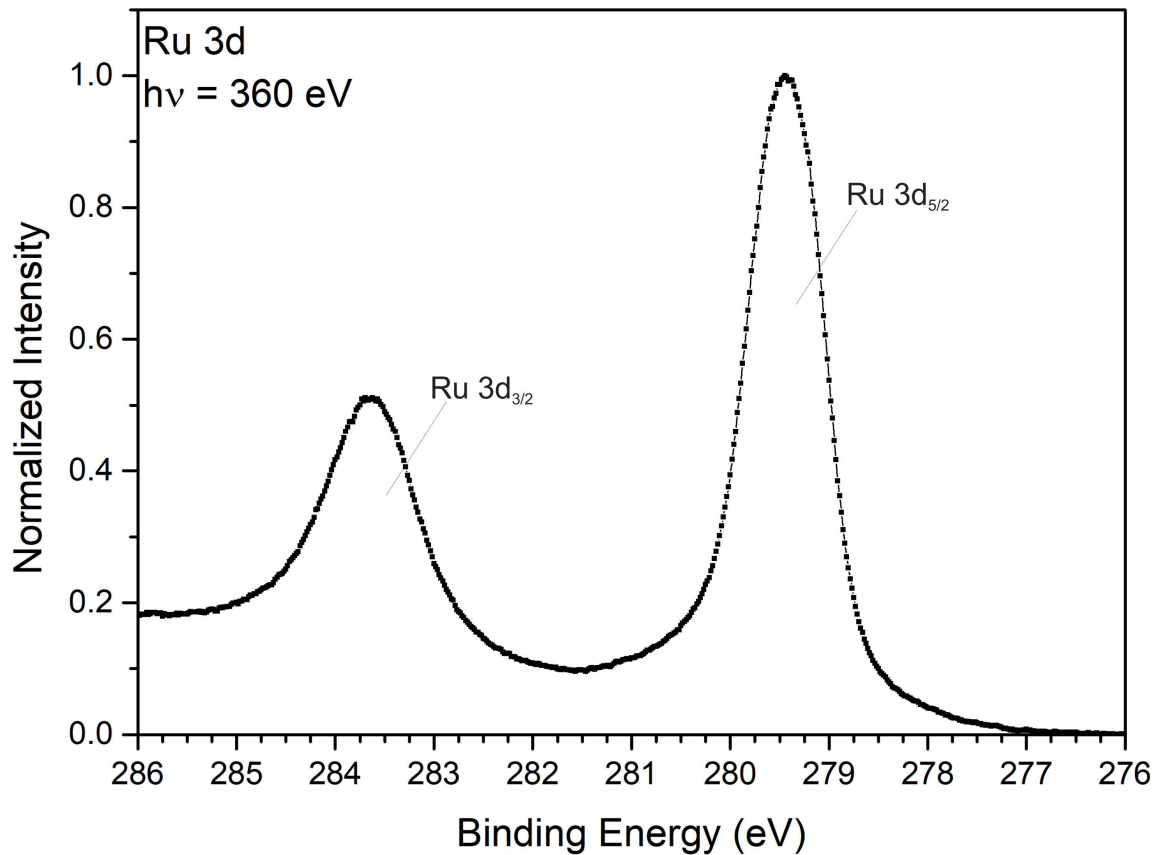


Figure 3.5: XPS spectra of Ru 3d core level peaks of clean Ru(0001) measured with 360 eV photon energy.

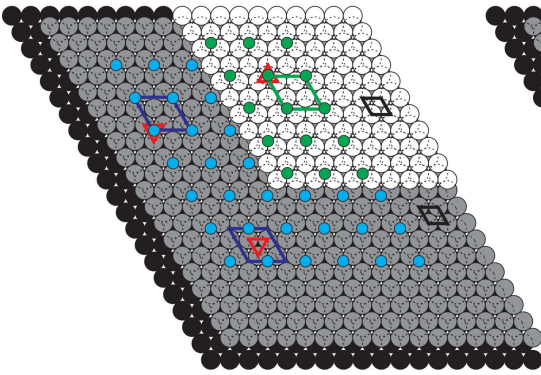
Figure 3.5 shows the photoelectron spectra of the Ru 3d region of clean Ru(0001). Two shoulders are visible at the Ru 3d_{5/2} peak at about 280 eV, they can be assigned to surface and (sub-) surface core level shifts of the first and second atomic layer of the clean Ru(0001) surface [67–69]. However the whole peak is shifted by about 0.5 eV to lower binding energies in comparison to the measurements in [69].

The oxygen terminations of Ru(0001)

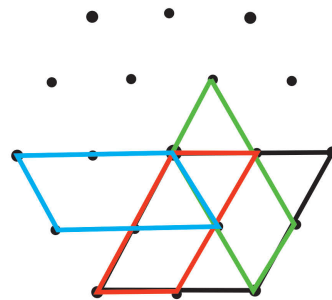
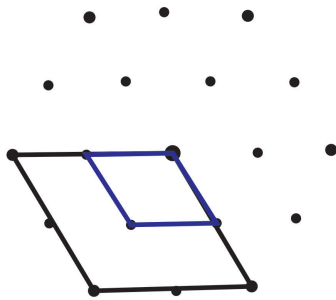
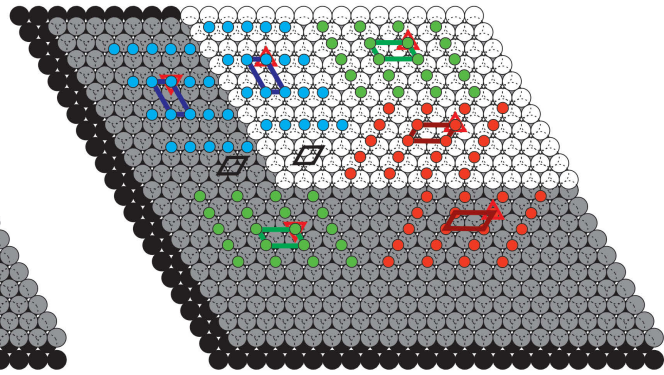
4.1 The oxygen covered ruthenium surface

Oxygen can adsorb in different amounts on the surface. The preferred adsorption site is the hcp hollow site of the Ru(0001) surface, where it strongly chemisorbs [70]. The different coverages lead to four different ordered arrangements [63, 71–73]; three show a “(2x2)” reconstruction and one a (1x1) reconstruction in LEED. The main difference is the amount of oxygen atoms in a (2x2) unit cell, so they are here referred as: 1O termination corresponding to a coverage Θ of 0.25 ML, 2O termination corresponding to a coverage Θ of 0.50 ML, 3O termination corresponding to a coverage Θ of 0.75 ML and 4O termination with a corresponding coverage Θ of 1.00 ML [74] (see figure 4.1). A further exposure to an oxygen atmosphere will lead to an oxide formation with the stoichiometry RuO₂ [75–77], crystallizing in a rutile structure, or nonstoichiometric RuO_x [78, 79].

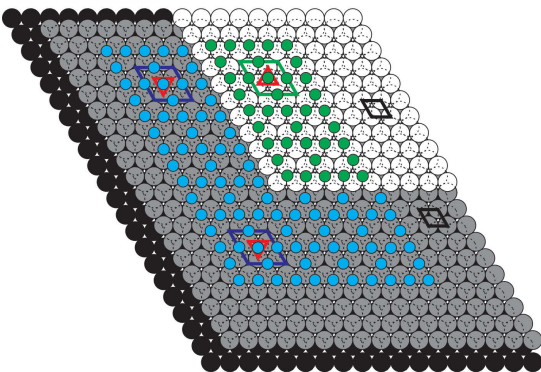
1O - Termination



2O - Termination



3O - Termination



4O - Termination

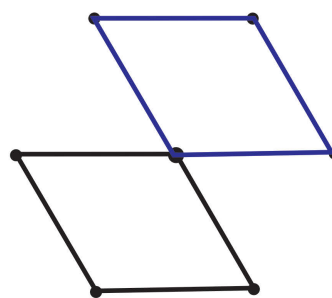
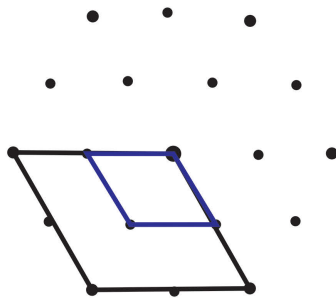
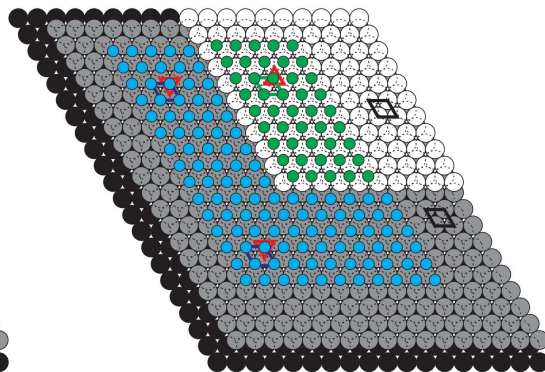


Figure 4.1 (facing page): Ball models and corresponding diffraction patterns of the different oxygen terminations on Ru(0001). Black, grey and white balls represent the Ru atoms in different layers/terraces of the surface. Blue, green and red balls represent adsorbed oxygen atoms. For each model the unit cells are drawn in the ball model, in the diffraction pattern the unit cell of Ru(0001) are indicated as thin black lines and the corresponding oxygen unit cell is marked as thick dashed line.

A plot of the overall intensity in DF-LEEM of one (1/2) spot during oxygen exposure at room temperature is shown in figure 4.2 a) (next page). It resembles the LEED intensity behavior published in [63] quite well. However, the structures are shifted to lower exposures than in [63] and they are in good agreement with data reported in [69]. A possible explanation for the difference to [69] would be that the initial surface in our experiments was already pre-covered with a small amount of oxygen. At the beginning of the oxygen exposure the intensity increases very fast and goes through a sharp maximum, indicating the appearance of the 1O termination (point c) in the curve). With increasing oxygen amount the intensity decreases and goes through a local minimum, marked d) and increases again steeply afterwards. A broad maximum indicates the formation of the 2O termination (point e)). With continuing exposure, the intensity decreases further until theoretically a 3O and then a 4O termination is formed.

The DF images in figure 4.2 b)-d) show the most critical changes during oxygen adsorption and are taken from the same data set as the intensity curve. a) shows the surface at the start of the experiment, before the introduction of oxygen into the chamber. As already mentioned in chapter 3, ruthenium has a threefold symmetry, so every second terrace is out of phase and appears dark at certain energies. b) After introducing oxygen the surface looks rougher and the formation of homogeneously distributed small white islands over the surface is visible. Comparing with [80, 81] this indicates the adsorption of oxygen onto the surface. c) The islands grow until their borders meet. Because of the statistical appearance of the islands, their unit cells can be shifted about half a unit cell to each other, leading to antiphase boundaries, visible as black lines in the image. The coverage corresponds to $\frac{1}{4}$ ML of oxygen at this point. With increasing oxygen amount on the surface, one atom is added to the $p(2 \times 2)$ unit cell transforming it to a (2×1) ; this starts at the antiphase boundaries and the 1O islands vanish. When a coverage of 0.375 ML is reached, one half of the surface consists of a 1O termination and the other half of a 2O termination (see point d) in the curve and the corresponding DF-image). When the entire area of 1O termination is converted into 2O the intensity reaches a second, global maximum, point e). The DF image in e) shows the three different domains of this structure: a bright, a grey and a black one on the terraces that are in phase, and the grey one on the terraces that are out of phase. Because of how the transformation is occurring, some similarities between the shape of the domains of the 2O and the 1O islands can be found. A further increase of oxygen leads to a dissolution of the domains, starting again at the phase boundaries (see image f). The formation of the 3O and 4O terminations could not be visualized by DF field imaging. Possible reasons could be that the temperature was too low, the formation of the domains are below the resolution limit of the microscope or a significantly longer exposure would be needed [74].

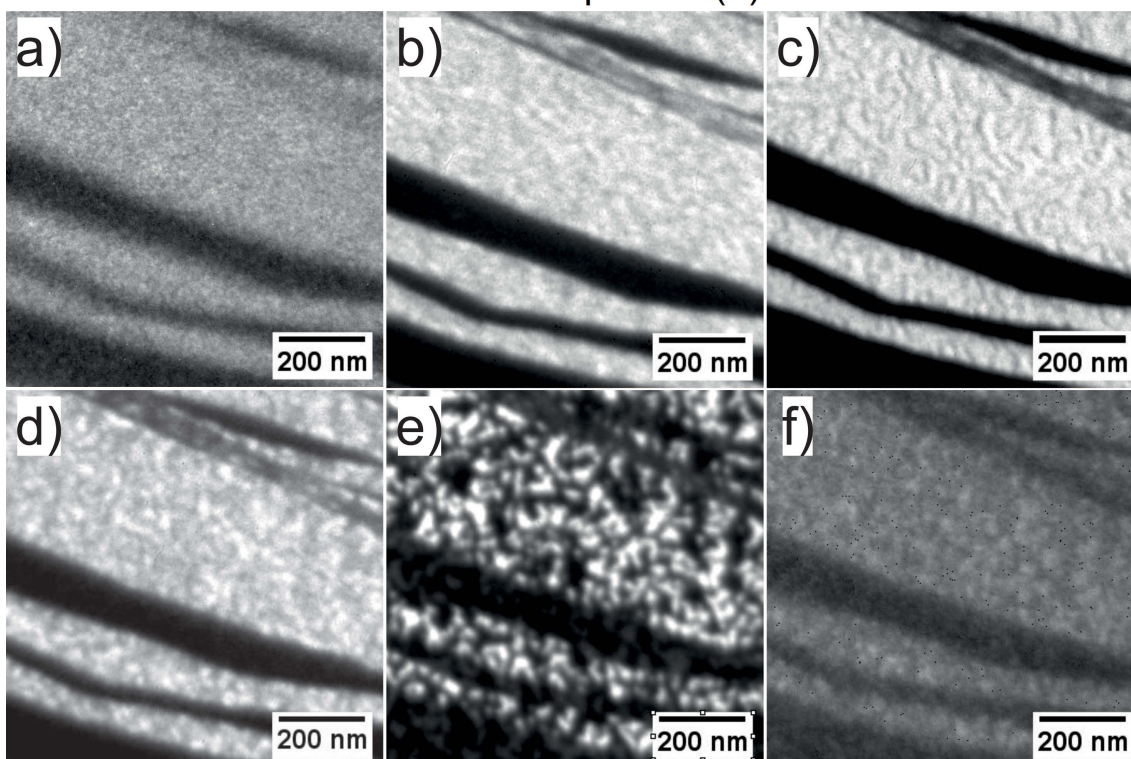
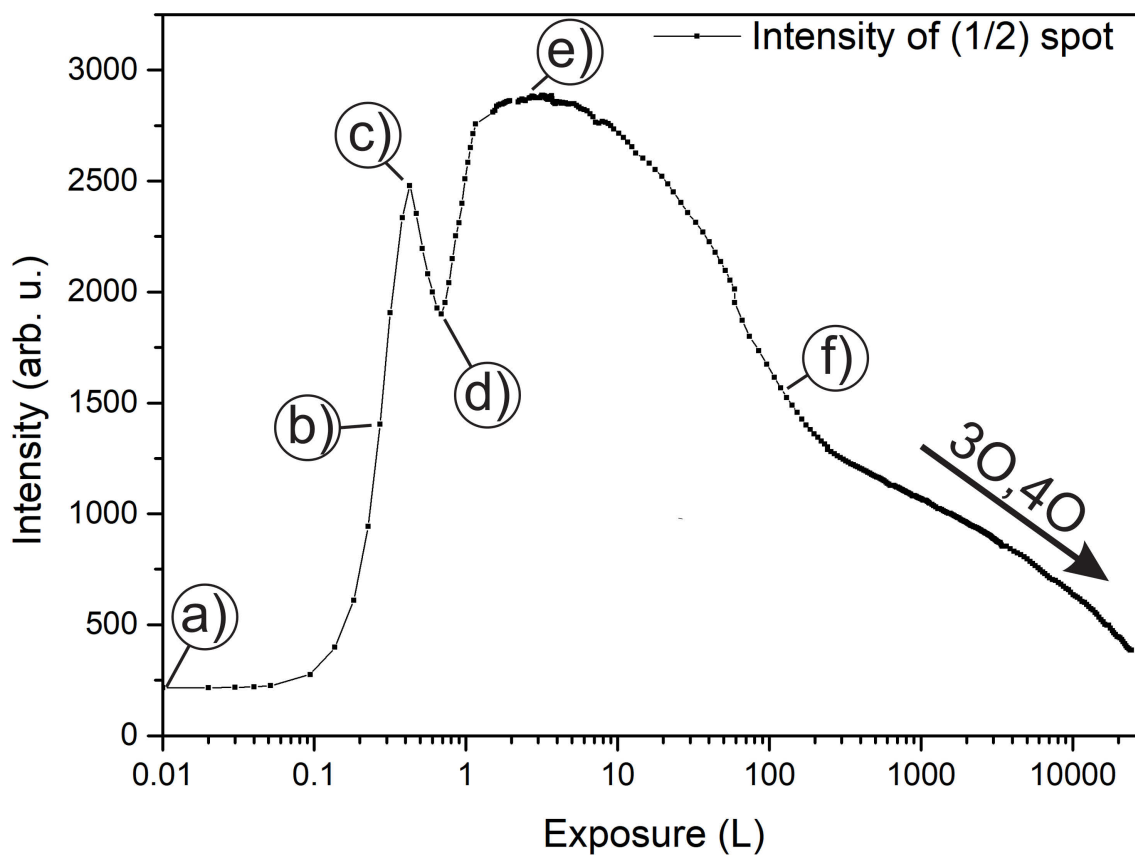


Figure 4.2: Plot of the overall intensity in DF-LEEM of the (1/2) spot as a function of oxygen exposure on a clean Ru surface at 320 K. The points a-f mark critical points in the curve and the according images of the measurement are shown in the lower half of the figure (for a detailed description see text). A kinetic energy of 16 eV was used.

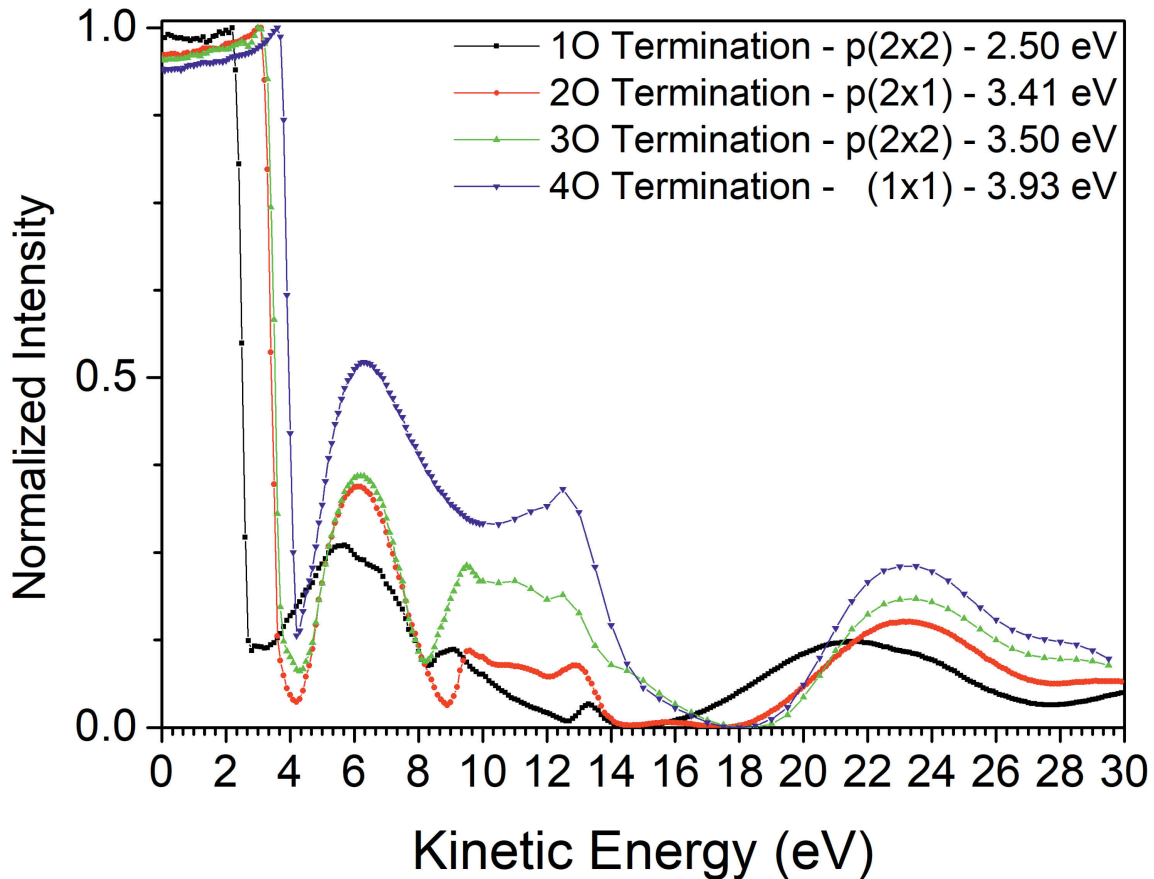


Figure 4.3: Comparison of the LEEM(IV) curves of the different O-Terminations of Ru(0001) measured in bright field. The curves are normalized to the MEM region, where 100 % of the electrons are reflected.

In figure 4.3 the LEEM(IV) curves for the different terminations are shown. Four main points are clearly visible.

First, while increasing the oxygen amount, the work function (also known as MEM to LEEM transition) also increases. The values for each curve's transition are given in the legend of the figure. The measured differences are in agreement with [63], only for the lowest coverage of $1/4$ ML the value differs and is lower than expected.

Second, with increasing amount of oxygen the peaks arising between 6 to 14 eV are clearly assignable to oxygen. Especially the peaks between 10 to 14 eV seem to be connected to the rising amount of oxygen in the unit cell.

Third, the “dip” of the unoccupied 4f surface states at around 13 eV for clean Ru(0001) vanishes (compare to figure 3.3), while the minimum for the unoccupied bulk states is still present, just shifted by the same amount as the MEM to LEEM transition to values about 17.5 eV. The same shift can be assigned to the peak of the maximum of clean Ru(0001) at 20 eV (see figure 4.3) that shifted to around 23 eV.

Fourth, with increasing amount of oxygen the overall reflectivity increases, a possible reason could be the increased amount of scattering centres on the surface. The shown measurements fit very well to vLEED measurements reported in [82], comparing there to measurements with a small offset of the surface normal. A special option of LEEM/LEED microscopes is the possibility to measure with very low energies, even lower than vLEED, and to access so the range between 0 to 10 eV kinetic energy.

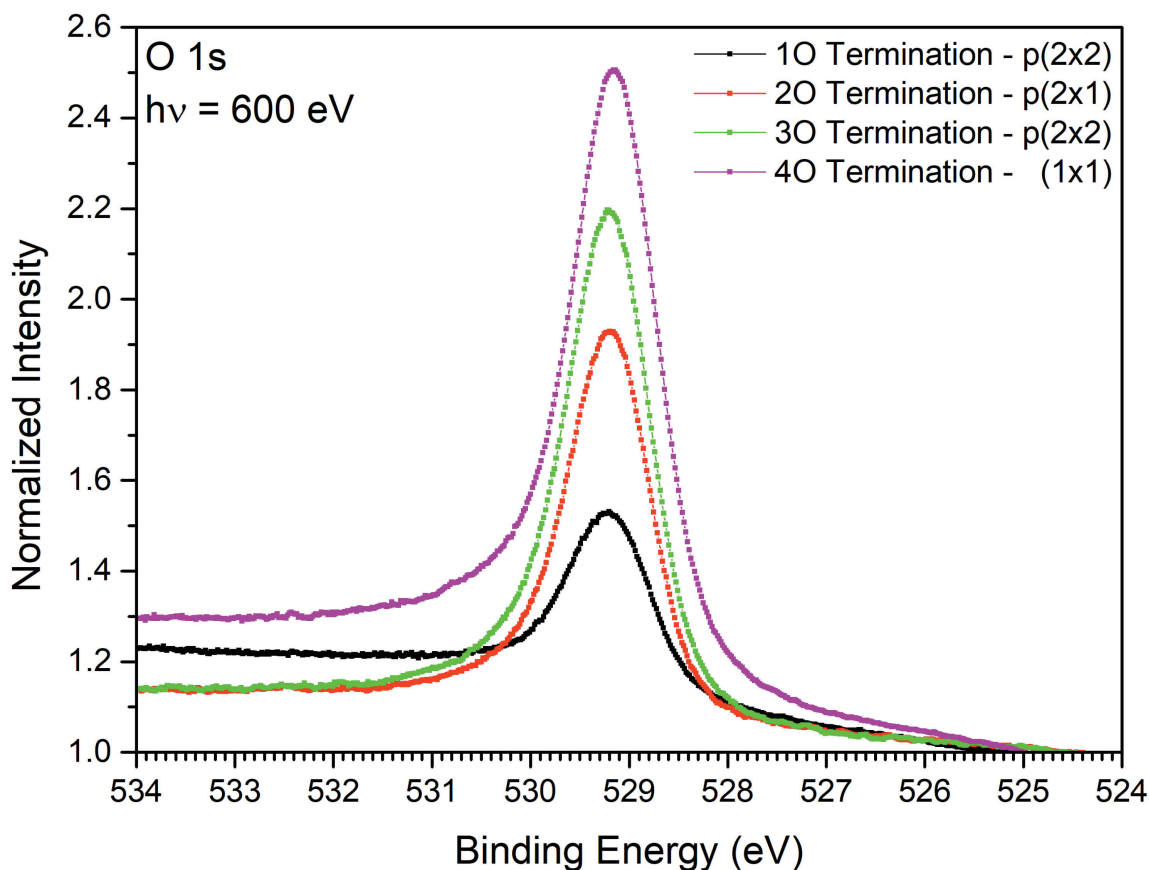


Figure 4.4: Photoelectron spectra of the O 1s binding energy region for the different oxygen terminations on Ru(0001). The intensities are normalized to the background level before the O 1s peak at around 525 eV.

Figure 4.4 shows the measured photoelectron spectra of the O 1s region. The 1O, 2O, 3O and 4O termination exhibit a peak at 529.2 eV binding energy. Within the given resolution of our system no energy shift was found, only an increase in intensity with increasing oxygen amount could be observed. A slight asymmetry in the peaks is visible. One explanation is the difference in the experimental setup in comparison to standard hemispherical XPS analysers, so the background behaviour is not necessarily comparable and the influence of hexapoles in the Omega filter could lead to an x dependent spreading in the y-axis of the energy dispersive plane. Another explanation is the coadsorption of another oxygen species like H₂O [83] or CO. Also,

a strong interaction of the chemisorbed oxygen with the metallic ruthenium atoms and their DOS near the Fermi energy could be a reason, as described in [84] for the oxidation of Ni on Cu. A possible explanation of the peak shift for the 4O termination could be that, in comparison to the lower termination now in the unit cell that some fcc positions are also occupied. Another could be that the formation of buried oxygen between the first and second surface layer of ruthenium took place [85], but in this case, a shift to lower binding energies would be expected [79].

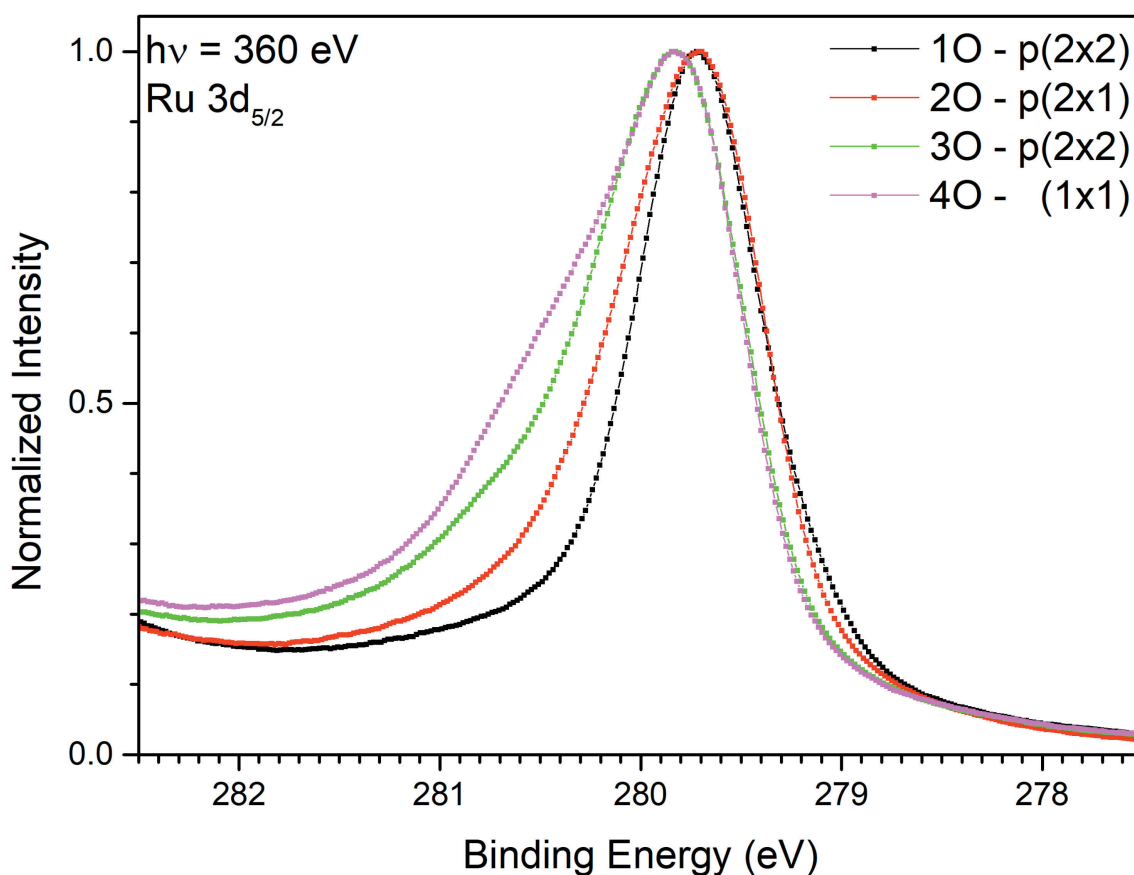


Figure 4.5: Photoelectron spectra of the Ru $3d_{5/2}$ binding energy region for the different oxygen terminations on Ru(0001). The intensities are normalized to their maxima and minima.

Figure 4.5 presents the Ru $3d_{5/2}$ peak for the different O terminations. In contrast to the O 1s spectra a slight peak shift and prominent change of the peak shape in dependence of the O termination is found. In [69] this is explained by surface core level shifts of the first and second layer of the ruthenium surface. Considering the energy resolution of SMART these results fit very well to [69].

The preparation of the different O terminations and some details to each of them are discussed in the following:

4.2 1O Termination p(2x2) – 0.25 ML

As already shown in figure 4.2 oxygen is dosed at room temperature until the first maximum in intensity in DF is reached, this preparation is very close to the one used in [70]. In our case this was done by exposing the sample to 2.0×10^{-9} mbar oxygen for around 2 min.

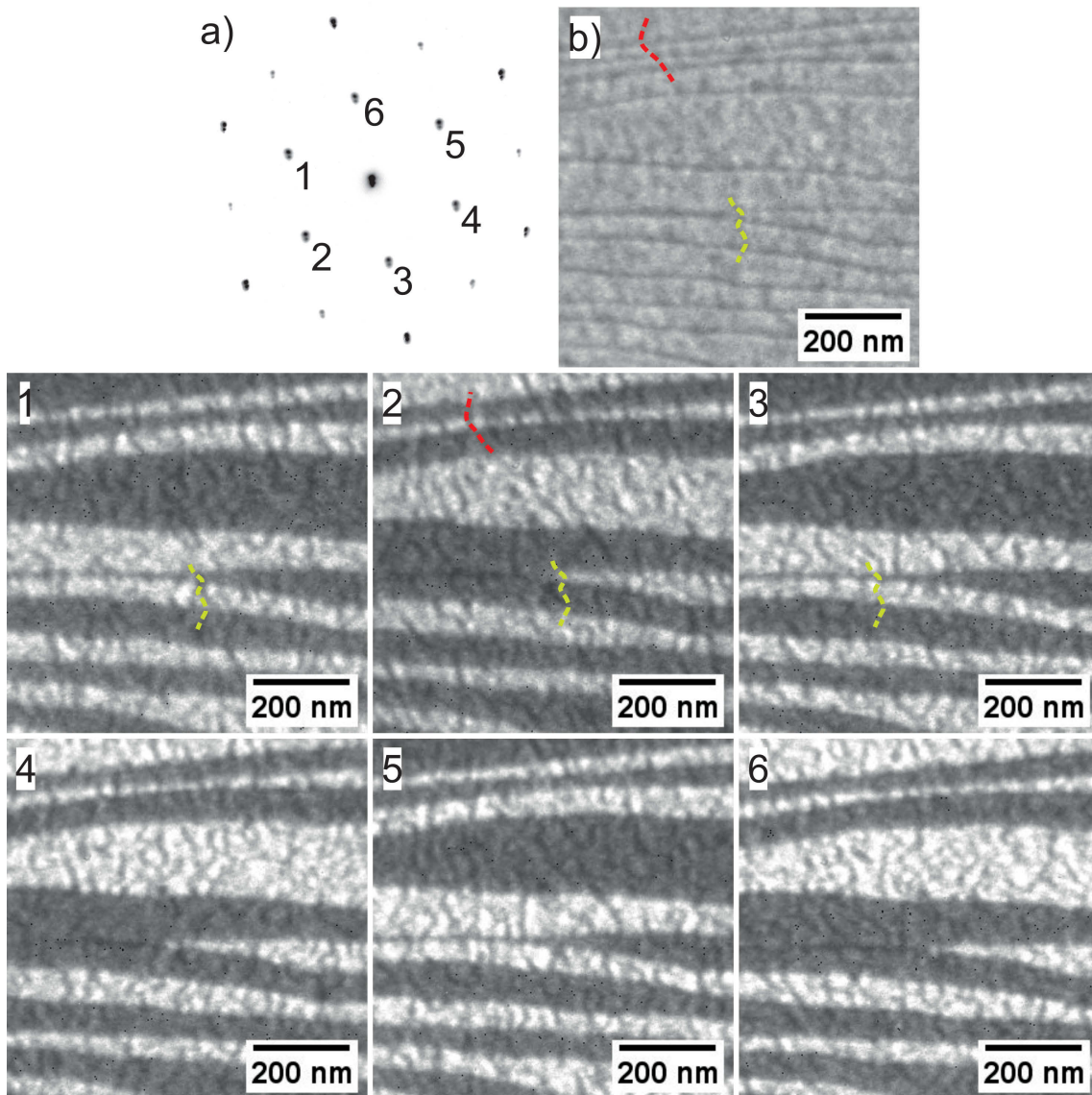


Figure 4.6: Image sequence marked 1-6 are DF images, the numbers indicate the spots in the LEED pattern a) above them. b) bright field image of the same area. All images are taken at 17.5 eV, this energy was chosen because the 1O termination is best visible on the surface. The LEED was taken at 42 eV kinetic energy. Coloured, dashed lines mark antiphase domain boundaries in the bright field and in the corresponding DF images.

Figure 4.6 shows the surface after this preparation. The typical p(2x2) LEED pattern is shown accompanied with a bright field image in the same row, below them are DF

images from the same area as the bright field image. First, it should be noted that the contrast changes of the terraces reflects the ABAB stacking of the (0001) orientation, already mentioned in chapter 3, and inverts for a terrace when the selected diffracted spot for imaging is switched. So the reflectivity of a terrace for a single image depends on the spot and on the kinetic energy used, but independent of the spot all bright and dark terraces show the same intensity behaviour (see figure 4.7). The contrast also flips in one image from bright to dark for adjacent terraces separated by one atomic step. Terraces separated by a dark line, but with the same contrast therefore are separated by at least an atomic double step or multiples of it. As already described above, oxygen islands (white) separated by antiphase domains are visible. Comparing the images 1, 3, 5 and 2, 4, 6 it is easily visible that, depending on the $(1/2)$ spot used for imaging, different antiphase domain boundaries are visible. A closer look reveals that the antiphase boundaries and also the oxygen islands are not necessarily stopped by atomic steps from one terrace to the other (highlighted by coloured dashed lines in the DF images). This was found already by LEED(IV) and SPA-LEED analysis of this O termination [86, 87] and predicted in [88]. Here it is shown in real space for the first time. Because of the strong chemisorption of oxygen changes in the spatial distribution of the electron density are given in [87] as a possible explanation for this coupling over steps. An interesting point is that some of these boundaries are found in the bright field image b) again (they are marked with the same colour like in the DF images). Looking at the bright field images shows that the surface seems to be very “rough” at this oxygen coverage; with the observation above, this contrast could be a consequence of the superposition of all the antiphase boundaries.

A special feature of LEEM is the possibility to do DF-LEEM(IV) of selected areas and to experimentally disentangle in this way their contribution to a diffracted reflection. In figure 4.7 this is shown for the contrast behaviour of the 1O terminated surface in DF for the $\{1/2, 0\}$ spots. The black curve represents the reflectivity of terraces bright at 16 eV in a DF image, the red one those dark at this energy, the green the sum of both curves. An important point is that the highest contrast difference occurs at energies around 12 and 16 eV, close to the energies of the minima for the clean Ru(0001) surface connected to unoccupied f states. The sum curve resembles the LEED(IV) curve of the $\{1/2, 0\}$ spot shown in figure 4.8.

Figure 4.8 shows the LEED(IV) of the 1O termination. The curves resemble very well the measurements done in [71, 82].

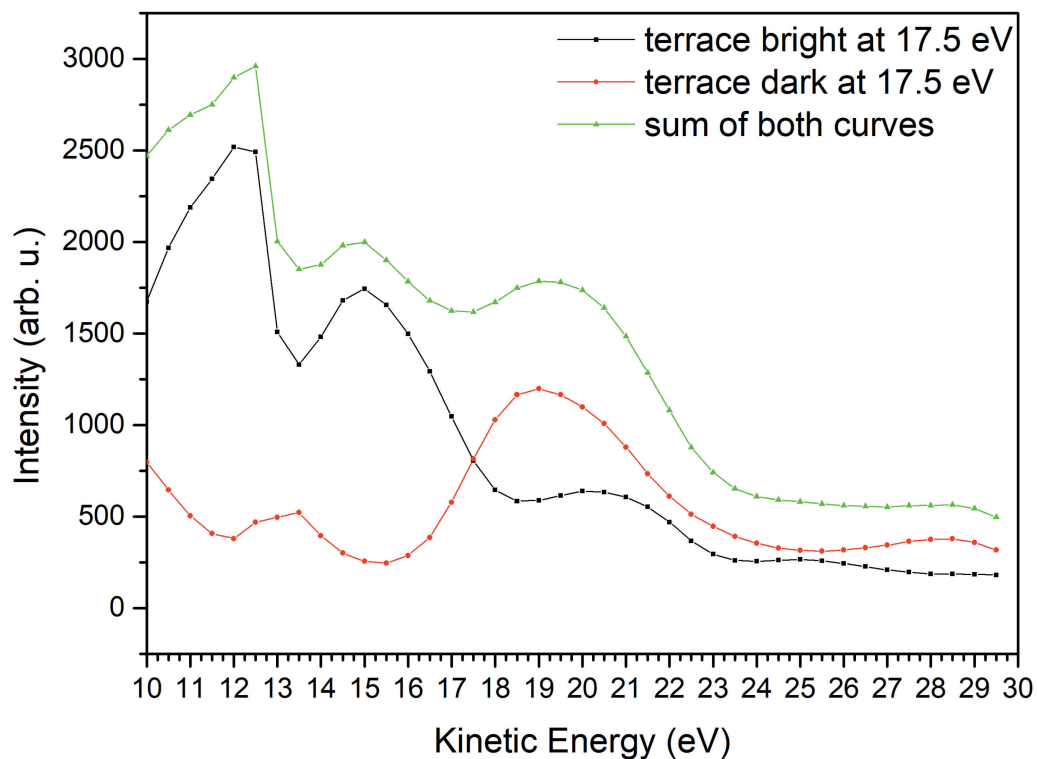


Figure 4.7: DF-LEEM(IV) measurements of selected terraces.

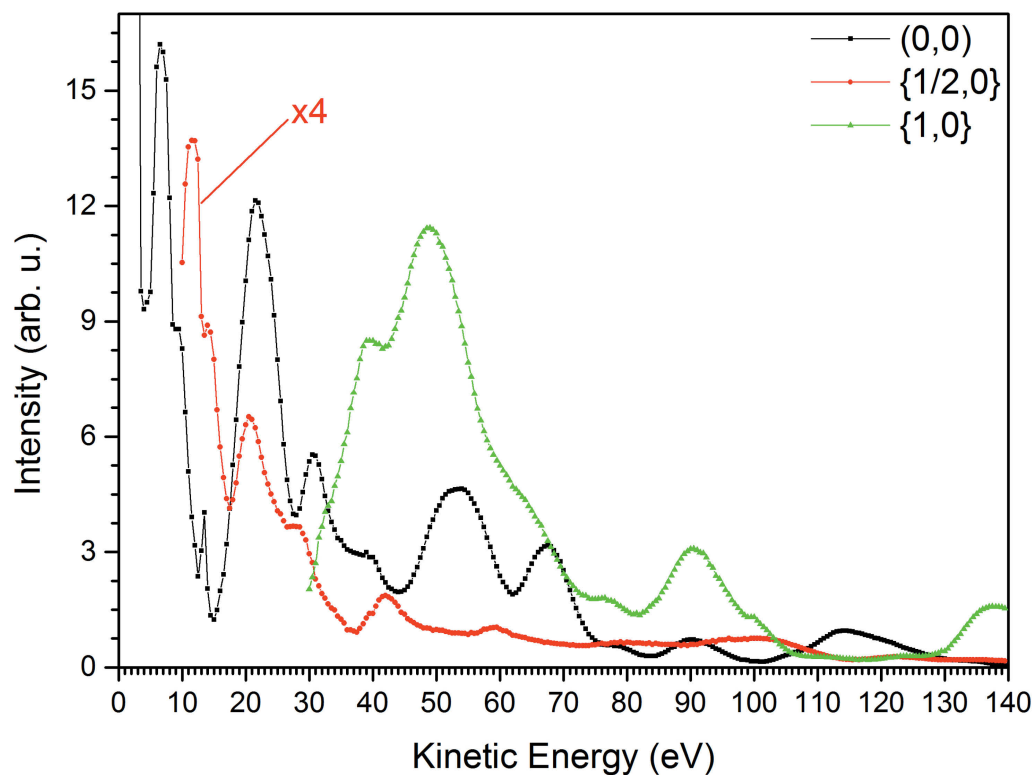


Figure 4.8: LEED(IV) curve of the 10 termination. The (0,0) spot (black), the average of the $1/2,0$ (red) and $1,0$ (green) are shown.

4.3 2O Termination p(2x1) – 0.5 ML

The 2O termination was produced by annealing the crystal in UHV up to 1170 K, introducing oxygen up to 5.0×10^{-8} mbar oxygen at this temperature and holding for 1 min, cooling down and closing the oxygen valve at 470 K. In this way, the overall oxygen exposure is about 3-4 L until RT and UHV better than 1.0×10^{-9} mbar are reached. Corresponding to figure 4.2 this will lead to the highest reflectivity of the (2x2) spots at RT.

Figure 4.9 shows the diffraction pattern and microscopy images after the 2O treatment. Image a) shows the p(2x1) LEED pattern of this coverage and b) a bright field image. Image c) highlights the 3 oxygen domains visible in the DF-images 1-6. In comparison to figure 4.9 e) the domains are about 10 times bigger. In [88] the strong influence of steps is already described. It is visible in the DF 1-6 that the domains do not tend to cross the steps. However, the red ellipse highlights an area where domains cross a step. In [87] this was already described for the 1O termination, but not expected for this termination. Examining the large scale DF image in figure 4.10 reveals that even very long range order extending over a few micrometres is possible (highlighted by red dashed lines in the images). A possible explanation for the shape of these large domains could be a dislocation network in the crystal and the resulting formation of small-angle dislocations. However, this is not an explanation how the orientation is preserved over several atomic steps. The contrast switching for areas belonging to one domain, but on different terraces is again a result of the ABAB stacking of Ru. This is nicely visible comparing DF images in one column in figure 4.9 and comparing with corresponding spots image a) because they are opposite of each other with respect to the (0,0) spot.

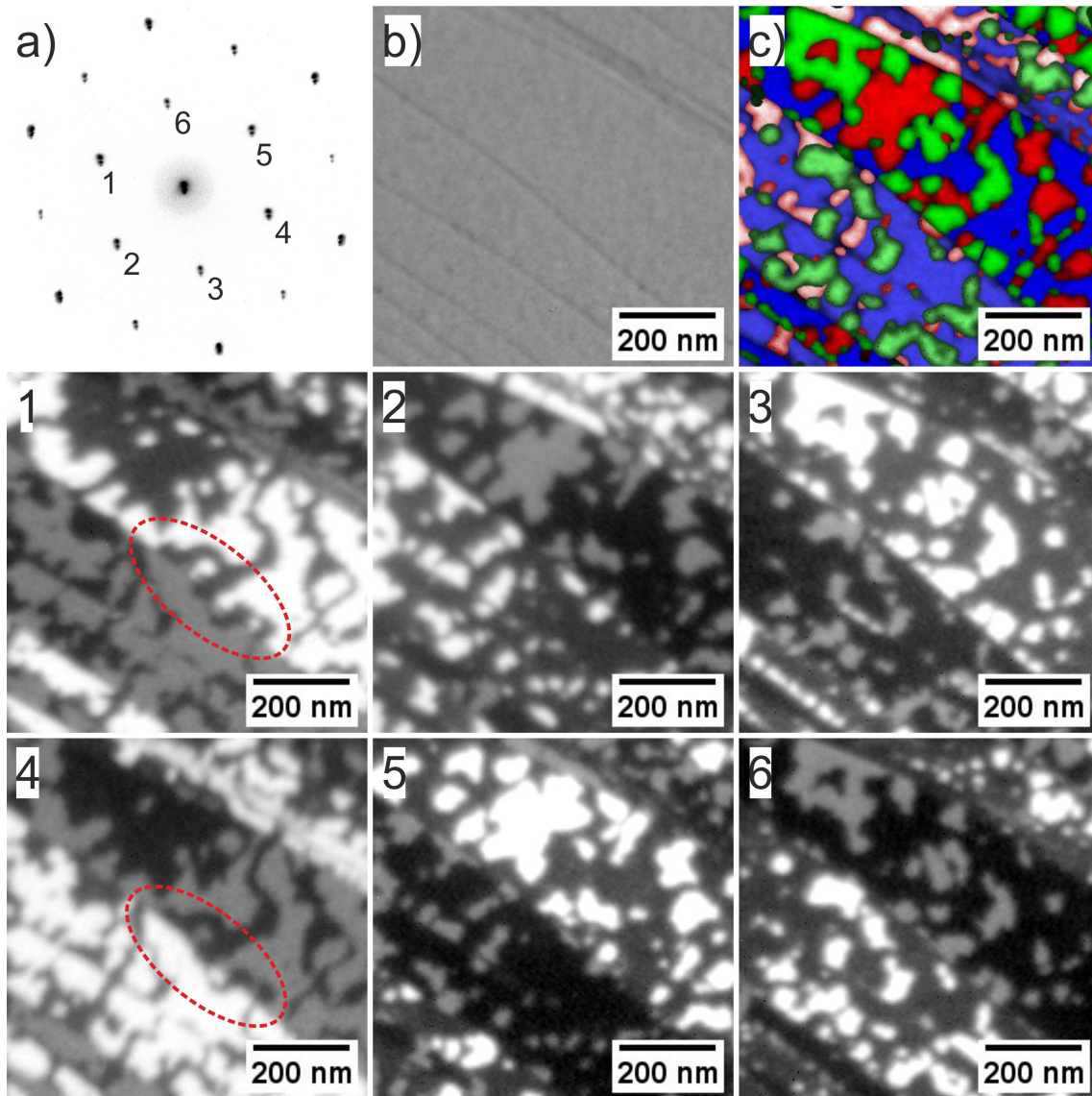


Figure 4.9: a) $p(2 \times 1)$ LEED pattern of the 2O termination, taken at 42 eV. b) Bright field image of the same area as the dark field images 1-6. All pictures are imaged with 16 eV and use a logarithmic contrast scaling. The numbers in the image indicate the spot in a) that was used for imaging. c) pseudo-colour superimposition of the three oxygen domains of the images 1-6.

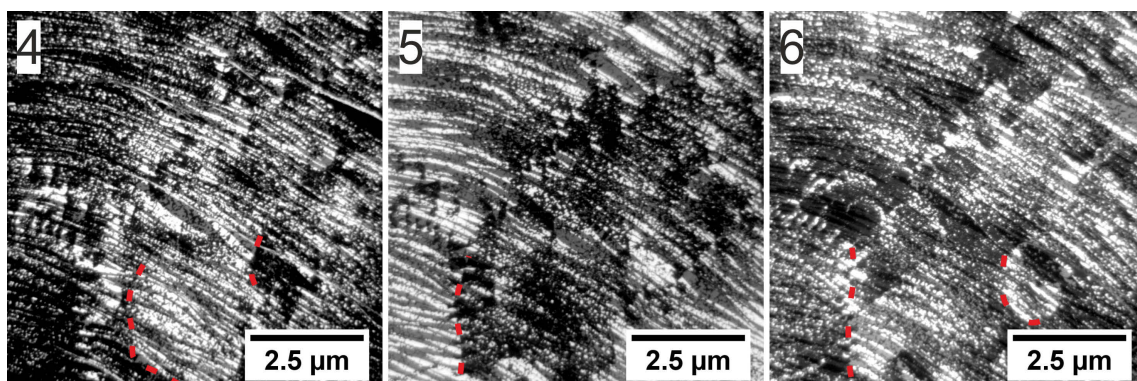


Figure 4.10: Large scale DF images showing the 2×1 domains, the numbers indicate in the LEED image of figure 4.9 a) the spot used for imaging. All images are taken at 16 eV. (Details see text)

Figure 4.11 shows reflectivity curves of the bright and dark areas belonging to the same domain but on different terraces. The black curve represents the domains which are bright in the DF images 1-6 in figure 4.9, red the grey ones, and green the sum of both. Comparing the dark field LEEM(IV) curves of 2O termination with the ones from the 1O termination (Figure 4.7) two things are clear. First, different terminations have peaks at the same energy. Second, they are much more pronounced for the 2O termination, especially the peaks of the darker areas. The sum curve fits very well to the LEED(IV) curves in figure 4.12, which are in good agreement with the results of [71].

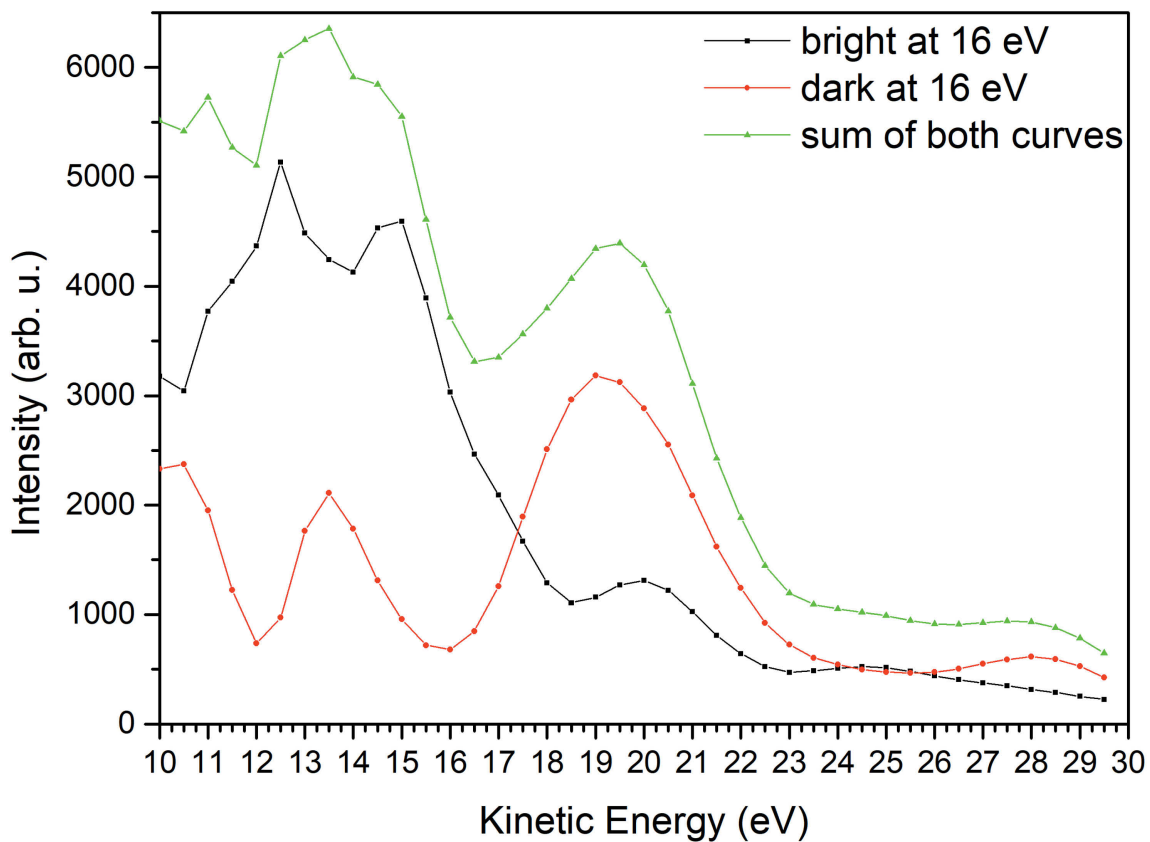


Figure 4.11: DF-LEEM(IV) curves of selected domains

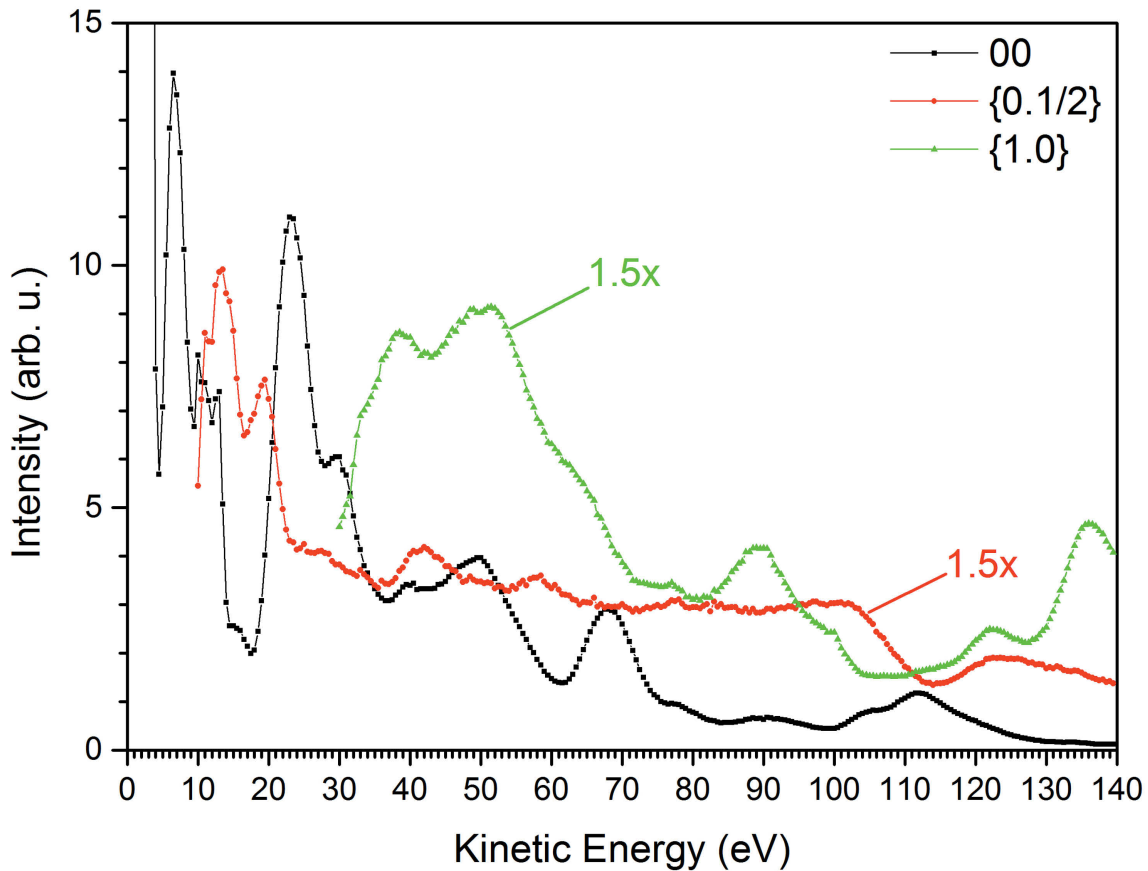


Figure 4.12: LEED(IV) curve of the 2O termination. The $(0,0)$ spot (black), the average of the $1/2,0$ (red) and $1,0$ (green) are shown.

Annealing this sample in UHV leads to a diffusion of oxygen atoms on the surface [89]. At 470 K the domains start to fluctuate and rearrange. With rising temperature the diffusion rate increases and at 500 K the domain size decreases rapidly. At around 530 K the domains disappear and the reversible order-disorder transition is reached as described in detail in [90]. While cooling down the domains reappear at 510 K and start to grow with decreasing temperature, but still tend to fluctuate until 400 K (see figure 4.13). An explanation for the difference between heating up and cooling down is that the thermocouple is positioned at the side of the crystal, spot welded to the sample holder. While cooling down the thermal mass of the sample holder leads to measured slower cooling rates than the surface actually has. Because of the reversibility of this process it is most likely that in both cases, at heating up and cooling down, the sample has the same temperatures when the ordered domains disappear/appear and their fluctuations start/stop. This hypothesis is supported by the fact that the intensity and sharpness of the LEED spots enhances drastically at a temperature of 540 K while cooling down to prepare this surface in the first step.

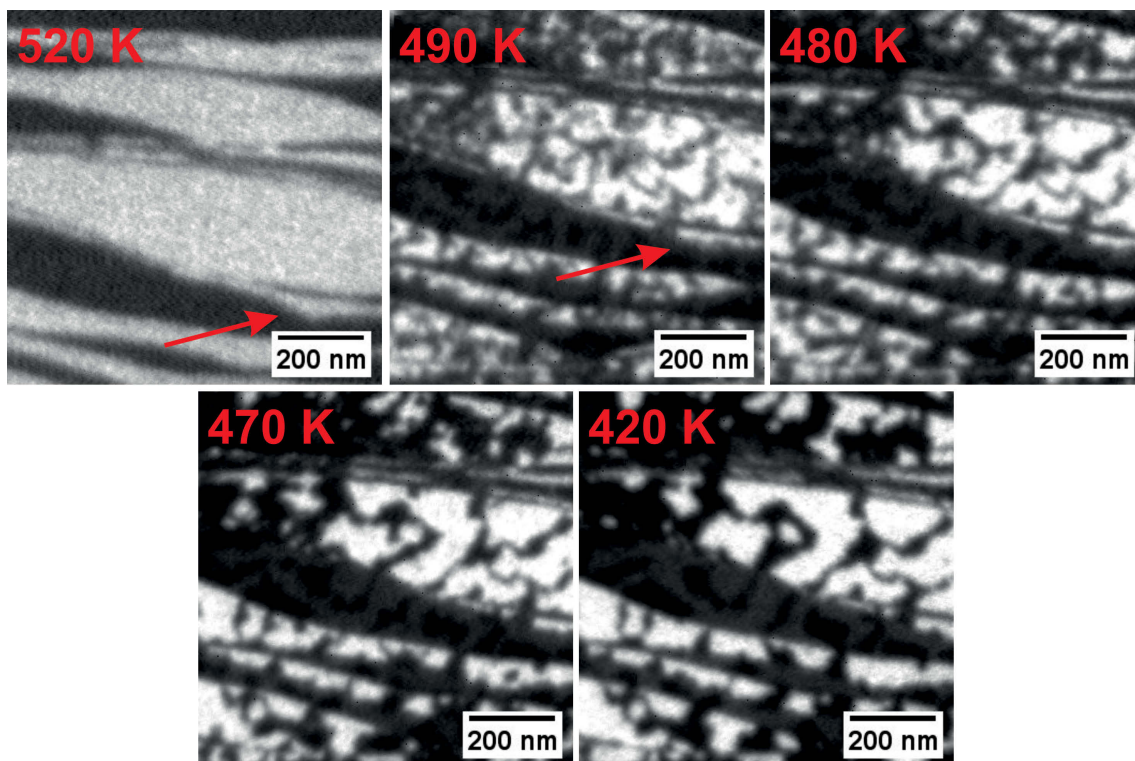


Figure 4.13: DF-LEEM image series of cooling down a 2O terminated Ruthenium surface in UHV. In the first image the area of interest drifted out of the field of view, so it is slightly shifted to the rest. As guide for the eye a red arrow marks the same positon in the next image. The temperatures are indicated in the images, the kinetic energy is 16 eV (details see text).

4.4 3O Termination $p(2 \times 2)$ – 0.75 ML

The 3O termination is produced by annealing in UHV up to 1170 K and introducing oxygen up to 1.0×10^{-6} mbar holding at this temperature for 10 min, cooling down and closing the oxygen valve at 520 K. The oxygen exposure in this case is about 800 L. Again a $p(2 \times 2)$ diffraction pattern is visible after this treatment. Figure 4.14 shows LEED images and the intensity increase of (0,0) and $p(2 \times 2)$ over decreasing temperature for this treatment. At 1170 K the LEED shows a very blurry $p(2 \times 2)$ reconstruction, where the spots sharpen with decreasing temperature until 540 K is reached and very sharp spots start to appear, that are the only remaining ones below 500 K. The intensity over temperature plot shows that the (0,0) spot increases linearly over temperature until a fast increase happens in the range of 540 K to 500 K, afterwards a slow increase of the intensity is found. The $p(2 \times 2)$ spots increase their intensity slowly until 700 K, then their intensity begins to increase faster, until from 540 K to 500 K a very fast increase happens and afterwards a slow increase continues. These results indicate an order-disorder phase transition and are consistent with the

findings in the paragraph before for the 2O termination. However, a contribution of the Debye-Waller factor should not be neglected [91].

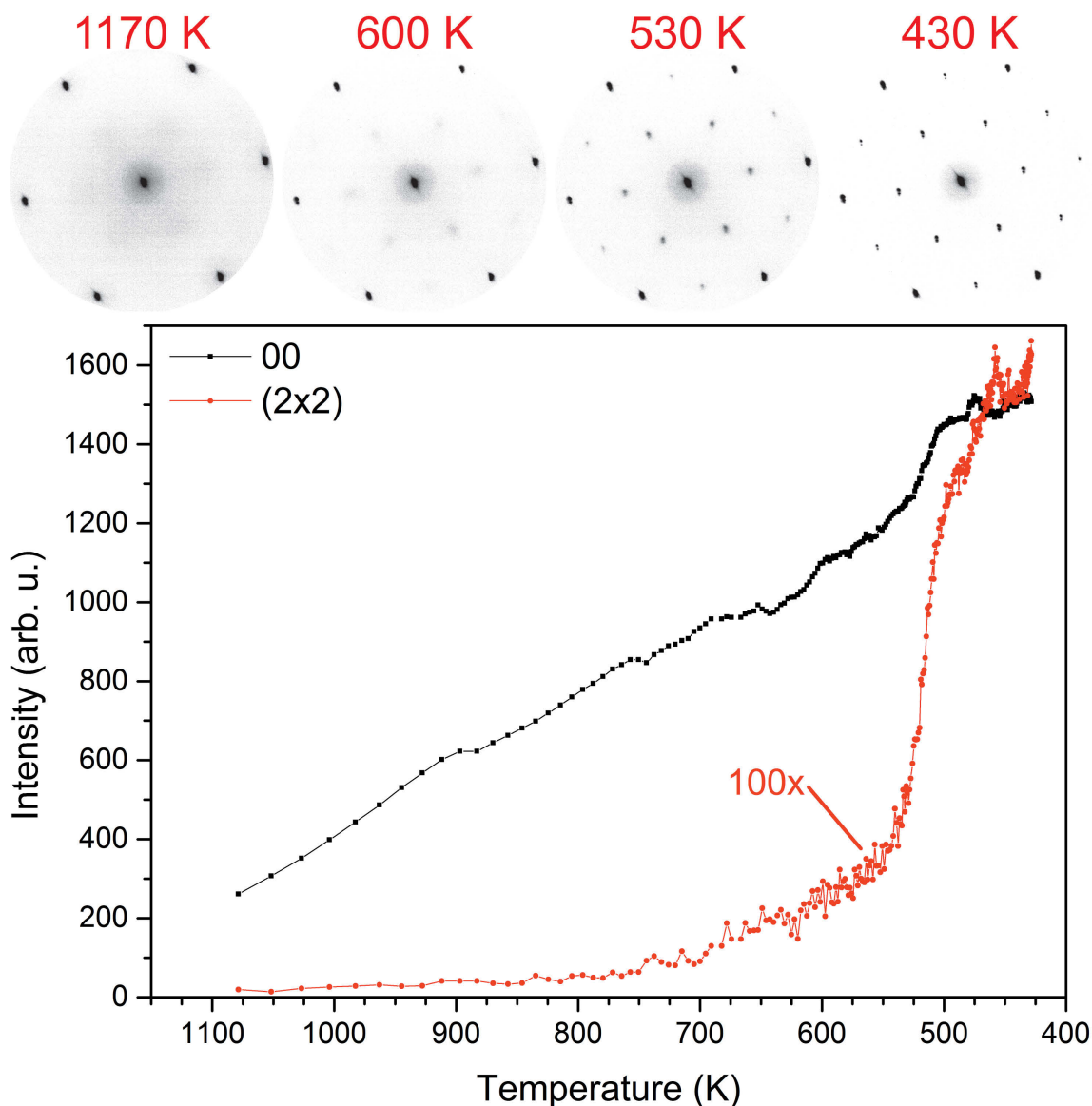


Figure 4.14: In the upper panel LEED images during the cooling down in 1.0×10^{-6} mbar oxygen are shown. Below them the intensity evolution of the $(0,0)$ and $p(2 \times 2)$ spots over temperature is plotted. For the measurement a kinetic energy of 42 eV was used.

Figure 4.15 shows a LEED pattern and microscopy images of the surface after this treatment at room temperature. In bright field the atomic steps of the surface are visible and the terraces look rather smooth. In the DF images 1-3 show the same contrast behaviour as for the 1O coverage: the contrast inversion from step to step because of the ABAB stacking of the Ru support and the appearance of antiphase boundaries depending on the chosen spot for imaging. On the other hand, because of the preparation conditions the islands are much larger.

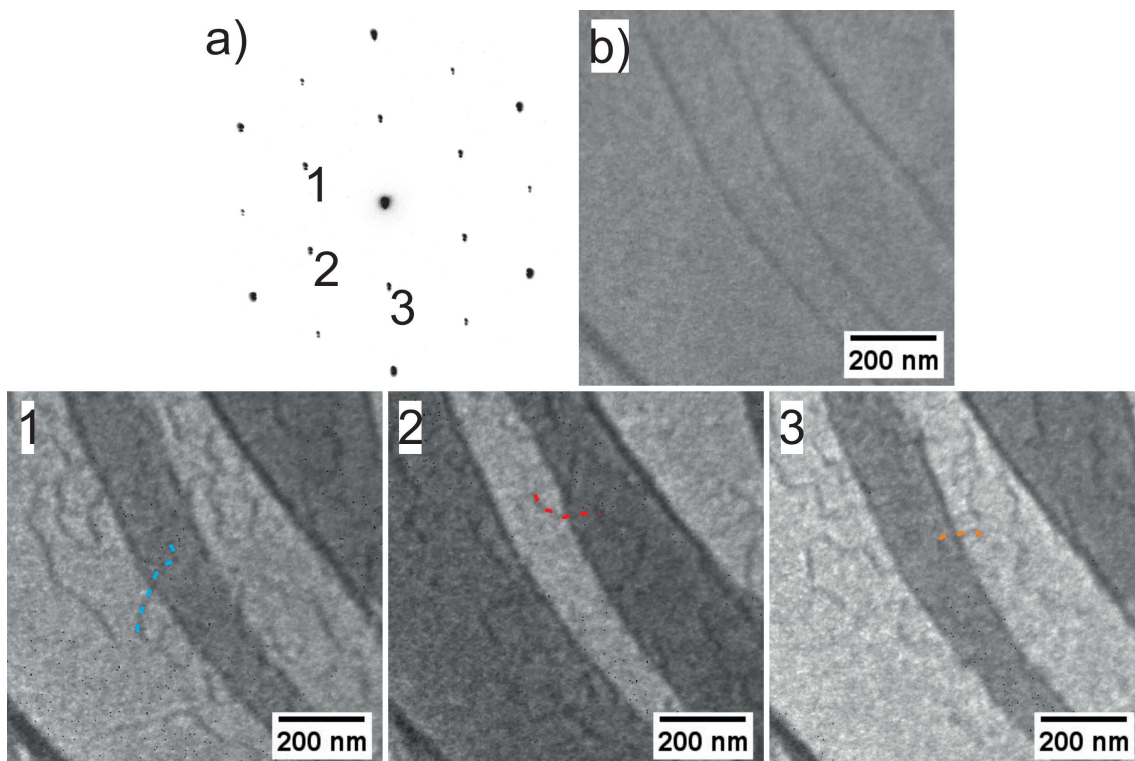


Figure 4.15: 3O termination in bright and DF field at room temperature. a) shows the $p(2 \times 2)$ pattern of the 3O termination, taken at 42 eV. b) is a bright field image of the same area as the DF images 1-3, all are taken at 18.5 eV and the numbers in a) indicate the used spot. The coloured, dashed lines in 1-3 highlight antiphase domain boundaries crossing steps.

The energy depending reflectivity of two adjacent terraces in dark field is shown in figure 4.16. In comparison to the DF-LEEM(IV) curves of the 1O and 2O termination (Figure 4.7 and figure 4.11) it is visible that peaks appear again at the same energy and that the trend already observed for the LEEM(IV) is continued; i.e., with increasing oxygen coverage the features in the curves get more pronounced. So the LEEM(IV) and DF-LEEM(IV) will give a good fingerprint for the oxygen coverage on Ru(0001).

The LEED(IV) curves in figure 4.17 resemble the measurement in [72,92] very well.

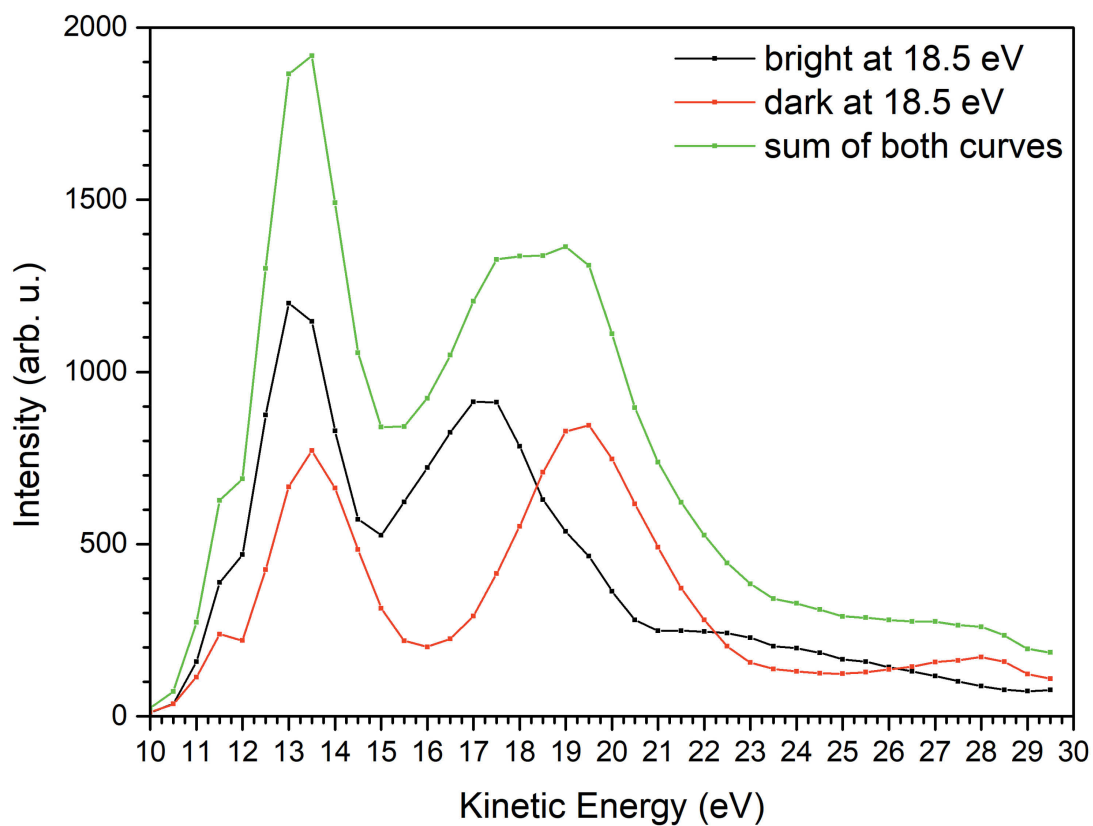


Figure 4.16: DF-LEEM(IV) curves adjacent terraces of the 3O surface at room temperature.

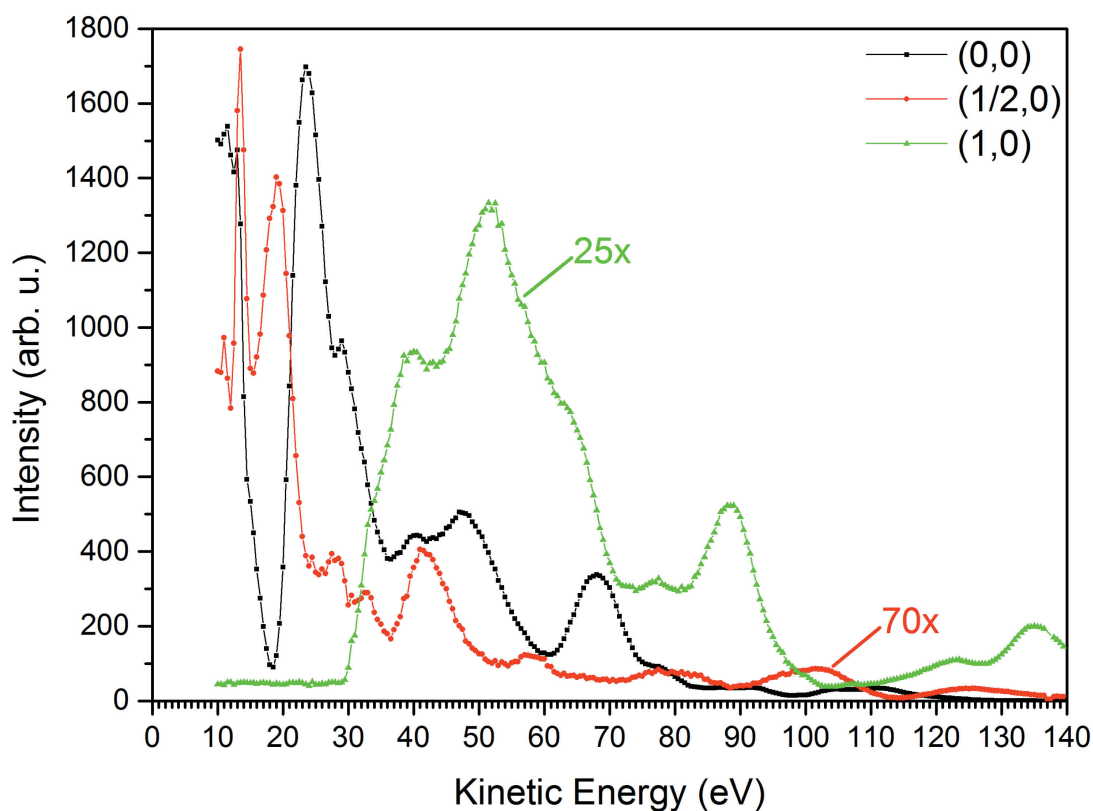


Figure 4.17: LEED(IV) measurement of 3O coverage at room temperature.

4.5 4O Termination (1x1) – 1 ML

The 4O termination is produced by annealing in UHV up to 1170 K and introducing oxygen up to 5.0×10^{-6} mbar, holding at this temperature for 10 min, cooling down and closing the oxygen valve at 520 K. The oxygen exposure in this case is about 4000 L.

Figure 4.18 shows a LEEM and a LEED image of the surface after the 4O treatment. The terraces look again rather smooth and the LEED is (1x1) as expected for this coverage.

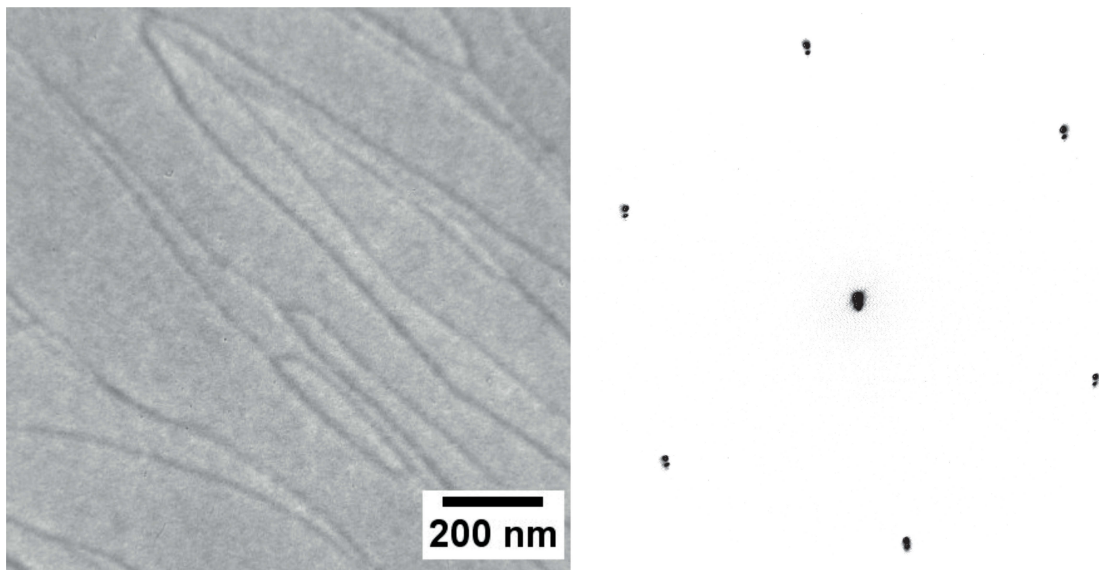


Figure 4.18: Bright field image of the 4O terminated Ru(0001) surface at room temperature, the kinetic energy in both images is 42 eV.

Figure 4.19 shows a LEED(IV) measurement of the 4O termination, the curve fits very well to [74].

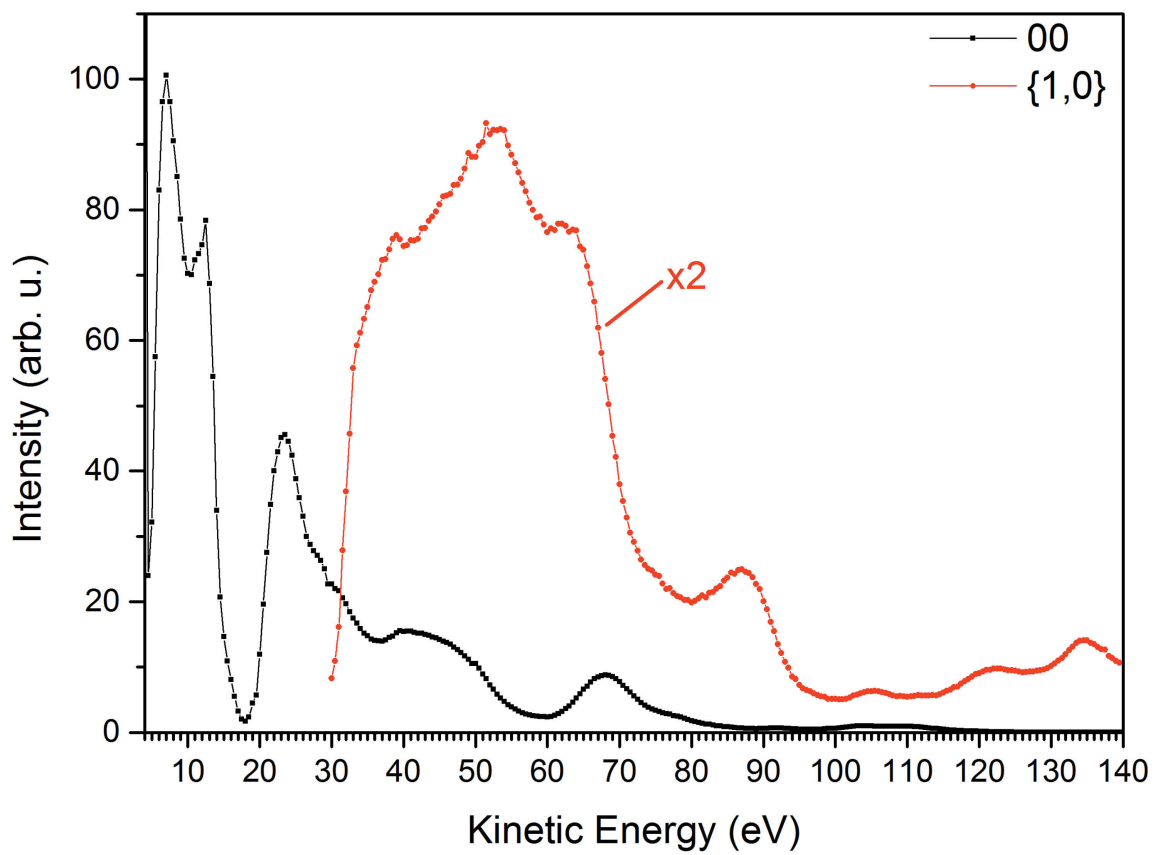


Figure 4.19: LEED(IV) measurement of the 4O termination on Ru(0001).

The silicon deposition

In this section the calibration of the Si-evaporator will be described first, because it is one of the most crucial parts of the sample preparation. Later on, the actual sample preparation conditions will be discussed.

5.1 Calibration of deposition rate

The flux rate of the e-beam evaporator depends, strongly, on the emission current of the filament and the acceleration voltage applied between the filament and the silicon rod. However, the shape of the tip formed at the end of the rod, where the actual silicon evaporation happens, plays a major role on the flux measurement and can change over time depending on the usage of the evaporator. For this reason, it turns out to be necessary to calibrate the evaporator in regular intervals in order to guarantee a fine control of the thickness of the oxide film.

Silicene is a 2-dimensional hexagonal network, analogous to graphene, but instead of carbon atoms it has silicon atoms. Inspired by the findings in [93–95] showing the growth of silicene on Ag substrates and its study by LEEM [96], the same procedure was adopted for silicon on ruthenium. The growth of an silicon over-layer on Ru(0001) was consistently imaged in many occasions, thus allowing its use for the calibration of the flux rate for a given evaporation geometry and parameters of the system. Afterwards, samples with different amounts of silica were prepared and transferred in air to the Fritz-Haber-Institute to perform IRRAS measurements for silica thickness determination [11]. With the accurate flux rate measurements and the IRRAS references it is possible to calibrate the silicon evaporator. Moreover, it will be shown that with the given knowledge described above it is possible to determine the expected silica thickness via the LEED decay in-situ (see subchapter 5.2).

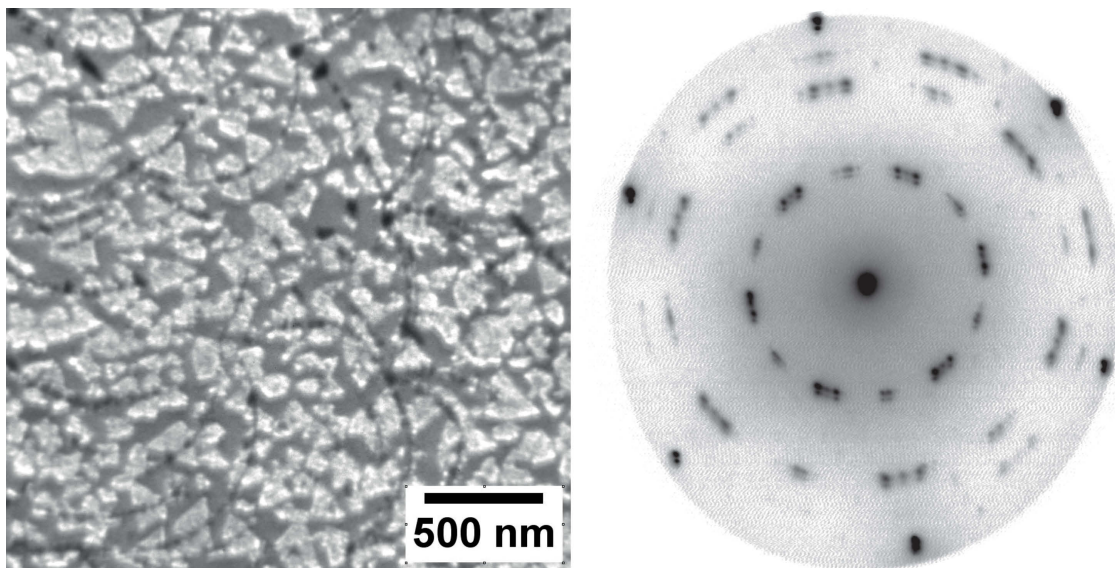


Figure 5.1: Silicene grown on Ag(111). A LEEM image at an energy of 5 eV (left) and the corresponding LEED pattern with an energy of 28 eV (right) are shown. (for details see text)

First the deposition on Ag(111) was revisited to get a first indication on the expected deposition times needed. Figure 5.1 shows a LEEM and LEED image of a silver surface after one hour of silicon deposition in UHV at 510 K. The bright areas in the LEEM image are silicene islands, while the grey ones are the Ag substrate. Silicene resembles in its triangular shaped growth the 3-fold symmetry of the fcc structure in $\langle 111 \rangle$ orientation quite well. 50% of the surface is covered with silicene and the LEED pattern corresponds very well to the one in [97] assigned to a $\sqrt{13} \times \sqrt{13}R13.9^\circ$ structure.

As a next step silicon was deposited under nearly the same conditions onto Ru(0001) (UHV, 520 K). However, in comparison to the growth on Ag(111), silicon first decorates the step edges and then starts to grow from one side of the terrace to the other (see figure 5.2). The images show that around 1 ML islands are forming on the deposited silicon, and with increasing coverage new layers seem to form, indicated by the contrast in the images between 1.5 – 5 ML. Interestingly, after 5 ML the film starts to close, looking more homogenous. One possible explanation for this behaviour could be that the surface is very disordered and, consequently, all the imaging contrast is lost. This observation fits to the observed behaviour in the LEED images: it is visible that at the beginning an ordered phase is formed, but with increasing coverage it starts to disappear and only the 1,1 spots of the substrate are visible, until the whole surface is covered and only a (0,0) spot is left.

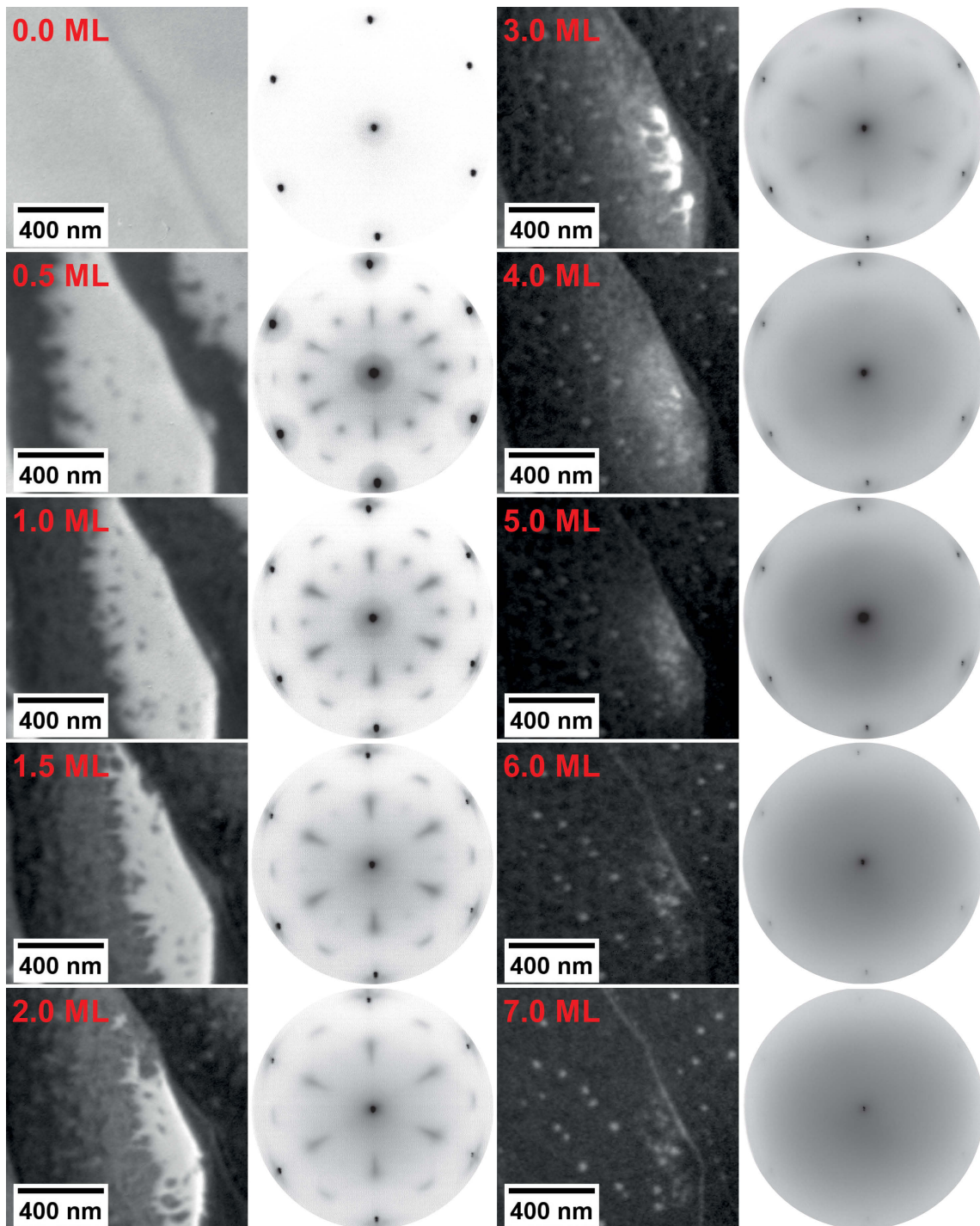


Figure 5.2: Snapshots of the silicon deposition in UHV at 520 K on Ru(0001). Right of the LEEM image (5 eV) is the LEED (42 eV) image corresponding to it. The deposited amount in terms of silica ML is indicated in red, which was calculated afterwards.

After the deposition of 7 ML the film looks closed and the LEEM(*iV*) (see figure 5.3) measurement shows no structure with nearly no intensity for higher kinetic energies than 3 eV. The MEM to LEEM transition is shifted to 1.82 eV, indicating a 0.76 eV lower work function than for clean Ruthenium.

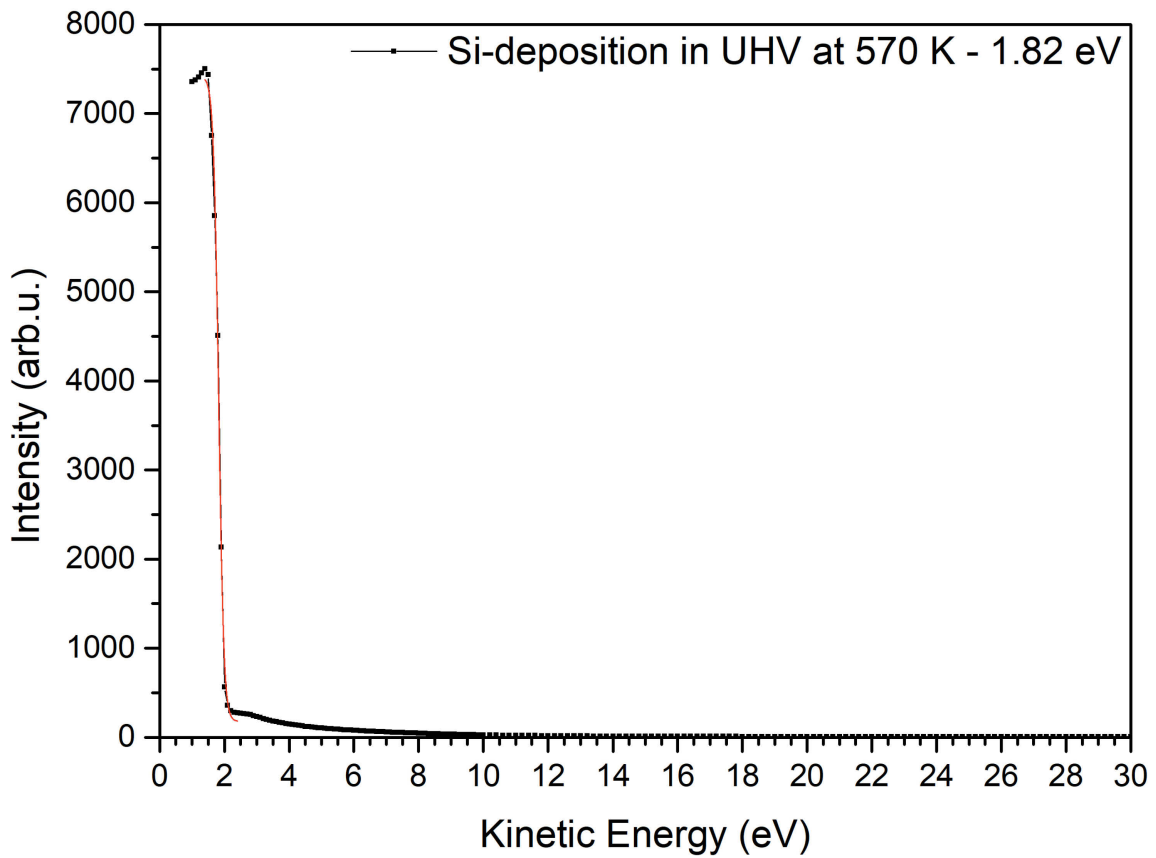


Figure 5.3: LEEM(*iV*) after the deposition of silicon in UHV at 520 K, the amount corresponds to 7 ML silica. In the inset the MEM to LEEM transition is given.

Figure 5.4 shows in-situ photoelectron spectra of the Si 2p line collected during silicon deposition in UHV at 520 K on Ru(0001). The inset in the upper plot in figure 5.4 reveals that the very first silicon atoms at the surface lead to a peak at around 103.3 eV, while after the deposition of about 0.075 ML another Si peak starts to grow at around 99.2 eV. With increasing deposition time only the intensity of the peak with the lower binding energy increases and splits into two different contributions (99.3 eV and 99.75 eV), thus showing the typical peak splitting and intensities ratio associated with a 2p line. This behaviour continues for a coverage up to 0.6 ML. In the lower plot the Si 2p line for an amount between 1.8 to 2.2 ML is shown. In this coverage range the peak with the lower binding energy shows a shoulder on the high binding energy side. This signal vanishes for higher coverage followed by a peak shift towards higher binding energies (upper inset in the lower plot in figure 5.4). Finally, for high silicon amounts mainly one peak is visible (lower inset in the lower plot in figure 5.4).

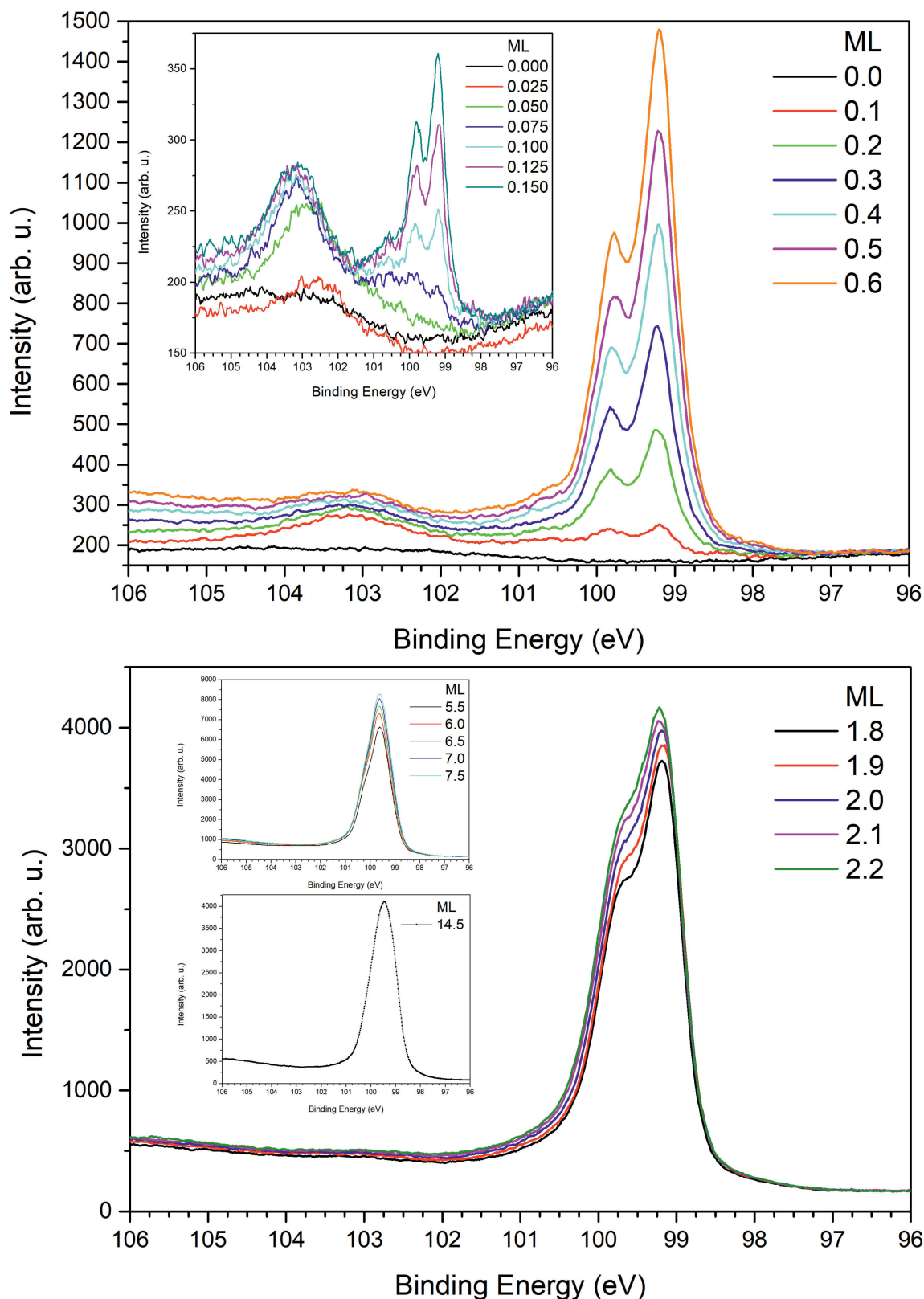


Figure 5.4: In-situ photoelectron spectra of the Si 2p line during the deposition of silicon in UHV at 520 K onto Ru(0001). The upper plot shows the initial stages of the deposition in 0.1 ML steps up to 0.6 ML silicon, its inset shows the very beginning of the deposition up to 0.15 ML in 0.025 ML steps. The lower plot shows the deposition in 0.2 steps from 1.8 ML up to 2.2 ML silicon, its insets shows the continuing deposition, the upper one up to 7.5 ML and the lower for 14.5 ML. $h\nu = 175$ eV.

Taking into account the previously mentioned observations, the following scenario is proposed for all the processes during the silicon deposition. First residual oxygen in the background gas can re-adsorb on the ruthenium surface, although the base pressure in the experimental chamber was below 5.0×10^{-10} mbar during the whole measurement and ruthenium was flashed several times to 1520 K in UHV right before the start of the experiment. This oxygen layer does not lead to a (2x2) LEED pattern because of the low amount and substrate temperature of 520 K (compare to the findings in chapter 4 above and the LEED image for 0 ML in figure 5.2). When the first silicon atoms reach the surface they immediately are oxidized. In this step silicon atoms may diffuse towards an adsorbed oxygen ad-atom, or the oxygen ad-atom can diffuse to meet Si (or both situations). In this case, none of them can be discarded based on the experimental results presented. The binding energies of 99.2 eV for metallic and 103.3 eV for the oxidized state and chemical shift of about 4 eV fit very well to values associated in the literature with 'metallic' and Si^{4+} in SiO_2 [98–100]. Metallic is kept in quotation marks, because pure silicon is a semiconductor and not a metal, it is used here to refer to the unoxidized state '0'. Later on metallic silicon will be used in the test following this assignment. These results reflect on one hand the high affinity of ruthenium towards oxygen, and on the other hand, that if silicon is available oxygen will prefer to bind to it, which is in line with data reported in the literature for ruthenium silicides and other noble metal silicides exposed to oxygen [101–103]. When residual oxygen is consumed by silicon, silicon starts to grow in a metallic state showing the expected value for the spin-orbit splitting and the binding energy of bulk silicon. However, the substrate temperature seems to be too low to get an ordered over structure for higher silicon content at the surface (see the LEED images above 2 ML in figure 5.2), which leads to a smearing of the Si 2p line as observed for amorphous silicon [104, 105]. The formation of ruthenium silicide cannot be excluded, but seems very unlikely - the Si 2p is shifted about 0.3 eV or more to higher binding energies [106, 107] and in comparison to the in-situ study in [103] no additional shoulders appear, also all reported silicides on ruthenium were prepared above 650 K so far [106, 108]. Interestingly a newer publication [109] suggests the formation of silicene on Ru(0001) by depositing amounts of less than one ML silicon at room temperature and annealing up to 750 K in UHV. No chemical analysis of these samples was performed, but it is highly likely that small amounts of silicon behave like the carbon/ruthenium system, where a 2D growth of graphene is preferred instead a 3D growth of ruthenium-carbide [110].

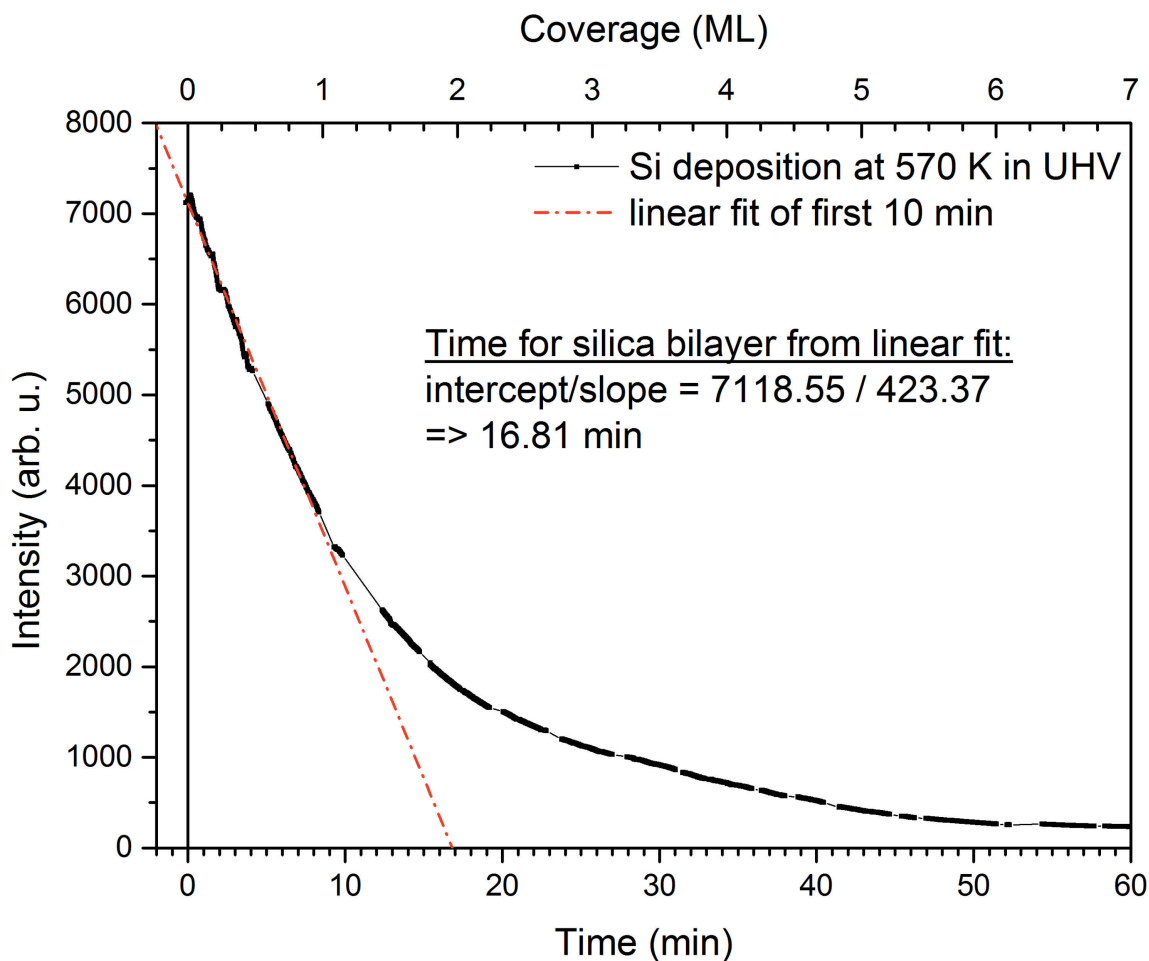


Figure 5.5: Plot of the intensity decay (black) over time from the deposition in UHV and at 570 K shown in figure 5.2. A linear fit of the first 10 minutes is shown as a red curve. The coverage is calculated after the deposition and refers to ML of silica.

Figure 5.5 is the overall intensity over time during the deposition shown in figure 5.2. In the first 10 minutes the intensity decays very fast linearly, afterwards an exponential like behaviour is observed corresponding to the growth rate of the over layer across the Ru(0001) terraces. The linear decay was fitted to determine a deposition time corresponding to a closed over layer at this growth rate and hence a flux rate can be calculated to 8.41 minutes per monolayer.

With the calculated flux rate, different amounts of silica were prepared as described in the beginning of this chapter and transferred from BESSY-II (HZB) to the location of the chemical physics department of Fritz-Haber-Institute for IRRAS measurements. There, the samples were first measured as received and afterwards annealed to 900 K in 1.0×10^{-6} mbar oxygen to get a contaminant-free surface and exclude drastic changes due to annealing. Comparing to reference measurements already done in the Fritz-Haber-Institute it was then possible to calculate a deposition time

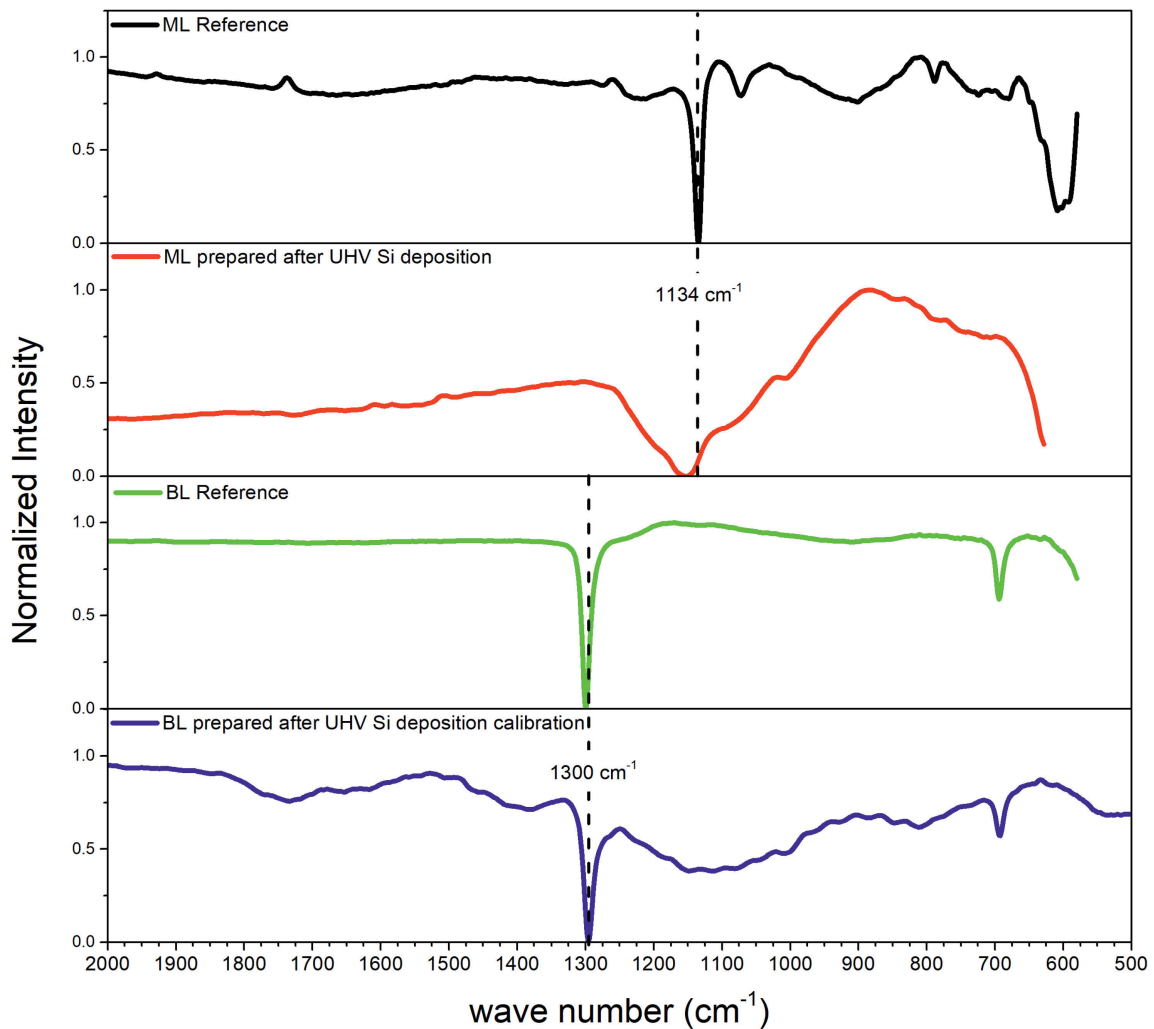


Figure 5.6: Comparison of IRRAS measurements of mono- and bilayer silica on Ru(0001). First the reference measurement of the Fritz-Haber-Institute and below the sample grown in the SMART microscope are shown

for a mono- or bilayer of silica for a given flux rate. Figure 5.6 shows the comparison IRRAS reference measurements of the FHI and samples prepared as described as above aiming for the amounts of a mono- or bilayer of silica. The monolayer films exhibit a characteristic phonon peak at 1134 cm^{-1} and the bilayer films at 1300 cm^{-1} [11].

5.2 Silicon deposition in oxygen at room temperature

As already described in the introduction of this chapter the deposition of silicon for the silica is done in an oxygen atmosphere and at room temperature. The oxygen background pressure for the deposition is 2.0×10^{-7} mbar and room temperature is here referred to the thermocouple showing less than 320 K.

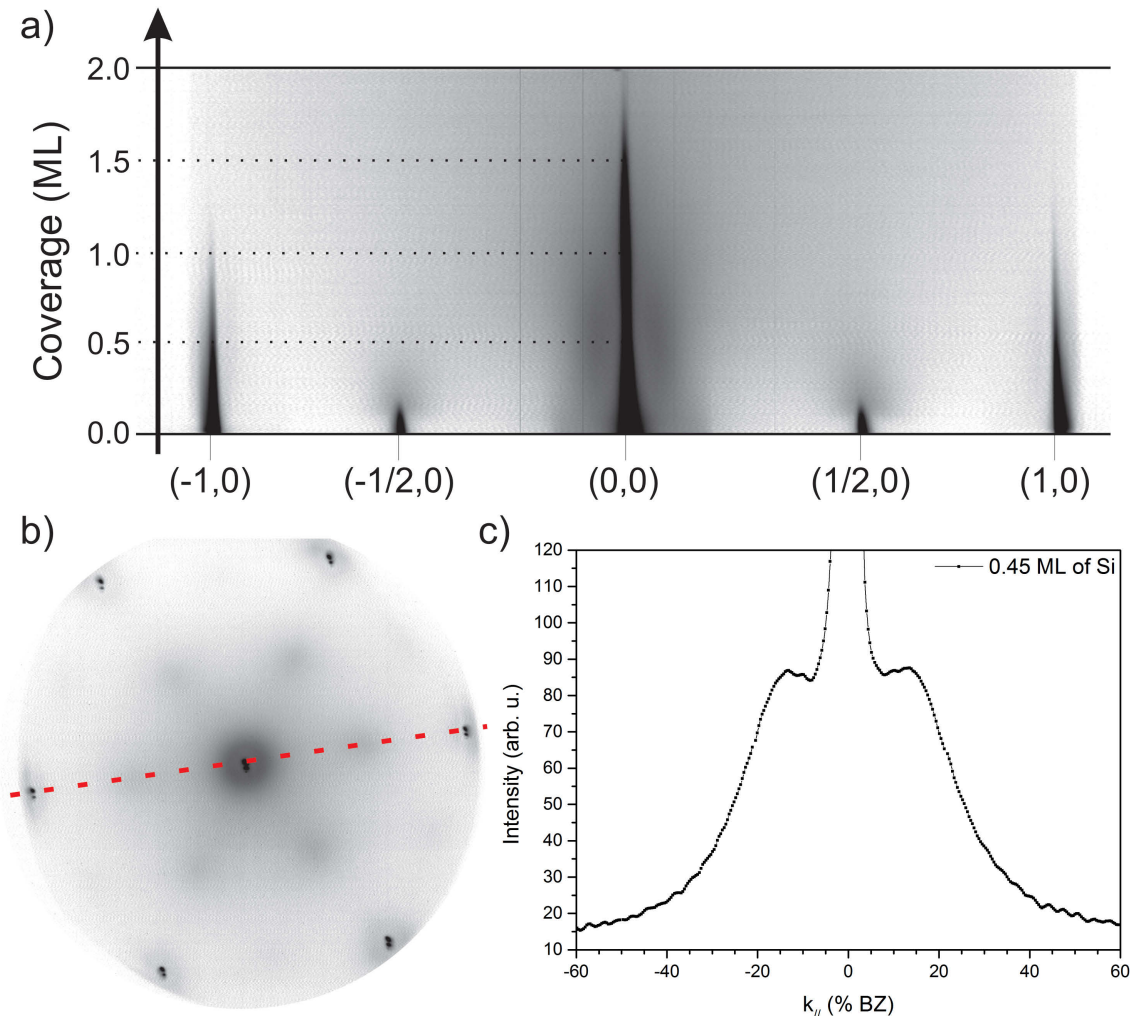


Figure 5.7: LEED investigation during silicon deposition onto 3O terminated Ru(0001). a) shows the added cuts through the reciprocal space over coverage in logarithmic scaling. b) LEED picture from the surface with a coverage of 0.45 ML, the dashed red curve highlights the cut, which was used for image a) and c). c) Cut through the intensity around the (0,0) spot at 0.45 ML coverage, showing a Henzler ring. The measurement was done with $E_{kin} = 42$ eV

Figure 5.7 a) shows the intensity evolution of a cut through reciprocal space from the (-1,0) to the (1,0) spots during the silicon deposition over time. At the beginning all spots are very sharp and with high intensity. First the (-1/2,0) and (1/2,0) spots belonging to the p(2x2) pattern of the 3O termination start to vanish, decreasing in size and brightness. At around 0.2 ML (amounts refer to silica coverage) the initial p(2x2) spots vanish, leaving behind a very blurry and weak spot and at this time the formation of a Henzler ring [111, 112] around the (0,0) spot is visible. With further silicon deposition, the intensity of the remaining p(2x2) spots decrease and the intensity of the Henzler ring increases. At 0.5 ML the p(2x2) spots disappear while the Henzler ring has its maximum intensity (see figure 5.7 a), b) and c) and the green curve in figure 5.8). The diameter of the (0,0) spot reaches at this stage a first

minimum. In figure 5.7 b) a LEED image is shown where the Henzler ring around the (0,0) spot is very visible and c) is a magnified cross section of the (0,0) spot and its close surrounding. Above a coverage of 0.5 ML only faint traces of the p(2x2) spots are visible, the Henzler ring starts to decrease its intensity while the diameter of the (0,0) spot increases again. At 1 ML the (0,0) spot intensity reaches a local maximum and the Henzler ring has nearly vanished. Above 1 ML the (0,0) spot decreases its diameter and starts to disappear rapidly around 1.5 ML. The p(2x2) spots and the Henzler ring vanish for a coverage higher than 1 ML. The (1,0) spots show no special behaviour, they decrease in intensity and diameter right from the beginning until they disappear at around 1.25 ML.

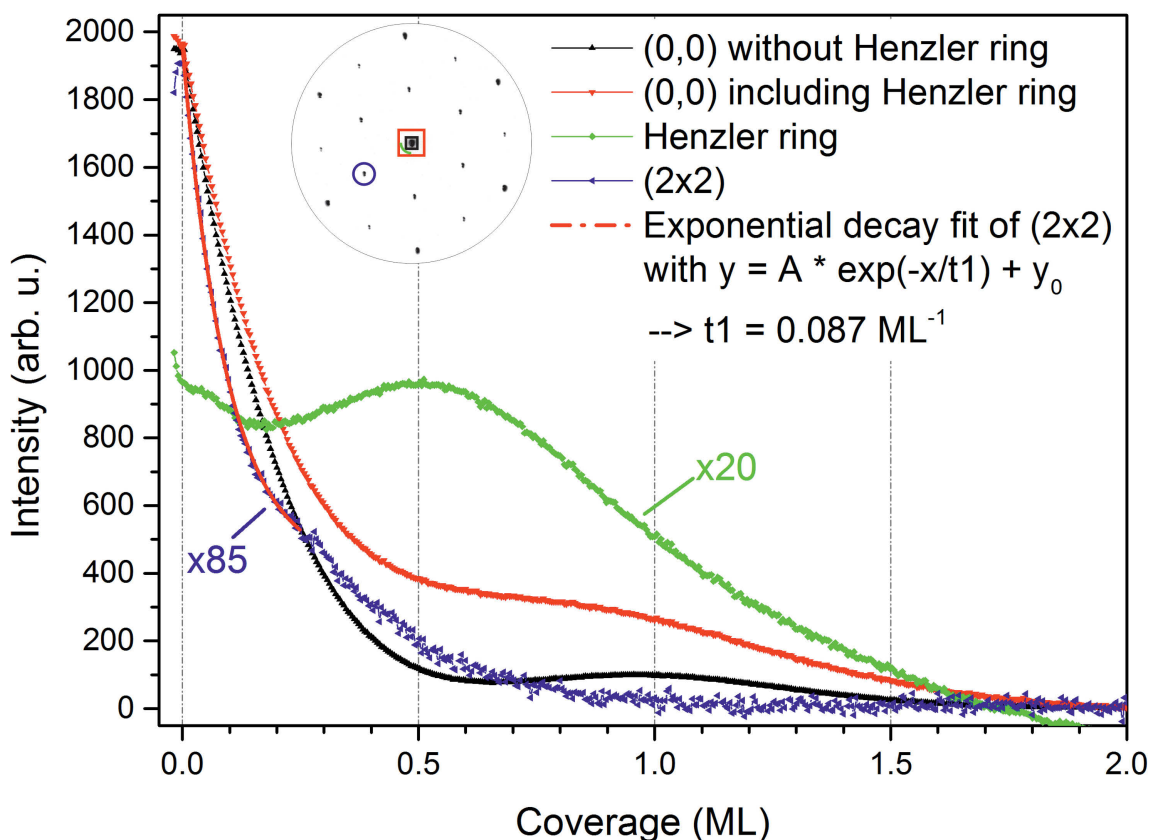


Figure 5.8: LEED intensity decay during deposition in oxygen and at room temperature onto a 3O terminated Ru(0001) surface. The black curve is the intensity of the (0,0) spot, green the intensity of the Henzler ring and blue the intensity of the first order of the p(2x2) pattern. For the red curve the area of interest for analysis included (0,0) spot and the Henzler ring. The kinetic energy was 42 eV.

The presented curves in figure 5.8 show a detailed analysis of the spot intensity decays already described above. It includes the intensity analysis of all the 1/2,0 and 1,0 spots visible in figure 5.7 b). The black curve shows the intensity decay of the (0,0) spot where the background between the (0,0) spot and the Henzler ring

was subtracted. The intensity decays at the beginning with an exponential like behaviour until 0.5 to 0.6 ML and has there a first minimum. Then the intensity increases again until a maximum at 1 ML is reached and decays afterwards again. At around 2 ML nearly no intensity of the (0,0) is left. The red curve represents the usual result by following the deposition in-situ and in real time at the SMART microscope, including the intensity of the (0,0) spot and its surrounding Henzler ring. Three different slopes in the intensity can be noticed: First a fast exponentially like decay behaviour until 0.5 ML; followed by a slow linear decay that increases at around 1 ML until 2 ML coverage, where nearly no intensity of the (0,0) spot is left. The p(2x2) spots follow an exponential like decay until a 0.25 ML coverage is reached, then a linear decay continues until their intensity is as the background level above 1 ML. On the other hand, the intensity of the Henzler ring reaches a maximum at 0.5 ML (see figure 5.7 and figure 5.8). The intensities at the beginning and the above 1 ML are most likely an artefact due to the influence of the background signal around the (0,0) spot. Comparing to figure 5.7 a) it is clearly visible that the Henzler ring is appearing only above 0.25 ML and nearly vanished at 1 ML.

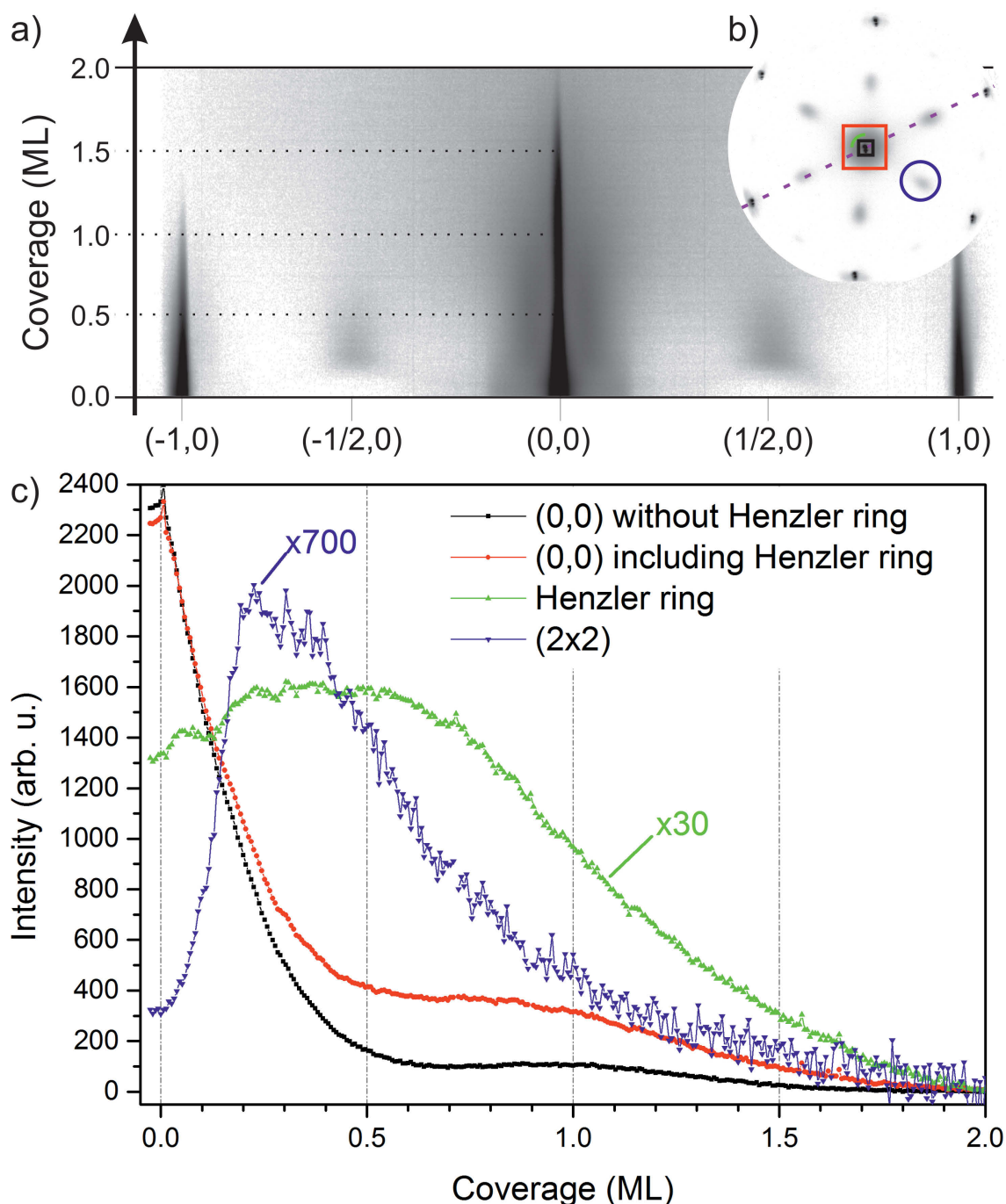


Figure 5.9: LEED investigation during silicon deposition onto 4O terminated Ru(0001). a) shows the added cuts through the reciprocal space over coverage in logarithmic scaling. b) inset of a LEED picture from the surface with a coverage of 0.25 ML, the dashed red curve highlights the cut, which was used for image a). c) Intensity decay of the LEED spots during deposition. The black curve is the intensity of the (0,0) spot, green the intensity of the Henzler ring and blue the intensity of the first order of the p(2x2) pattern. The area of interest for the red curve in the analysis included (0,0) spot and the Henzler ring. The kinetic energy was 42 eV.

Figure 5.9 shows the LEED intensity behaviour of the deposition of silicon onto a 4O terminated Ru(0001) surface. a) presents the cross-sections of the reciprocal

space from the $(-1,0)$ to the $(1,0)$ spots as a function of coverage. The $(0,0)$ and the $\{1,0\}$ spots resemble very well the behaviour already seen for the deposition onto a 3O terminated Ru(0001) surface (compared to figure 5.7 and figure 5.8). Because of the (1×1) pattern of the 4O termination there are no $p(2 \times 2)$ spots at the beginning of the deposition. However, already after 0.1 ML an increasing intensity at the position of the $(-1/2,0)$ and $(1/2,0)$ spots can be noticed that reaches a maximum at 0.25 ML. Two oxygen atoms are required to fully oxidize one silicon atom, if the oxygen atoms are supplied by the 4O termination, assuming that no additional oxygen adsorbed, 0.25 ML silicon will leave an amount comparable to the 2O termination. This agrees with the intensity behaviour of the $(1/2,0)$ spot during oxygen exposure of clean Ru(0001) (see figure 4.2). With the ongoing consumption of the oxygen of the Ru(0001) surface the $1/2,0$ intensities start to decay, but in comparison to the 3O terminated surface this process takes longer. Again a formation of silica islands is indicated by the formation of a Henzler ring around the $(0,0)$ spot starting at around 0.25 ML. It is worth mentioning that the $(0,0)$ spot shows the same behaviour in terms of intensity and a local maxima is found at a coverage of 1 ML (see figure 5.8). Thus, it is possible to calculate the deposition times needed for films with more than 1 ML silica in real time.

Figure 5.10 shows the progress of the Si 2p line during the silicon deposition in 2.0×10^{-7} mbar oxygen onto a 3O terminated Ru(0001). During the deposition, the sample was periodically moved (every 5 min) over $50 \mu\text{m}$ to minimize the effect of beam damage. The opposite behaviour than the deposition in UHV at 420 K is seen (see figure 5.4); i. e., starting with a more metallic character for very low coverages and evolving to more oxidized. In the inset in figure 5.10 a) the chemical state of the first fractions of a silica ML are shown, with the first peak appearing at 99.6 eV for a coverage around 0.01 ML. With increasing coverage, the intensity and binding energy increases rapidly to about 101 eV for about 0.1 ML. As the silicon amount increases further the intensity of the Si 2p line increases as well and the energy shifts even more, until 102.42 eV binding energy for 1 ML is reached. Figure 5.10 b) shows that for amounts higher than 1 ML not only an intensity increase and binding energy shift is seen, but also new components start to appear at the lower binding energy side, which increase with coverage. The inset in figure 5.10 b) shows the continued shift of the Si 2p peak and its strong dependence on the coverage. It has an exponential dependency for low coverages (as can be seen from the fitting results) until 0.25 ML coverage is reached. Then the shift shows a linear behaviour until 1.5 ML, when a constant binding energy of about 102.6 eV is reached for the main peak.

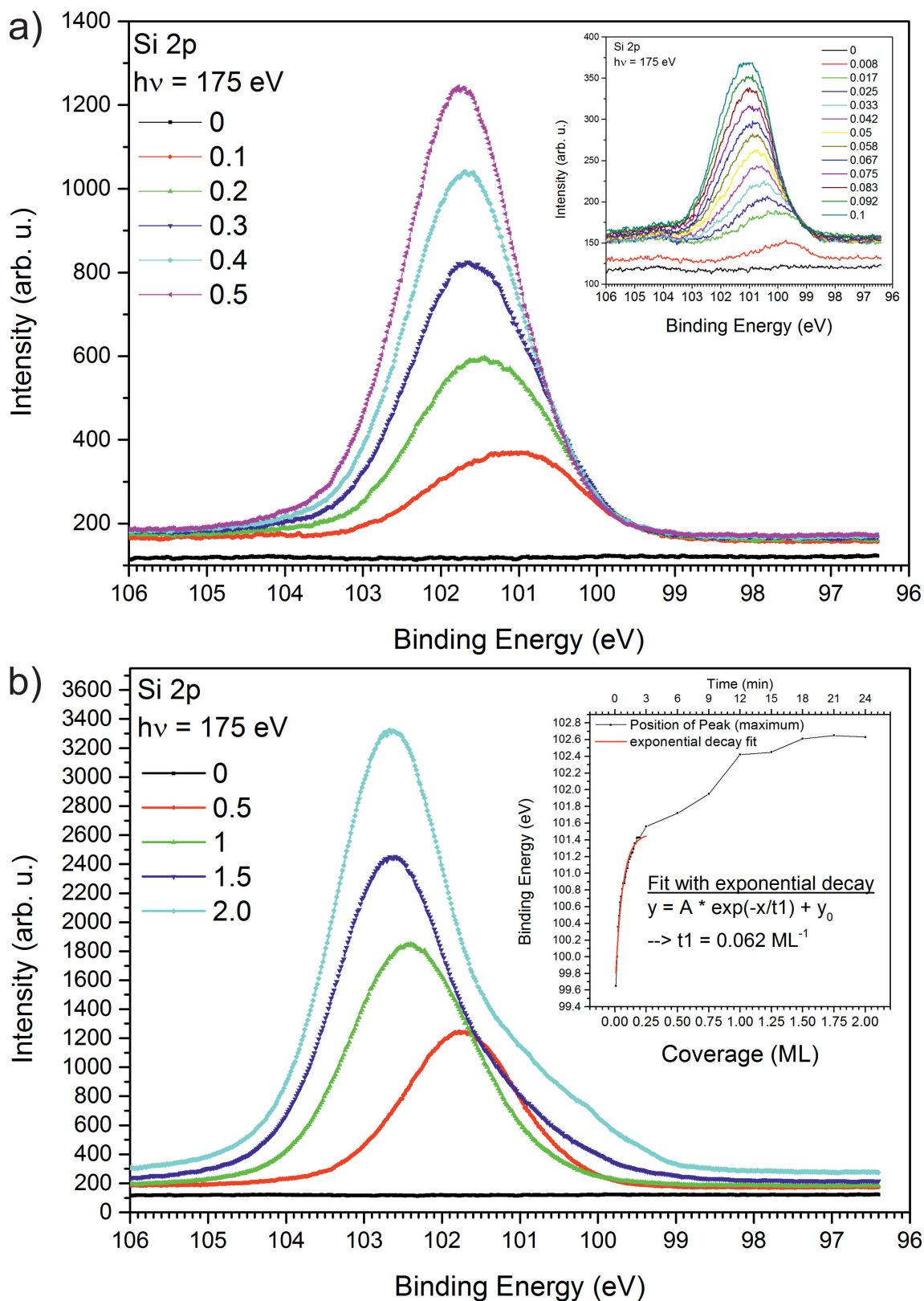


Figure 5.10: In-situ photoelectron spectra of the Si 2p line during the deposition in O_2 onto 3O terminated Ru(0001). In a) the large spectrum shows the deposition from 0 to 0.5 ML in 0.1 ML steps, while the inset shows the very initial deposition from 0 to 0.1 ML in about 0.01 steps. In b) the spectra shows the deposition in O_2 onto 3O terminated Ru(0001) from 0 to 2.0 ML in 0.5 ML steps. The small inset on the right shows the energy shift of the absolute peak maximum during deposition.

5.2.1 After deposition of 1 ML

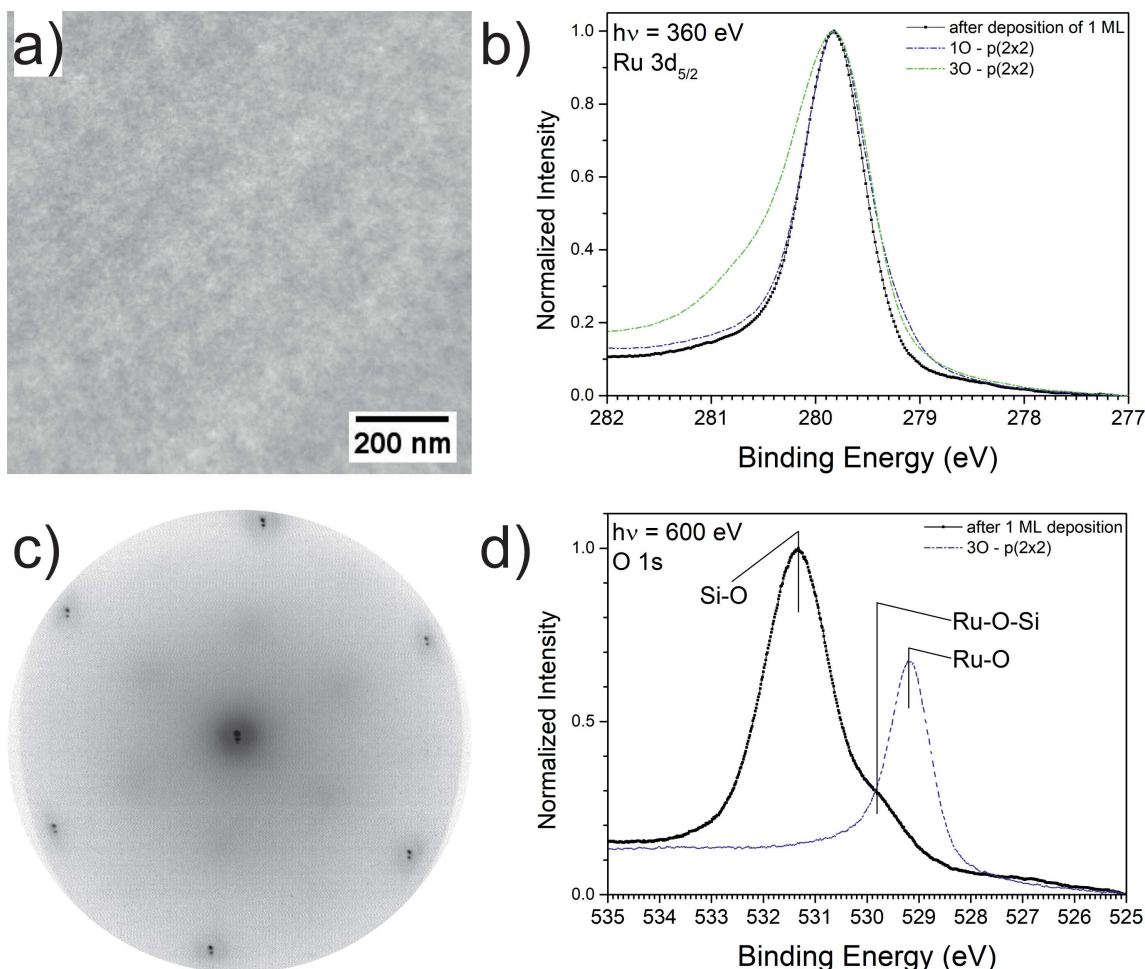


Figure 5.11: After the deposition of 1 ML at room temperature in O_2 ; a) LEEM and c) LEED image measurement with 42 eV b), d) photoelectron spectra of $Ru\ 3d_{5/2}$ and $O\ 1s$. In b) are the spectra of the 1O and 2O termination for comparison included.

Figure 5.11 a) shows a LEEM image of the surface after the deposition of 1 ML silicon. As can be seen from the picture, it looks blurry and has very low contrast. Nevertheless, atomic steps and step bunches of the $Ru(0001)$ surface are still visible and also brighter areas island-like areas can be found. In the LEED image in figure 5.11 c) a blurry $p(2 \times 2)$ and a Henzler ring is still visible suggesting a very un-ordered surface, in agreement with the LEEM image. In XPS the $Ru\ 3d_{5/2}$ line got much narrower in comparison to the one from the 3O termination (see figure 5.11) and even narrower than the 1O termination (indicated by the red dashed line in figure 5.11 b). The $O\ 1s$ line shows an additional component with high intensity at 531.3 eV indicating silicon-oxygen bonds (Si-O), which overlaps with another component at 529.8 eV (see figure 5.11 d)) ascribed to ruthenium-oxygen-silicon bonds (Ru-O-Si). This is supported by a simulation in [11], where it is predicted that the

O 1s binding energies of Ru-O-Si and the binding energies of the different adsorption sides of ruthenium (hcp, top, fcc) are very close to each other in an energy range <1 eV. For the sake of comparison, the O 1s line of a 3O terminated Ru(0001) surface is also shown.

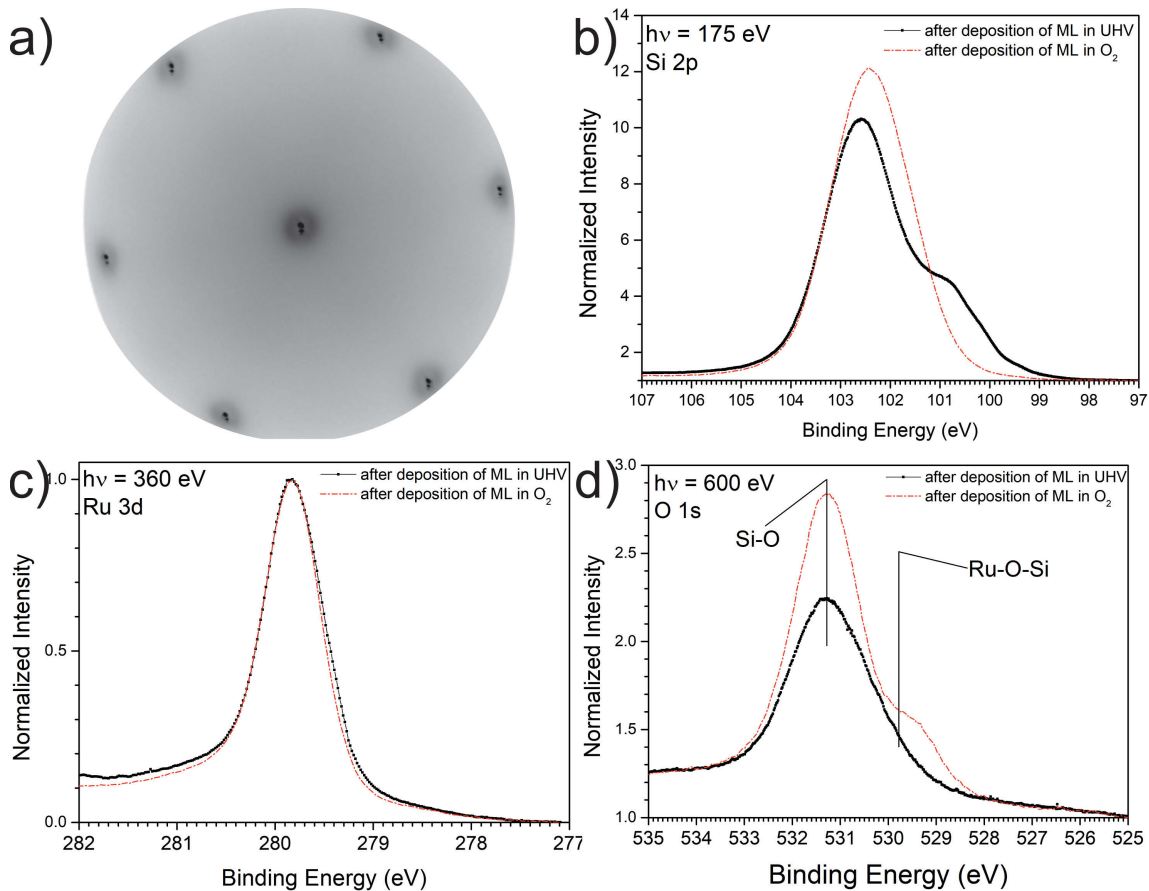


Figure 5.12: After the deposition of 1 ML silicon in UHV onto a 3O terminated Ru(0001) surface. a) is a LEED image with 42 eV kinetic energy. The photoemission spectra of the Si 2p, Ru 3d and O 1s are shown in b), c), d).

In order to study the influence of the oxygen pressure during deposition, Silicon was deposited in UHV at room temperature onto a 3O terminated Ru(0001) surface. The obtained LEED pattern and photoemission spectra for Si 2p, Ru $3d_{5/2}$ and O 1s lines are shown in figure 5.12. For comparison, the photoelectron emission lines of a deposition with oxygen background pressure are shown as red dashed lines. In comparison to figure 5.11 c) the LEED pattern does not exhibit a $p(2\times 2)$ reconstruction, but the Henzler ring has an higher intensity around the (0,0) and $\{1,0\}$ spots. The Si 2p line at 102.59 eV in figure 5.12 b) is slightly shifted in comparison to the Si 2p line for the deposition in oxygen atmosphere (102.42 eV) and also shows a wide feature at the lower binding energy side with at least two components. The Ru $3d_{5/2}$ line in c) is narrow, but not as narrow in the case

where deposition takes place in oxygen. Moreover, the O 1s line in d) shows again a component at 531.3 eV, but is less intense and broadened at the low binding energy side.

5.2.2 After deposition of 2 ML

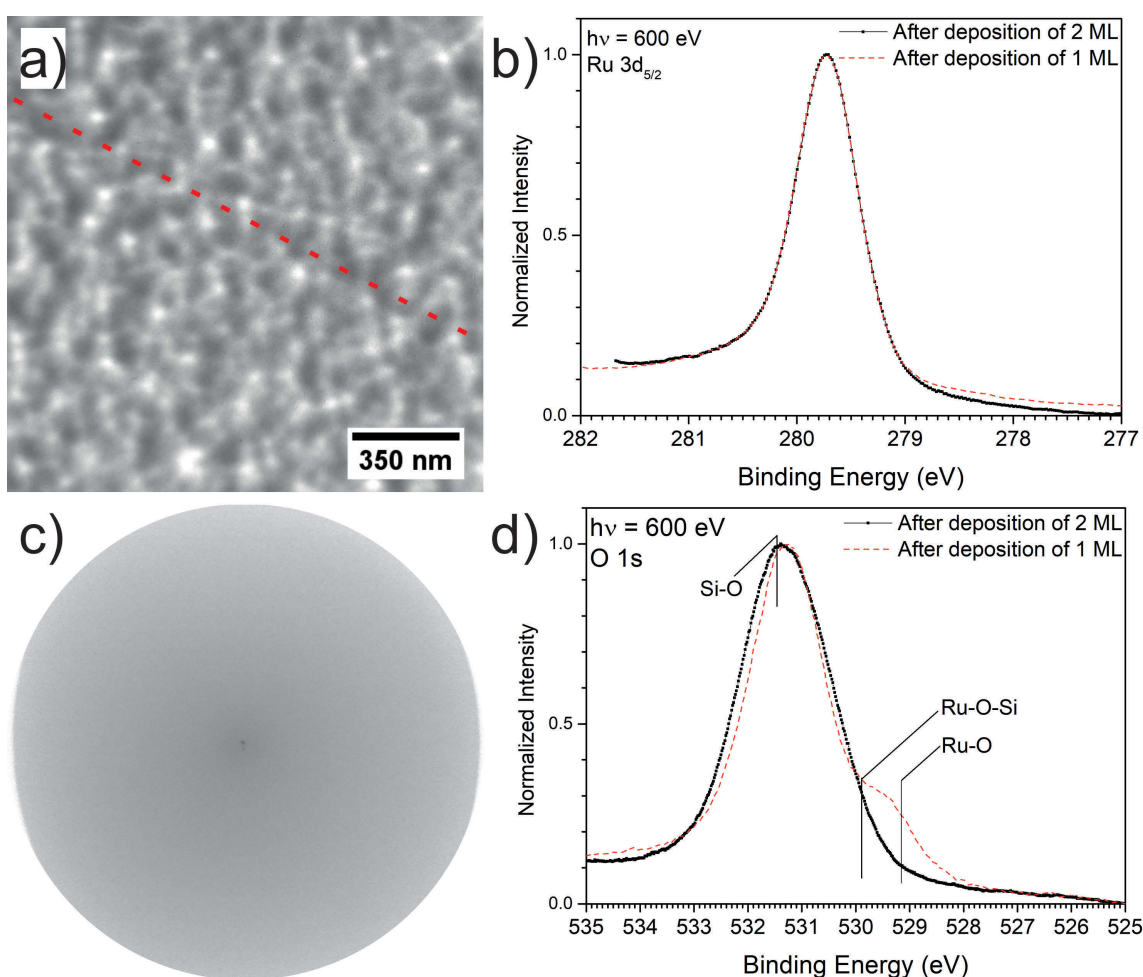


Figure 5.13: LEEM, LEED and photoemission spectra of Ru $3d_{5/2}$ and O 1s after the deposition of silicon corresponding to 2 ML silica. The LEEM image is done in the MEM to LEEM transition with a kinetic energy of 3 eV, the LEED image with 42 eV. The plot of the photoemission spectra includes the results for 1 ML as comparison (red dashed dotted line).

Figure 5.13 a) shows a LEEM image that is taken after the deposition of 2 ML silicon in 2.0×10^{-7} mbar oxygen at RT onto a 3O terminated Ru(0001) surface with in the energy range of the MEM to LEEM transition, because in LEEM no contrast for an unordered surface is found. This fits to the LEED image shown in c) where only a (0,0) spot is visible. Although the high sensitivity on work function differences in MEM leads to mainly blurred images, it is still possible to distinguish small particles on the surface and to see even step bunches of the substrate (marked as red line in

the image). Otherwise, because of this special contrast, it is not possible to say if the black round features are holes between the particles or if they are particles too, just with a much lower work function or blurred by a lens-effect due to their geometry. Figure b) compares the Ru $3d_{5/2}$ spectra after the deposition of one and two ML, where no significant difference can be distinguished. The O 1s spectrum shown in d) exhibits one peak at 531.39 eV, in comparison to the deposition of 1 ML it has no shoulder at lower binding energy, but has the same maximum intensity, but is slightly broadened.

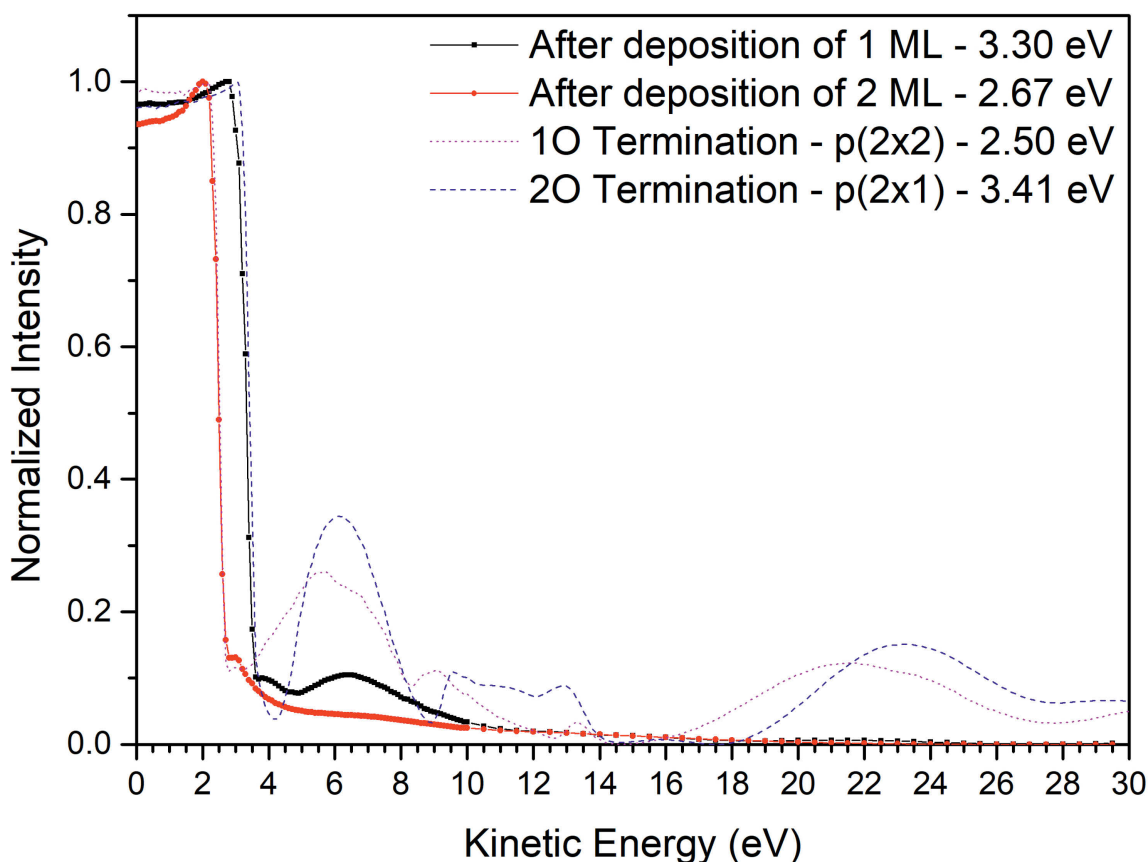


Figure 5.14: *LEEM(iV) curves after the deposition of 1 ML (black) and 2 ML (red) silicon, for comparison the dashes lines show the 1O (purple) and 2O (blue) LEEM(iV) curves.*

Figure 5.14 shows the LEEM(iV) obtained after the deposition of 1 ML or 2 ML silicon on a 3O terminated Ru surface in oxygen. For 1 ML the MEM to LEEM transition is lowered from the 3O value of 3.50 eV to 3.3 eV close to the value of the 2O termination. For 2 ML it is lowered even more to 2.67 eV, close to the value obtained for a 1O termination. The LEEM(iV) curves for 1 ML still show some features for low kinetic energies, which could be related to an oxygen coverage or a low ordered silica over-layer, while the 2 ML coverage does not exhibit any special structure and is completely amorphous.

5.2.3 The role of Ru as a catalyst during the deposition in oxygen

The oxidation of pure crystalline silicon occurs at either considerably higher oxygen pressure (1 bar at room temperature) or higher temperatures (700 K at low pressures) than the conditions used in this study [113–115]. To explain the oxidation at low pressure and low temperature in this subchapter: The possibility of Ruthenium acting as catalyst for silicon oxidation by supplying atomic oxygen should be considered. A possible scenario is proposed for the processes occurring during sample preparation.

When the first silicon atoms adsorb on the ruthenium surface, they diffuse and most likely occupy adsorption sites of ruthenium (hcp, fcc, bridge, top). Then, silicon oxidizes by a transfer of oxygen atoms from the surrounding hcp sides, most likely at defects of the 3O termination, to form a Si-O molecule. Afterwards, another oxygen atom of the surrounding 3O termination is transferred to the Si-O molecule to oxidize it further, leading to O-Si-O molecule. At the same time this reaction recovers adsorption sites and makes them available for new oxygen dissociation and adsorption from the oxygen background atmosphere. The subsequent silicon atoms adsorb on the surface and diffuse until they attach to an already existing silica O-Si-O precursor. They get oxidized by the precursor and by an additional oxygen atom of the 3O termination. With increasing coverage silica cluster form, that grow to islands with some Ru-O-Si bonds, forming an unordered silica tetrahedra network, until a closed ML is reached. The growth of silica over the surface inhibits the oxygen dissociation until the entire surface is covered and ruthenium loses its catalytic activity. Since the growth occurs at room temperature, the film is quite unordered, but already nearly completely oxidized. Additional silicon atoms adsorbing on this surface cannot find free atomic oxygen anymore to get completely oxidized, finally leading to a partially oxidized amorphous silicon bilayer.

The transfer of oxygen atoms from hcp sides to silicon at adsorption sites and the simultaneous overgrowth of hcp sides lead to an exponential decay of the initial p(2x2) spots as seen in figure 5.7 and in figure 5.8. The decay constants (0.086 ML^{-1}) of the p(2x2) LEED spots and the decay constant (0.062 ML^{-1}) of the fitted Si 2p peak shift (see figure 5.10) are in the same order of magnitude indicating a correlation between both decays. The FWHM of the Si 2p line decreases with coverage implying the formation of a uniform chemical state of SiO_2 , see figure 5.10. A possible reason could be a large size distribution of silica clusters at the very beginning of the deposition, which narrows with continuing growth. Taking into account that extra charge can be localized at the perimeter of small clusters [116–

118], a size dependent charging effect can be assumed and could be responsible for the peak shift observed. Especially under the consideration that the interior of the cluster is not affected [119] and so the ratio of circumference to interior decreases rapidly with growth. The amount of 0.25 ML seems to be a breaking point, when a unification of the cluster size happens. A possible reason therefore could be that the average distance between the clusters decreases when adding more silicon/silica, consequently merging together and forming two-dimensional islands. This is supported by the appearance of a Henzler ring that indicates a uniform size distribution on the surface [120]. At the same time the sharp $p(2 \times 2)$ LEED spots disappear leaving behind a blurry $p(2 \times 2)$ reconstruction possibly attributed to very small and slightly ordered silica domains. This assumption is supported by the appearance of these spots for the deposition onto 4O terminated ruthenium at 0.25 ML too. For 0.5 ML the intensity of the Henzler ring reaches a maximum and starts to decay. Considering the stoichiometric ratio of silica (SiO_2), the oxygen of the 3O termination is completely consumed. However, the Si 2p line still does not show any features attributed to lower oxidation states. This finding suggests that atomic oxygen is still supplied for the silicon oxidation through the ruthenium via dissociation of oxygen from the gas phase. To prove this assumption, silicon was deposited in the absence of gas phase oxygen on a 3O terminated ruthenium surface. This preparation leads to silicon species with lower oxidation states, indicated by the low energy shoulder of the SiO_2 component in the Si 2p line (see figure 5.12 b) and a smaller intensity of the SiO_2 component accompanied with an absence of chemisorbed oxygen on ruthenium in the O 1s line (see figure 5.12 d). The increasing intensity of the (0,0) spot for more than 0.5 ML is the result of the increasing SiO_2 amount on the surface, leading to a local maximum in its reflectivity for a closed layer of low ordered silica (see figure 5.8 and the shallow $p(2 \times 2)$ reconstruction in figure 5.11). At this point the catalytic property of Ruthenium is inhibited, leading to the appearance of components attributed to lower oxidation states at the Si 2p line and their increase with continuing deposition (see figure 5.10). The second layer grows less ordered, decreasing the intensity further of the (0,0) spot (see figure 5.8 and the LEEM(iV) comparison in figure 5.14). In [121] the formation of an oxidized ML was already assumed, without a proof. The photoelectron spectra in this work prove this and the proposed model gives a reasonable explanation.

The (2x2)R30° ML-phase

6.1 Preparation, and characterization of properties

The 1 ML silica films described in subchapter 5.2.1 were annealed to about 1000 K under UHV conditions, the annealing pressure was always lower than 5.0×10^{-9} mbar. The results of this work expand the already published ones of our institute, where only ex-situ measurements have been done with STM, IRRAS, XPS and LEED [16]. It is shown, that an annealing in oxygen is not necessary to prepare this structure, it can be achieved just with a UHV anneal of the *as-deposited* silica film. This leads to much less additionally adsorbed oxygen at the ruthenium surface than reported before.

Figure 6.1 shows the intensity analysis of the appearing LEED spots during these treatments. The LEED images were acquired in-situ and in real time. In the upper left of the figure, the usual temperature progress during such a preparation step is shown. It starts with a heating ramp of 6.5 K/s until nearly the final annealing temperature was reached. The heating rate was lowered at the end to prevent exceeding the target temperature. When the final temperature was reached, the sample temperature was held for 70 s. Then, the sample was cooled down starting with a 4.5 K/s rate until the thermal mass of the sample holder restricts the cooling rate. At this point the temperature drops exponentially. Thus, the experiment can be divided in three sections, namely: heating, holding and cooling of the sample, marked as a, b and c in the diagram. For each section, the most representative LEED images are shown. They are connected to the plot of the intensity of the spots in the lower part of the image by roman numerals. The plot is divided into the three sections of the temperature treatment, beginning with the heating, continuing with the holding, and finishing with cooling down. The temperature dependence for the

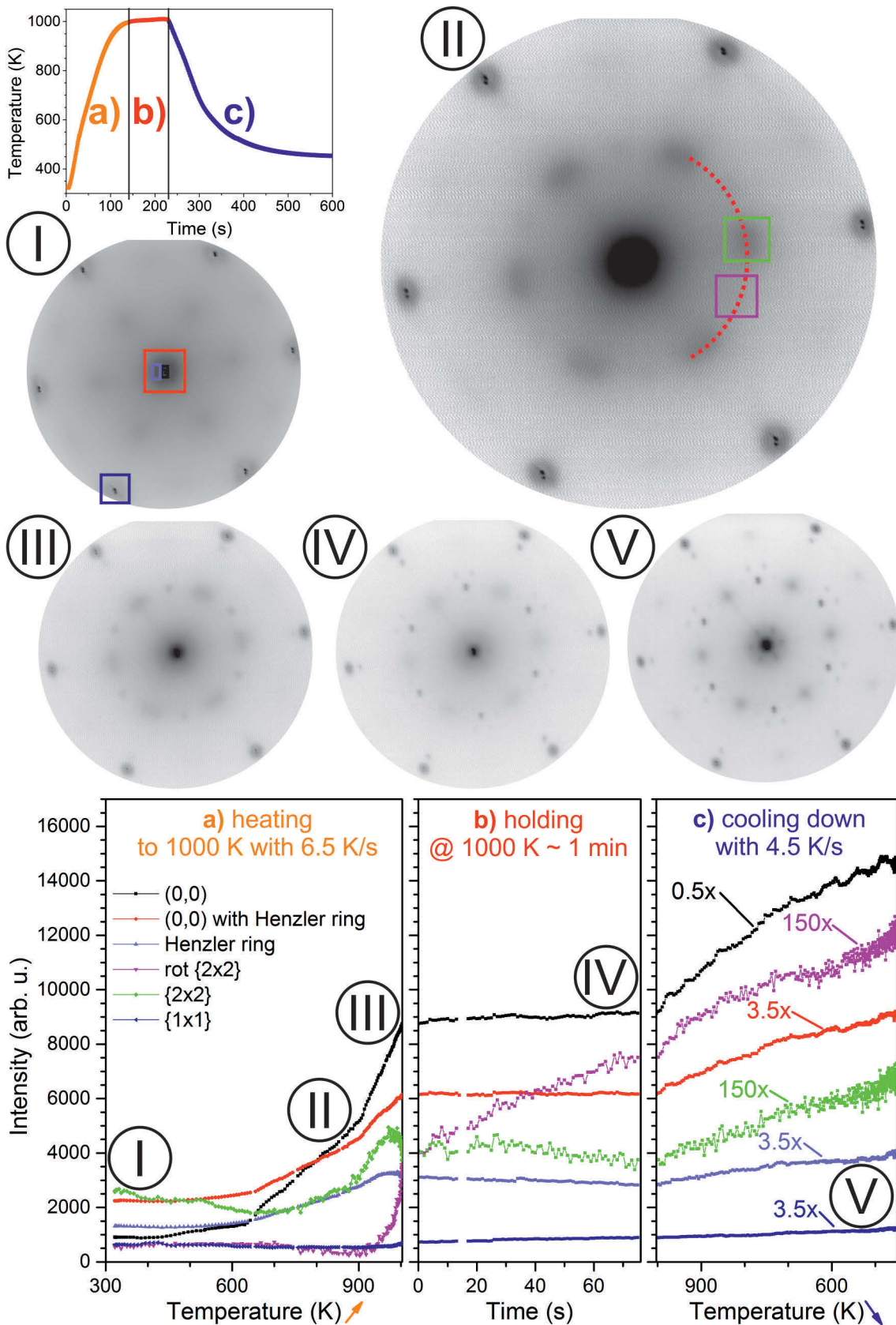


Figure 6.1: Analysis of LEED spots appearing during UHV annealing to 1000 K. In the upper left, the temperature-time profile is shown, and in the middle part LEED images occurring during this temperature treatment. The lower part presents the analysis of the intensity of the individual LEED spots during heating, holding and cooling steps, as indicated. An electron kinetic energy of 42 eV was used. (for more details see text)

heating and cooling steps and for the holding stage are plotted. The areas of interest used for the analysis are highlighted in the LEED images by the corresponding coloured boxes.

The LEED image I shows the film at room temperature after deposition. The $(0,0)$ spot surrounded by a Henzler ring and $\{1,1\}$ spots are visible. Also, between them a blurry (2×2) structure can be found. In an intensity versus temperature plot, it can be seen that with increasing temperature the intensities of the $(0,0)$ spot and the Henzler ring increases, first linearly until 650 K, and a larger slope for higher temperatures. On the other hand, the intensity of the $p(2 \times 2)$ structure's LEED spots decreases until 650 K, but then starts to increase linearly. At 700 K, another increase of the slopes is found. At this temperature, the formation of additional 30° rotated (2×2) spots ($(2 \times 2)R30^\circ$) can be found (see the LEED image II). The image also shows that the intensity of the $p(2 \times 2)$ spots increases and that they change their shape into elongated structures. In the background between the $(2 \times 2)R30^\circ$ and the $p(2 \times 2)$ spots a weak ring structure is visible, highlighted with a red dashed ring segment on the image. Around the $\{1,1\}$ spots sharp and intense Henzler rings are visible. The intensities of the Henzler ring and the $p(2 \times 2)$ structure have a maximum at 970 K and decrease with increasing temperature. The intensity of the $(0,0)$ spot continues to increase with a much steeper slope, while the intensity of the $(2 \times 2)R30^\circ$ structure shows an exponential-like behaviour. During the heating step, the $\{1,1\}$ spots linearly decrease in intensity until, at 980 K, their intensity starts to increase linearly. LEED image III shows the end of the heating ramp and the beginning of the holding time. The $(2 \times 2)R30^\circ$ spots are clearly visible and faint spots in front of the $\{1,1\}$ spots also appear. During the holding time the intensity of the $(2 \times 2)R30^\circ$ spots increases, while the intensity of the $p(2 \times 2)$ spots decreases. The same intensity drop is found for the Henzler ring, while for the $(0,0)$ spot and the $\{1,1\}$ spots the intensity rises. At the end of the holding step the LEED pattern of image IV is found. The $(2 \times 2)R30^\circ$ spots are very intense and sharp, with additional moiré spots surrounding them. The intensity of the $p(2 \times 2)$ spots is much lower and their elongated shape is barely visible. The Henzler ring has disappeared completely. The spots in front of the $\{1,1\}$ spots are also intensified, and a shallow moiré pattern has appeared around the $(0,0)$ spot. During cooling the intensity of the $(0,0)$ spot increases faster with decreasing temperature than the intensities of all the other spots. The final LEED pattern is shown in the LEEM image V: very sharp $(2 \times 2)R30^\circ$ spots are visible, also the $p(2 \times 2)$ have sharpened and the moiré spots are clearly visible. The intensity evolution of the moiré spots during the annealing is

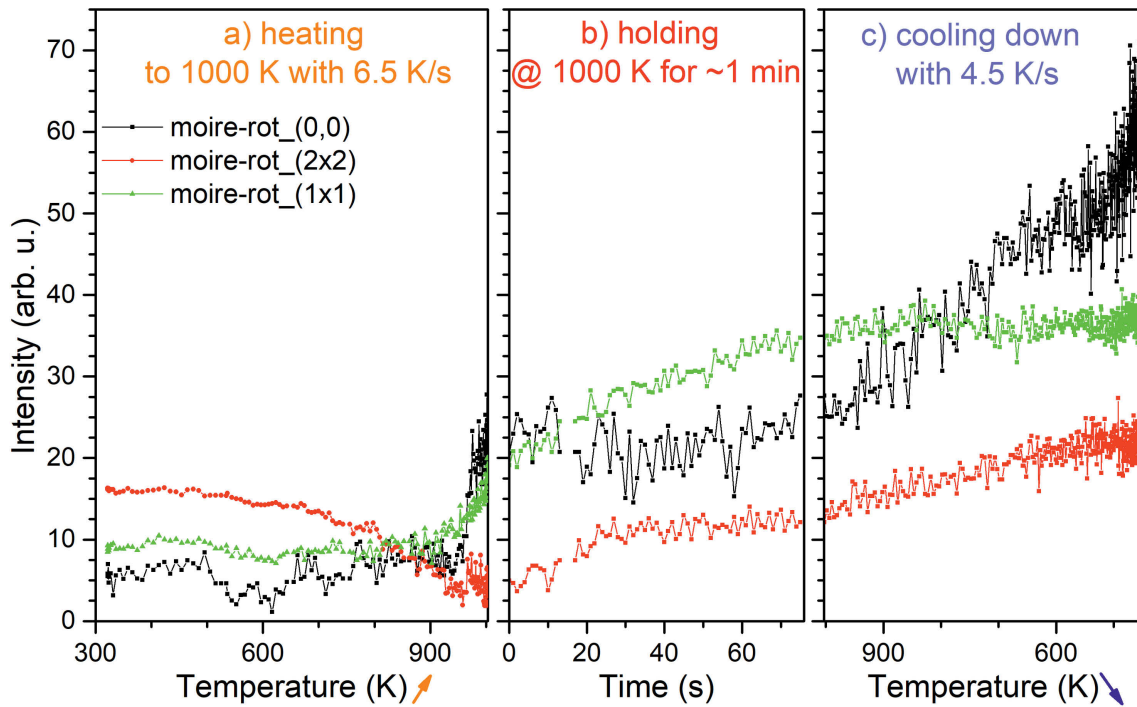


Figure 6.2: Intensity-temperature curves of the moiré spots during the temperature treatment in UHV.

shown in figure 6.2. They appear at 970 K and resemble the intensity progress of the main spots close to them.

Figure 6.3 shows a LEED pattern (upper part) and a series of LEEM and DF-images of the (2x2)R30° ML-phase taken at room temperature after annealing in UHV of a *as-deposited* ML. The LEED image shows a p(2x2) and a (2x2)R30° reconstruction with additional moiré spots. The unit cell of the (2x2)R30° is indicated. The bright field LEEM image shows a surface with three different bright features: white and grey islands that are delimited by dark areas or lines. The islands are about 25 nm in size and homogeneously distributed over the surface. To correlate these structures with the LEED image dark field microscopy was applied. In all three dark field images of the (2x2)R30° spots the same features are bright, but the contrast between them is much higher than in the bright field image. In the dark field images of the p(2x2) spots again three different types of bright features are visible. Grey and bright islands delimited by dark areas and black and white terraces. The terraces switch in contrast and islands appear and disappear by changing the spot, some of them are highlighted in the images. Comparing the bright islands with the dark areas in the bright field image shows that they are the same features. It is also visible that the dark lines in the bright field image are steps of the Ru(0001) surface.

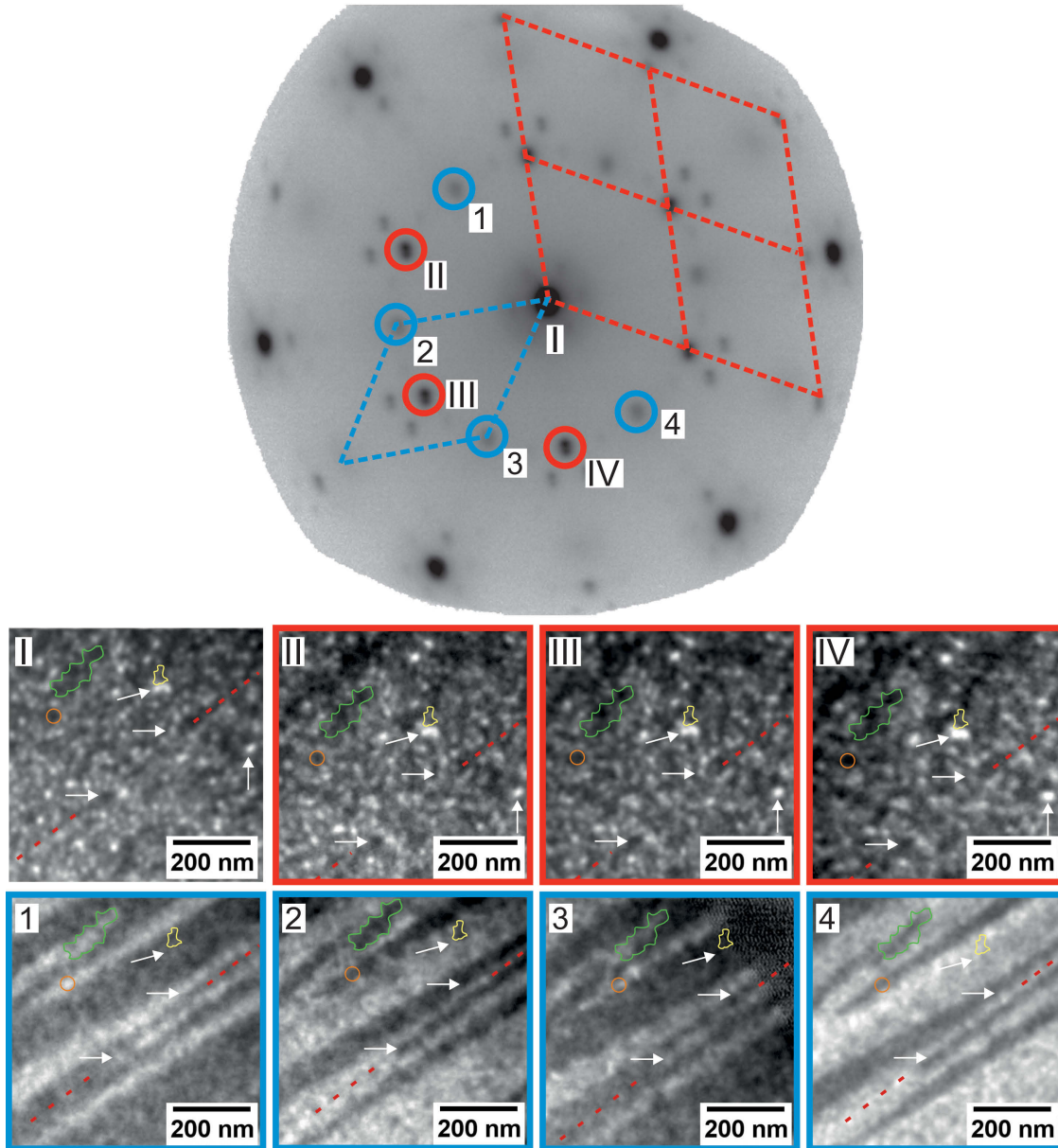


Figure 6.3: LEED, LEEM and DF-LEEM images of a ML annealed in UHV to 1010 K at room temperature. I is the bright field image and II-IV are dark field images from a $(2 \times 2)R30^\circ$ spot, 1-4 are dark field images from $p(2 \times 2)$ spot. The unit cell of the $(2 \times 2)R30^\circ$ structure (red) and of the $p(2 \times 2)$ structure (blue) are indicated. For a better visualization of the features of the $(2 \times 2)R30^\circ$ film, the $p(2 \times 2)$ spots and atomic steps are highlighted. The kinetic energy for the LEED images is 52 eV and for the LEEM and dark field images 20 eV.

The annealing parameters were slightly varied to investigate their influence. In figure 6.4 the results for three different temperature treatments are shown. In the first row the used parameters are given. They differ for film I and II in the final annealing temperature (995 K or 1015 K), the holding time (25 s or 50 s) and the heating (2 K/s or 4 K/s) and cooling rates (2 K/s or 4 K/s). Both films show in the bright field LEEM image the same features. Very bright and grey islands are

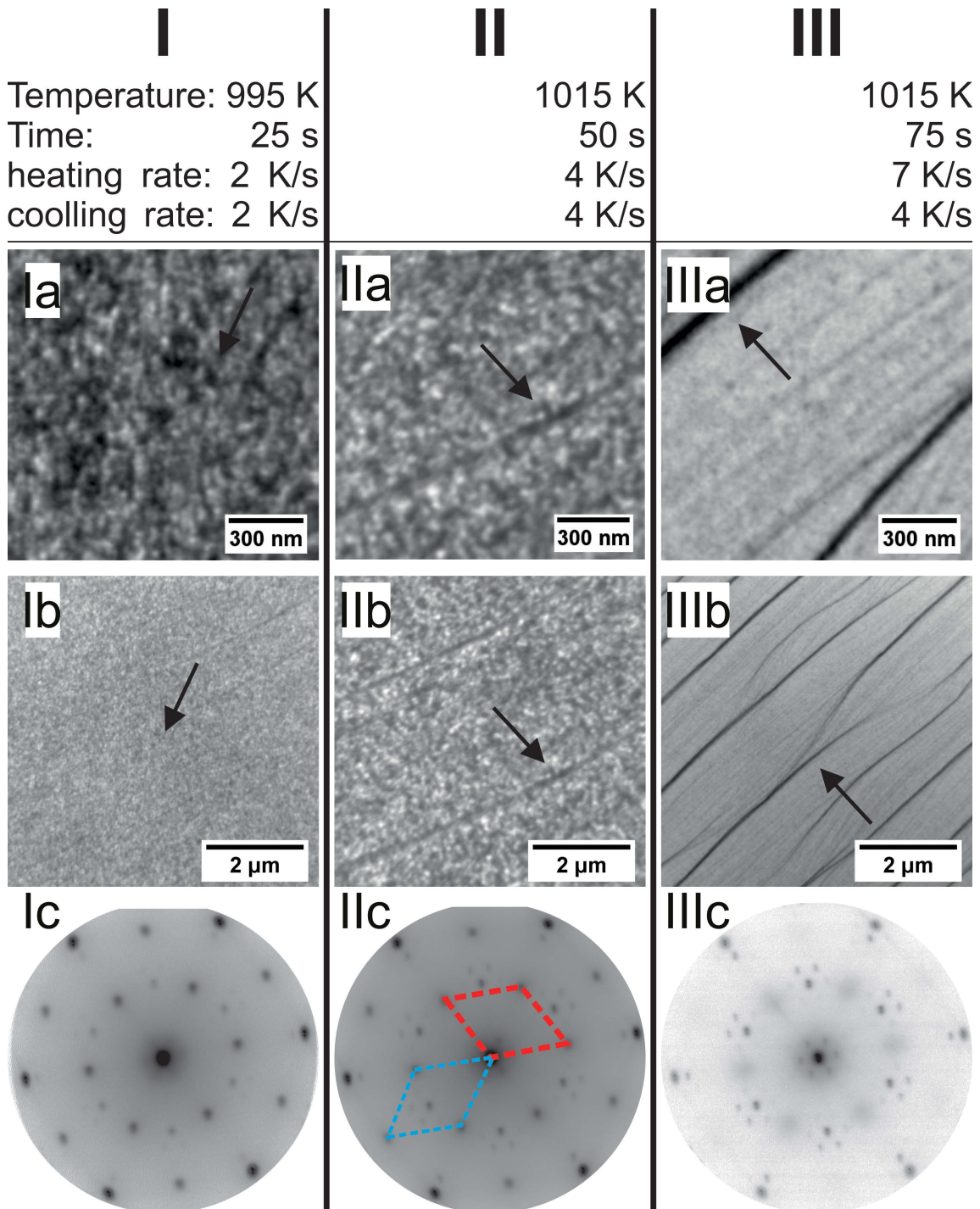


Figure 6.4: The influence of different annealing conditions on the structures of the film. In the first row the annealing conditions are shown, below them the resulting LEEM and LEED images are shown. The unit cell of the (2x2)R30° structure (red) and of the p(2x2) structure (blue) are indicated. All images were taken at room temperature and with an electron kinetic energy of 42 eV.

delimited by black lines or areas. The islands are homogeneously distributed over the surface (see the images Ia and IIa). However, the islands in IIa seem to be much larger and closer together. In a larger field of view the steps and step bunches of the Ru(0001) surface are visible (see Ib and IIb). In IIb the larger size of the islands is more obvious. The LEED images Ic and IIc show a very sharp $(2 \times 2)R30^\circ$ pattern and a somewhat blurry $p(2 \times 2)$ pattern. In the image IIc the structures of the moiré pattern are more intense than in image IIc. Film III was heated up using a faster rate (7 K/s vs 4 K/s) to the same final temperature as film II (1015 K), but holding the annealing temperature for 75 s. The cooling rate was also the same (4 K/s) as for film II. After this temperature treatment the film shows a very homogeneous surface. The islands have grown in size much more, atomic steps and step bunches of the surface are clearly visible. In the large field of view in IIb the surface looks very smooth. The LEED image shows a very sharp $(2 \times 2)R30^\circ$ pattern with an enhanced moiré pattern. The $p(2 \times 2)$ spots are very blurry and have a low intensity.

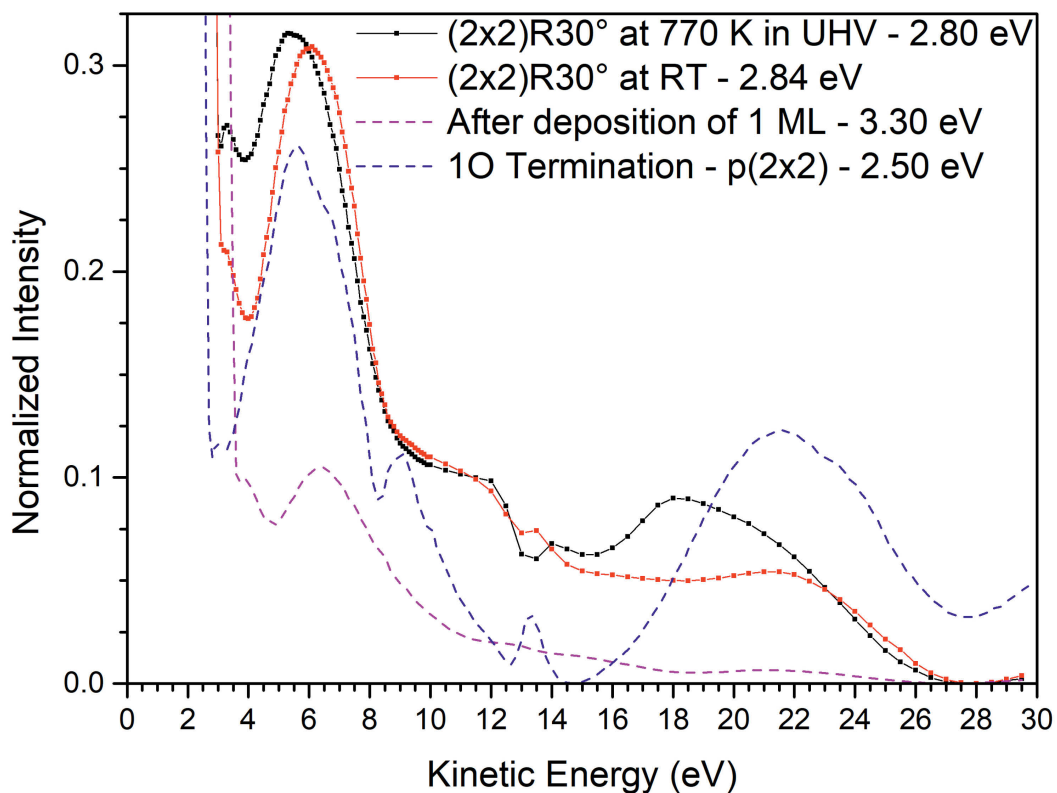


Figure 6.5: LEEM(IV) curves of a ML film at RT and heated up to 770 K after a temperature treatment in UHV. The intensity of the curves is normalized to the MEM intensity and the MEM to LEEM transition is given in the legend.

Figure 6.5 shows LEEM(IV) curves of a ML film at room temperature after a temperature treatment in UHV (red) and heated up to 770 K again (black). Additionally, the curves of the 1O termination and after the deposition are shown. The film was

again heated to 770 K and held there, because the intensity of the p(2x2) spots was very blurry then. In this way, it was tried to lower their contribution to the reflectivity and to enhance the part attributed to the (2x2)R30° spots. In comparison to room temperature, the features are much more pronounced at 770 K and the MEM to LEEM transition changed by only about 0.04 eV. For low energies (0 – 6 eV) maxima and minima are visible that were already found for the 1O termination and the pre-annealed film. The minimum at about 13 eV could be connected to the unoccupied surface and bulk 4f states on Ru(0001). Between 14 eV and 20 eV both curves have a maximum that is shifted to lower energies for the film annealed at 770 K. Both curves and the curve of the 1O termination show a minimum at 25 eV. For the sake of completeness figure 6.6 shows the DF-LEEM(IV) curves of the film at 770 K. They show a decaying intensity with increasing kinetic energy and have maxima at 13 eV, 19 eV and 25 eV.

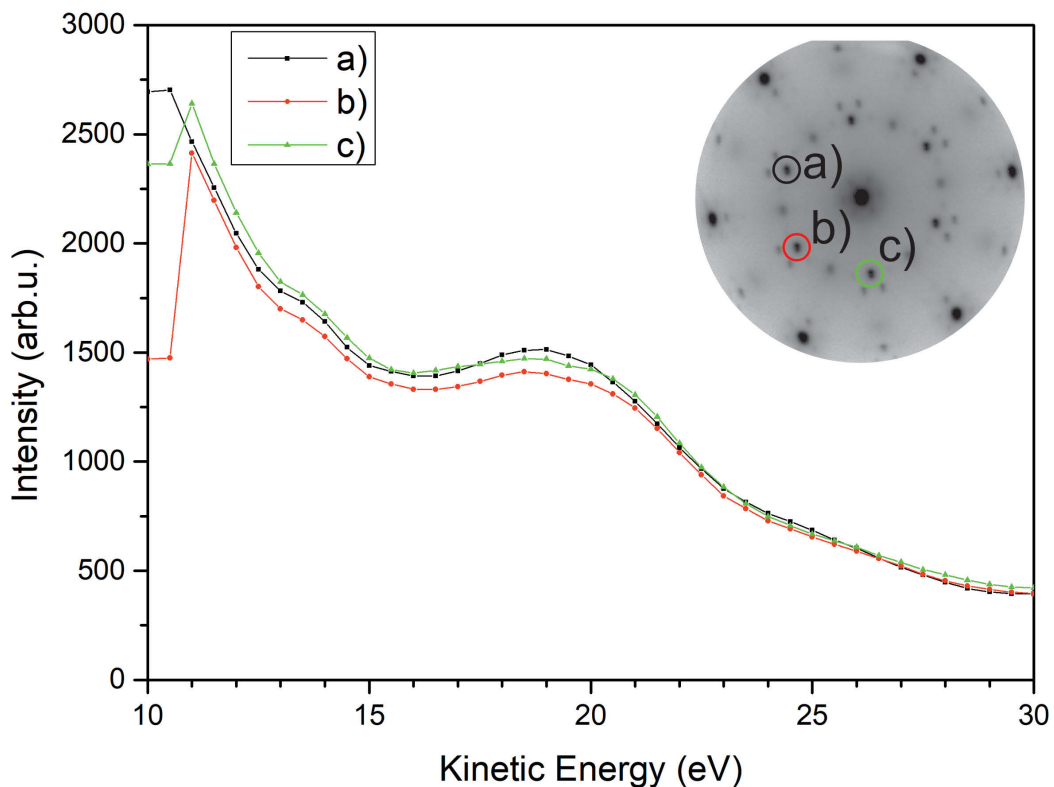


Figure 6.6: DF-LEEM(IV) curve of the (2x2)R30° spots of a ML film after temperature treatment in UHV. The spots used are highlighted in the inset.

Figure 6.7 shows the LEED(IV) curves for a ML after the UHV anneal, that was again held at 770 K to minimize the contribution of the p(2x2) reconstruction. All curves show many minima and maxima, as expected for a crystalline structure. A careful scaling for the data reveals a very weak but sharp ring structure. To enhance this feature, LEED images were summed up over the energy ranges where it was

very distinct. The ranges are marked in the LEED(IV) curve with boxes and the summed up LEED images are shown below the graph. The ring feature was always prominent, where the $(2 \times 2)R30^\circ$ structure has a maximum in intensity.

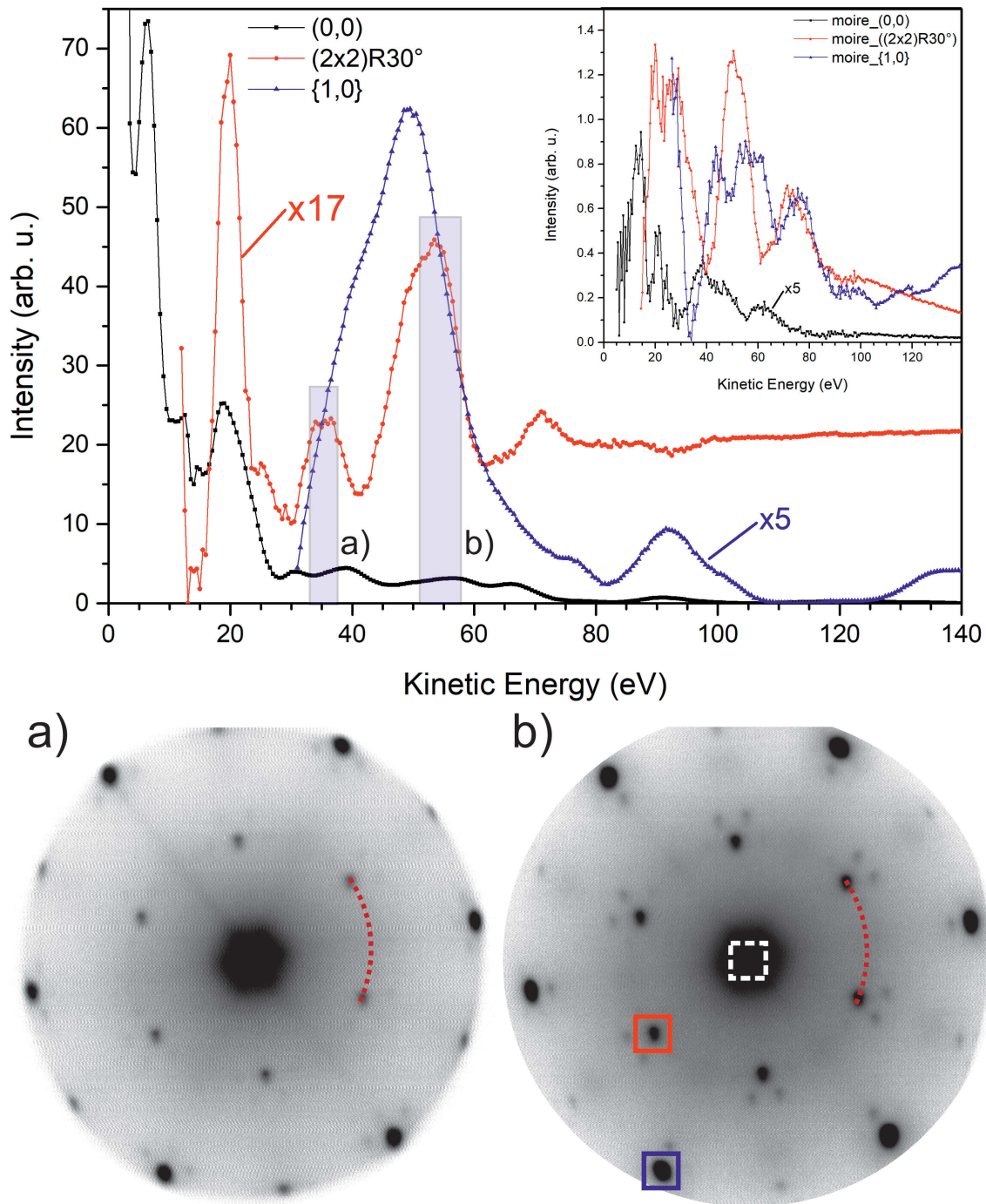


Figure 6.7: LEED(IV) curves of a ML prepared in UHV at 770 K. The LEED(IV) curves of the moiré spots are shown as inset. Below the graph there are two LEED images showing a faint but sharp circle indicated by a red curve segment, additionally the used spots for the LEED(IV) curves are indicated (the $(0,0)$ as white box). Both images are the average of LEED images for a) 33 eV - 37 eV and for b) 52 eV - 59 eV. The energy ranges are marked in the LEED(IV) graph with transparent boxes.

Figure 6.8 shows the photoelectron spectra after a temperature treatment in UHV. The Si 2p line in a) has a maximum at 102 eV and, in comparison to the Si 2p spectra recorded after the deposition (red), it is shifted about 0.5 eV to lower binding energies and the FWHM is significantly smaller. In b) the Ru 3d_{5/2} line is shown. It has a maximum at 279.8 eV. In comparison to the peak as deposited spectrum (red) it has broadened and closely resembles the features of the 1O termination (blue). Graph c) shows the O 1s line with two different components. The one with lower intensity and lower binding energy (529.8 eV) is assigned to oxygen bound to ruthenium and silicon (Ru-O-Si), in agreement to the findings from chapter 4. For comparison, the O 1s before the deposition is shown as blue curve. The second one is higher in intensity and at higher binding energies (531.2 eV) and is assigned to oxygen bound to silicon, shown in 5.11. In comparison to the *as-deposited* spectrum (red), the line of Si-O has no shift in the binding energy and the peak has a larger FWHM. Moreover, the ratio of both components (Ru-O-Si to SiO₂) has increased. The binding energies found in this study are shifted about 0.4 eV to lower binding energies than in the lab-XPS study in [16].

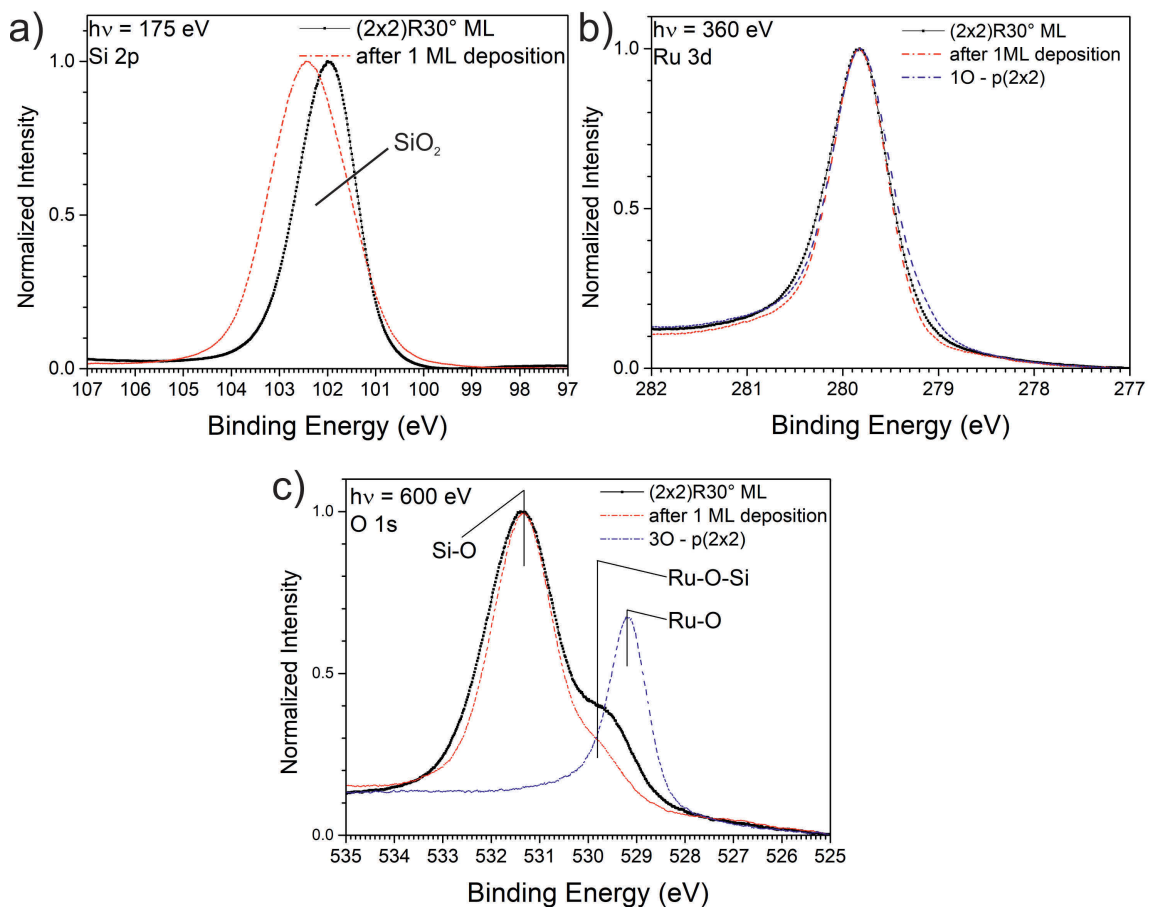


Figure 6.8: Photoelectron spectra of a ML after a temperature treatment in UHV. a) shows the Si 2p core line, b) the Ru 3d_{5/2} line and c) the O 1s.

6.2 Interpretation: Formation and morphology of the (2x2)R30° ML-phase

Following, the processes taking place during the temperature treatment in UHV described in chapter 6.1 will be discussed.

The already oxidized but still quite unordered silica ML is transformed by the temperature treatment to a very well ordered crystalline surface. It exhibits a (2x2)R30°-structure with a moiré -pattern surrounding the substrate spots. So far, only the preparation of silica MLs on Ru(0001) via a temperature treatment in oxygen (2.0×10^{-6} mbar) has been reported [9]. Therefore, this is the first time there the processes taking place during a temperature treatment under UHV conditions of the *as-deposited* silica film are described and discussed.

The starting surface exhibits features as described in section 5.2 (completely oxidized silica, that has small p(2x2) ordered islands mixed with an amorphous phase, highly likely surrounding it). Thus, the intensity of the p(2x2) reconstruction decreases at the beginning of the heating stage, while the intensities of the Henzler ring and the (0,0) spot increases (see figure 6.1 in the graph). This is pointing to the growth of islands or the formation of new ones with similar size distribution. At 650 K the formation of p(2x2) ordered areas starts to be preferred because the intensity of the p(2x2) spots begins to increase. Up to 900 K the formation of the (2x2)R30° ML-phase is favoured. Two scenarios here are possible. First, the still amorphous areas start to get ordered in a rotated way, with multiple rotations, leading to the formation of a shallow ring and the (2x2)R30° spots seen in LEED (see LEED image II in figure 6.1). Second, some p(2x2) areas rearrange, probably at their rim, by rotating around 30°. At this point on the surface are p(2x2) and (2x2)R30° domains coexisting and growing at the same time. The growth of the (2x2)R30° ML-phase shows an exponential-like behaviour on temperature. However, at 975 K the transformation of the p(2x2) areas to the (2x2)R30° areas starts to be faster than the growth of these areas. The intensity of the initial p(2x2) spots starts to decrease drastically with increasing temperature. Holding the sample at 1000 K shows a linear increase of the intensity over time of the (2x2)R30° spots and a decrease with a smaller absolute slope of the p(2x2). New (2x2)R30° areas are formed and growing in size, while the p(2x2) areas are increasingly transformed into the (2x2)R30° ML-phase. When cooling down this situation is quenched and all spots increase in intensity.

The exponential-like dependency on temperature of the ordering of the film is also found in the image series in figure 6.4, where the influence of various annealing parameters was studied. The annealing and cooling rates do not seem to have a strong influence on the structure of the film, while the final holding temperature and the holding time have strong influence. The higher the temperature, the faster the formation is happening (exponential-like dependency on temperature) and the longer the holding time (linear dependency on time) the larger the single islands grow. This suggests a process where an energy barrier has to be overcome to start it. Additional annealing experiments with different holding temperatures and long holding times could be used for an Arrhenius plot to determine the activation energy.

At room temperature, the surface shows clearly the existence of a (2x2)R30° ML-phase, without any rotational domains (see DF images II-IV in figure 6.3). However, the film is not completely closed. Instead, it has holes or areas without the (2x2)R30° ML-phase, wherein a p(2x2) pattern is found, and line features, connected to step bunches, over which the film could not grow. A comparison of the dark field images series 1 - 4 of the p(2x2) spots in figure 6.3 suggests that at the bottom of some of these holes there are oxygen p(2x1) domains. This would also agree to the seen blurring of these spots during re-annealing to 770 K. For different kinetic energy ranges a weak ring structure is visible in LEED, because the film used for the LEED(IV) was quenched during the transformation of the p(2x2) areas or the growth of small rotated areas. The ring is only visible for high reflectivity of the (2x2)R30° ML phase and seems in this way to be connected with it. However, the narrow ring hints for a different ring size distribution than the one already found in the BL or for certain defects in the layer [8, 122–126]. An additional possible explanation for the sharp ring structure might be, that the material in excess forms 2 dimensional or 3 dimensional islands of well-ordered structure but arbitrarily rotated on the ML film, which is also referred to as texture.

This finally leads to the following conclusion for the morphology of the film: Large (2x2)R30° areas exist on the surface, which have holes with a (2x1) oxygen termination in them. Between or at the rim of the (2x2)R30° areas is a zone with highly unordered silica. It could be very small crystalline p(2x2) domains rotated in various angles like in brash ice or a completely vitreous phase without exhibiting a p(2x2) order in it.

To investigate the surface with the ring feature further, a flash anneal in UHV of the as-deposited ML could be applied to freeze this situation. The suggested values for

this are: a background pressure $< 5.0 \times 10^{-9}$ mbar, about 700 K final temperature and heating and cooling rates with 7.5 – 10 K/s.

6.3 The adsorption site model

Considering the understanding reached so far, the question arises: Why is the film forming a (2x2)R30° ML-phase instead of a p(2x2) reconstruction as already known for oxygen? A possible explanation and the driving force for this rotated structure will be given in the next paragraphs. As a hypothesis we propose that the oxygen atoms from the SiO₄ units pointing downwards in the direction of the ruthenium surface tend to occupy as many hcp and fcc sites of ruthenium as possible. The film therefore relaxes or even contracts as it is chemisorbed via Ru-O-Si bonds onto the surface. The Ru-O-Si could be not vertical but tilted to the Ru-surface, in the following model only small changes of the bonding angles will be allowed. Also, structural defects (combinations of 4-, 5- and 7-member rings) in the film like the ones found in STM in [16] are not considered.

To visualize the effect of the occupation of the possible adsorption sites on Ru(0001), silicon atoms occupying an adsorption site were marked. The procedure and its result is illustrated in figure 6.9. Each adsorption site (hcp, fcc, bridge, top) was marked with individual colour code and its size was defined as large as possible, but without allowing to overlap with another one. Then the silicon atoms, centred over an adsorption site, are coloured by the colour assigned to the adsorption site. Silicon atoms that are not above a specific adsorption site are coloured in yellow.

Looking at the $\langle 001 \rangle$ direction of ruthenium in figure 6.9, it is visible that 3 out of 4 possible silicon positions are occupied. They have a distance of $\sqrt{1/3} * a_{SiO_2}$ (a_{SiO_2} is the lattice constant of the p(2x2) silica ML bound to ruthenium [11]) from each other. The hcp sites in the $\langle 001 \rangle$ direction of ruthenium have a distance of the ruthenium lattice constant a_{Ru} of 2.71 Å.

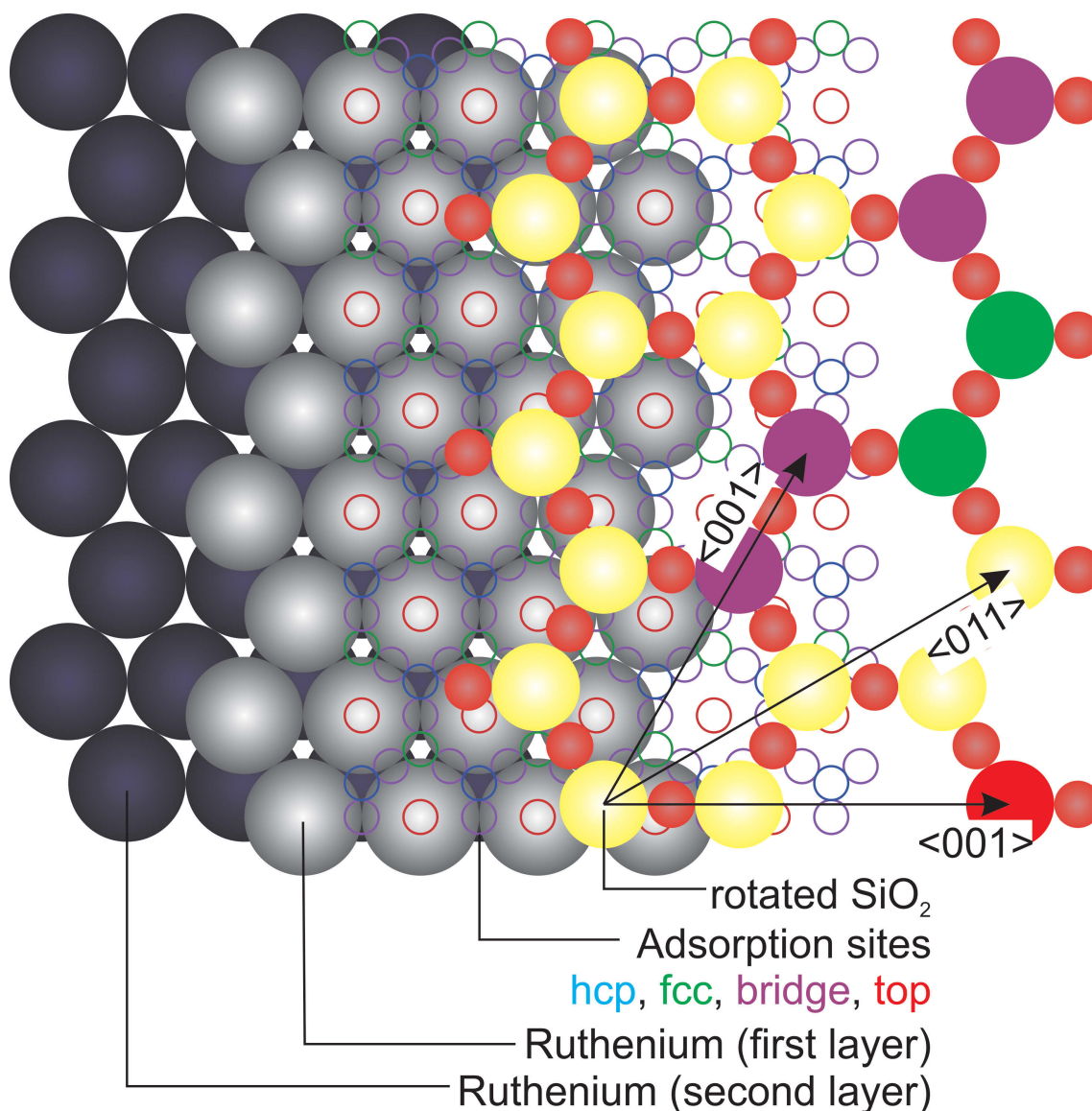


Figure 6.9: An illustration of the procedure to colour silicon atoms, which are above adsorption sites on Ru(0001). Directions of the ruthenium lattice are indicated. (Details see text)

In figure 6.10 cross sections of LEED images in the $\langle 001 \rangle$ direction are shown. By comparing the position of the $(2 \times 2)R30^\circ$ silica spot during the temperature treatment in figure 6.10, it is visible that the silica directly forms this structure without a stressed or compressed transition state. It is also visible that the spots in front of the (0,1) spot have a distance of 0.905 times that of the ruthenium unit cell to the (0,1) spot.

With the assumption that this spot belongs to the first order spots of the $(2 \times 2)R30^\circ$ silica ML, it is possible to calculate the lattice constant a_{SiO_2} via:

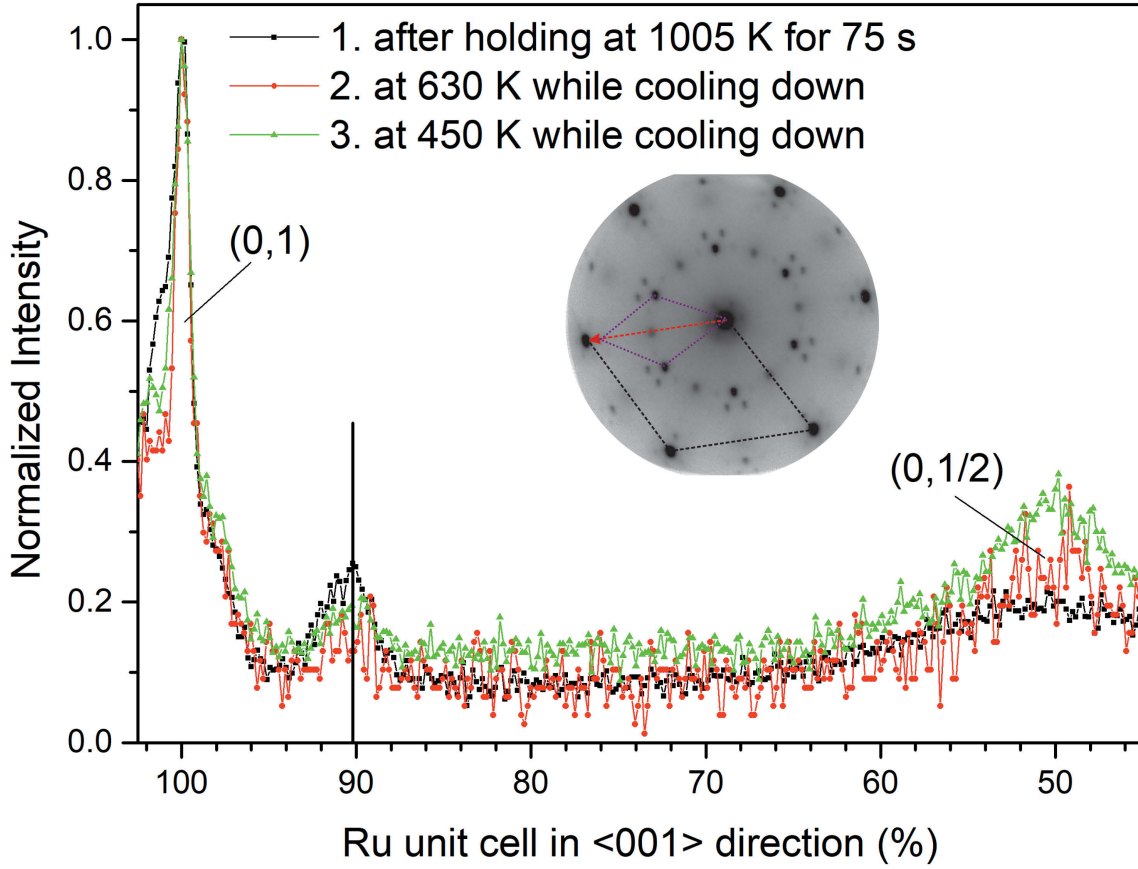


Figure 6.10: Cross section of a LEED image in direction of $\langle 001 \rangle$ of Ru at various temperatures during the temperature treatment. The LEED image in the inset indicates the cross section. The kinetic energy used for the LEED images was 42 eV.

$$k_{Ru} = \frac{2\pi}{a_{Ru}} \quad (6.1)$$

$$k_{SiO_2} = 0.905 * k_{Ru} \quad (6.2)$$

$$k_{SiO_2} = \frac{2\pi}{\sqrt{\frac{1}{3}} * a_{SiO_2}} \quad (6.3)$$

with k_{Ru} and k_{SiO_2} the distances of ruthenium and silica units in the reciprocal space.

$$\Rightarrow k_{Ru} = \frac{1}{\sqrt{\frac{1}{3}} * 0.905 * a_{SiO_2}} = \frac{1}{a_{Ru}} \Rightarrow a_{SiO_2} = \frac{1}{\sqrt{\frac{1}{3}} * 0.905} * a_{Ru} \quad (6.4)$$

and with a_{Ru} of 2.71 Å:

$$a_{SiO_2} = 5.19 \text{ \AA} \quad (6.5)$$

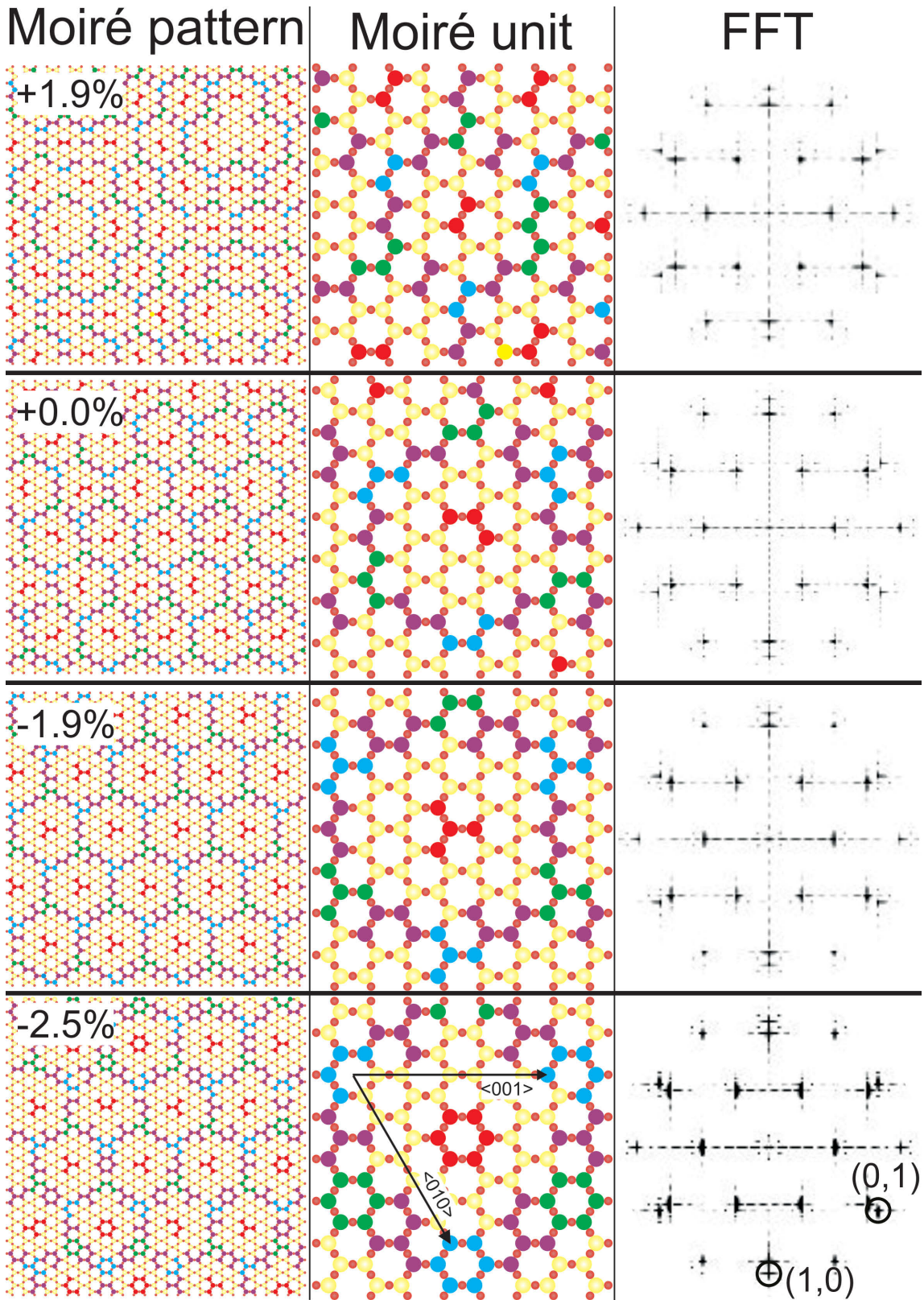


Figure 6.11: Occupation of adsorption sites of stressed, relaxed and compressed rotated silica layers on Ru. In the left column, a large view of the resulting moiré pattern is shown and the applied distortion is given in % in comparison to the relaxed free standing state in UHV. In the middle a unit of the moiré pattern are shown. The right column presents its resulting Fourier transformation on the Ru(0001) surface.

The silica ML is then compressed by about 2.4 % relative to its relaxed free standing state in UHV (5.31 Å [11]) and 4.3 % to its stressed state when annealed in oxygen (5.42 Å [11]). Taking into account that the LEED image could be distorted due to experimental reasons of about 1 %, the value given in [17] of 5.23 Å, corresponding to a compression of about 1.5 %, is in the experimental error (5.19 ± 0.05 Å). Using these values to compress or stretch the film and combining it with the described model above, the occupation of adsorption sites is shown in figure 6.11. The model applies a long-range distortion via the overall lattice constant and a short-range distortion by giving local silica tetrahedra the possibility to relax into adsorption sites. It is visible that the resulting moiré pattern of the occupation site gets denser when the silica ML is compressed. Also the number of occupied hcp and fcc sites in the 'unit' of the moiré pattern increases (middle column in figure 6.11). The Fourier transformations of these silica layers on Ru(0001) show good agreement with the LEED pattern of the structure of the experiment.

In figure 6.12 a defect pattern found in STM (figure 4b of reference [16]) is superimposed with the adsorption site model. The best match between the defect pattern and adsorption site model was found for the pattern of the top adsorption sites in the relaxed free standing silica ML in UHV (see figure 6.11 second row). This is in contrast to the calculated lattice constants before: 5.31 Å (relaxed free standing silica ML) versus 5.19 Å (LEED in this work and STM analysis in [16]). A possible explanation for the differences between the model and the defect pattern in STM is that in the adsorption site model defects were not considered that could change the distances of on top sites. It is highly likely that defects will appear especially above top adsorption sites. The stress in the layer should have a maximum at this positions because of the height difference to the rest of the film. In the middle column of figure 6.11 it is clearly visible that the compression of the film leads to the occupation of more adsorption sites, while the

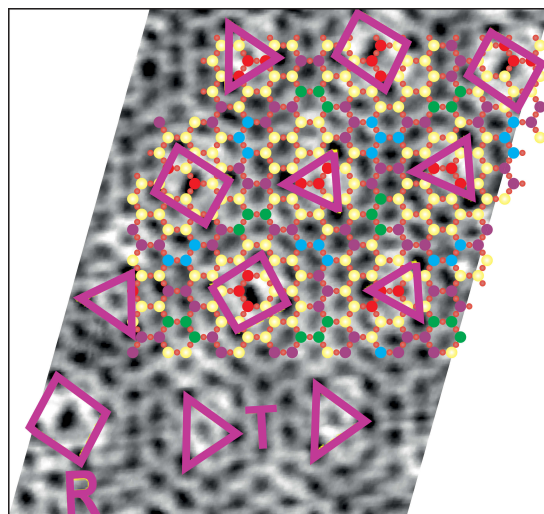


Figure 6.12: STM image (figure 4b of reference [16]) of the defect pattern found for the (2x2)R30° ML phase (purple rectangles and triangles) superimposed with the adsorption site model.

distance between the top sides increases. So the occurrence of these defects may lead to an additional increase of the occupation of hcp and fcc adsorption sites in their close surrounding and decreases the distances of top sites in the 2.5 % compressed film.

This leads to the conclusion that the driving force to form the $(2 \times 2)R30^\circ$ structure on Ru(0001) during UHV annealing is the energy gain by the occupation of as many adsorption sites by oxygen on Ru as possible. It is counterbalanced by the energy needed to compress or stress the local chemical bonds in the silica layer or to make the Ru-O-Si bonds not vertical but tilted to the Ru-surface or to produce defects. Consequently, the $(2 \times 2)R30^\circ$ structure seems to be an equilibrium situation between these forces. The occupation of hcp and fcc sites with oxygen from the silica tetrahedra is supported by the photoelectron spectra shown in figure 6.8 c). The ratio of the R-O-Si and Si-O-Si groups is increased, suggesting the formation of more Ru-O-Si bonds, because the layer is much more ordered. This observation is also supported by the behaviour of the Ru $3d_{5/2}$ line before and after the treatment.

The $(2 \times 2)R30^\circ$ silica ML-film has an incommensurate super-lattice with $\begin{pmatrix} 2.2072 & 1.1036 \\ 1.1036 & -1.1036 \end{pmatrix} = (1.1036\sqrt{3} \times 1.1036\sqrt{3})R30^\circ$ as lattice vectors for the Ru base lattice. A LEED simulation done with LEEDpat [127] is superimposed in figure 6.11 with a LEED image of the silica over-layer after the UHV temperature treatment. Because of a slight misalignment of the microscope the reciprocal plane is distorted, so the simulated pattern does not fit exactly, but is in rather good agreement with the observed LEED pattern.

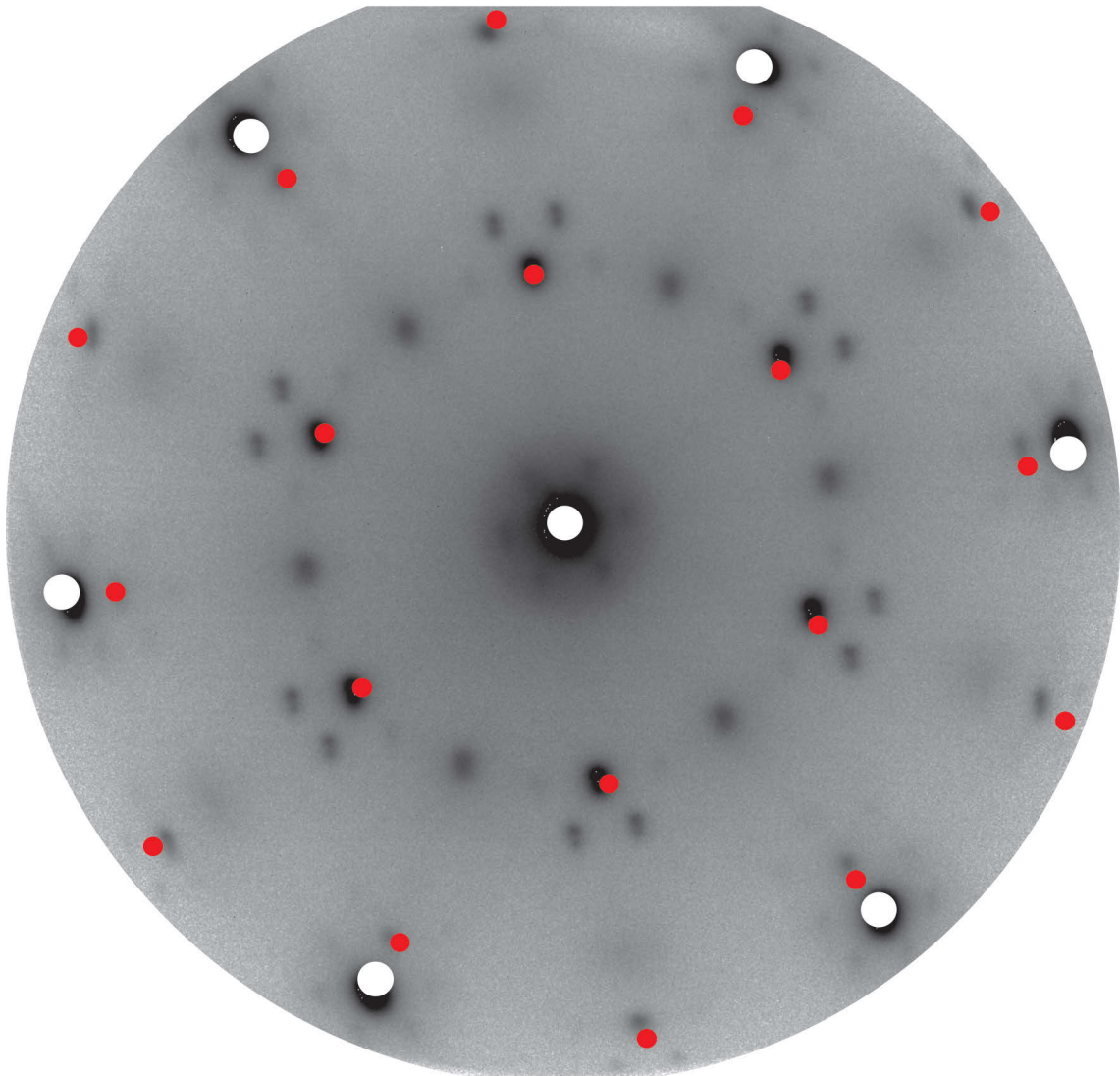


Figure 6.13: Superimposition of a LEED pattern simulation of the incommensurate super-lattice of SiO_2 on $\text{Ru}(0001)$ with a LEED image of the silica ML after the UHV temperature treatment. White spots are the $\text{Ru}(0001)$ spots, red the incommensurate super-lattice. The kinetic energy for the LEED image was 53 V. (Details see text)

The p(2x2) ML-phase

7.1 Preparation, and characterization of properties

The annealing of a silicon ML in oxygen has already widely been investigated by different experimental techniques, and theoretical approaches, and for various substrates [128–135]. However, only one report describing its in-situ preparation [136] has been published so far. Our detailed results will be reported in the following. The procedures follow those reported above for the UHV annealing.

In figure 7.1 the results of the LEED measurements during annealing of a deposited silicon film in 5.0×10^{-6} mbar oxygen are shown. The LEED image I shows the initial surface. It exhibits a blurry p(2x2) pattern, a Henzler ring around the (0,0) spot and the (1x1) spots of ruthenium. Below the LEED image the intensity evolution of these spots during thermal treatment is plotted. As before, the experiment is divided in three sections: heating, holding, and cooling of the sample.

With increasing temperature, the intensity of the (0,0) spot (black curve) increases linearly until at around 500 K the slope decreases. After this, it begins to rise again at 800 K and reaches a plateau at 950 K, with no further increase visible for higher temperatures. On the other hand, the intensity of the Henzler ring increases linearly to 900 K where a maximum is reached and then begins to decrease linearly. The p(2x2) spots increase with the beginning of the annealing and show a broad maximum at 375 K. At 500 K their intensity starts to rise linearly with a high slope until at 600 K a maximum is reached and the intensity has plateau until it starts to drop linearly at about 900 K. The (1x1) spots increase linearly with temperature and increase their slope at 900 K. The LEED image II shows the pattern of the sample when a temperature of 1050 K is reached. Clearly, the increase of the spot intensity

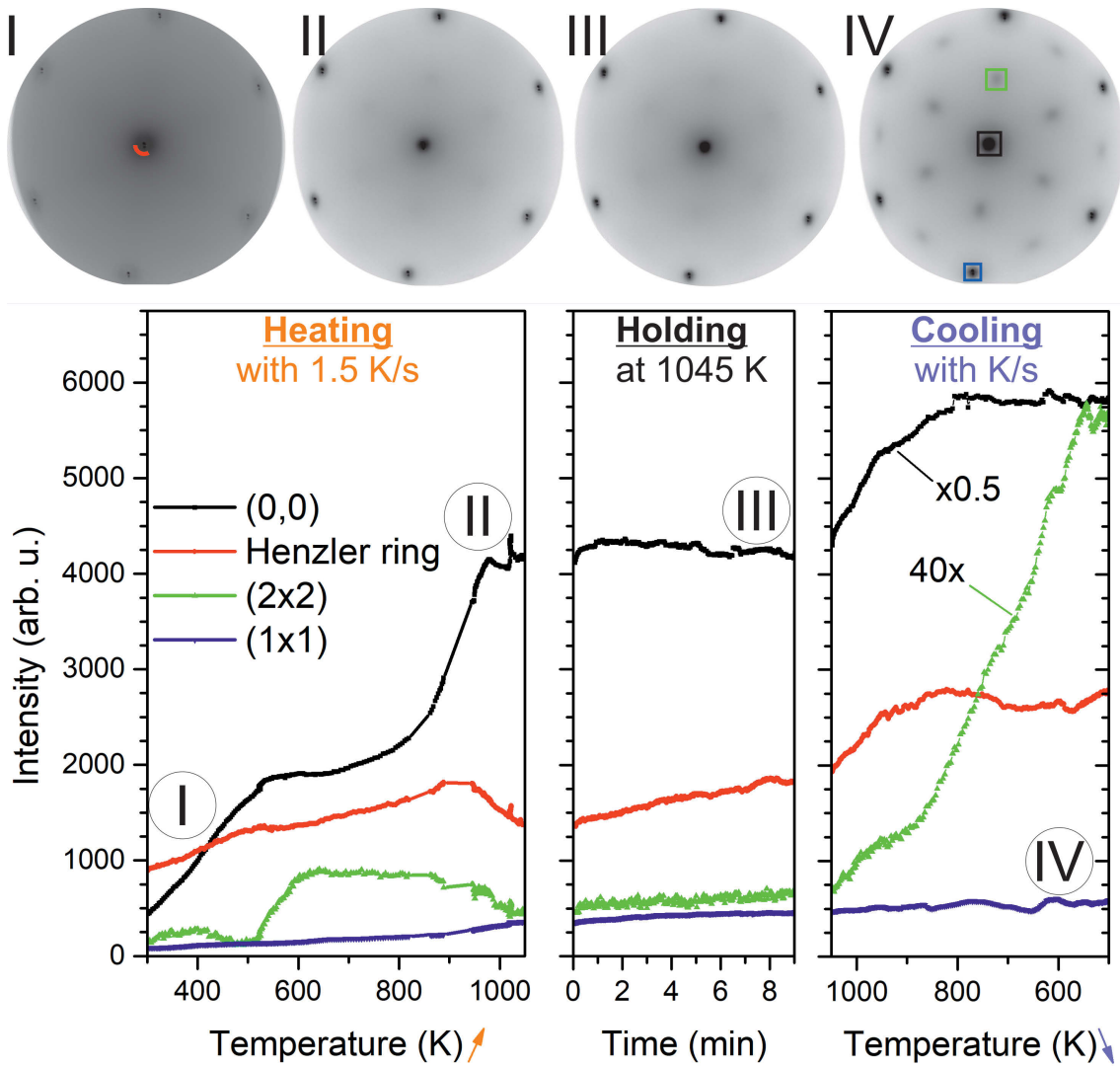


Figure 7.1: Analysis of LEED spots appearing while annealing in oxygen to 1050 K. The upper part shows LEED images collected during the temperature treatment, the lower part the intensities of the individual LEED spots during heating, holding and cooling down. An electron kinetic energy of 42 eV was used. (for more details see text)

is visible. However, the Henzler ring around the (0,0) spot disappears (compare images II – IV), so the intensities attributed to the Henzler ring in the holding and cooling section are most likely artefacts, maybe connected to the behaviour of the background signal which will not be discussed here. During holding the film at 1050 K, the intensity of the (0,0) spot remains the same as when the final annealing temperature was reached at the beginning of the holding time. The p(2x2) and (1x1) spots show a small linear increase while holding the sample at 1050 K for about 10 min. LEED image III shows the pattern of the sample after the holding time and before beginning of the cooling. With start of the cooling the intensity of the (0,0) spots increase linearly, lower their slope at about 925 K and at about 800 K the final intensity is reached and stays constant during further cool down. The intensity of the p(2x2) spots increases linear up to 925 K also where it reaches its final maximum. Then it remains constant with decreasing temperature, apart from small oscillations. Moreover, the (1x1) spots increase their intensity linearly for cooling down the sample with nearly the same slope as for the heating step. LEED image IV shows the pattern of the sample surface at 500 K. It is visible that the intensities of all spots have increased further. However, the p(2x2) spots have gained sharpness and intensity in comparison to the beginning of the thermal treatment. These spots and their second order are elongated in the 1,0 direction of ruthenium.

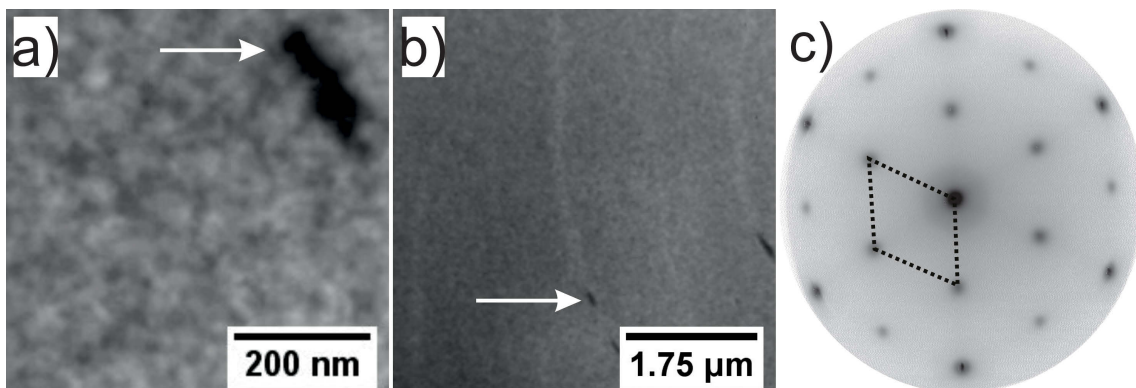


Figure 7.2: LEEM and LEED images at room temperature after annealing in oxygen to 1050 K and holding it for 10 min there. The white arrow marks the same area in the different fields of view in a) and b). In the LEED image c) the p(2x2) unit cell of silica is shown. For all all images a kinetic energy of 42 eV was used.

Figure 7.2 shows LEEM images of the sample surface at room temperature after thermal treatment in oxygen as described above. Small islands with an average diameter of 30 nm and larger islands with an average diameter of about 90 nm are visible as bright structures in image a) and are homogeneously distributed over the surface. They are separated by areas with much less intensity; sometimes there are

holes in them. The large scale LEEM image b) shows a very homogeneous surface. In the film some very large, black, elongated structures are visible with a length of about 200 nm. They are located at areas of the film with step bunches of ruthenium below, which are visible as white lines in picture b). At room temperature the spots in the LEED image are much sharper and the p(2x2) spots are not elongated anymore. The unit cell of the p(2x2) over layer is indicated in image c).

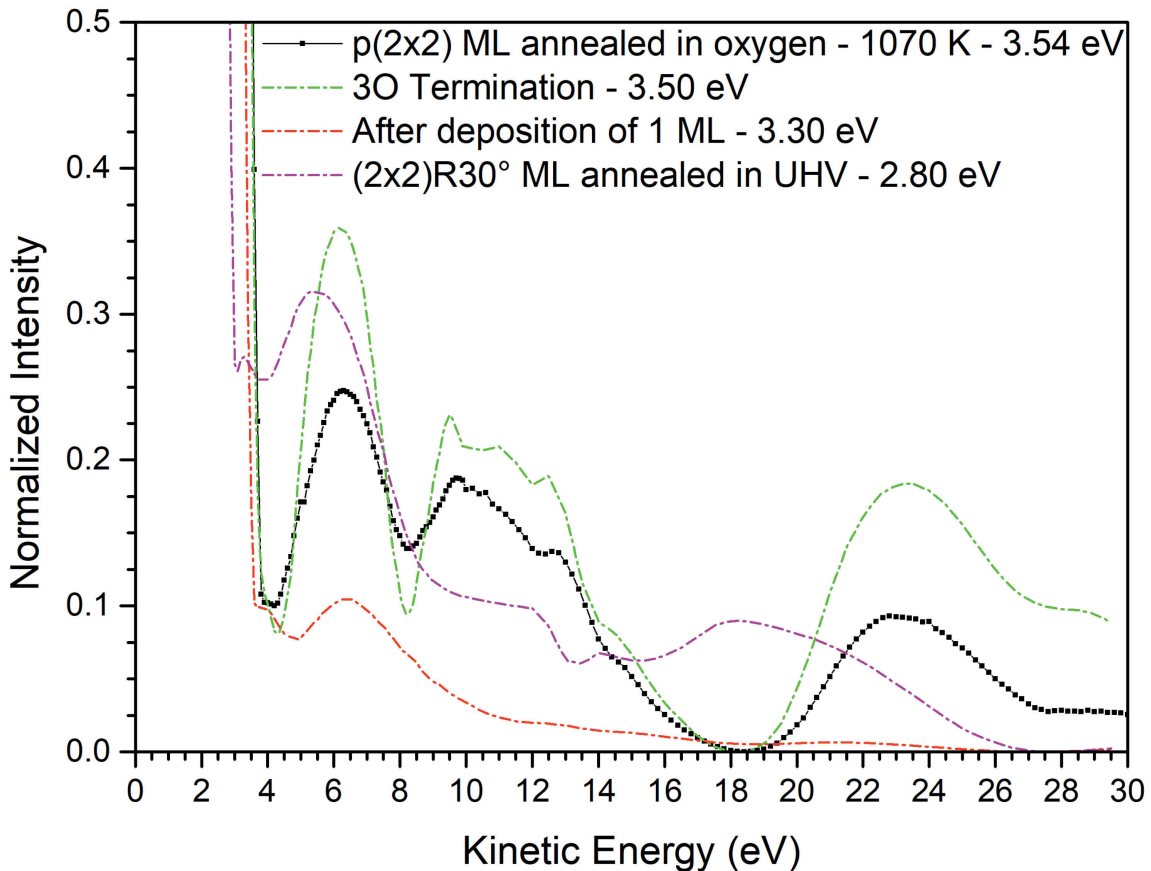


Figure 7.3: LEEM(IV) curve of 1 ML after the thermal treatment in oxygen at RT. For comparison, the LEEM(IV) curves of the 3O terminated ruthenium surface, after the silicon deposition and after the thermal treatment in UHV are shown. The intensities are normalized to the maximal intensity of the MEM mode. The values of the MEM to LEEM transitions are given in the inset of the graph.

In figure 7.3 the LEEM(IV) curve of 1 ML annealed in oxygen is shown in comparison to the curves found for the 3O terminated ruthenium surface, after the silicon deposition and the UHV annealing. After the thermal treatment the LEEM(IV) curve shows once again much more structures than after the deposition. For instance, the surface exhibits a first maximum of intensity at about 6.5 eV, followed by a region with broad maxima close together in an energy range from 10 eV to about 14 eV. At 14.5 eV is a shoulder in the intensity decrease before a minimum at 18.5 eV is reached. At about 23 eV is a broad maximum that decreases and shows

a plateau from 27 eV to 30 eV. A comparison with the 3O terminated ruthenium surface reveals that the features in both curves are quite similar. The LEEM(IV) curves of the film resulting from thermal treatment in UHV or in oxygen have only the maxima at about 6 eV in common and exhibit quite different features.

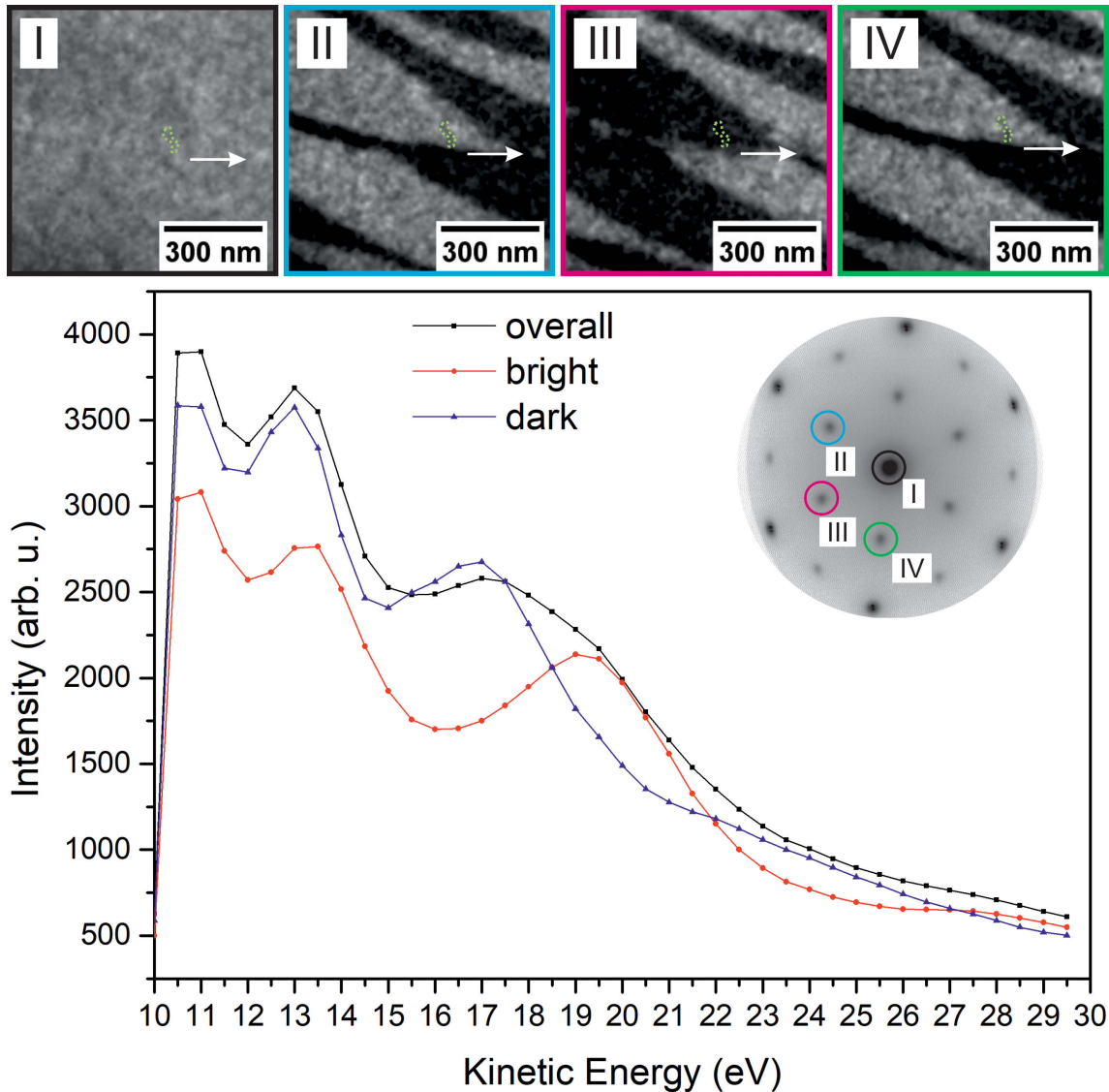


Figure 7.4: In the upper part of the figure a DF image series is shown. Image I is the bright field image belonging to an area of interest in DF. The spots used for the images II-IV are marked in the inset in the plot in the lower part of the figure. The plot shows the DF-LEEM(IV) curves of the black or white terraces in DF. The kinetic energy for the DF images series was 20 eV.

To study the crystalline structure of the film, the DF imaging mode was used and the results are shown in the upper part of figure 7.4. Image I shows the area of interest in bright field, images II - IV are the corresponding dark field images (the used spots are marked in the inset of the graph). In the dark field images the terraces of ruthenium appear as black or white areas. On them bright islands are visible in all

DF images. Now the LEEM(IV) curves show maxima at 13.5 eV, 17.5 eV and 20 eV. These were also found for the 3O terminated surface in subchapter 4.4, however the background intensity is much higher.

In figure 7.5 LEEM(IV) curves after thermal treatments in oxygen with different final annealing temperatures are shown. For each film a new samples was prepared and held for 10 min at the given temperature. The effect of the annealing temperatures is clearly visible. For instance, the curve with a final annealing temperature of 1170 K resembles quite well the LEEM(IV) curve of a 4O terminated ruthenium surface (see subchapter 4.5), suggesting that the film was partially dewetted, and the 4O holes have a dominating contribution to the integral measurement.

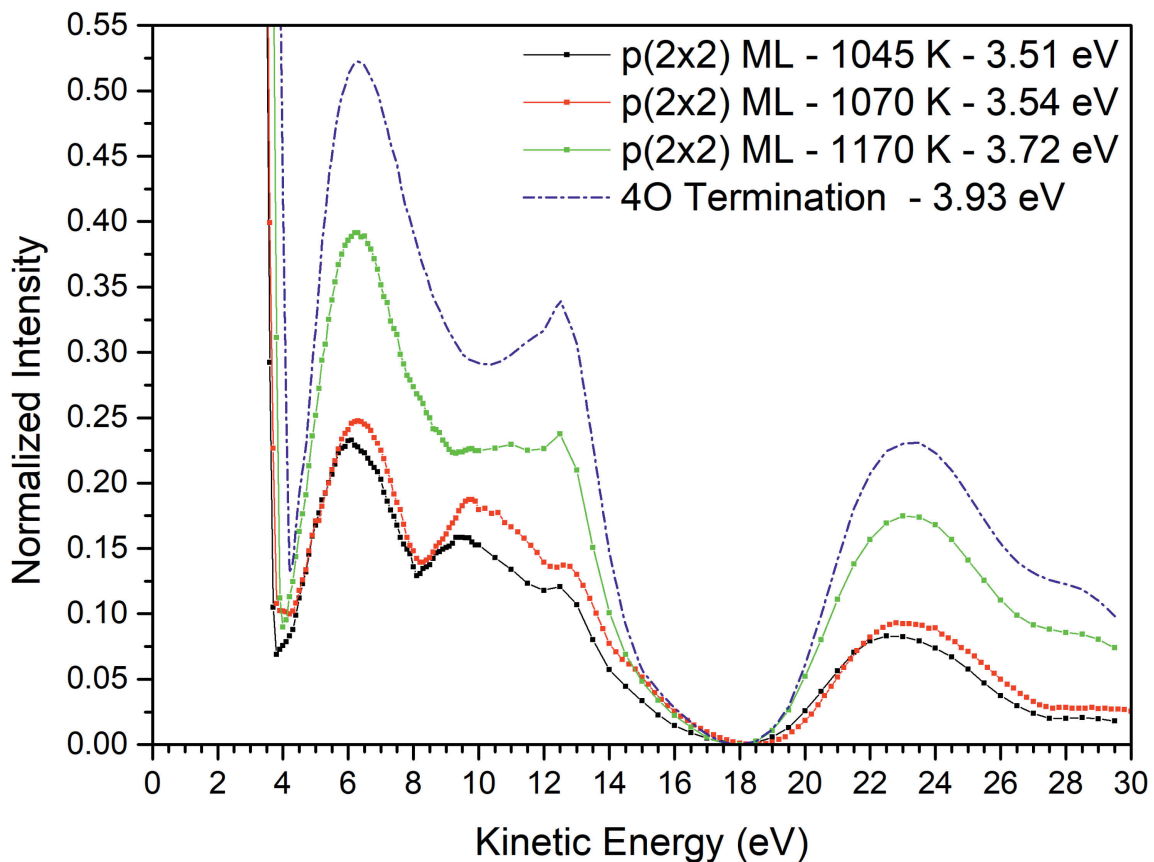


Figure 7.5: LEEM(IV) curves after different final annealing temperatures. For comparison the LEEM(IV) curves of the 4O terminated ruthenium surface is shown. The intensities are normalized to the maximal intensity of the MEM mode. The values of the MEM to LEEM transitions are given in the inset of the graph.

Figure 7.6 shows the intensity change as a function of electron kinetic energy for the (0,0), {0,1/2} and {0,1} spots. The curves show several maxima for each spot and resemble quite well the results of the LEED(IV) measurements for the 3O termination of ruthenium already found in figure 4.17 in subchapter 4.4.

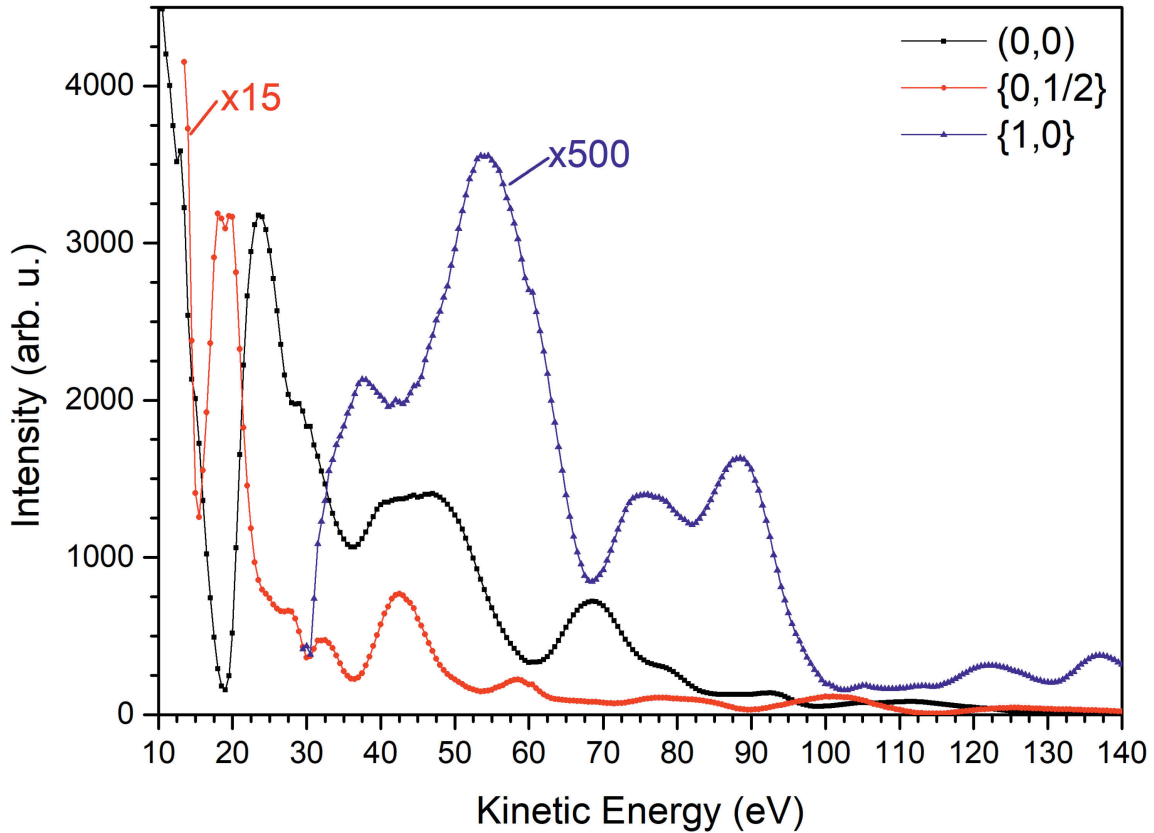


Figure 7.6: The LEED(IV) curves for the (0,0), 0,1/2 and 1,0 spots for a sample after a thermal treatment in oxygen.

Figure 7.7 shows the results of an XPS measurement after a thermal treatment in oxygen. The Si 2p, Ru 3d_{5/2} and O 1s lines are shown in a), b) and c), respectively. The Si 2p core line in a) has a maximum at 102.3 eV. For comparison, the curves after the deposition, after introducing oxygen in the analysis chamber up to 5.0×10^{-6} mbar and after the UHV annealing are given. After introduction of oxygen the Si 2p peak changes only slightly. However, after annealing it shifts to lower binding energies and has a smaller FWHM. In comparison to the thermal treatment in UHV the energy shift is lower (0.2 eV vs 0.5 eV relative to as deposited) and the FWHM is broader. The Ru 3d_{5/2} line in b) after the thermal treatment is much broader than after the deposition or the UHV annealing. In comparison to the Ru 3d_{5/2} line of the 3O terminated ruthenium surface, it is visible that for the high binding energy side the silica ML resembles it very well. The lower binding energy side however has slightly less intensity. The O 1s line in c) has clearly two peaks after the thermal treatment in oxygen. The more intense one is at higher binding energies (531.2 eV) and the less intense one is at lower binding energies (529.2 eV). For comparison, the O 1s lines after the deposition, after increasing the oxygen pressure, after a thermal treatment in UHV and that of the 3O terminated ruthenium

surface are shown. The increase of oxygen in the chamber after deposition has no strong influence on the O 1s line. Comparing the O 1s lines after the thermal annealing in oxygen with the ones from the annealing in UHV and of the 3O terminated ruthenium surface reveals the existence of a third peak, hidden between both lines. This peak is assigned to the Ru-O-Si bond and has a binding energy of 529.8 eV. This is in agreement with the findings for the ML annealed in UHV (see figure 6.8) and after the deposition of 1 ML (see figure 5.11 in subchapter 5.2.1).

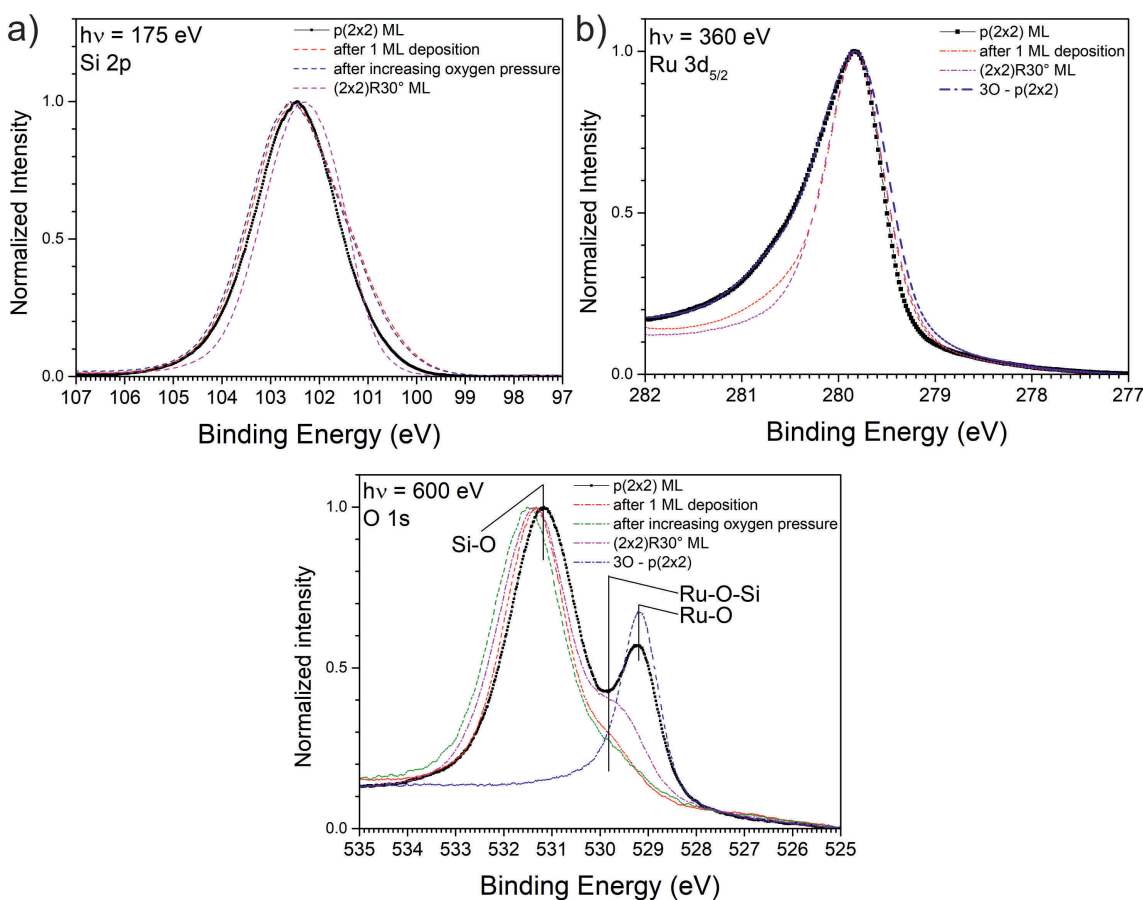


Figure 7.7: Photoelectron spectra of the Si 2p in a), Ru 3d_{5/2} in b) and O 1s in c) regions at room temperature after the thermal treatment in oxygen. For comparison, the photoelectron spectra after Si deposition, after increasing oxygen, of the UHV treatment and of the 3O terminated ruthenium surface are shown. (Details see text)

7.2 Interpretation: Formation, morphology and model of the p(2x2) ML-phase

In this section, an interpretation to the processes taking place during the annealing in oxygen will be given. The results found in [11] serve as model for the p(2x2) phase and the results of this work are brought in agreement with it.

The film starts to order with increasing the sample temperature. The islands of silica already existing after the deposition start to grow, as indicated by the increase of intensity of the Henzler ring (see figure 7.1). The intensity increase of the p(2x2) spots at 525 K could be attributed to the growth of p(2x2) islands. This could happen by the growth and ordering of the already existing silica islands or the formation and growth of new p(2x2) silica islands. The different islands sizes found after the thermal treatment in LEEM suggests a combination of both processes. As third possibility the co-adsorption of oxygen should be considered. This would explain the intensity decrease of the p(2x2) spots above 900 K, because the temperature is then above the disorder temperature of oxygen and leads to a high mobility of the free, disordered oxygen atoms on the surface. At the constant temperature of 1050 K, the increase of intensity is attributed to the growth of silica islands. On the other hand, a possible reorganization of the islands like the healing of antiphase domains could also be responsible for this behaviour. Moreover, the intensity behaviour of the p(2x2) spots suggests a formation process with an activation energy. Future experiments could determine this energy from the slope of the intensity increase of the p(2x2) spots during the holding time at different holding temperatures. Cooling down quenches this process, and the ordering in a p(2x2) pattern becomes favoured. At the same time the co-adsorbed oxygen starts to order, leading to a high increase in the intensity of the p(2x2) spots.

After the thermal treatment in oxygen the film could be described as followed:

The model in [11] suggest that the downwards pointing oxygen atoms of the silica tetrahedra units are either in fcc or top adsorption sites of the ruthenium surface. They are marked green (fcc) or red (top) in the model in the middle of figure 7.8. In this configuration, the film is compressed about 1.9 % in comparison to free standing in UHV [11]. The length of the silica unit cell is twice the unit cell length of ruthenium (5.42 Å vs. 2.71 Å). The lattice is commensurate with ruthenium and therefore no moiré structure is found (see figure 7.8). The additional low intense points in the image are an artefact of the fourier transformation due to an 'overstructure' formed

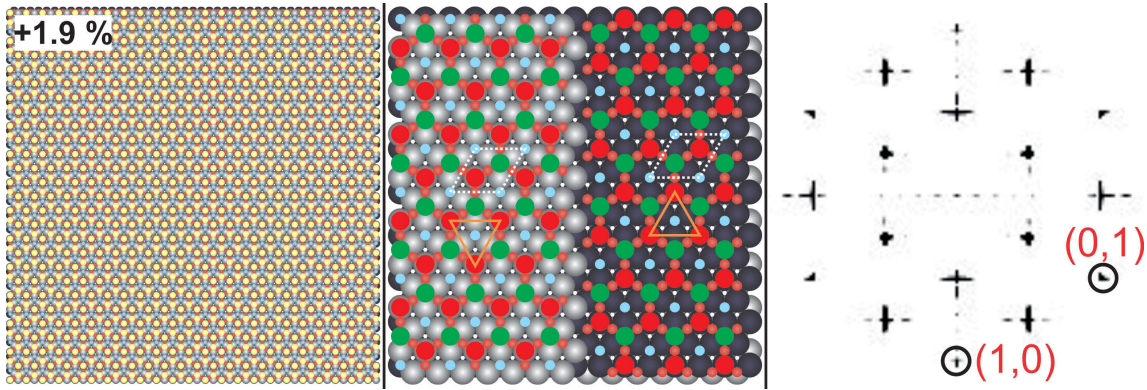


Figure 7.8: Atomic model of the surface and its Fourier transformation. Left a large field of view, in the middle a closer view of the proposed structure. The silicon atoms are coloured by their adsorption site on ruthenium (green = fcc and red = top) The first ruthenium layer is coloured grey, the second black. Coadsorbed oxygen is coloured light blue. In the Fourier transformation the $(1,0)$ and $(0,1)$ spot of ruthenium are highlighted. (Details see text).

by the bright and dark ruthenium atoms, the periodic boundary conditions lead to these periodic features.

Per silica unit cell one additional oxygen is found that is in the centre of the silica rings above a hcp ruthenium site, thus resembling a 1O termination. In such a $p(2 \times 2)$ cell on ruthenium, there are 3 oxygen atoms (1 Ru-O and 2 Ru-O-Si) leading to an overall oxygen content comparable to a 3O terminated surface. This effect is also seen in the Ru $3d_{5/2}$ line in figure 7.7 c) and in the LEEM(IV) and LEED(IV) curves (Figure 7.3 and figure 7.6). The additional oxygen bound to ruthenium shows up in the O 1s spectra as additional peak at lower binding energies next to the Ru-O-Si components. However, in contrast to the 3O termination, not only hcp sites but also fcc and on top positions are occupied. The surface could be described then as a combination of the lattice of 1O termination of oxygen and additional silica tetrahedra at $(1/4)$, $(1/4)$ and at $(3/4)$, $(3/4)$ positions in its unit cell.

Because of the adjustment of the film to the underlying ruthenium surface, nearly the same reflectivity as for the 3O termination in DF is found, with the AB stacking of ruthenium leading to terraces appearing as black or white features. The symmetry change induced by the stacking is marked as orange triangles in the middle image of figure 7.8.

With the findings exposed in 6 a lowering of the surface energy due to the co-adsorbed oxygen at ruthenium is indicated. It could be a driving force for the appearance of the $p(2 \times 2)$ phase instead of the UHV phase.

The Xmas star BL-phase

8.1 The oxidation of the BL

8.1.1 Preparation, and characterization of properties

Before the annealing of the deposited BL in UHV a mild pre-annealing in oxygen is needed to oxidize silicon completely. This procedure leads to an amorphous, but completely oxidized silica template on ruthenium. It consists of the following steps:

1. Introduction of 5.0×10^{-6} mbar oxygen in the analysis chamber
2. Increasing the sample temperature up to 625 K with a rate of 1 K/s
3. At 625 K evacuating the chamber and decreasing the temperature with about 2 K/s to room temperature

Figure 8.1 shows the LEED pattern and the results of the intensity analysis of the (0,0) spot and its surrounding Henzler ring during the thermal treatment. It is divided into two sections: the heating and the cooling. For both sections, the intensity of the spots vs. temperature is shown in the graph at the lower part of the figure. In the cooling section the oxygen pressure during cooling is included.

Image I shows the LEED pattern after the deposition. The (0,0) spot and its surrounding Henzler ring are slightly visible. Both intensities decrease at the beginning of the heating step and have a minimum at about 400 K. Then they increase up to 500 K and stay constant for the rest of the temperature rise at nearly the same value as at the beginning of the heating. The image II shows the LEED pattern collected at 625 K in oxygen. No change in comparison to the beginning is visible. The

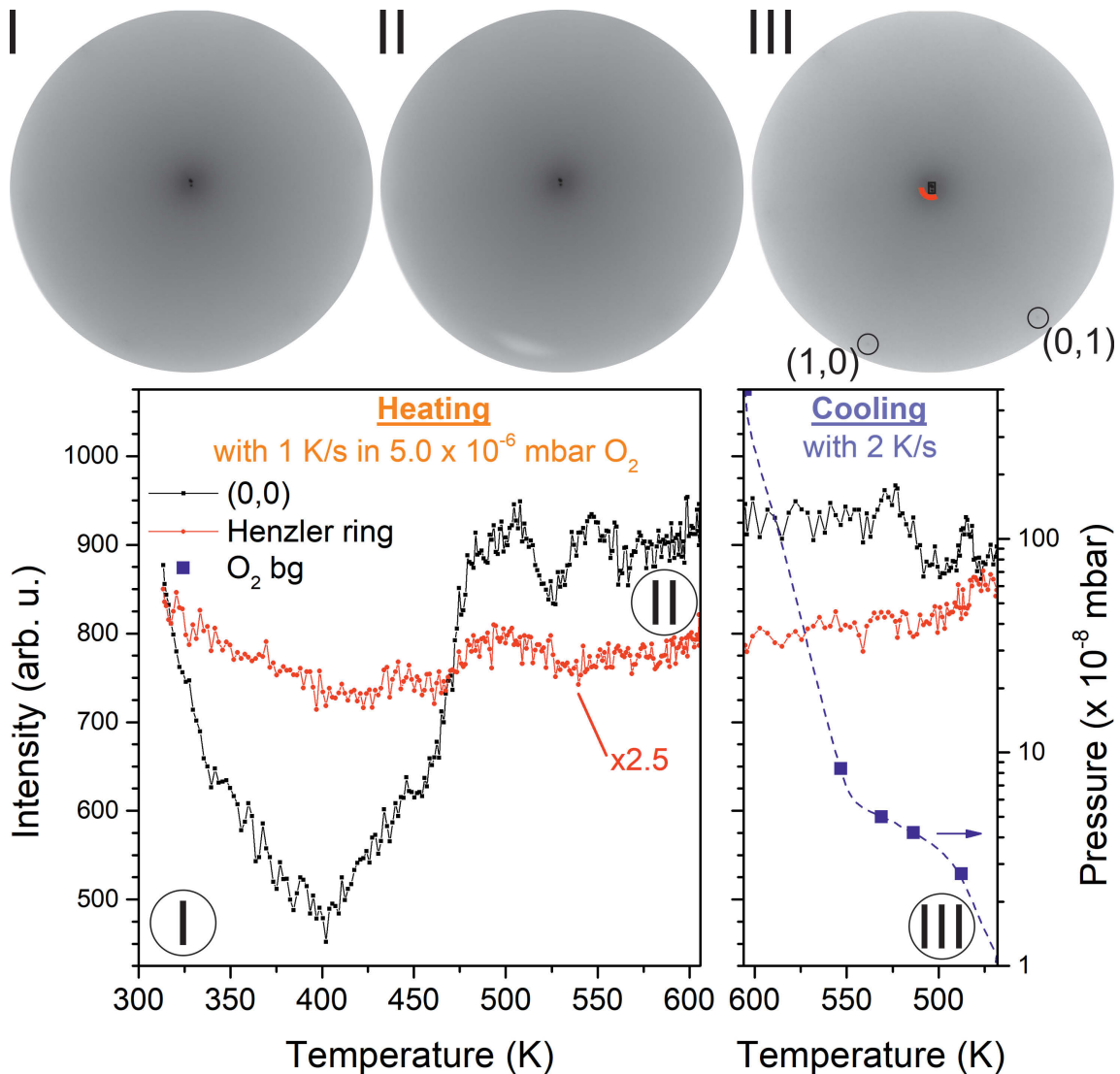


Figure 8.1: LEED images and LEED spot intensity behaviour of a BL during a pre-annealing to 605 K in oxygen. In the upper part three LEED images collected at room temperature (I), at 605 K (II) and at 425 K (III) are shown. In the lower part, the temperature dependences of the spot intensity for the heating and cooling sections are shown. The blue line marks the oxygen background pressure during cooling. An electron kinetic energy of 42 eV was used.

white elongated feature in the image is an artefact due to the slight defocus of the objective lens and is attributed to the contrast aperture. The intensity of the (0,0) spots stays constant during cooling and starts to decrease slightly at 550 K, while the Henzler ring shows a slight increase with decreasing temperature. The oxygen background pressure decreases very fast during cooling to less than 1.0×10^{-8} mbar. Image III shows the LEED pattern at 440 K. No noticeable differences compared to the situation before the treatment are found.

Figure 8.2 shows two LEEM images of the film after the pre-annealing in oxygen. The film consists of bright features, which appear to be small islands homogeneously

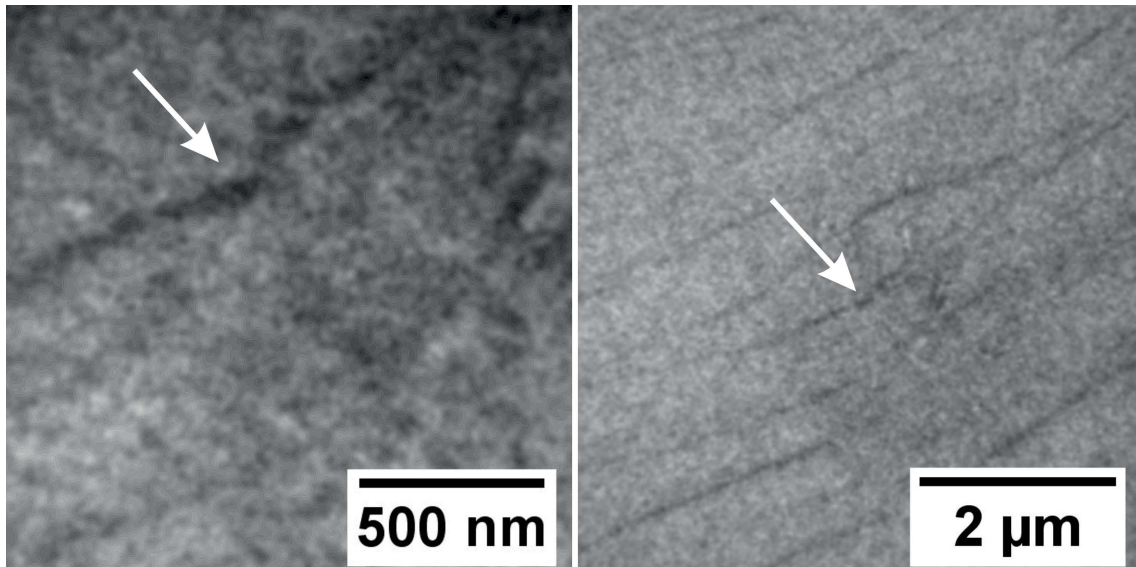


Figure 8.2: LEEM images of a BL silica after the pre-annealing in oxygen. The white arrows mark the identical surface region in both images. An electron kinetic energy of 42 eV was used.

distributed over the surface with a diameter of about 35 nm. In addition, areas with very low intensity in the film can be seen, especially at step bunches of the ruthenium surface.

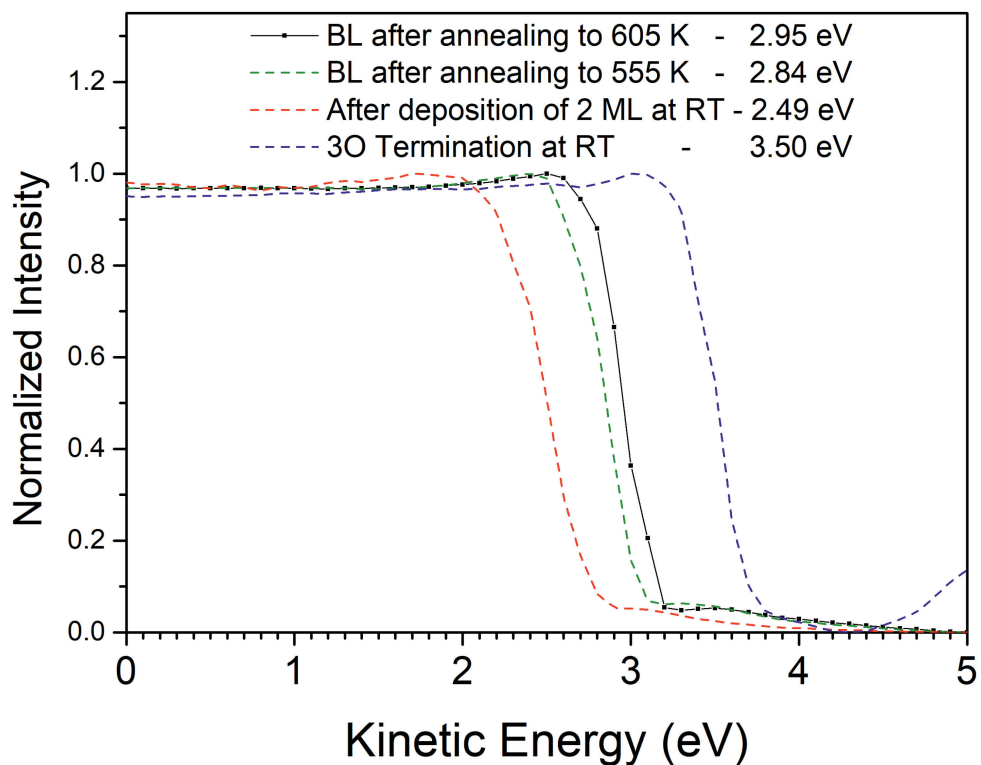


Figure 8.3: MEM to LEEM transitions of films with different annealing temperatures in oxygen. The electron energy of the MEM to LEEM transitions is given in the insert. For comparison, the MEM to LEEM transition of the 3O surface is included.

Figure 8.3 shows MEM to LEEM transitions of films pre-annealed in oxygen to various temperatures, appearing as a drop in the reflected intensity with increasing electron energy meaning that the illuminating electrons are able to overcome the vacuum level of the surface. The energy of the transition shifts towards higher electron energies with increased final annealing temperature (2.95 eV for 605 K), but stays below the value for the 2O (3.41 eV) and 3O (3.50 eV) terminated ruthenium surface.

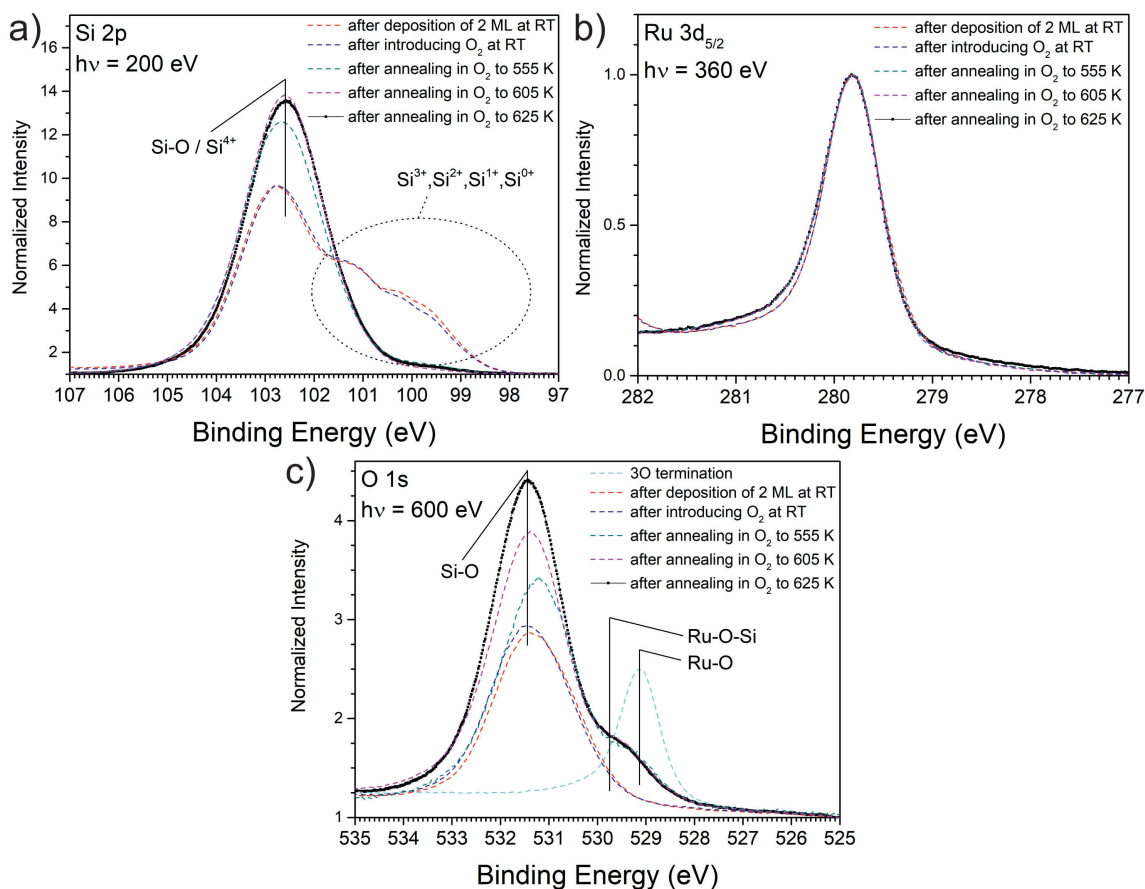


Figure 8.4: Photoelectron spectra of the Si 2p, Ru 3d_{5/2} and O 1s lines at room temperature after pre-annealing to various maximal temperatures in oxygen. The temperatures are given in the legend. (Details see text)

Figure 8.4 shows Si 2p, Ru 3d_{5/2} and O 1s XPS spectra at room temperature after a pre-annealing step in oxygen. The results for experiments with various final annealing temperatures are shown. For the Si 2p line in a) it is visible that introducing oxygen up to 5.0×10^{-6} mbar has only a slight influence on the features of the deposited film. Before and after introducing oxygen an intense component of Si⁴⁺ is found accompanied by features attributed to lower oxidation states of Si. With increasing final annealing temperature, the intensity of the Si⁴⁺ component increases while the intensity of the lower oxidation states decreases. For tempera-

tures above 605 K only minor changes appear; Si^{4+} is then the main component of the film and only minor traces of lower oxidation states are found. The Ru $3d_{5/2}$ line in b) shows only minor changes at its higher binding energy side after introducing oxygen and annealing in it. The O 1s line in c) is only slightly shifted by about 0.2 eV after the introduction of oxygen into the chamber, it shows a component at 531.4 eV attributed to Si-O bonds on the surface. After the pre-annealing to 555 K in oxygen, a new, less intense feature appears on the lower binding energy side of the Si-O component. It mainly consists of a component attributed to Ru-O-Si bonds (529.8 eV) and a smaller component attributed to Ru-O (529.2 eV) on the surface. For comparison, the O 1s line of a 3O terminated ruthenium surface is also shown. The peak connected to Si-O bonds increases in intensity in comparison to after the introduction of oxygen. With increasing the final pre-annealing temperature, the intensity of the Si-O component increases while the components of Ru-Si-O and Ru-O remain constant.

8.1.2 The morphology and chemical state of film pre-annealed in oxygen

The silicon BL after deposition has already been described in subchapter 5.2: the amorphous film consists of silicon islands in various oxidation states, mainly of Si^{4+} . It is assumed that the silicon at the ruthenium interface is completely oxidized, while the additional silicon on top of it is not completely oxidized. The catalytic effect of ruthenium by supplying atomic oxygen for the further oxidation of silicon is inhibited due to the blocking by the silicon layer itself. Therefore, increasing the oxygen background pressure does not change the state of the film. This raises the question, how the oxidation of the entire layer could happen?

With the described treatment, complete oxidation of the entire silicon film is reached at 625 K. This fits to reports in the literature: it is already known that the oxidation state of amorphous silicon films grows linearly with time and temperature [137, 138]. However, the pressures and temperatures used in these studies exceeded those used here. A detailed spectroscopic study [105] reported that amorphous silicon films (0.2 to 3 ML) on top of SiO_2 tend to be incompletely oxidized after a thermal treatment in 2.7×10^{-4} mbar oxygen at 725 K for 10 min. With this knowledge, a mechanism including only silicon/silica and oxygen for the oxidation can be excluded and with the results of the deposition in subchapter 5.2, it is more likely that the ruthenium substrate somehow supports the oxidation with atomic oxygen. Therefore, the oxygen of the background gas has to reach the ruthenium surface, where it dissociates to

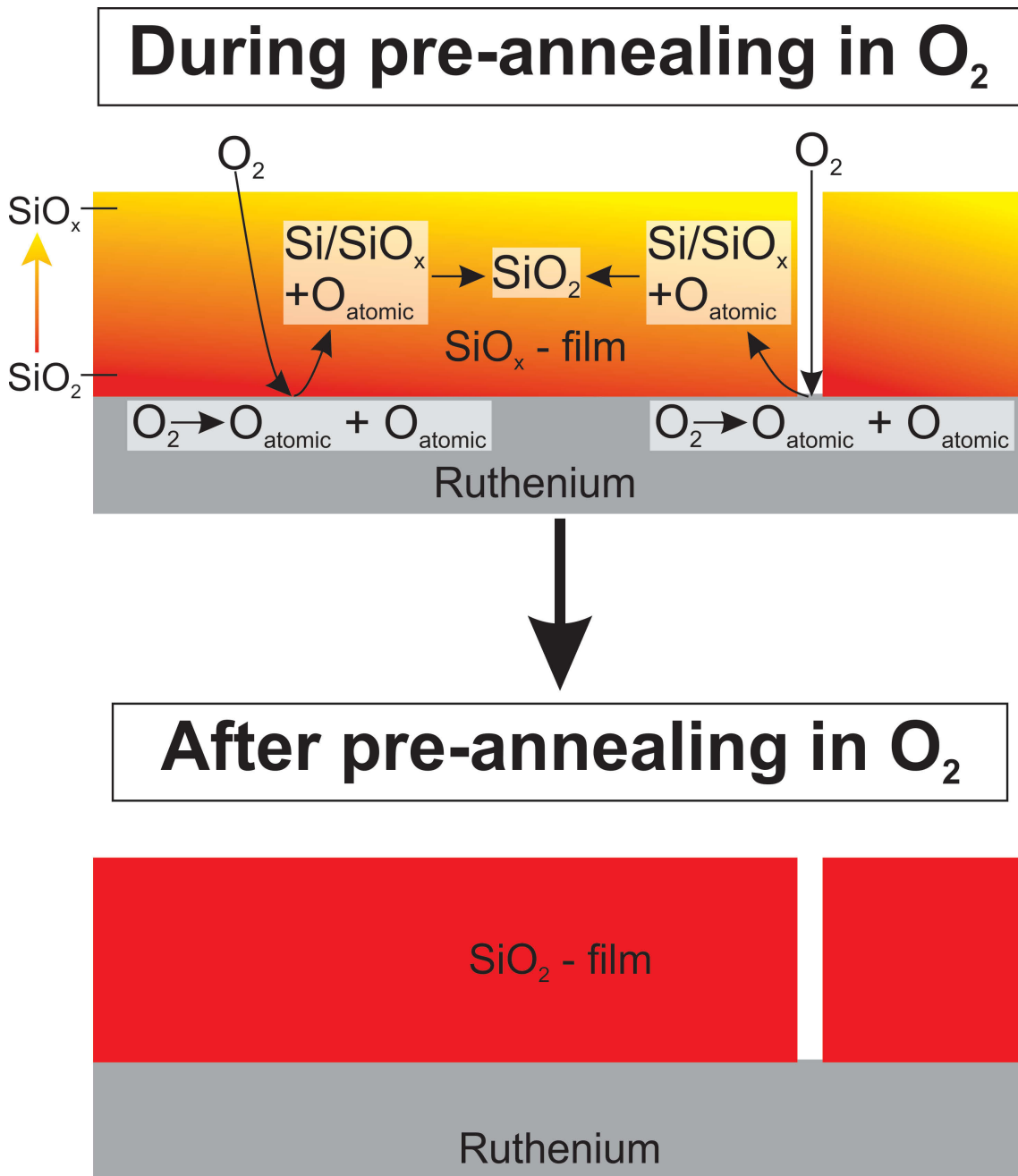


Figure 8.5: Model of the processes during (top) the pre-annealing in oxygen to 625 K and of the surface after it (bottom). (For details see text)

atomic oxygen and then can react with incompletely oxidized silicon. The processes are sketched on the left side in figure 8.5. Oxygen could reach the ruthenium surface only in two ways, through holes in the film down to the ruthenium or by diffusing through the amorphous silicon film. The assumption that oxygen molecules can diffuse through amorphous silicon has already been made in [137] and it is highly likely that the diffusion will be temperature dependent. However, when the oxygen reaches the ruthenium surface, it needs to find an adsorption site to dissociate which

is not occupied by a Ru-O-Si or Ru-O bond. From subchapter 4 it is already known that oxygen atoms are mobile on the ruthenium surface above 400 K and that would give an explanation why the further oxidation of silicon next to holes is hindered at room temperature. So, with rising temperature the supply of atomic oxygen through dissociation of oxygen molecules will be increased. Furthermore, it is highly likely that atomic oxygen diffuses much better than oxygen molecules through the amorphous film and will find incompletely oxidized silicon centres to oxidize them. This interpretation is supported by the observation of the temperature dependent behaviour of the Si 2p and the O 1s lines in figure 8.4. However, the temperature still seems to be too low to allow an ordering of the established silica network (see the LEED results in figure 8.1), but instead leads to the growth of unordered silica islands on the ruthenium surface (see figure 8.2). The islands do not lift off from the ruthenium substrate and are still attached to the ruthenium surface. On one hand, the occurring of Ru-O-Si bonds support this (see figure 8.4 c)). On the other hand, if adsorbed oxygen below the silica film on the ruthenium surface would be expected, it would manifest itself in a change of the Ru $3d_{5/2}$ line and additional Ru-O bonds in the O 1s line (see figure 8.4 b) and c) and subchapter 4). The situation after the pre-annealing step is sketched on the right side in figure 8.5.

8.2 Preparation in UHV, and characterization of properties

After the pre-annealing in oxygen, the silica template formed is annealed in UHV up to 1080 K. Figure 8.6 shows LEED images and the intensity behaviour of different diffraction spots during the annealing. As in the previous sections, three stages are examined: first a heating, then holding at a defined temperature, and finally cooling down. The LEED image A shows the initial diffraction pattern, containing the (0,0) spot, a very faint p(2x2) pattern and a blurry Henzler ring. During heating the p(2x2) pattern vanishes while the Henzler ring first slightly increases in intensity (see LEED image B) but then disappears above 700 K. At this point the intensity in of the sharp peak in the centre of the (0,0) starts to decrease in the plot, due to an increase of the diameter exceeding the chosen measurement box, while the overall intensity of the (0,0) spots remains the same. The comparison of the intensity versus temperature curves of the inner part of the (0,0) spot with the entire (0,0) spot ((0,0) large) and the comparison of the LEED images B and C (in C only a low intense peak in the (0,0) is visible) show this behaviour quite clearly. The diameter reaches a maximum at 975 K. At 1050 K the intensity of the (0,0) spot increases and additional

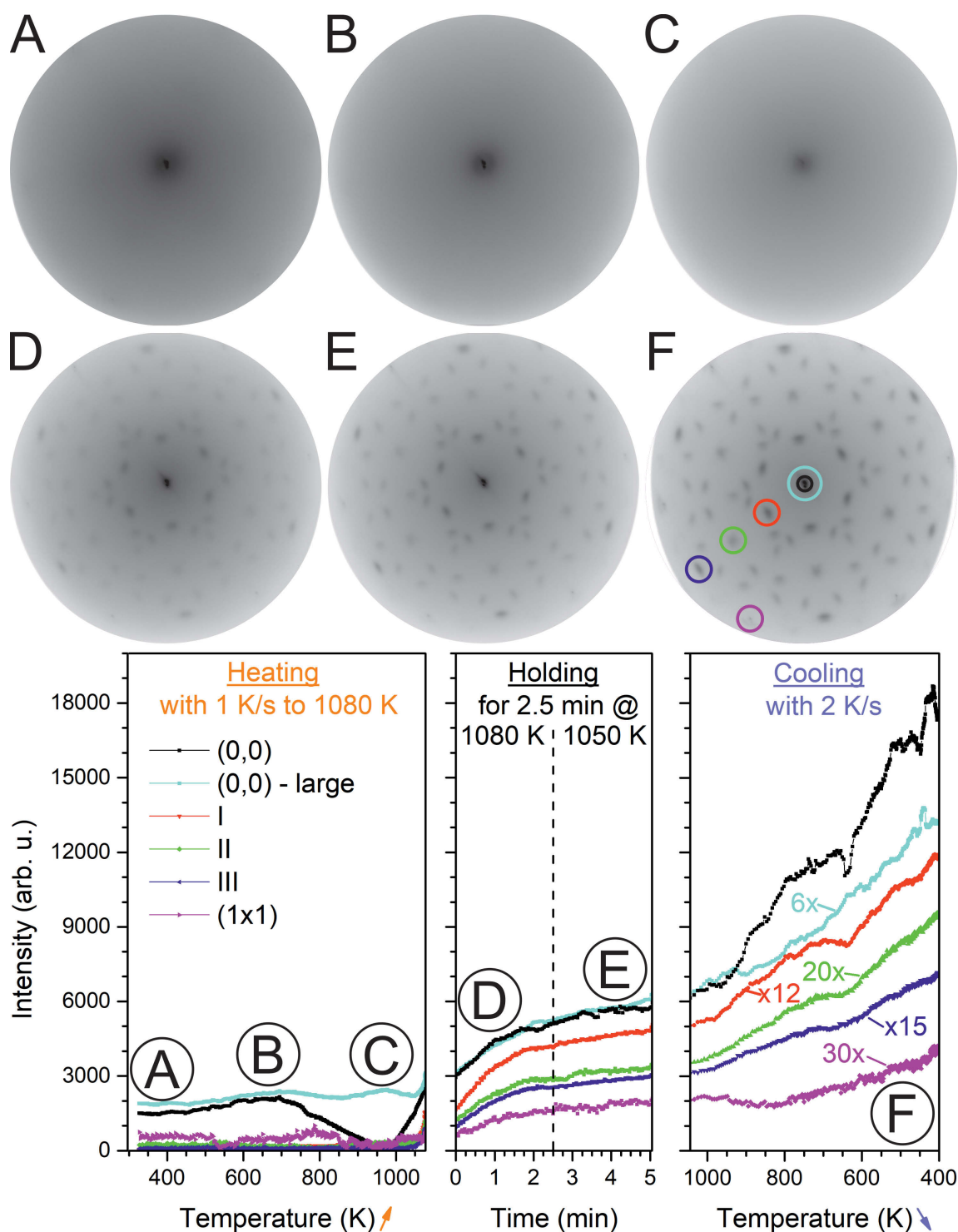


Figure 8.6: Analysis of LEED spots appearing during UHV annealing to 1080 K. In the upper part LEED images during this temperature treatment are shown and the lower part presents the analysis of the intensities of the individual LEED spots during heating, holding and cooling steps, as indicated. The black (0,0) is only connected to the sharp peak in the centre of the (0,0) peak, while the (0,0) - large (cyan curve) includes its close surrounding. An electron kinetic energy of 42 eV was used. (for more details see text)

spots start to appear (see LEED image D). During the holding time at 1080 K their intensity increases first quite fast, going over to a linear increase with time after 2 min, which continues also when holding the sample at 1050 K. During cool down the intensity of the spots increases further, but no additional spots appear (compare LEED images D-F). It is stressed that all additional spots besides the (0,0) spot appear at the same time.

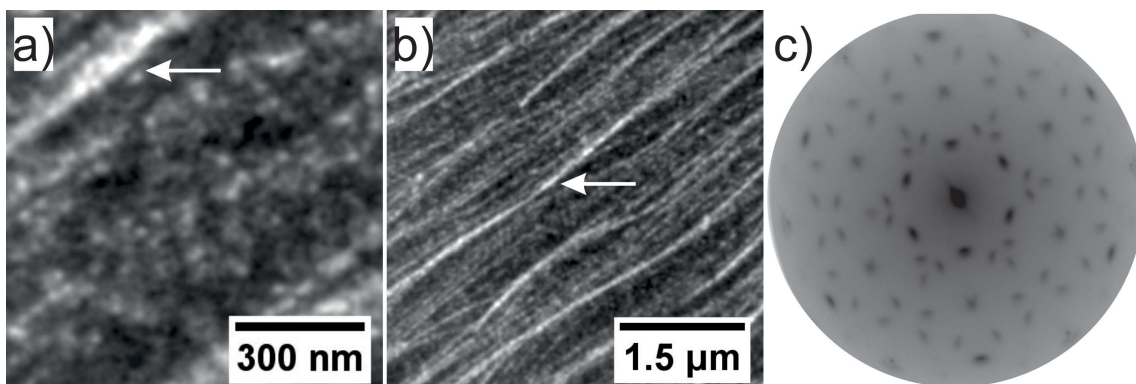


Figure 8.7: LEEM and LEED images recorded at RT after the annealing in UHV to 1080 K. The white arrow marks the same area in the different field of views in a) and b). In the LEED image c) the Xmas star like pattern is shown. For all images a kinetic energy of 42 eV was used.

Figure 8.7 shows LEEM and LEED images of the silica film after the UHV annealing. Bright and dark areas with sizes around 15 nm are visible in image a). The bright areas decorate the steps and step bunches of the Ru(0001) surface, while the dark areas are mainly distributed in the middle of the terraces. The large field of view in b) supports these findings. A very complex LEED pattern is found after the annealing and is shown in c); its star-like pattern will be addressed as Xmas star in the ongoing discussion and it is stressed that this pattern appears at every position of the sample.

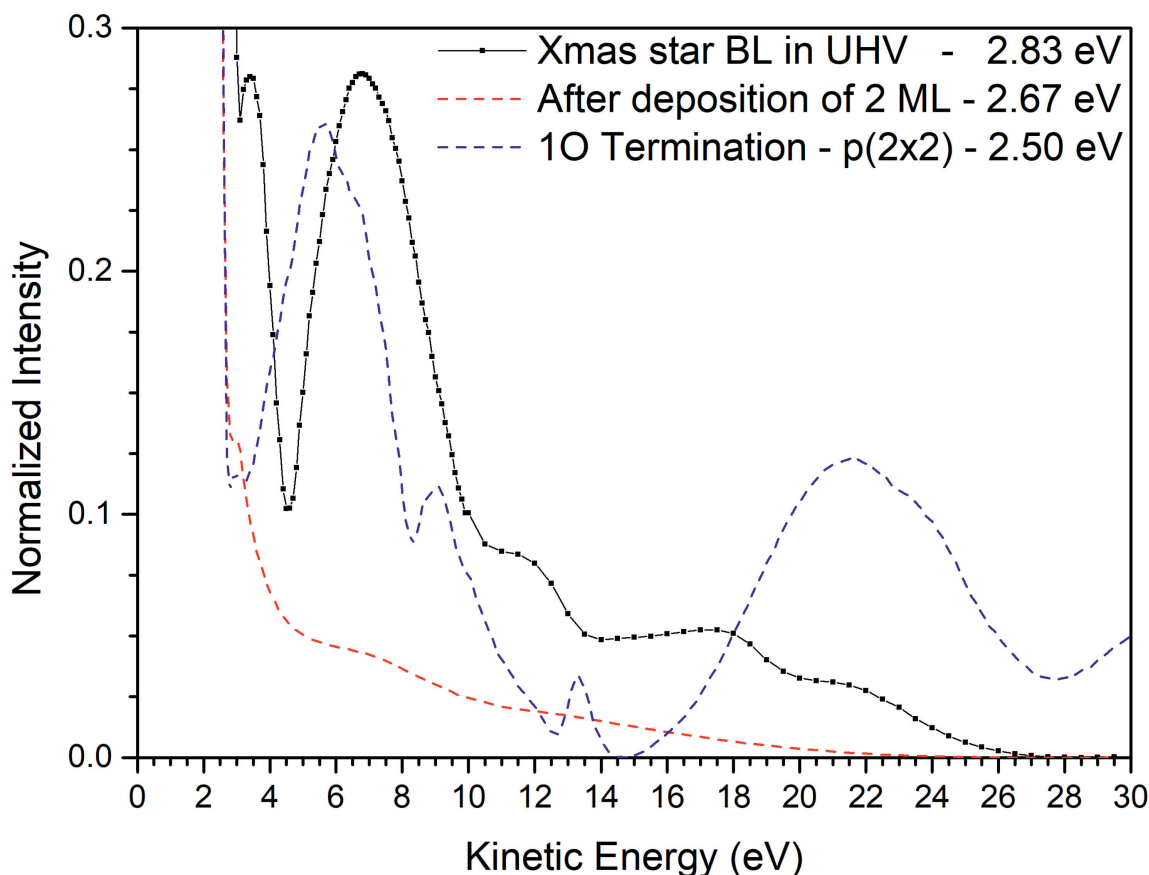


Figure 8.8: LEEM(IV) curves of the silica film annealed in UHV (black), after the deposition of 2 ML (red) and of the 1O Termination (blue). The kinetic energies of the MEM to LEEM transitions are given in the legend.

Figure 8.8 shows the LEEM(IV) curves of the silica film after UHV annealing. First it should be noted that the MEM to LEEM transition decreased to 2.83 eV from 2.95 eV after the pre-annealing in oxygen, indicating a decrease of the work function of about 0.1 eV. In comparison to the LEEM(IV) curves after deposition it shows various structures. It has its first maximum at about 3 eV, i.e. very close to the MEM to LEEM transition, followed by a deep minimum at about 4.5 eV. A broad maximum at about 7 eV is found, afterwards the intensity decreases stepwise with increasing kinetic energy of the electrons, with plateaus at about 12 eV, 18 eV and 22 eV. For comparison, the LEEM(IV) curve of the 1O termination is shown, and, as can be clearly seen, it has no features in common with the curve for the UHV annealing of silica.

Figure 8.9 shows DF-LEEM images and DF-LEEM(IV) curves of a silica film after UHV annealing. In contrast to the bright field images of figure 8.8, the DF images show bright islands with an average size of 10 nm, homogeneously distributed over the terraces. The steps and step bunches, which were decorated with white islands

in the bright field image appear black in all DF-images. The images T0, T1 and T2 (DF-LEEM labels correspond to used LEED spots, labeled in the same way) show no resemblance within the white islands structures. T0 and T3 (corresponding to the opposite LEED spot) however show the same features. All DF-LEEM(IV) curves exhibit the same features, with maxima at 10 eV, 15 eV and 20 eV.

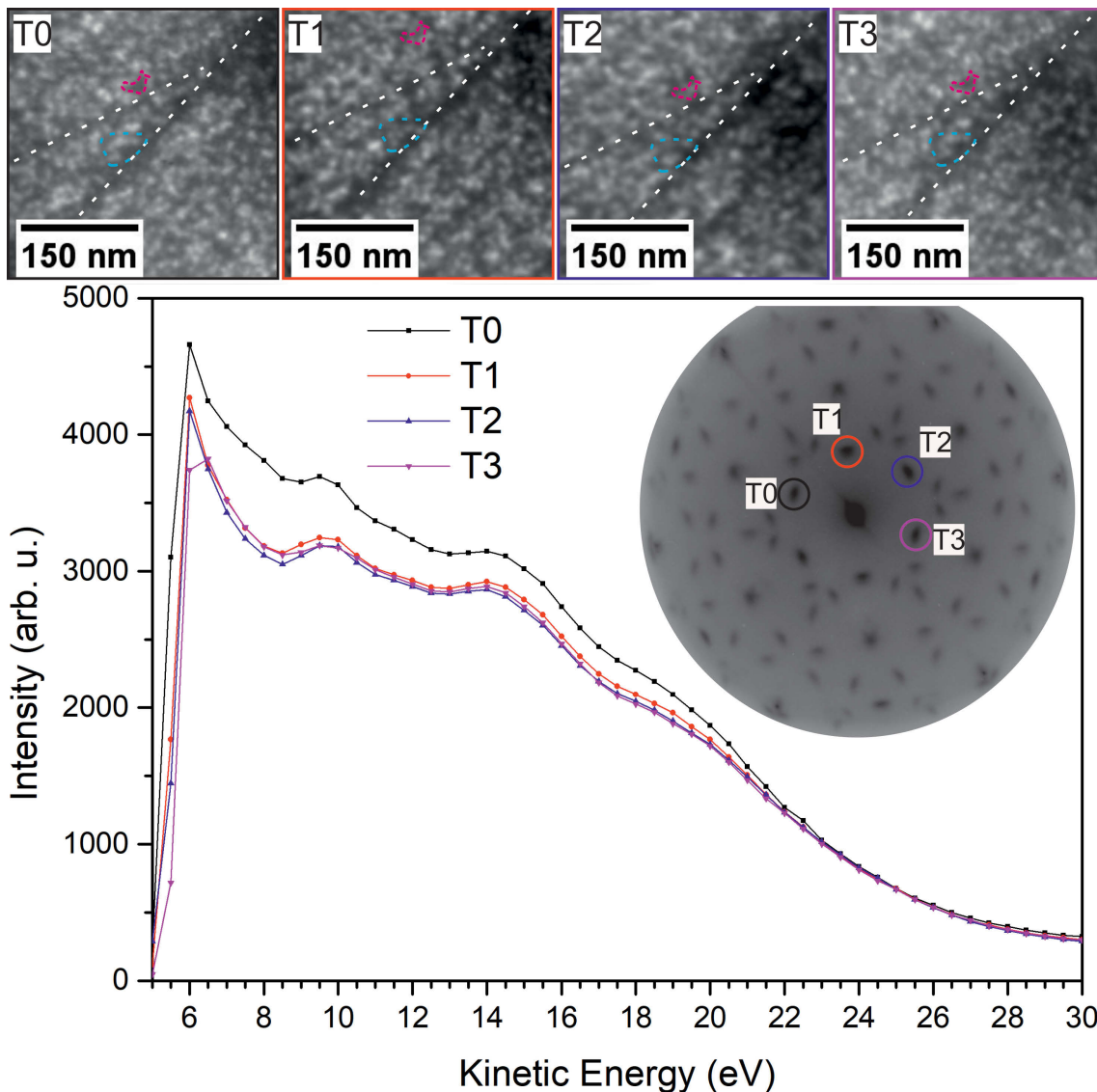


Figure 8.9: DF-LEEM images and DF-LEEM(IV) curves of a silica film after UHV annealing. The DF-LEEM(IV) images T0 - T3 were taken with a kinetic energy of 15 eV. Step bunches (white lines) and equal areas are marked as guide for the eye. In the lower part of the figure the DF-LEEM(IV) curves of the indicated spots in the inset are shown. The LEED was taken at 42 eV.

Figure 8.10 shows the photoelectron spectra of the Si 2p, Ru 3d_{5/2} and O 1s regions. The Si 2p line in a) has one maximum 102.8 eV binding energy, which is shifted about 0.2 eV higher in comparison to the pre-annealed silica template. Again, no traces of incompletely oxidized silicon are found. In b) the Ru 3d_{5/2} line is shown,

it has not changed in comparison to before the UHV annealing and resembles quite well that of a 1O termination of Ru(0001). The O 1s line in c) comprises two visible components: an intense one at 531.7 eV assigned to Si-O bonds and a weak one as small shoulder at its lower binding energy side assigned to Ru-O-Si bonds. In comparison to the pre-annealing in oxygen, the second component is much less intense. Furthermore, only a very slight contribution of Ru-O bonds is found, which appears at lower binding energy (529 eV).

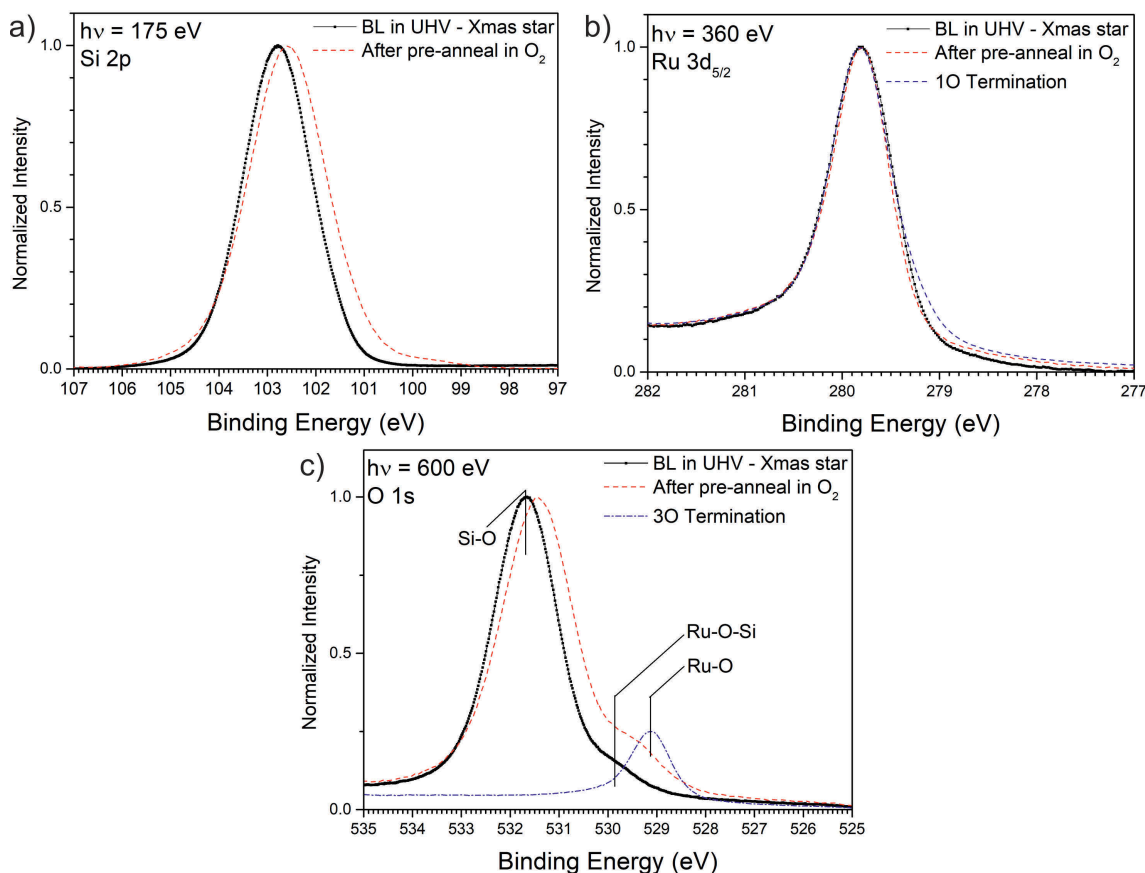


Figure 8.10: XPS spectra of a silica BL annealed in UHV. The regions of the Si 2p (a), Ru 3d_{5/2} (b) and O 1s (c) are shown.

8.3 Preparation in oxygen, and characterization of properties

The heating rate for the preparation of the silica bilayer in oxygen has a large influence on the formed silica phase. For slow heating ramps of about 1 K/s the crystalline or vitreous silica phase is formed depending on the final holding temperature (see chapter 9). For faster annealing rates greater than 5 K/s the UHV phase of the silica bilayer, the Xmas star like bilayer, appears. Its formation under an oxygen atmosphere was studied here with in-situ LEED measurements as well;

the results are shown in figure 8.11. The intensity of LEED spots shows the same behaviour as the UHV annealing. At the beginning of the heating no change in the pattern occurs (see images A and B). At about 1050 K the formation of the UHV phase starts (see image C) and the intensity of its diffraction spots increases exponentially with temperature. During the holding at 1080 K a further small intensity increase is found, leading to a sharp Xmas star pattern (see image D)

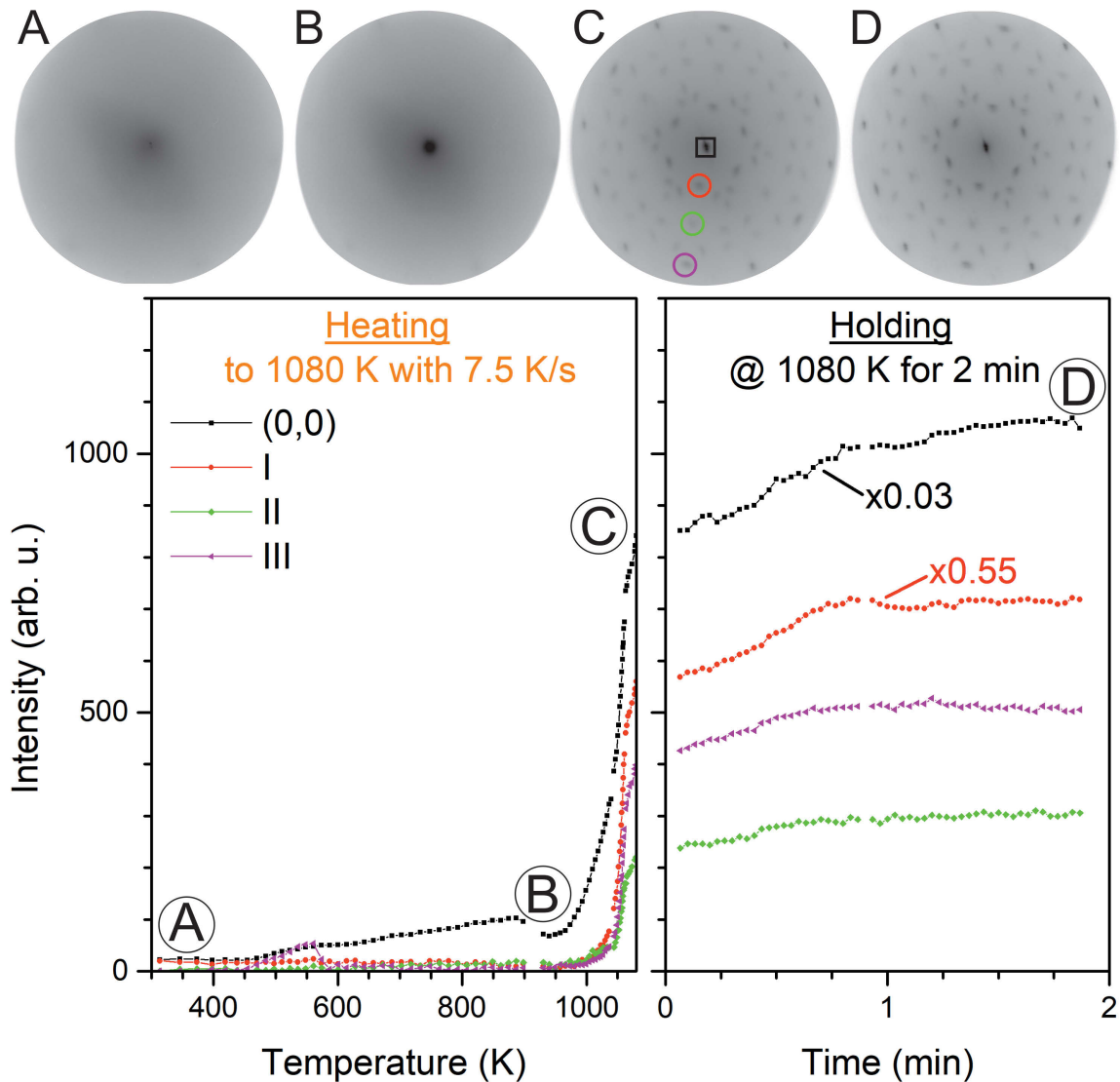


Figure 8.11: Analysis of LEED spots during annealing in 5.0×10^{-6} mbar oxygen with an increased heating ramp to 1080 K to form the Xmas star bilayer. The upper part shows LEED images collected during the temperature treatment, and the lower part the intensities of the individual LEED spots during heating and holding stages. The electron kinetic energy was 42 eV. (For more details see text)

Figure 8.12 shows LEEM and LEED images of the silica film after the UHV anneal. Bright and dark areas with sizes around 75 nm are visible in images a) and b). The Xmas star LEED pattern is found after the annealing and is shown in c).

The morphology resembles very well the one found for the annealing in UHV (see figure 8.7).

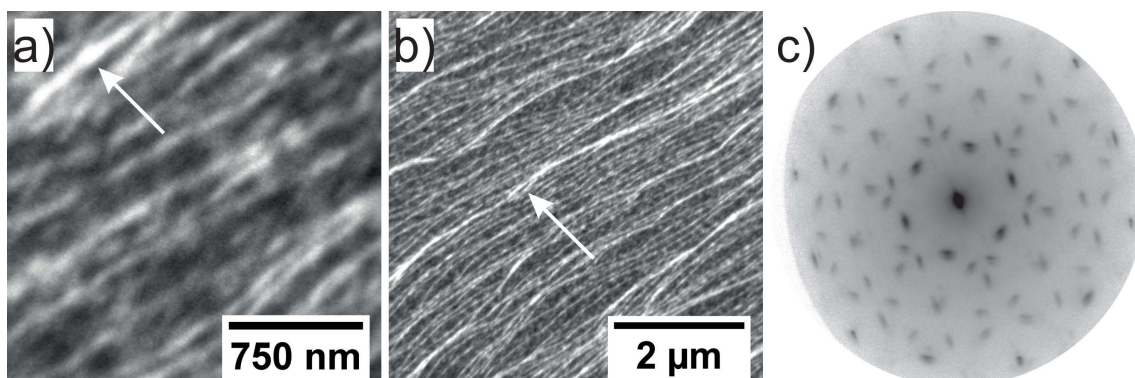


Figure 8.12: LEEM and LEED images recorded at RT after the annealing with 7.5 K/s in oxygen to 1080 K and holding it for 5 min. The white arrow marks the same area in the different field of views in a) and b). In the LEED image c) the Xmas star like pattern is shown. For all all images a kinetic energy of 42 eV was used.

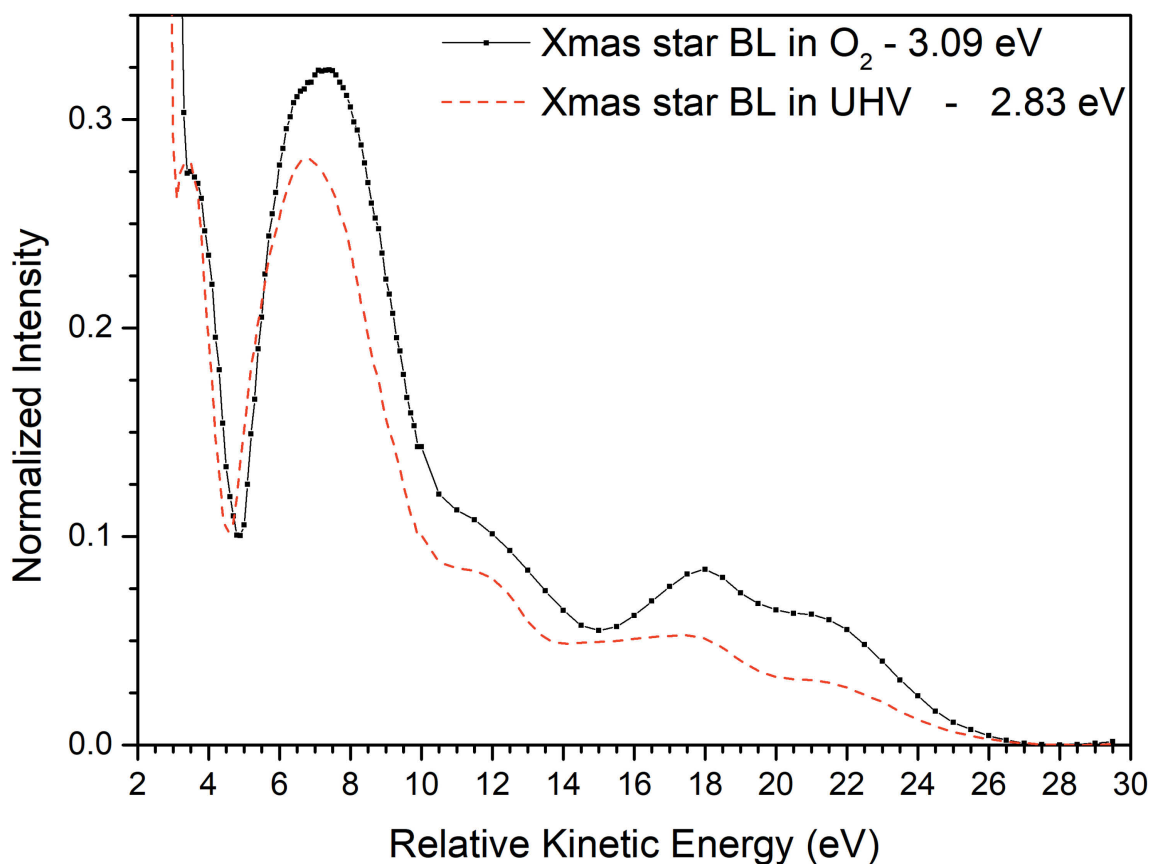


Figure 8.13: LEEM(IV) curve of the Xmas star silica bilayer prepared under an oxygen atmosphere. For comparison, the LEEM(IV) curve for the Xmas star bilayer in UHV is shown. The MEM to LEEM transition for each phase is given in the inset.

Figure 8.13 shows the LEEM(IV) curve of the Xmas star silica bilayer prepared under an oxygen atmosphere with a heating rate of 7.5 K/s. It resembles very well the LEEM(IV) curve for the UHV preparation. A slight difference in both curves is found in the intensity of the features and in the region between 14 eV and 16 eV. In contrast to the UHV preparation the value of MEM to LEEM transition is increased by about 0.26 eV, to a value of 3.09 eV. For better comparison, the kinetic energy in the x-axis was offset corrected to the MEM to LEEM transition for each curve.

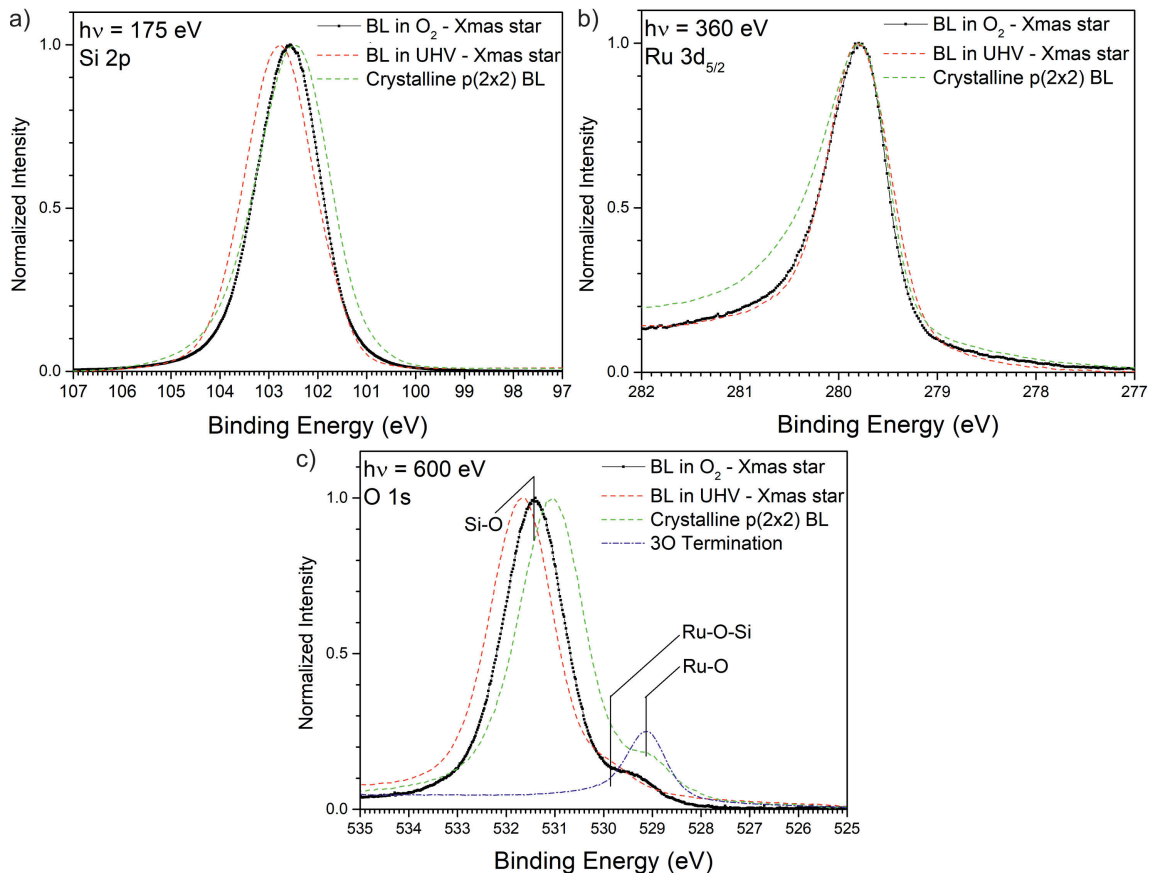


Figure 8.14: XPS spectra of a Xmas star silica bilayer prepared in oxygen. The regions of the Si 2p (a), Ru 3d_{5/2} (b) and O 1s (c) are shown. For comparison, the results for the Xmas star bilayer prepared in UHV and for the crystalline p(2x2) bilayer prepared in oxygen are given.

Figure 8.14 shows the XPS results of the Xmas star silica bilayer prepared in oxygen by fast heating. The Si 2p line shown in a) has one maximum at about 102.6 eV that is shifted about 0.2 eV to lower binding energy than the maximum found for the UHV preparation, but very close to the one of the crystalline p(2x2) BL-phase. The Ru 3d_{5/2} line resembles very well that of the UHV preparation and is different from that of the crystalline p(2x2)BL-phase. The O 1s line has an intense maximum at 531.4 eV due to Si-O bonds, and a small shoulder at the lower binding energy side. The small maximum fits very well the feature found for the UHV preparation of the

Xmas star phase. However, the Si-O component is slightly shifted to lower binding energies than of the UHV preparation. The crystalline p(2x2) BL-phase has similar features, however, the Si-O component is shifted to even lower binding energies and the small shoulder has a higher intensity.

These results show that the preparation of the Xmas star silica bilayer under an oxygen atmosphere leads to similar features as the UHV preparation. However, minor differences are found in the LEEM(IV) curves and XPS spectra of the Si 2p and O 1s line. The observed energy shifts in the XPS spectra could be due to a slightly higher amount of oxygen at the ruthenium interface. A similar oxygen dependency is found for the intercalation of oxygen (see figure 9.19). It can be concluded that during annealing of the deposited silicon the initial oxygen amount at the ruthenium interface plays a major role for the formation of the different silica phases. The high heating ramp seems to prevent an intercalation or diffusion of oxygen below the silica BL, meaning the Xmas star BL structure is produced faster than the oxygen can intercalate to the Ru interface. This interface oxygen would block the formation of the Xmas star structure, most likely it would passivate the Ru surface so that no Si-O-Ru bridging bonds can be formed.

8.4 Interpretation: The formation, morphology and chemical state of the Xmas star BL-phase

At the beginning of the annealing of the silica template in UHV, only the overall intensity of the (0,0) increases indicating no change of the structure of the film (see figure 8.6 and 8.11). At 700 K the spot diameter starts to increase and has a maximum at 975 K. The likely reason could be the beginning of a reconstruction of the silica template, but conclusions about the atomic arrangement are not possible. However, the film is still in an amorphous state. At 1080 K a drastic change in the film structure is happening: the film reorders and a very complex LEED pattern appears. All spots appear at the same temperature and increase in intensity during holding and cooling. A possible reason for the observed behaviour in LEED could be the formation of small domains of this new phase all over the surface. The domains grow over time until the whole layer is transformed. This is supported by the LEEM and DF-LEEM images, where islands are found on the whole surface (see figure 8.7, figure 8.9 and figure 8.12). A study with different holding temperatures could be

useful to determine the activation energy for the formation of this overlayer via an Arrhenius plot.

On the other hand, the LEEM(IV) curve indicates a highly ordered, crystalline phase of this film and shows a quite different behaviour than the LEEM(IV) curves for *as deposited* silica films or oxygen terminated Ru(0001) support. The narrow Si 2p peak in figure 8.10 suggests a well ordered structure, in which all silicon atoms are in a similar chemical environment, most likely as silicon dioxide tetrahedra. This is supported by the large contribution of the Si-O bond to the O 1s line. The Ru 3d_{5/2} line suggests an occupation of ruthenium adsorption sites as for a 1O terminated surface. However, the O 1s line shows only a very small contribution of Ru-O bonds, so it is very likely that the ruthenium sites are occupied by Ru-O-Si bonds, which are clearly visible in the O 1s line. With this assumption the film may consist of two types of areas: an ordered silica BL structure, which is bound in itself and therefore lifts off the ruthenium, while there are other areas that have a backbone of silica tetrahedra attached to ruthenium and therefore are covalently bound to the surface.

In figure 8.15 a possible structure for the observed LEED pattern of the overlayer is suggested. It consists of a rectangular unit cell with the matrix

$$\begin{pmatrix} 4 & 2 \\ 0 & 2.8 \end{pmatrix} \quad (8.1)$$

with respect to the Ru(0001) unit cell, corresponding to side lengths of $2 \times \sqrt{3}$ and 2.8 in Ru unit cell length ($2.8 \times 2\sqrt{3}$). It has a side length of $a = 9.37 \text{ \AA}$ and $b = 7.58 \text{ \AA}$ and the area is 11.2 times larger than the ruthenium unit cell. The structure is commensurate for its $2 \times \sqrt{3}$ direction and incommensurate for its 2.8 direction to Ru(0001). It has 3 rotational and 3 mirror domains. A diffraction pattern simulated with LEEDpat [127] is shown at the right side in figure 8.15. The spots marked with a cross are not found in the LEED image on the left side, possibly due to the glide plane symmetry of the silica structure. The lattice model of the overlayer and the ruthenium highlights the larger size of the incommensurate unit cell in comparison to the ruthenium unit cell. The assumption of 3 rotational domains is supported by the DF-images in figure 8.9. The DF images of opposite spots (like T0 and T3) belong to the same domain and hence show the same features, indicating additionally a two-fold symmetry. Contrary, T1 and T2 belong to different domains and thus show completely different structures. Moreover, all DF-LEEM(IV) curves show similar features, speaking for the same structure contributing to the intensity

behaviour of each curve and supporting the model of 3 equivalent domains rotated by 120° against each other.

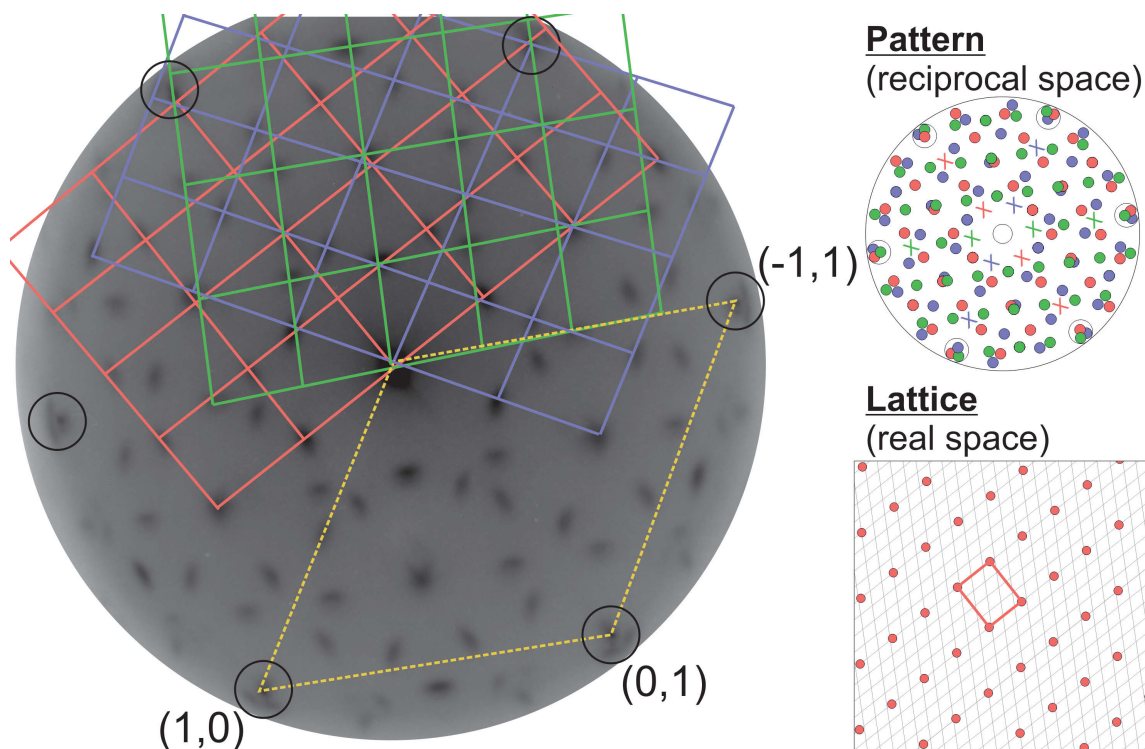


Figure 8.15: Model of the structure of Xmas star layer produced by annealing the silica template in UHV. Left, the 3 rotational domains (12 unit cells each) are superimposed on the complex pattern, and the main spots for the Ru(0001) unit cell are indicated. Right, a calculated pattern and the lattice of the incommensurate phase in reciprocal space and real space are shown. In the pattern red, green and blue circles donate the 3 domains, white circles represent the Ru(0001) pattern. The spots marked with X are not observed in the LEED image. In the lattice model the Ru(0001) lattice is represented as grey lines, one domain of the incommensurate lattice as red circles with its unit cell as red rectangle.

During the time of this work the Xmas star bilayer phase was investigated by means of Fourier-transform infrared spectroscopy (FTIR) and STM by Xin Yu of the Structure and Reactivity group and by David Kuhness and Hyun Jin Yang of the Scanning Probe Microscopy group of the Fritz Haber Institute. The sample for the STM measurements were prepared at the Fritz-Haber-Institute by annealing in oxygen (see section 8.3) with the following parameters: heating rate >15 K/s, holding temperature 1135 K and holding time 15 min. In figure 8.16 a) an STM image of the sample with a field of view of 3.8×3.8 nm² is shown, the tunnel parameters were $V_S = 2.9$ V and $I_T = 21$ pA. A homogenous surface is visible with jugged parallel line structures. Because of this feature the Xmas star phase is referred to as zig zag phase in STM. The [0001] direction of ruthenium substrate is indicated and the topmost atoms of an atomic model are overlaid. The field of view of a) is indicated

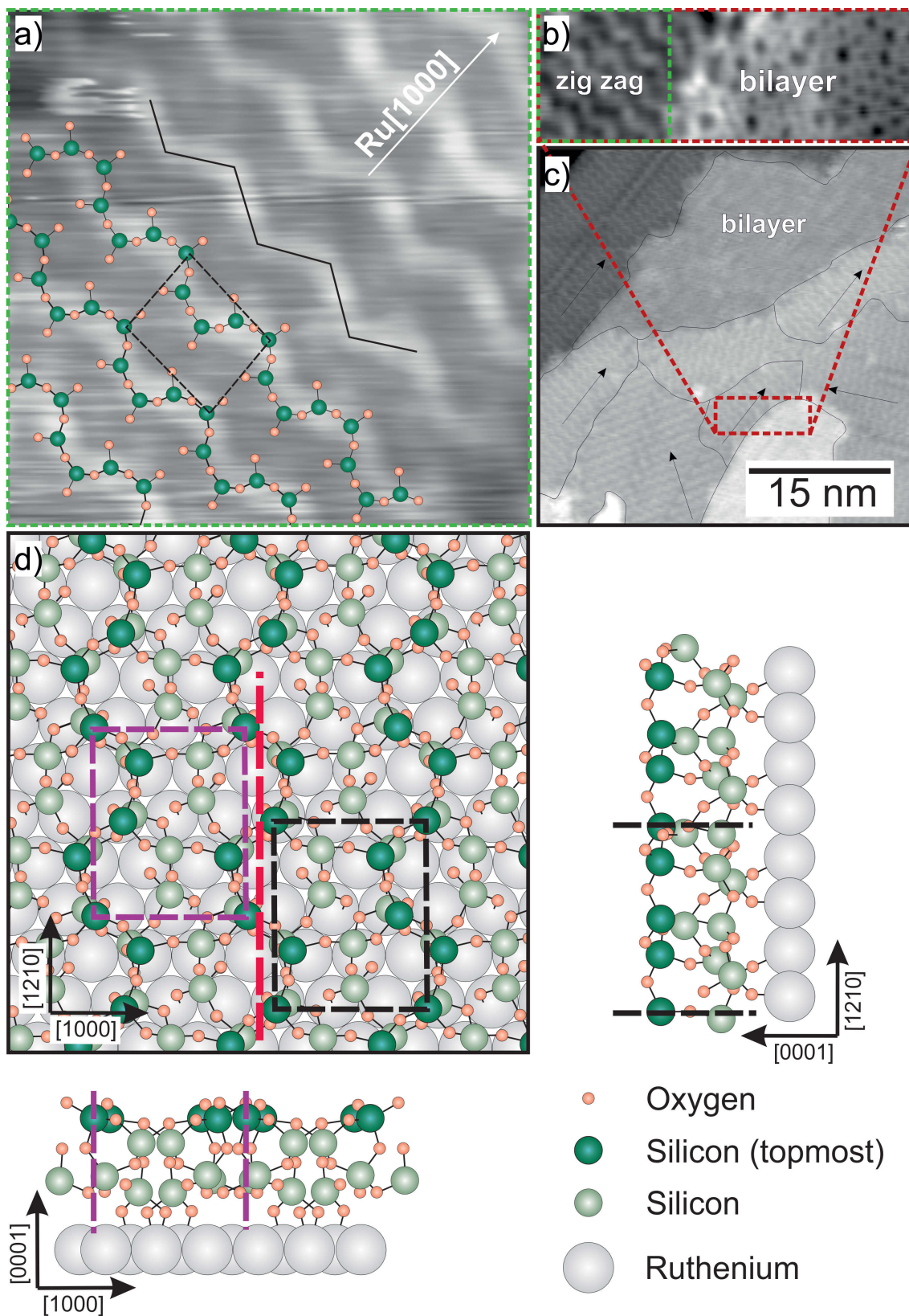


Figure 8.16: STM images (a-c) done by Scanning Probe Microscopy group (David Kuhness) and atomic model (d) of the Xmas star (zigzag) phase calculated by theoretical Chemistry department (Denis Usvyat).

by a green box in b). B) is an STM image with a field of view of $10 \times 3.8 \text{ nm}^2$, with tunnelling parameters $V_S = 2 \text{ V}$ and $I_T = 30 \text{ pA}$. It is visible that the Xmas star (zig zag) phase and the vitreous BL phase coexist next to each other on the surface. In the STM image with a large field of view in c), three different domains of the Xmas star phase are indicated by black arrows, the tunnelling parameters were $V_S = 2 \text{ V}$ and $I_T = 30 \text{ pA}$. The three rotational domains were found in DF-LEEM as well, see figure 8.9. In image c) it is also visible that the vitreous BL phase exists as islands in the Xmas star phase. The islands are possibly the first signs of the beginning of a phase transition of the Xmas star phase into the p(2x2) or vitreous silica phase. The transitions of the Xmas star were investigated by in-situ LEED as well, but they are not discussed in detail in this work. LEED images of the transition state can be found in figure 10.2.

An atomic model was first suggested by the Scanning Probe Microscopy group and in cooperation with Denis Usvyat from the Theoretical Chemistry department of the Humboldt University Berlin an atomic model was calculated by density functional theory (DFT). Its structure was optimized by using a PBE functional [139] and a linear combination of atomic orbitals based code. The structure with the lowest calculated energy has a unit cell consisting of 12 silicon atoms and 26 oxygen atoms giving a stoichiometry of $\text{SiO}_{2.17}$ (see figure 8.16 d)). In the structure silicon is coordinated by 4 oxygen atoms forming silica tetrahedra that are connected with each other in a rather complicated arrangement where some areas of the film are lifted off while others are bound to the ruthenium surface. Both areas form parallel lines on the surface and the lifted off area is slightly higher than the bound one, thus explaining the investigated zig zag structure (see the topmost silicon atoms in the model). The closest commensurate unit cell has a size of $a = 9.37 \text{ \AA}$ and $b = 8.12 \text{ \AA}$, and corresponds to a $(3 \times 2\sqrt{3})$ Ru(0001) overlayer. The lattice parameter a calculated by DFT is the same value as for the LEEDpat simulation of 9.37 \AA , while the calculated value for b is larger than the value of the LEEDpat simulation of 7.64 \AA . The calculated crystal structure has a glide plane symmetry fitting to the LEED pattern, its translation vector is $1/2 \vec{b}$ in the $[1210]$ direction of ruthenium. The glide plane symmetry is indicated by the purple and black unit cell and by the mirror plane as red dashed line in figure 8.16 d).

The p(2x2) BL-phase and the vitreous BL-phase

9.1 The appearance of p(2x2)-BL-phase and vitreous BL-phase in oxygen

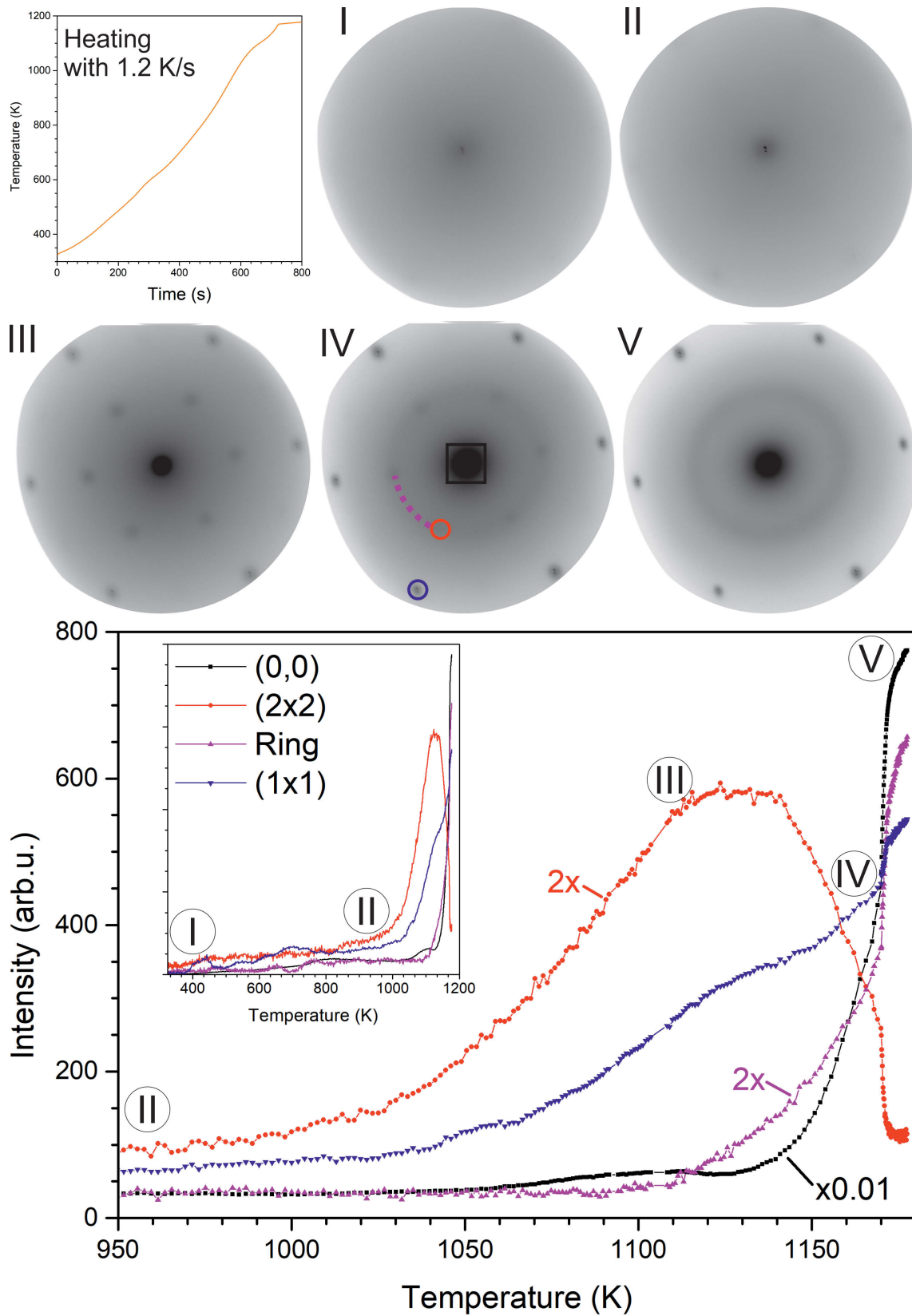
The annealing of a silicon amount for a BL silica in an oxygen atmosphere of 10^{-6} mbar has widely been investigated [8–12, 15, 140]. However, all the results are ex-situ measurements, performed after the oxygen annealing step. No in-situ measurements for the preparation have been published so far.

Figure 9.1 shows the analysis of an annealing experiment in an oxygen atmosphere with a heating ramp of 1.2 K/s. The silicon amount is comparable to a closed bilayer of silica. LEED images for different temperatures are shown in the upper part of the figure, in the lower part the intensities of LEED spots as a function of temperature are depicted. Up to 950 K no additional spots to the (0,0) spot are observed (see LEED image I). At 950 K new faint spots, ordered in a p(2x2) pattern, start to appear (see image II and the intensity-temperature plot). The intensity of the p(2x2) pattern increases with a broad maximum at 1140 K (see image III). While increasing the temperature further, the intensity of the p(2x2) decreases and the p(2x2) spots disappear. At the beginning of the intensity maximum of the p(2x2) pattern a ring starts to appear in the diffraction pattern with its centre in the (0,0) spot. Its radius corresponds to the distance of a first order p(2x2) spot to the (0,0) spot. The ring intensity increases with increasing temperature and reaches a maximum at 1080 K. The (1x1) spots start to appear at 1040 K (see LEED image III) and their intensity increases linearly with increasing temperature. At about 1150 K, the p(2x2) pattern

and the ring have the same intensity (see LEED image IV). Above 1170 K the p(2x2) pattern disappears (see LEED image V).

To emphasize the difference between the two here described silica BL phases, the p(2x2) BL-phases will be addressed as "crystalline p(2x2) BL", while the disordered BL phase (ring in LEED) will be addressed as "vitreous BL".

Figure 9.1 (facing page): Analysis of LEED spots during annealing in 5.0×10^{-6} mbar O₂ to 1180 K. In the upper part the heating ramp and LEED images observed during this temperature treatment are shown and the lower part represents the analysis of the intensity of selected LEED spots during the annealing. The large diagram shows the intensity as a function of the temperature between 950 K to 1180 K, while the inset shows the whole temperature range (RT – 1180 K). An electron kinetic energy of 42 eV was used. (for more details see text)



9.2 p(2x2) BL-phase: Preparation, and characterization of properties

These findings above enable the controlled and reproducible preparation of a pure, crystalline p(2x2) BL-phase by annealing it to 1050 K in 5.0×10^{-6} mbar oxygen. The in-situ results of such annealing are shown in figure 9.2. The experiment consists again of three stages: a heating ramp up to 1050 K, holding at 1050 K for 10 min and cooling down. As before no extra spots additionally to the (0,0) spots appear up to 950 K (see LEED images I and II). At 950 K a faint p(2x2) pattern appears and its intensity and that of the (0,0) spot increases exponentially with temperature up to 1050 K (see image IV). The (1x1) spots show a linear increase in intensity with temperature up to 950 K that can be attributed to a rising background signal, because no (1x1) spots are visible in image II. However, above 950 K they appear and have an exponential intensity increase like the (0,0) spot and p(2x2) spots. During the holding of the sample at 1050 K for 10 minutes, the p(2x2) and (1x1) spot intensities increase only slightly. The (0,0) spot instead shows a quasi-exponential increase of the intensity with time. During cooling, the intensity of the (0,0) spot continues increasing down to 900 K, but decreases rapidly with further cooling. The p(2x2) spots gain slightly in intensity with the temperature decrease, while the (1x1) spots show opposite behaviour. Image V represents the final LEED pattern, where the p(2x2) and (1x1) spots are clearly visible.

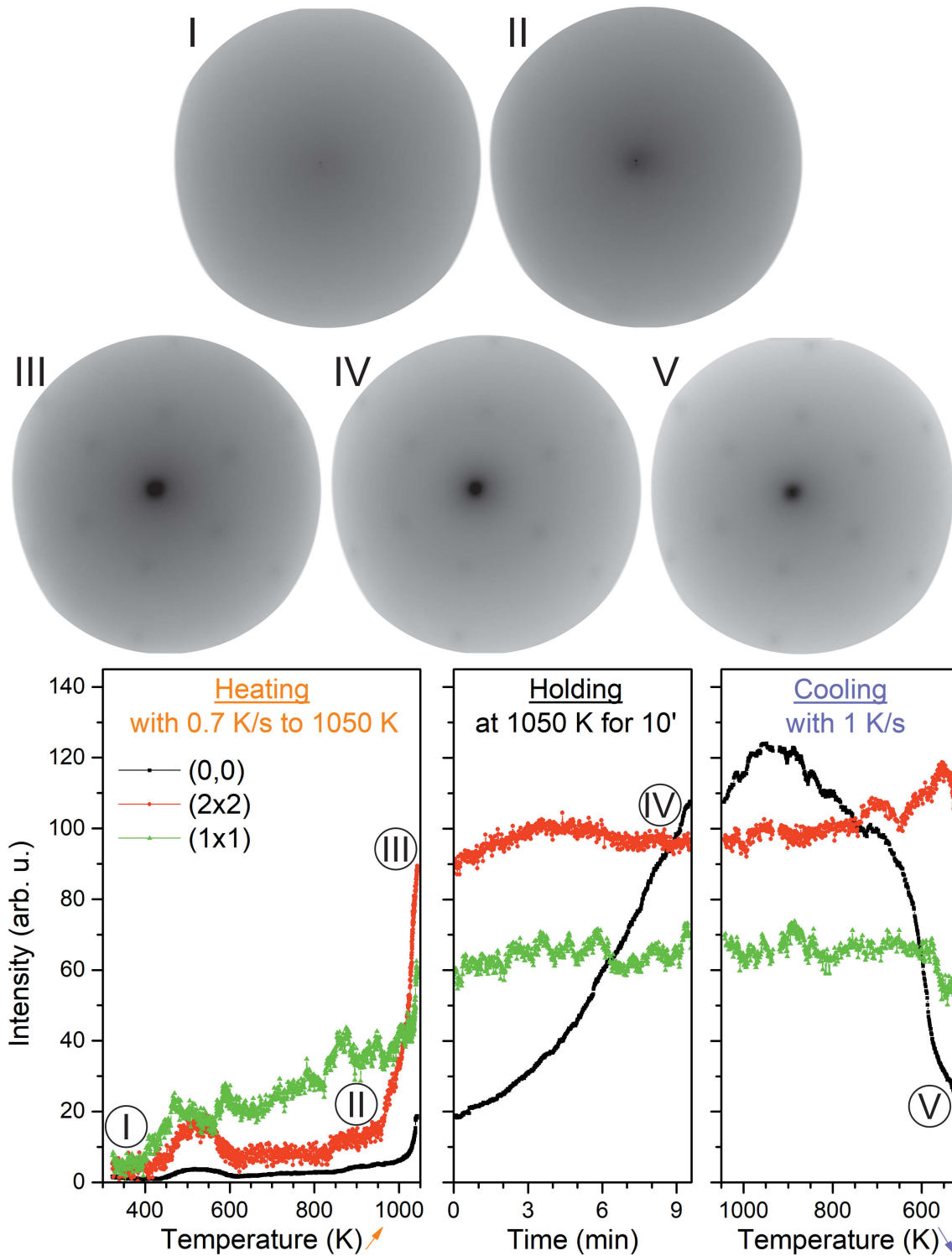


Figure 9.2: Analysis of LEED spots while annealing a bilayer of silicon in oxygen to 1050 K. The upper part shows LEED images collected during the temperature treatment, the lower part the intensities of the individual LEED spots during heating, holding and cooling down. An electron kinetic energy of 42 eV was used. (for more details see text)

Figure 9.3 shows the LEEM(IV) curve of the silica bilayer measured at room temperature after the annealing in oxygen. The MEM to LEEM transition is increased

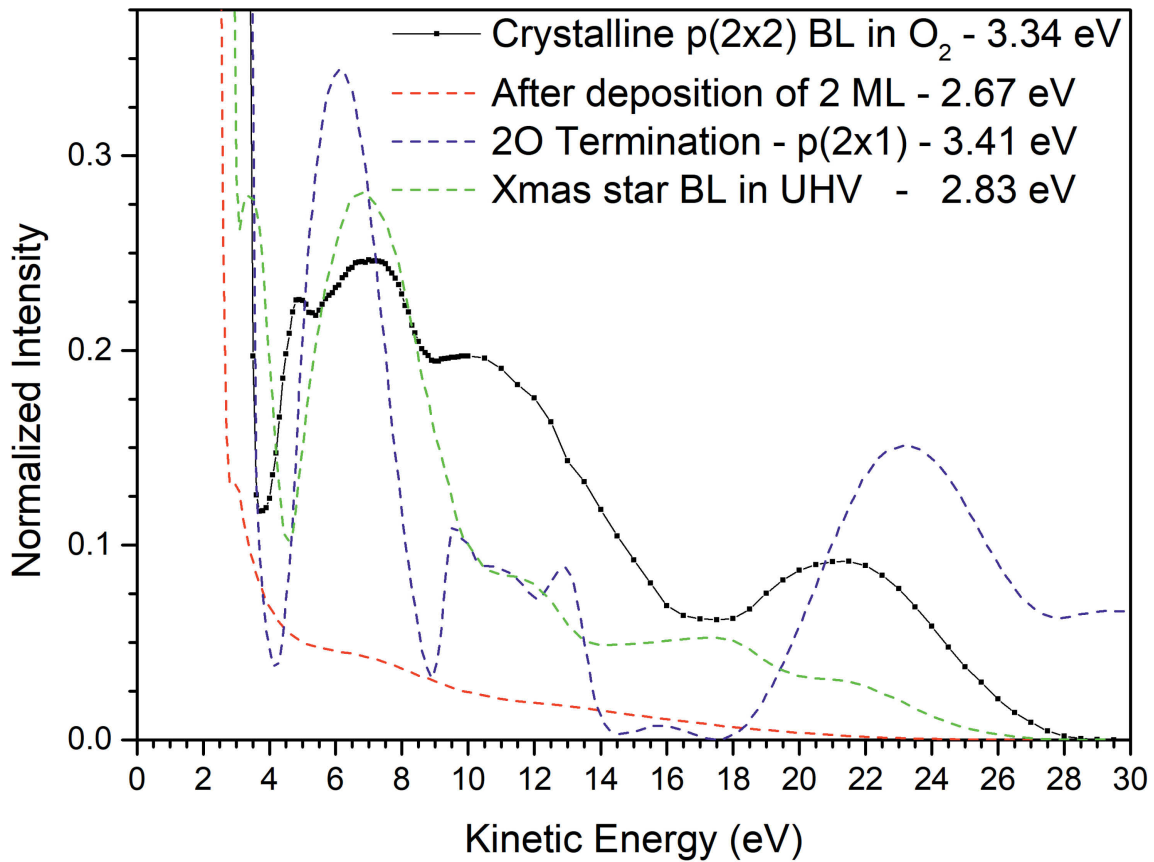


Figure 9.3: LEEM(IV) curve of a crystalline $p(2 \times 2)$ silica bilayer after the thermal treatment in oxygen at room temperature. For comparison, the LEEM(IV) curves of the 2O terminated ruthenium surface, after the silicon deposition and after the thermal treatment in UHV are shown. The energies of the MEM to LEEM transition are given in the inset and the intensities are normalized to the maximum of intensity of the MEM mode.

by about 0.7 eV to a final value of 3.34 eV compared to the as deposited film and is very close to the value of the 2O terminated ruthenium surface. The LEEM(IV) curve starts with a deep minimum directly after the MEM to LEEM transition at about 4 eV. With increasing kinetic energy of the electrons up to 14 eV, the intensity change shows four maxima. Afterwards, the intensity decreases and has a minimum at about 17 eV followed by a maximum at 21 eV. Up to 8 eV, the LEEM(IV) curve shows similar features like the xmas star bilayer prepared in UHV or like the 2O termination. It has also a broader minimum at 17 eV like the 2O termination. Besides this similar features, the LEEM(IV) curve does not resemble the other LEEM(IV) curves (see also chapter 4 figure 4.3).

Figure 9.4 shows DF images and DF-LEEM(IV) curves at room temperature after the annealing of a bilayer silicon in oxygen. The DF images show bright or dark areas that are the terraces of the ruthenium surface. There are small islands of a size between 20 to 35 nm on the terraces. For all diffraction spots used for imaging in the

DF mode, the islands appear bright and similar features are found (see the arrows and box in the images I-III). The DF-LEEM(IV) curves for the terraces including the islands exhibit the same features, except for kinetic energies above 21 eV, where differences are noticeable.

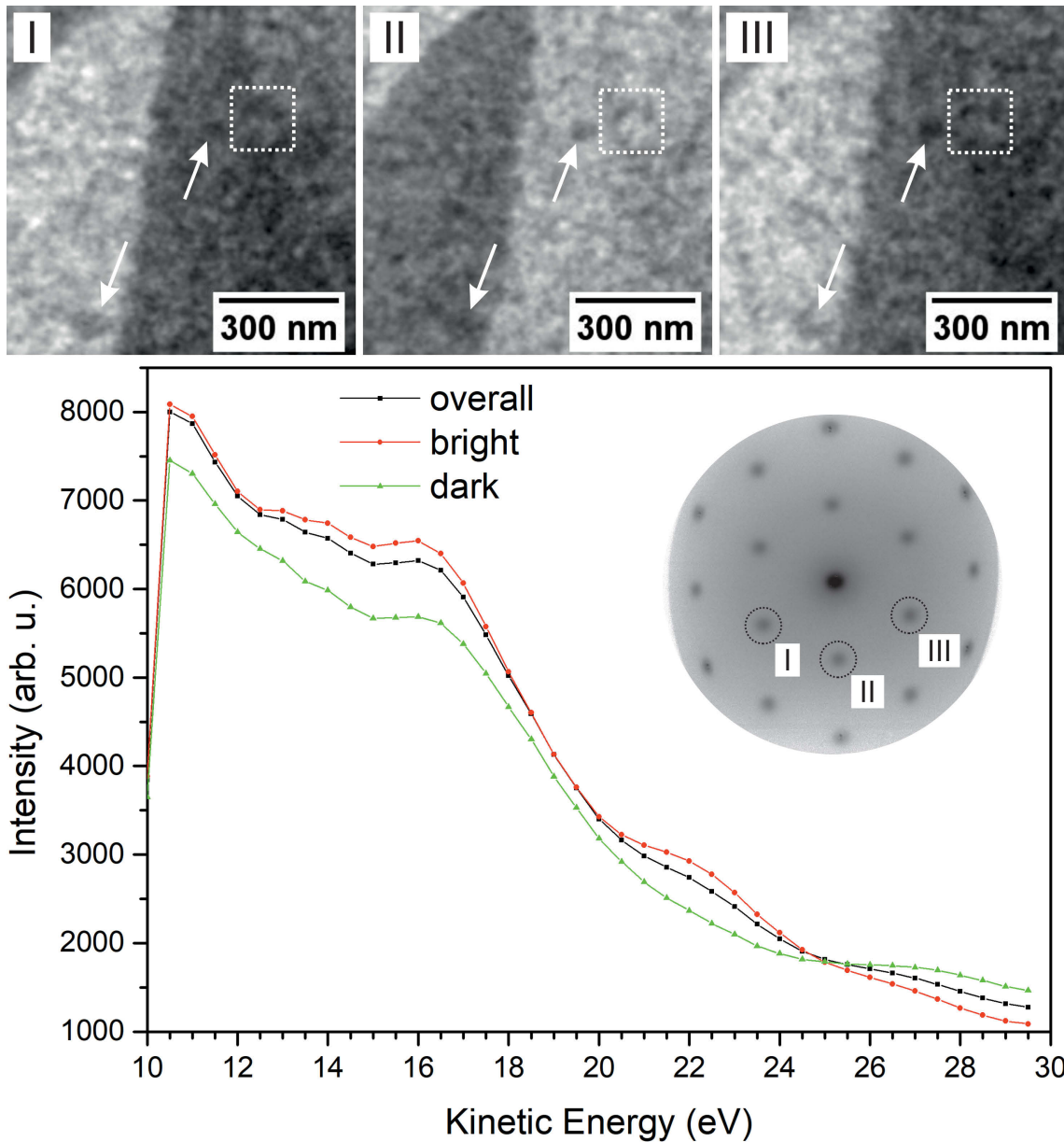


Figure 9.4: In the upper part of the figure a DF image series is shown. The spots used for the images I-III are marked in the inset in the plot in the lower part of the figure. Similar areas are highlighted by a box or arrows in the images. The plot shows the DF-LEEM(IV) curves of the black or white terraces in DF. The electron kinetic energy used for the DF images series was 17 eV.

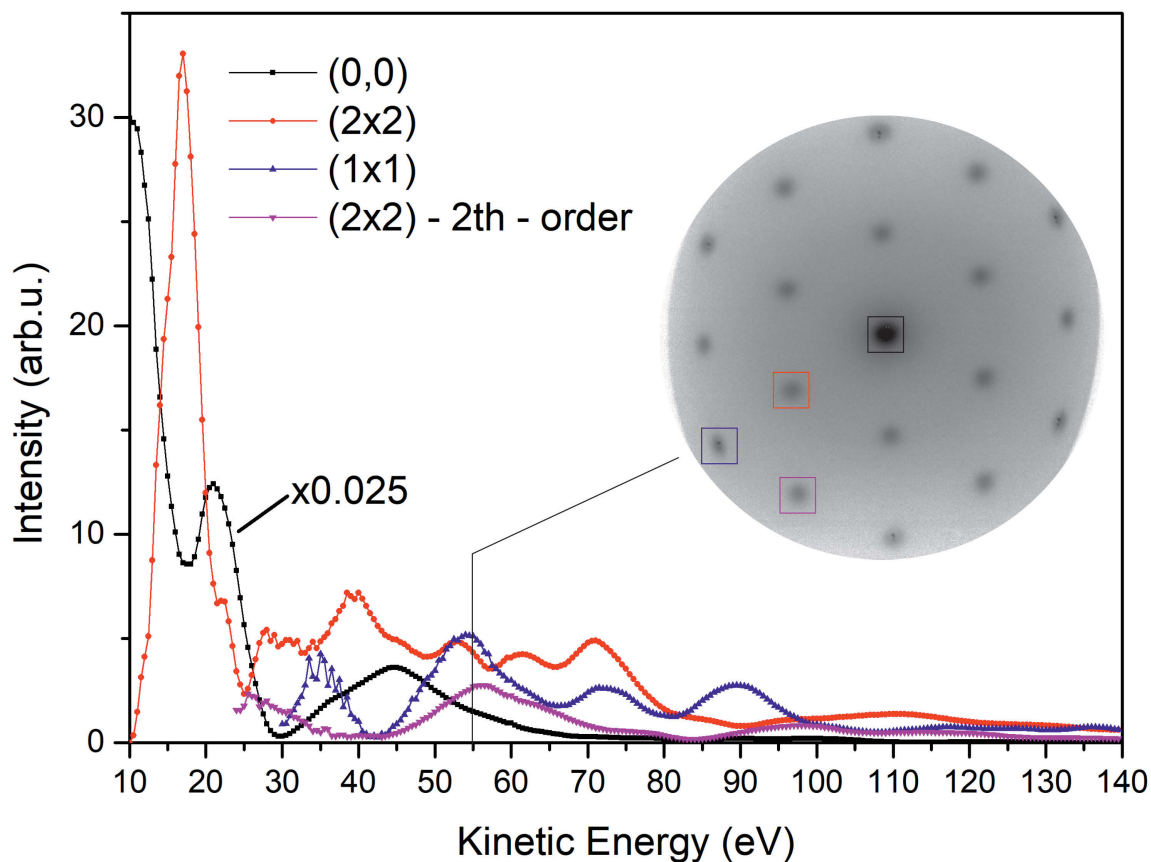


Figure 9.5: LEED(IV) curves of a crystalline $p(2 \times 2)$ silica bilayer. The LEED image in the inset has an energy of 55 eV and the investigated spots are indicated in it.

Figure 9.5 shows the LEED(IV) curves of the crystalline $p(2 \times 2)$ silica bilayer. The (0,0) curve has three main features in the range of 10-70 eV, for higher energies only very small changes in intensity are found. The $p(2 \times 2)$ pattern shows a lot of maxima up to 80 eV with an average distance of 10 eV. Above 90 eV a very broad, but low intense maximum up to 140 eV is found. The (1x1) spots show four maxima in intensity up to 100 eV with an average distance of 20 eV. As for the $p(2 \times 2)$ a broad, but low intense maxima up to 140 eV is found. The second order of the $p(2 \times 2)$ has multiple maxima over the whole scan range, which are in average 20 eV distant from each other. In the range of 55 eV all the investigated diffraction spots have maxima and are clearly visible in LEED (see the inset in figure 9.5).

Figure 9.6 shows the XPS measurements of Si 2p, Ru $3d_{5/2}$ and O 1s line of the crystalline bilayer of silica on ruthenium. The Si 2p line has a strong maximum at 102.5 eV binding energy and no traces of a state lower than the +4 oxidation state are found. The Ru $3d_{5/2}$ line has broadened at the higher binding energy side and has no resemblance to the *as-deposited* spectrum, thus fitting very well to the spectrum obtained for a 3O terminated ruthenium surface. The O 1s line

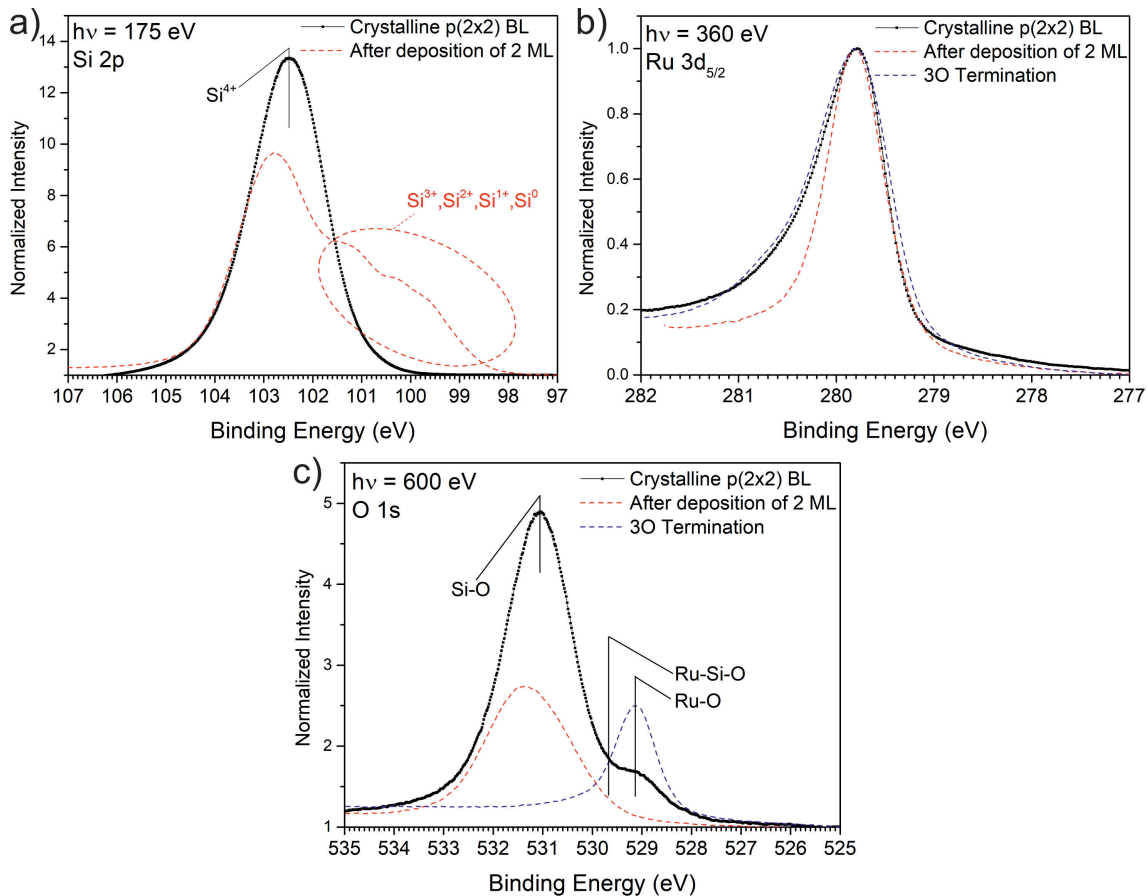


Figure 9.6: XPS spectra of the Si 2p in a), Ru $3d_{5/2}$ in b) and O 1s in c) lines at room temperature of a crystalline p(2x2) silica bilayer on ruthenium. For comparison, the XPS spectra after Si deposition and of the 3O terminated ruthenium surface are shown. (Details see text)

has an intense maximum at 531 eV binding energy and a less intense shoulder at lower binding energies. In comparison to the *as-deposited* spectrum the intensity of the O 1s line has increased and a new peak appeared about 529.2 eV at a position connected to Ru-O bonds.

9.3 Interpretation: The formation, morphology and chemical state of the p(2x2) BL-phase

At the beginning of the annealing in oxygen of the deposited silicon bilayer no structural change in LEED is observed (see figure 9.2). However, from the pre-annealing in oxygen in subchapter 8.1 it is already known that above 625 K the silicon film is completely oxidized to silica. At 950 K a dramatic change in the film structure occurs. A crystalline p(2x2) silica phase is formed, which increases very fast in intensity with rising temperature up to 1050 K. This suggests a very high

transformation rate at the beginning of the transformation. In the following a very slight increase of the intensity during the holding time and cooling is found, speaking for only minor changes in the ordering of the film. The islands seen in the DF-images imply also that the nucleation centers are homogeneously distributed over the whole surface and that no rotational domains exist in the film.

IRRAS studies done in the institute and theoretical calculations [9,10], support the model that the crystalline p(2x2) silica bilayer lifts off the ruthenium and that the ruthenium surface is 3O terminated after the preparation. This model is confirmed by the results of this work: The contrast changes of the terraces in DF (see figure 9.4) supports the model of the lift off, in contrast to the DF-images of the BL prepared in UHV (see figure 8.9), which is still attached to ruthenium via Ru-Si-O bonds and shows no intensity change of the terraces. The shape of the O 1s line suggests that two peaks, one for Si-O and one for Ru-O, exists and the Ru 3d_{5/2} line supports the 3O termination of ruthenium.

9.4 Vitreous BL-phase: Preparation, and characterization of properties

As presented in the introduction of the beginning of this chapter, annealing the crystalline p(2x2) silica bilayer at temperatures above 1100 K in an oxygen atmosphere transforms it into a vitreous phase (see figure 9.1). So it is possible to prepare a purely vitreous silica bilayer. Figure 9.7 shows the in-situ measurement of the formation of the vitreous phase. During heating up to 1100 K, the formation of a crystalline p(2x2) BL-phase is observed (see images I and II). While holding the temperature at 1100 K the intensity of the p(2x2) spots of the crystalline phase has a maximum after one minute and then disappears. At the same time, a ring connecting all p(2x2) spots around the (0,0) reflection (see image III) starts to appear. The intensity of the ring increases constantly within the first 4 min, but then starts to increase slower until a constant intensity increase is found after 2 min. The (0,0) intensity shows a quasi-exponential increase over time.

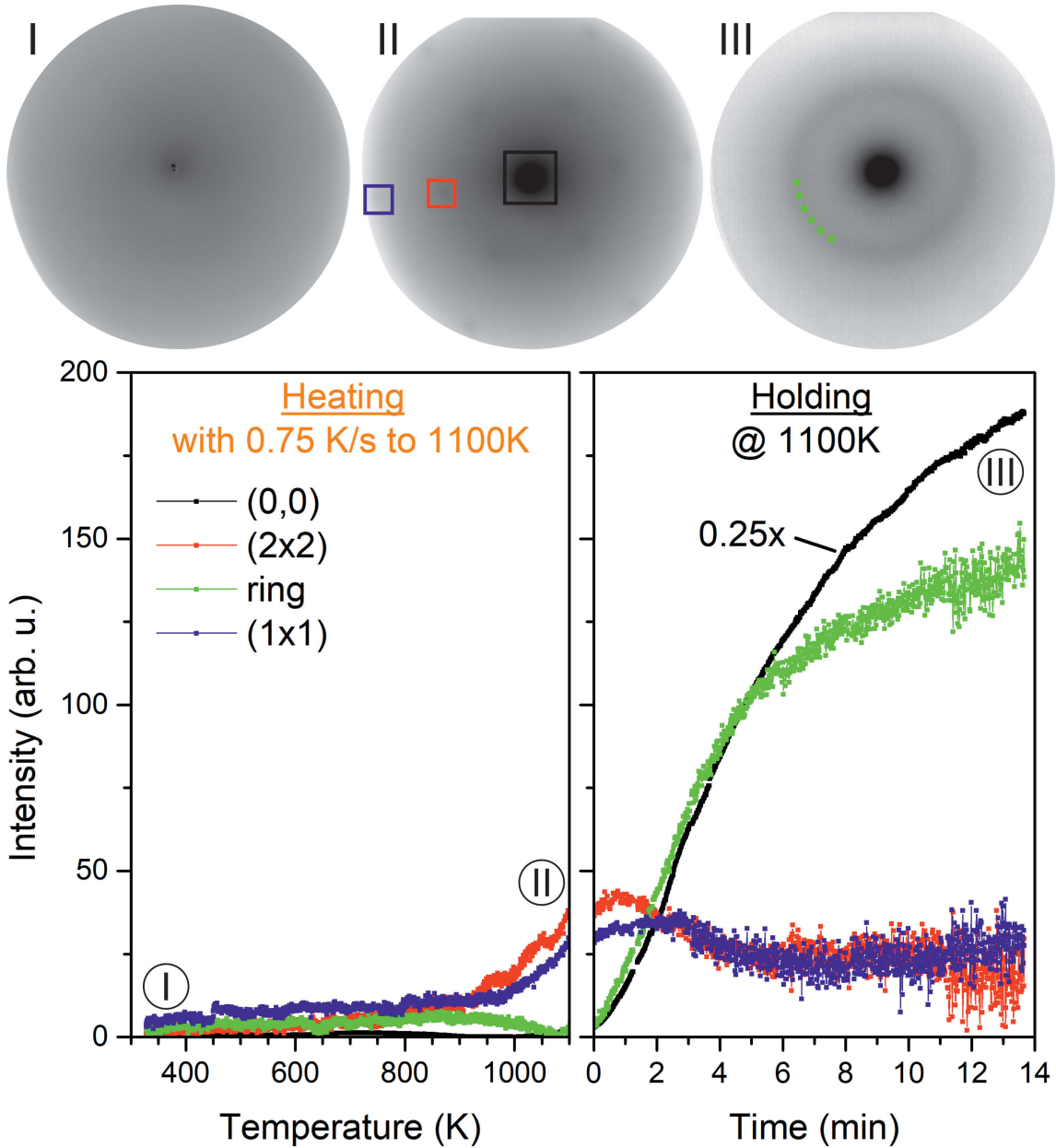


Figure 9.7: Analysis of LEED spots appearing while preparing the vitreous silica bilayer phase in oxygen at 1100 K. The upper part shows LEED images collected during the temperature treatment and the lower part the intensities of the individual LEED spots during heating and holding stages. An electron kinetic energy of 42 eV was used. (For more details see text)

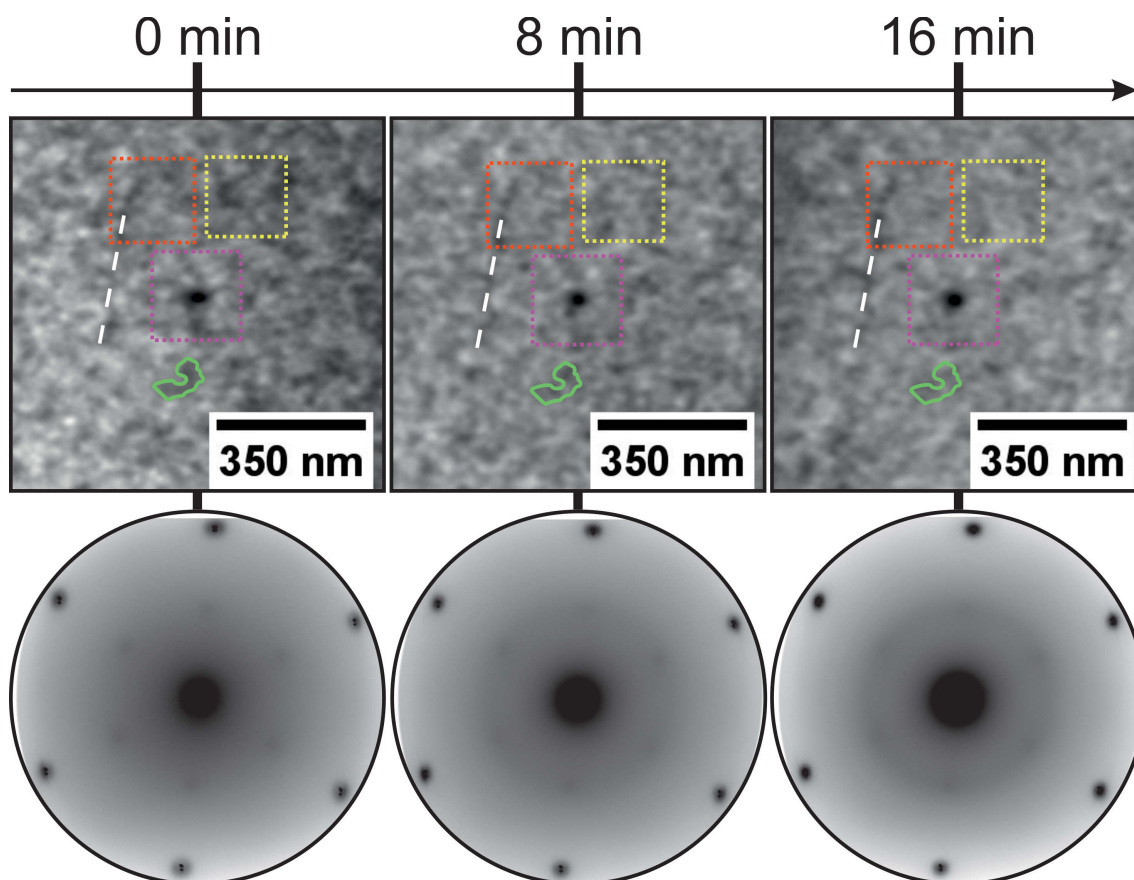


Figure 9.8: LEEM and LEED during the phase transition from crystalline p(2x2) to vitreous at 5.0×10^{-6} mbar. The time of the image is indicated in the upper part of the figure and the corresponding LEED images in the lower part. The white line marks a step bunch of the surface and the coloured boxes highlight the same areas for each image. For the LEEM images, an energy of 14.5 eV, and for the LEED images, an energy of 42 eV was used. (For details see text)

Figure 9.8 shows LEEM images taken during the transition of a crystalline p(2x2) bilayer to the vitreous one. The sample was held at 1075 K in an oxygen atmosphere of 5.0×10^{-6} mbar. At the beginning of the experiment the surface is covered with islands that appear bright in the image. They have a size distribution from 30 nm to 50 nm and are loosely connected with each other. A step bunch of the surface is indicated by a white line and a dark feature is found in the middle of the image. The LEED image shows a p(2x2) pattern indicating the crystalline bilayer phase. After 8 min of annealing the islands have the same size as in the beginning; however, they appear more connected as before. The LEED image shows a p(2x2) pattern and a faint ring feature. The third image shows the surface after 16 min. In comparison to the first images the surface appears more homogenous. Some features that existed already before the transformation are still visible (see for example the green or purple area) besides newly formed features (see for example the red or yellow area). The contrast of the step bunch (white line) increased possibly due to a slight change in

focus. In LEED the ring structure gained in intensity, while the intensity of the $p(2 \times 2)$ spots decreased.

Figure 9.9 shows LEEM and LEED images of a prepared vitreous silica bilayer. Bright islands with a size of 40-100 nm form a dense network (see image I) that is interrupted by dark lines following step bunches of the ruthenium surface (see image II). In the LEED image III an intense ring is visible at the position where the first order $p(2 \times 2)$ spots would appear for a crystalline bilayer in oxygen. A less intense, second order ring is visible at the (1×1) positions of ruthenium.

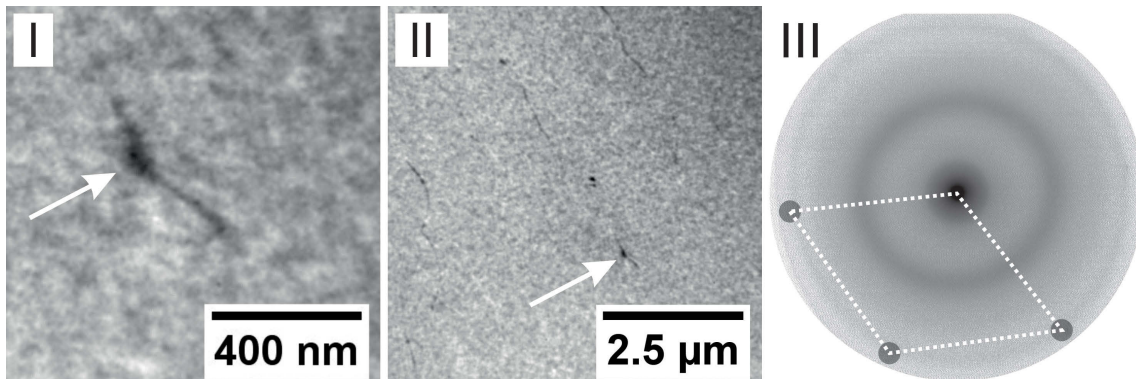


Figure 9.9: LEEM and LEED images at room temperature after the preparation of a vitreous silica bilayer in oxygen at 1150 K and holding for 30 minutes at this temperature. The white arrow indicates the same area in the different fields of view in I and II. In the LEED image III the (1×1) unit cell of ruthenium is indicated. For all images a kinetic energy of 42 eV was used.

Figure 9.10 shows the LEEM(IV) curve of a vitreous silica bilayer. The MEM to LEEM transition is at 3.43 eV and about 0.1 eV higher than the one for the crystalline silica bilayer in oxygen, close to the value of the 3O termination (3.41 eV). The LEEM(IV) curve has at least 6 maxima between a kinetic energy of 4 to 28 eV of the electrons, 4 deep minima occur at 4, 6, 16 and 28 eV. Only for kinetic energies below 10 eV similar features appear in comparison to the crystalline $p(2 \times 2)$ silica bilayer in oxygen and the Xmas star BL phase in UHV.

A DF-LEEM(IV) was done to study the nature of the dark features found in the LEEM images (see figure 9.9). The results of the analysis are shown in figure 9.11. Five different positions on the ring in reciprocal space were used, indicated in the LEED image. One dark feature and its change in intensity depending on the ring position is shown in the DF-LEEM images I-III, A and B, all taken at 13.5 eV. In image I two areas, a very bright and a dark one, can be distinguished in the dark structure at this energy. The contrast of the bright and dark areas changes depending on the selected position on the ring in reciprocal space. There is no contrast change between the images A and B. However, a strong change is seen in

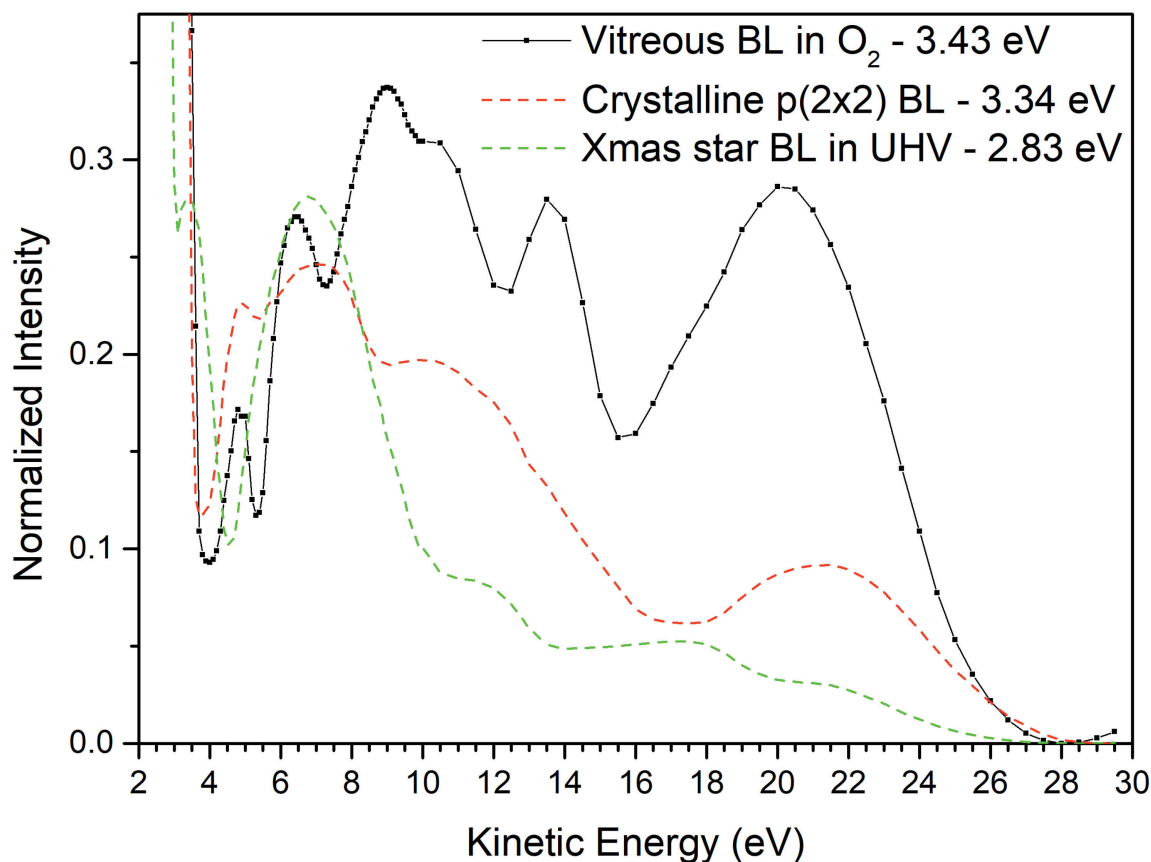


Figure 9.10: LEEM(IV) measurement of a vitreous silica bilayer at room temperature. For comparison, the LEEM(IV) curves of the crystalline p(2x2) silica bilayer in oxygen and of the Xmas star BL phase in UHV are shown. The energies for the MEM to LEEM transitions are given in the inset.

the images II and III. The contrast of the bright areas is inverted from image I to image II, and in image III new areas appear bright within the structure.

DF-LEEM(IV) measurements have been made for different areas, as indicated in image I and presented in the lower part of the figure. The black curve represents the black box in image I, the blue and the green curves represent the blue and green boxes. The LEEM(IV) curves of the crystalline p(2x2) layer and of the 2O termination are shown for comparison. The DF-LEEM(IV) curve of the vitreous silica is unique and has no resemblance to the others. However, the DF-LEEM(IV) curves of the blue and green areas resemble very well the 2O terminated ruthenium surface. With these results, it can be concluded that the dark features are holes in the vitreous silica bilayer going down to the ruthenium surface, which has a 2O termination. The existence of holes has been proven by XPEEM measurements in a publication connected to this work, see [141].

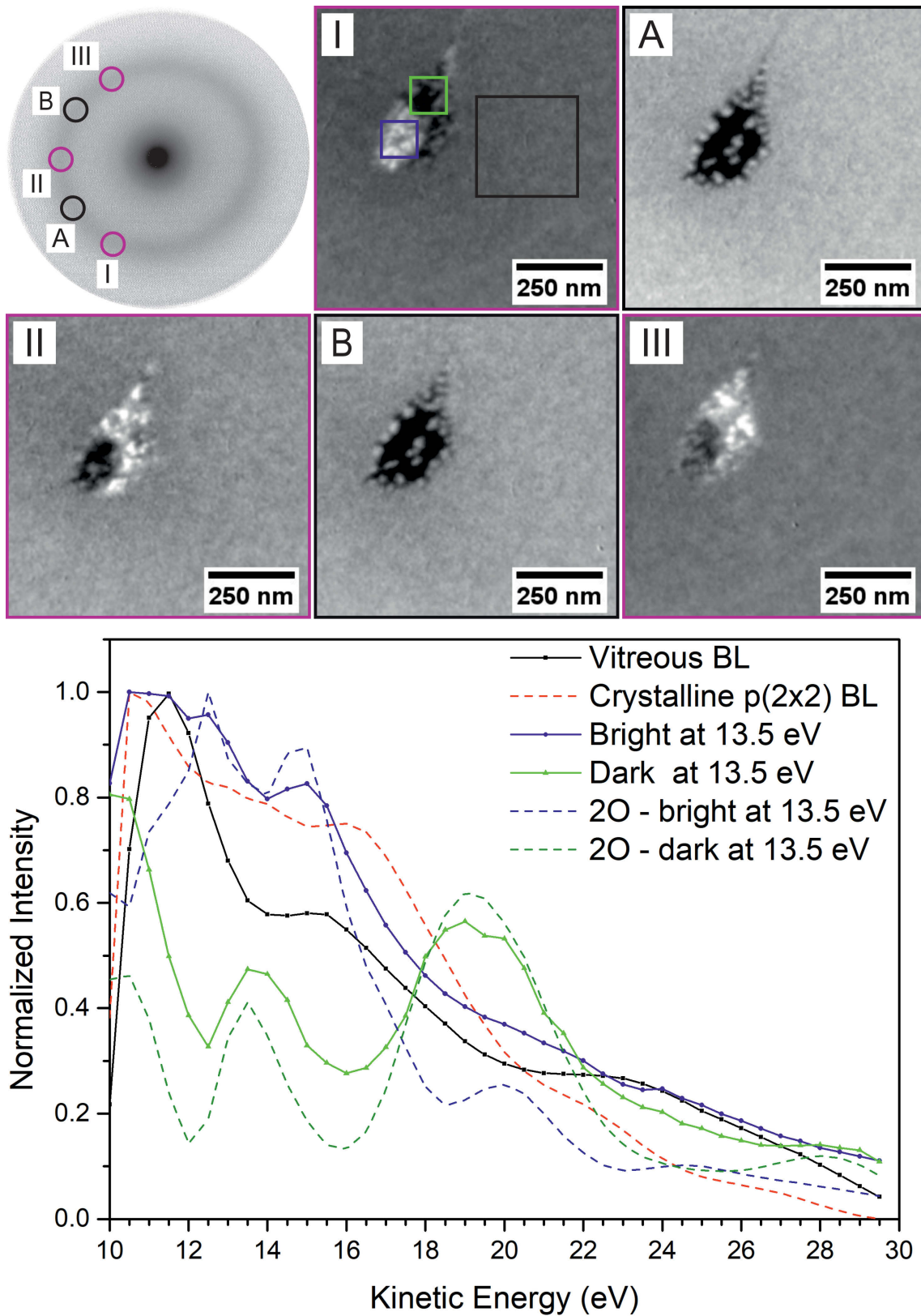


Figure 9.11: DF-LEEM and DF-LEEM(IV) curves taken at different positions of the ring in LEED. The positions in reciprocal space are indicated in the LEED image, the areas used for the DF-LEEM(IV) curves are shown in DF-LEEM image I. For the LEED image, a kinetic energy of 23 eV and for the DF image series 13.5 eV have been used. (For details see text)

For a better understanding of the structure of the holes in the silica layer, an additional dark field study has been made of the film shown in figure 9.11. In this case the reciprocal space along the ring was probed in DF-LEEM. The small inset in the plot in figure 9.12 illustrates this. For a constant kinetic electron energy, the position on the ring was changed, covering 180° of the whole ring with measurement points. The results are presented in figure 9.12. In the upper part, a bright field and dark field image series are shown. In the bright field image (0,0) a dark feature within the vitreous silica layer is visible; it is a hole that has a bright structure in itself. The dark field images I-V show the same area as before and their position on the ring is indicated in the plot and its inset. The plot shows the intensity over angle on the ring. The first point of the measurement is defined as 0° and the other points are plotted relative to it. Image I is a dark field image at this measurement point. It shows small bright structures at the rim of the hole, which appear again in image IV. In the images III and V the area inside the hole appears bright. Overall, three structures depending on the measurement position in reciprocal space are found in the dark field series: the vitreous silica bilayer around the hole, some structures at the rim of the hole, and a bright area inside of the hole. Image I indicates areas of interest for these structures, which were used in the plot of intensity versus angular position of the ring. The silica layer shows only a small change in intensity during the measurement. However, the plot reveals that the two structures appear alternately every 30° when probing the reciprocal space. It is possible to connect angular positions of the ring to spot positions in reciprocal space, because of the results in figure 9.11 where it was shown that the bright areas in the hole belong to an oxygen termination. The positions of $\{0,1/2\}$ spots are given below the angular x-scale. In this way, it is concluded that the structures at the rim of the hole belong to a rotated silica layer.

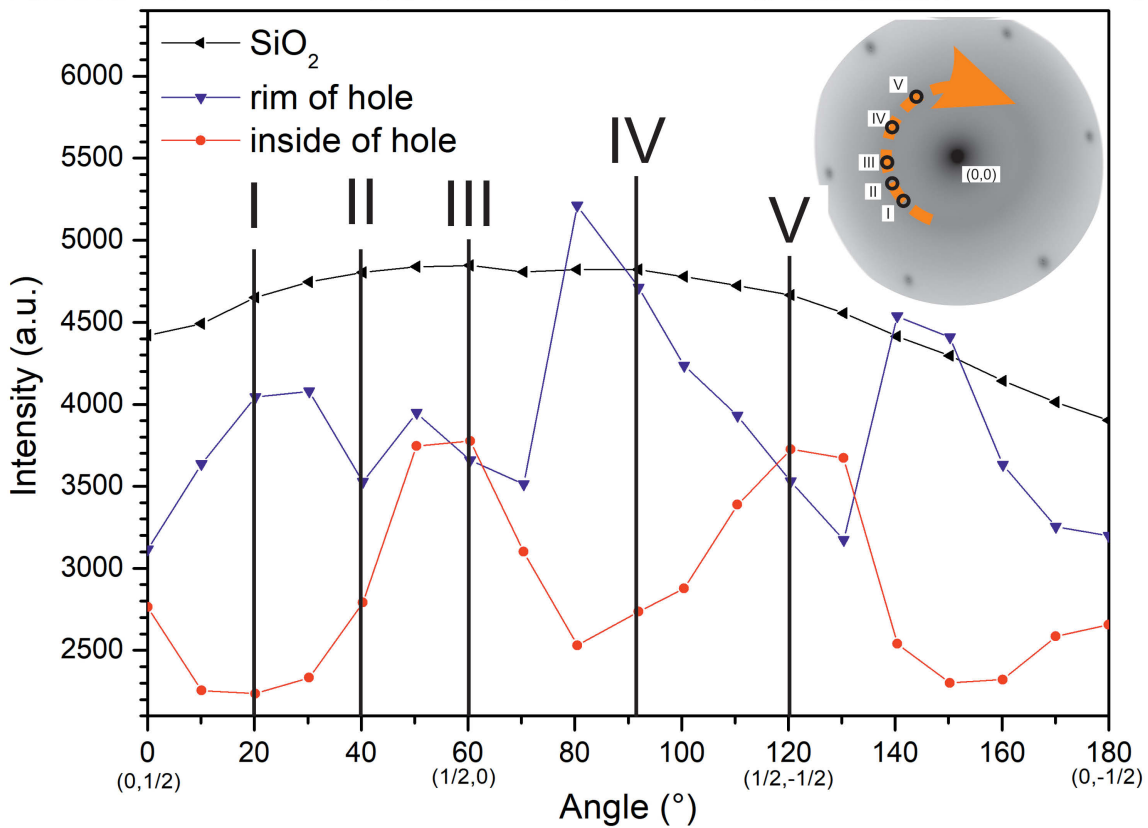
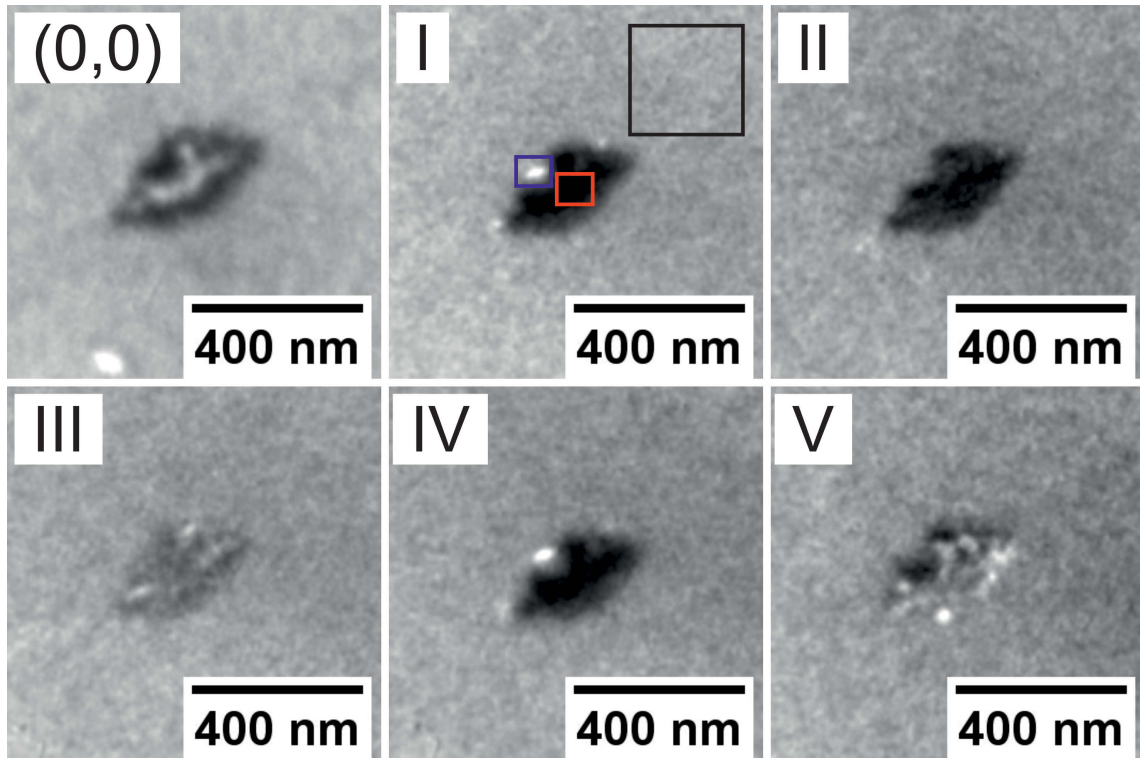


Figure 9.12: DF-probing of the ring in reciprocal space. The $(0,0)$ image shows a feature within the silica layer in bright field and images I-IV show the same area in dark field. The boxes in image I represent the areas used for the plot of intensity versus angle around the ring, as indicated in the inset. (For details see text)

Figure 9.13 shows the results of a LEED (iV) measurement of a vitreous bilayer at room temperature. In the upper part of the figure three LEED images for different kinetic energies are shown. They emphasize the intensity dependence of the structures in reciprocal space on the electron kinetic energy. The areas used for the plots a) are shown in image II. a) shows the intensity of the used areas as function of kinetic energy. b) is a cut through the reciprocal space along a fixed direction showing the intensity dependence on energy for a fixed cross section. It is composed of line cross-sections through the LEED images. c) plots the kinetic energies of the intensity maxima of selected spots in connection to parabolas found in the cross section.

All three LEED images show the (0,0) spot, the (2x2) and the (1x1) spots, and a first order (at the (2x2) position) and second order (at the (1x1) position) ring feature. All spots exhibit a distinct intensity versus kinetic energy dependence, and a closer look reveals that it seems that the radius of the second order ring structure changes with kinetic energy. In the cross-sections the maxima in intensity are also found. However, the background intensity between the structures reveals clearly a dependence on energy: parabolas around the (0,0) spot are found. They are highlighted by dashed lines in the plot b) and they account for the intensity behaviour of the second order ring observed in the LEED images I-III.

Figure 9.13 (facing page): LEED(IV) measurement of a vitreous silica bilayer at room temperature. The LEED images I-III show the LEED pattern for different energies. In image II the measurement areas of the intensity vs. kinetic energy plot in a) are shown. Plot b) shows a cut through the energy space for a fixed cross section indicated in LEED image III. c) emphasizes maxima connected to the parabolas found in the cross section. (For details see text)

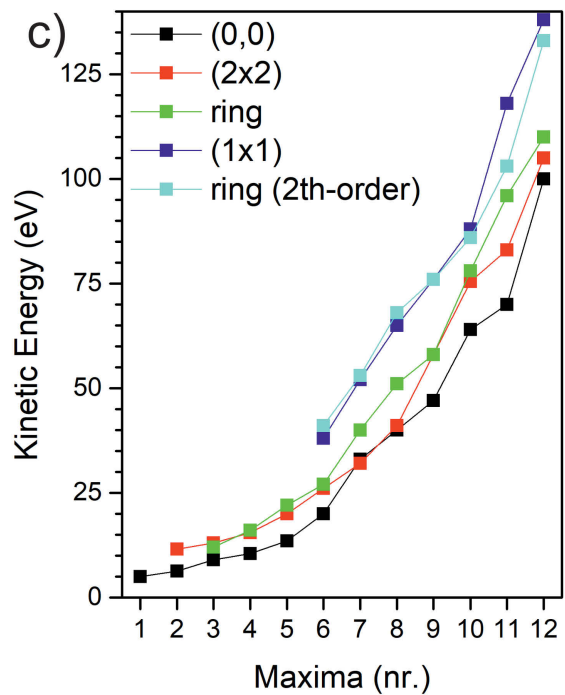
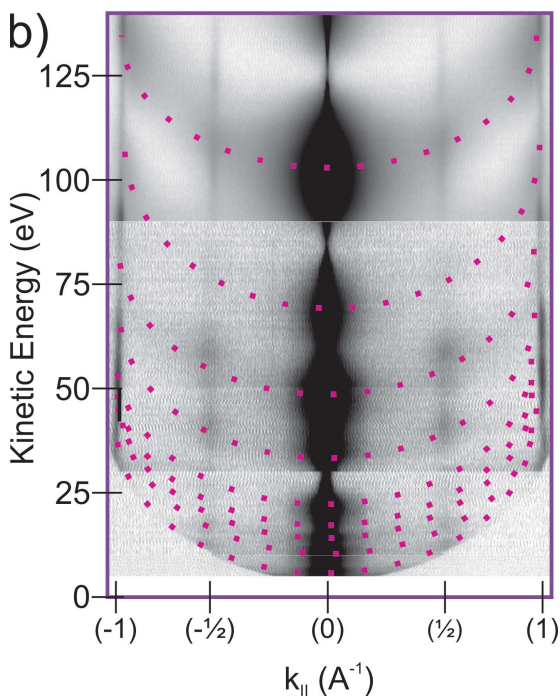
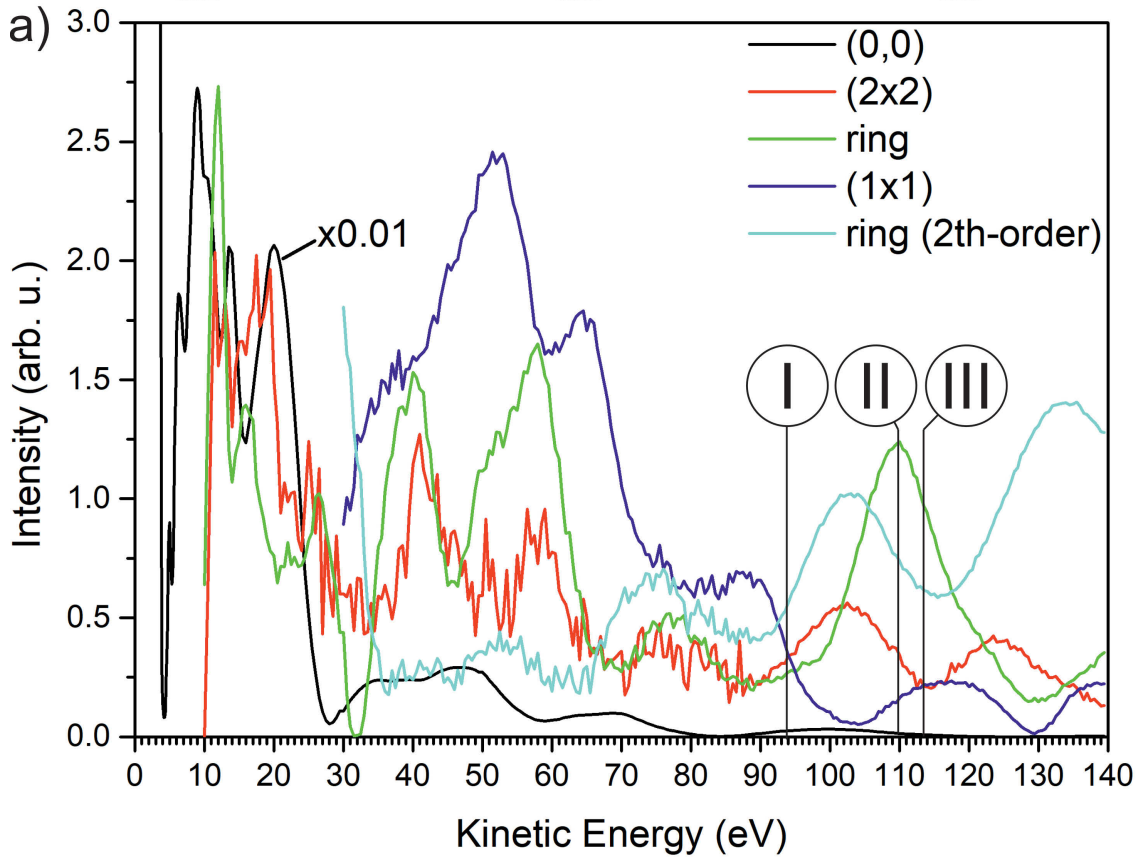
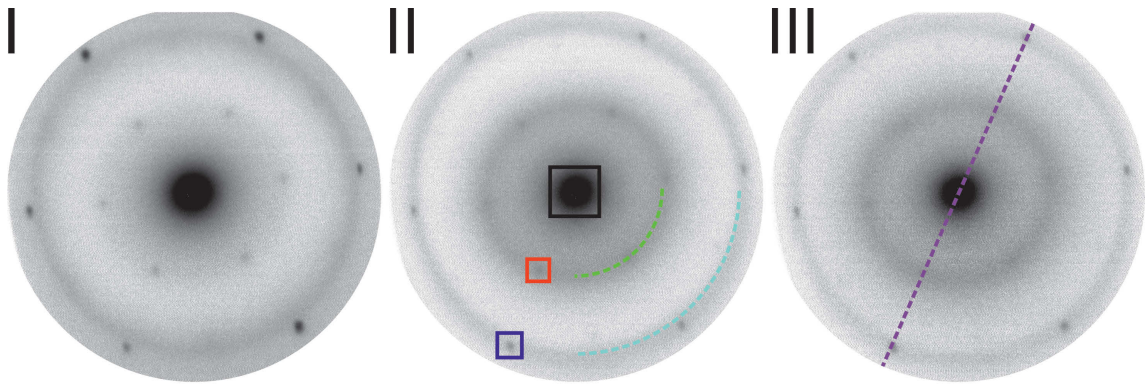


Figure 9.14 shows the results of an XPS measurement of a vitreous bilayer prepared in oxygen. The Si 2p line in a) shows no traces of silicon less oxidized than 4+. It is narrower and slightly shifted (about 0.1 eV to 102.4 eV) to lower binding energies than the crystalline p(2x2) bilayer in oxygen. The Ru 3d_{5/2} in b) is much broader than the line for the crystalline p(2x2) bilayer in oxygen and resembles very well the 4O termination of oxygen on ruthenium. The O 1s line has a broad maximum at 529.9 eV, and its shape is in good agreement with that of the crystalline p(2x2) bilayer in oxygen. It has a shoulder at the lower binding energy side, with a higher intensity than the crystalline p(2x2) bilayer in oxygen.

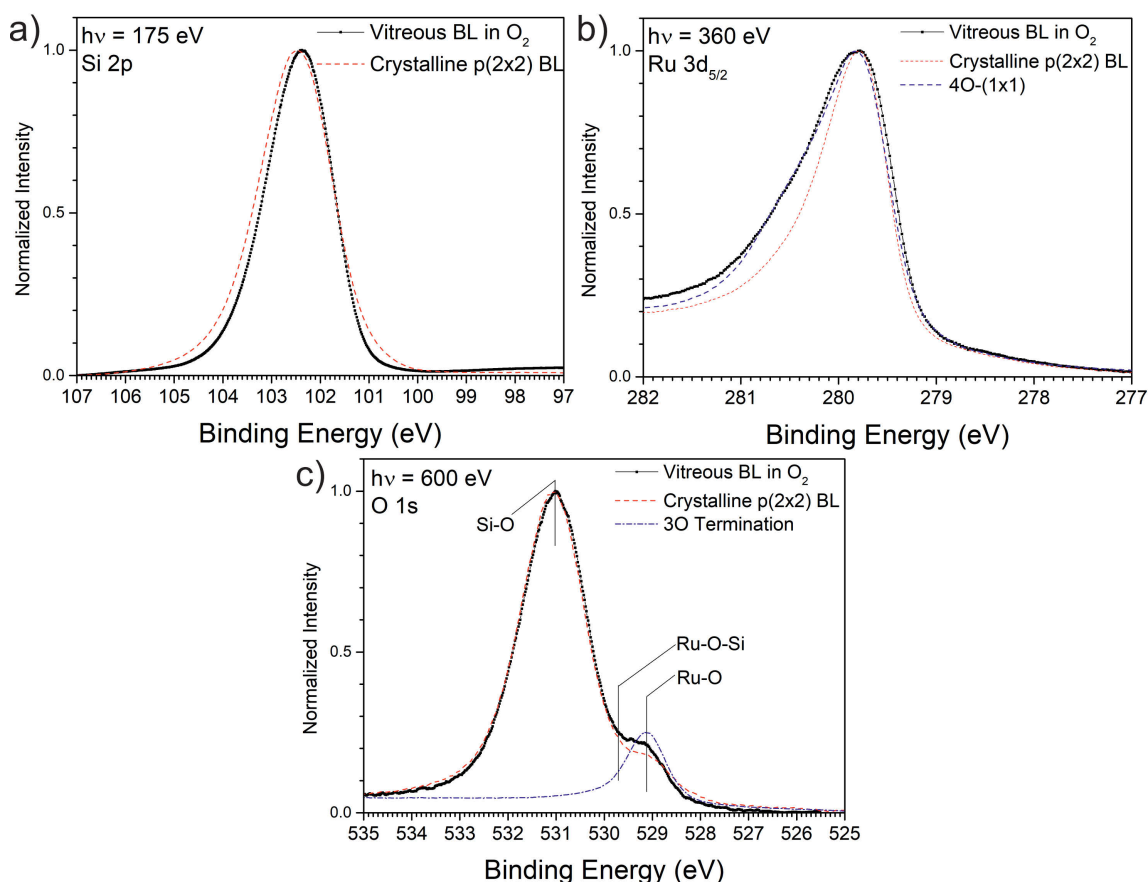


Figure 9.14: XPS spectra at room temperature of the Si 2p in a), Ru 3d_{5/2} in b) and O 1s line in c) of a vitreous silica bilayer prepared in oxygen atmosphere. (For details see text)

Additional to the preparation in oxygen, it is possible to prepare the vitreous BL-phase also in UHV. For this an intermediate preparation step was necessary: First the crystalline p(2x2) BL-phase had to be prepared as described in section 9.1 and subsequently this was annealed in UHV. The transition occurred at lower temperatures than in oxygen (see section 9.5 and figure 9.17). In figure 9.15 the XPS spectra for this preparation are shown in comparison with the corresponding spectra of vitreous BL prepared in oxygen. Clearly, both, the Si-O component of the

Si 2p and the O 1s lines are shifted by 0.8 eV to higher binding energies (102.9 eV and 532.0 eV), while the Ru 3d_{5/2} peak is not changed in position but in shape, indicating a lower oxygen concentration at the ruthenium-interface comparable to an 1O termination. This is supported by the much lower Ru-O component of the O 1s line that additionally shows a small amount of Si-O-Ru bonds.

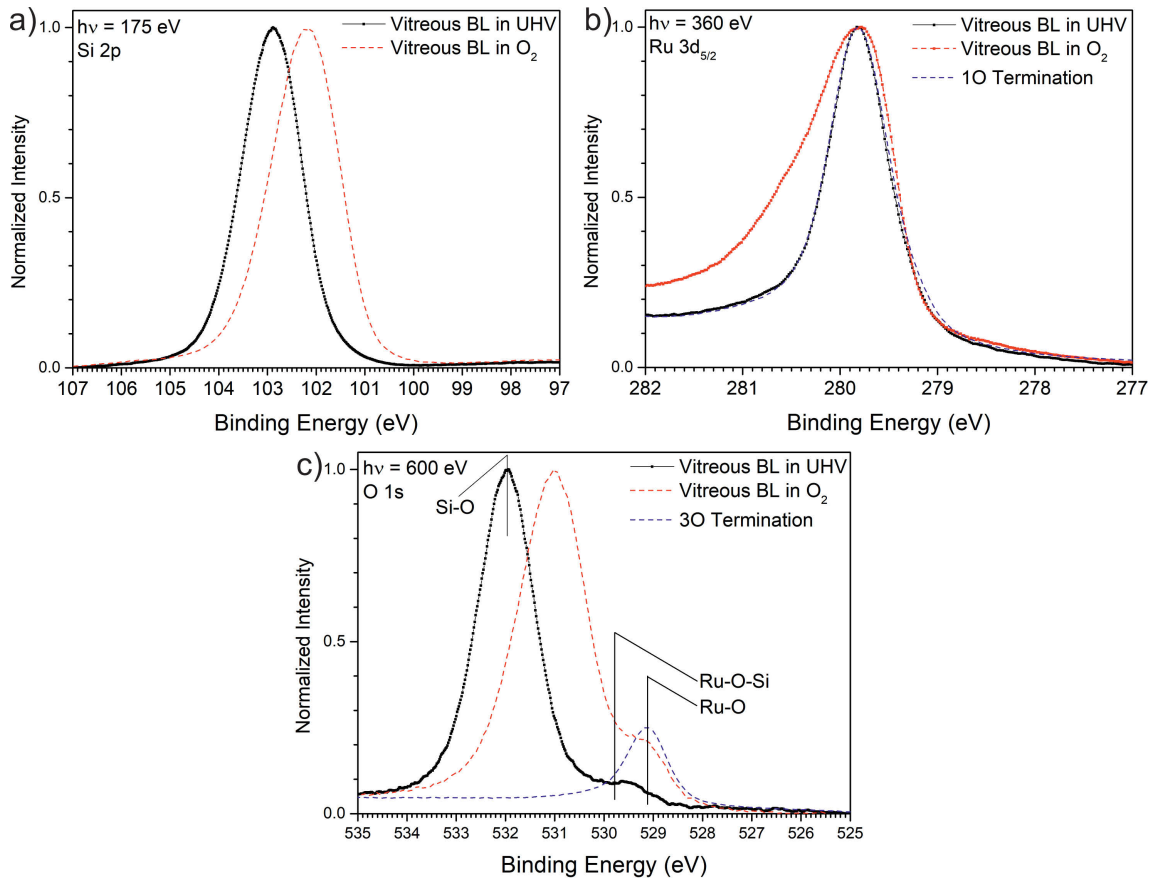


Figure 9.15: XPS spectra at room temperature of the Si 2p in a), Ru 3d_{5/2} in b) and O 1s line in c) of a vitreous silica bilayer prepared in UHV. (For details see text)

9.5 Interpretation: Formation, morphology and chemical state of the vitreous BL-phase

As described in the previous text the annealing of the bilayer in oxygen at temperatures above 1100 K transforms it from a crystalline to a vitreous phase. During the temperature holding stage a continuous transition over time is found (see figure 9.7). All crystalline islands transform uniformly on the entire surface; no transition front moving across the sample or special areas are observed within the lateral resolution of around 10 nm used in the experiments. The LEEM series of the transition (see

figure 9.8) does not reveal whether the transition starts at the border or within the islands. Also no effects from surface areas like step bunches or holes are found. However, the islands start to grow together and the step bunches of the underlying ruthenium show an increased contrast (see figure 9.9). A maximum of the stress in the bilayer, induced by the height step of a step bunch, could lead to the formation of cracks within the bilayer and to the observed enhanced contrast of the step bunches. It is not possible to conclude if the cracks are only in the topmost or in second layer, or extend through the entire bilayer. In image I of figure 9.9 a dark feature is found in the middle of a crack looking like a hole down to the substrate. These hole features are found at several places of the film. A closer investigation reveals that these holes indeed reach down to the ruthenium surface and that there is a $2O$ termination at the bottom (see figure 9.11). The rim of the holes consist partly of a 30° rotated structure that could be a rotated bilayer or a rotated monolayer (see figure 9.12). The existence of a rotated silica bilayer structure was already shown for the Fe-Si-O and the silica bilayer system on Ru(0001) in [125, 142, 143], and the rotated ML has been described in chapter 6 of this work.

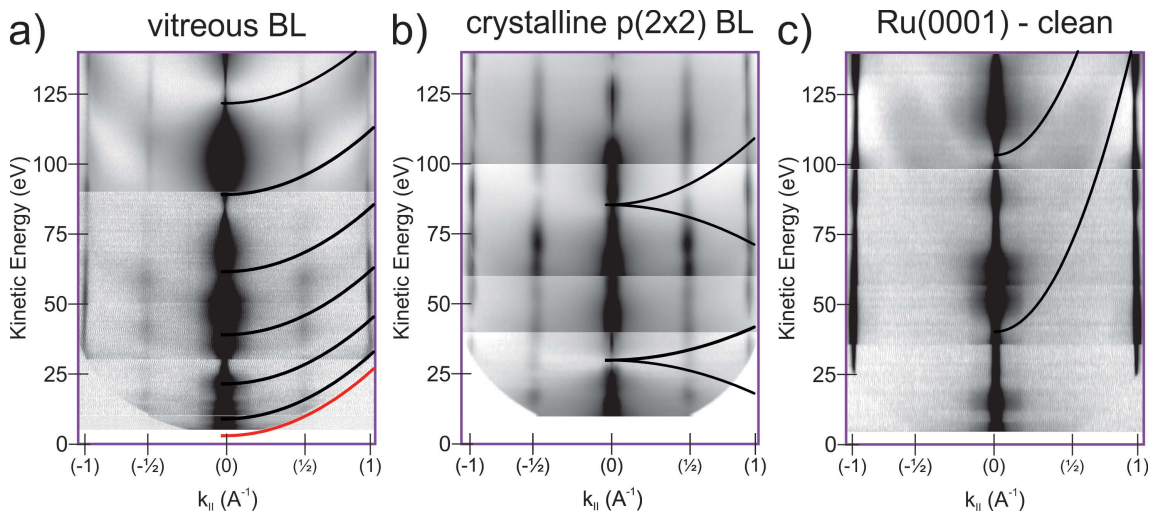


Figure 9.16: Cross sections of the LEED(IV) measurements of the vitreous BL-phase in a), the crystalline $p(2 \times 2)$ BL phase and of clean Ru(0001). The results of the fit of the electronic structure are superimposed on the right side in the cross-sections. (For details see text)

The LEEM(IV) shows many intensity features and is clearly distinguishable from the crystalline bilayer in oxygen (see figure 9.10).

The energy dependent reflectivity behaviour of figure 9.13 might be explained by electronic states. In case the incoming electron finds an electronic state in the sample surface with matching k -vector and energy, then the electron has a higher probability to penetrate into the sample, hence the reflectivity is reduced (bright areas in the cross sections). In contrast, if the incoming electron does not find a matching

state, then the probability of penetration is reduced and therefore the reflectivity is increased (dark areas in the cross sections). With other words, the maxima and minima in the reflectivity curve might correspond to low and high density of states – additional to the interference effects due to the crystalline structure. Additional to the strong modulations in intensity of the LEED spots, the diffuse background shows as well a structure. This might be due to the scattering process in the silica/Ru system, where the reflection is affected by the probability for the electrons to find a suitable state. Therefore, the band structure of unoccupied states (above the vacuum level) might be visualized by the intensity modulation of the LEED background. Because, all LEED measurements are energy filtered ($\delta E = 0.5$ eV), only elastically backscattered electrons are observed and the modulations cannot be explained by simple energy loss processes.

A well-known example for quantized electronic state is the quantum well with infinite barriers and a width of L . Defining the parameter $G_{\perp} = 2\pi/L$, the quantized energies of this quantum well show a parabolic behaviour, whereas m is the electron mass and n the quantum number:

$$E_n = \frac{\hbar^2}{8m} G_{\perp}^2 n^2 \quad (9.1)$$

Expanding this one-dimensional model to three dimensions, whereas only one direction is confined (in the silica/Ru(0001) case this is normal to the surface), but the other two directions are free of barriers (this means along the surface), yields in a combination of quantum well states and free electron behaviour:

$$E_n = \frac{\hbar^2}{2m} \left(\left(\frac{G_{\perp}}{2} \right)^2 n^2 + k_{\parallel}^2 \right) + E_0 \quad (9.2)$$

The wave vector k_{\parallel} is given parallel to the sample surface and E_0 is the potential of the bottom of the quantum well, referred to a reference energy level (like Fermi level or vacuum level).

In figure 9.16 a), the experimental data are fitted with the formula, using $G_{\perp} = 1.62 \text{ \AA}^{-1}$, corresponding to $L = 3.9 \text{ \AA}$ and $E_0 = -1$ eV, meaning that the bottom of the quantum well is 4.5 eV below the vacuum level which is at +3.5 eV in our experimental setup. The values of the wave vector is calibrated by the position of the (10) Ru spot, which is at $G_{\text{Ru}} = 2\pi/a_{\text{Ru}} = 2.32 \text{ \AA}^{-1}$ with $a_{\text{Ru}} = 2.706 \text{ \AA}$.

For comparison the corresponding LEED(IV) cross section analysis for the crystalline p(2x2) BL phase (figure 9.16 b)) and the clean Ru(0001) (figure 9.16 c)) is shown.

Here parabolic structures are added as a help for the eyes. Especially the Ru crystal shows clear and sharp parabolic structures. The fitting curve is:

$$E_n = \frac{\hbar^2}{2m} \frac{m}{m_{eff}} k_{\parallel}^2 + E_0 \quad (9.3)$$

The curvature of the parabolas is five times larger than expected for the free electron (i.e. in figure 9.16 a)), meaning a 5 times smaller effective mass ($m/m_{eff} = 5$). The offset energies are 100 eV and 37 eV above the vacuum level. For the crystalline BL (figure 9.16 b)) four parabolas might be identified. The two top structures can be fitted with ($m/m_{eff} = 1$) and -0.6 with and offset energy of $E_0 = 86$ eV and the two bottom curves with ($m/m_{eff} = 0.5$) and -0.5 and $E_0 = 30$ eV. Obviously, these states of the crystalline silica and pure Ru(0001) cannot be described by free electron behaviour or one dimensional quantum wells.

Summarizing it can be stated, that the experimental data exhibits a clear difference in the reflectivity between the vitreous and the crystalline BL. The modulation in the background of the LEED might be described by the effect of (unoccupied) electronic states on the reflectivity, visualizing the dispersion of these states.

Furthermore, the transformation has been investigated in more detail and it is found that its transition time depends on temperature and oxygen pressure. Moreover, it has been shown that the transition itself occurs independently on the oxygen pressure (see figure 9.17). Two scenarios are given in figure 9.17, first in b) the transition under 5.0×10^{-6} mbar oxygen and second in c) the transition in UHV with a background pressure lower than 5.0×10^{-9} mbar. For the UHV experiments, as an intermediate step, the crystalline p(2x2) phase was produced in oxygen before, then was held at 775 K until the background pressure dropped below 5.0×10^{-9} mbar, and finally was annealed again. To determine the time constant of the transition an exponential fit of the intensity of the (0,0) spot over time was used; an example is shown in a) and the results of measurements at different holding temperatures are given in the insets of the graphs b) and c). The calculated time constants were plotted in an Arrhenius diagram in d) to determine the activation energy of the transformation.

For both scenarios (transformation in oxygen or UHV) a value of about 4.2 eV is found. This value fits very well to the value for the defect formation energy of the Stone-Wales-defect in a hexagonal silica bilayer given in [144], where a theoretical approach by using classical force field calculations was applied. Originally, the Stone-Wales defect was a theoretical approach to predict the formation of isomers

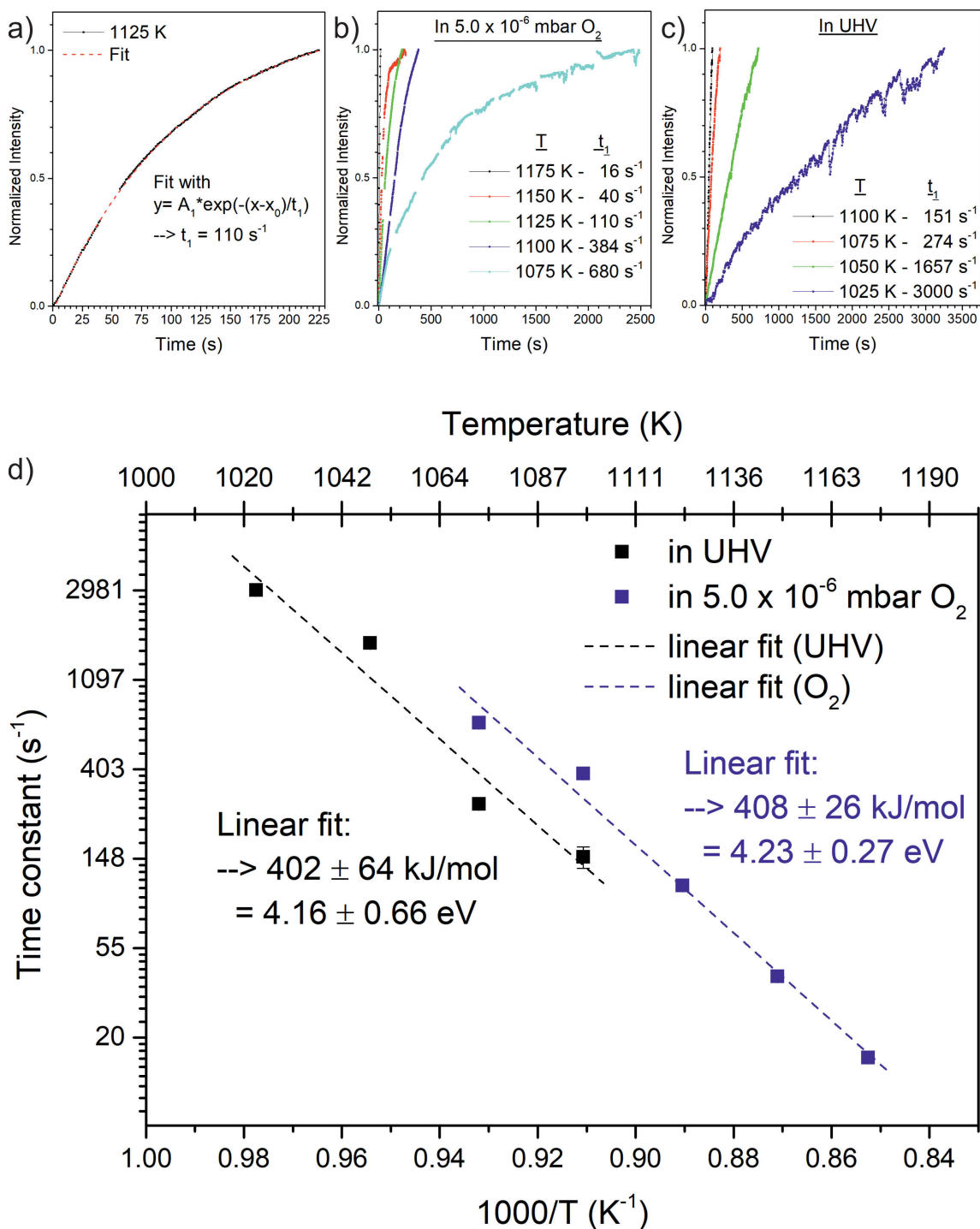


Figure 9.17: Transition from crystalline $p(2 \times 2)$ to vitreous on structure depending on temperature and oxygen background pressure – analysis of the recorded LEED pattern. a) shows as an example the intensity change of the $(0,0)$ spot during the transition in LEED at $5.0 \times 10^{-9} \text{ mbar}$ oxygen atmosphere at 1125 K. An exponential fit function was used to determine a time constant for the transition. b) and c) show the results of experiments done at different temperatures with or without oxygen background atmosphere. The determined time constants for each transition are given in the insets. d) is an Arrhenius-plot of the time constant. For both experimental conditions, a linear fit was done to determine the activation energy. (for details see text)

of C60 molecules [145]. Later it has been found experimentally in 2D systems like graphene as well [146,147]. In a hexagonal system (6-member rings) it consists of two 5-member and two 7-member rings (55-77). This structure is achieved by rotating two neighbouring nodes by 90° around their midpoints (see figure 6.1). In the case of the silica bilayer it is the rotation of four silica tetrahedra (two in each layer) would lead to the transformation. This observation is supported by earlier noncontact-AFM studies done in our department, where in the vitreous silica bilayer mainly 6-, 5- and 7-member rings have been found [8,123]. However, smaller amounts of 4-, 8- and 9-member rings have also been found; their origin could be ascribed to the fusion of multiple Stone-Wales defects, or to the rotation of multiple silica tetrahedra double units close to each other (for example to generate the “flower” defect, see [144]). However, another possibility could be the desorption of silica tetrahedra units and the rearrangement of the layer due to this. The latter is supported by the fact that after prolonged or high temperature annealing (>1175 K) mesoscopic holes in the silica bilayer are found (see the LEEM image series in 9.20). The homogeneous transition from crystalline to vitreous found in LEED implies the existence of a transition state, where the crystalline and the vitreous phases co-exist. From a statistical point of view, Stone-Wales defects can appear anywhere in a perfect crystalline p(2x2) silica bilayer film. However, in reality the film on the Ru(0001) surface has rotated domains, antiphase boundaries, and defects like Dauphiné twin boundaries [125]. Moreover, the Ru(0001) surface has atomic steps and step bunches, where the film is stressed. The stress induced by these defects on the covalent bonds within the silica bilayer and the surface morphology may influence the occurrence of the Stone-Wales process and other types of defects during annealing. This is supported by STM findings of crystalline and amorphous phases next to each other with a transition zone of about 1.6 – 2.4 nm [13,125]. Consequently, the transformation of the film will most likely start in these regions, as found in the LEEM measurements earlier, the crystalline p(2x2) silica bilayer film consists of small 20-35 nm large islands (see figure 9.4). The boundaries of these islands are possible candidates for the beginning of the transformation. Their size close to the resolution limit of the microscope is a possible explanation, why the transition followed in LEEM looks homogeneous. A possible scenario could be the following: Areas which are already defect rich transform to a vitreous state and enclose crystalline areas, -in which they grow. At the same time Stone-Wales defects occur in larger crystalline islands and maybe diffuse together or towards the phase boundaries. The interface of the crystalline and the vitreous silica bilayer phases consists mainly of 5- and 7-member rings supporting this scenario [13,125]. The

large amount of boundaries due to the small islands explains the high slope of the intensity of the (0,0) spot and the p(2x2) at the beginning of the transformation.

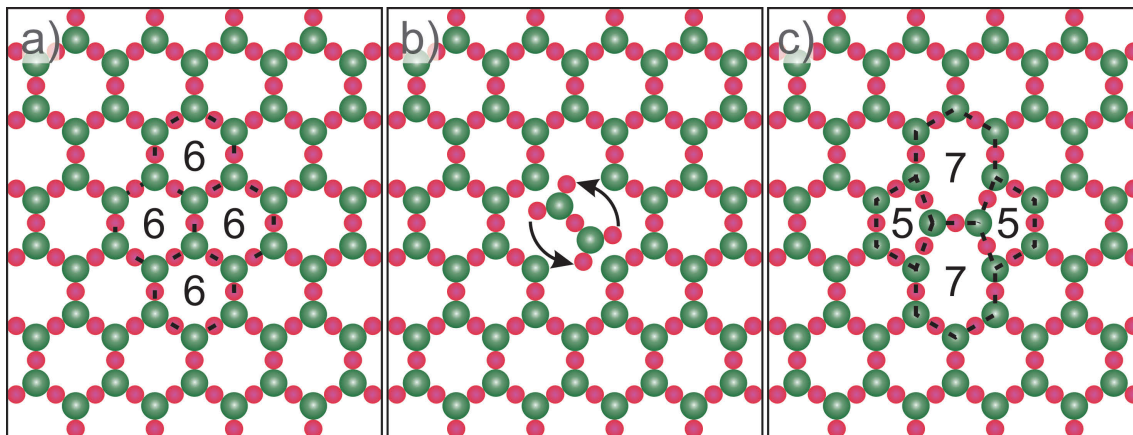


Figure 9.18: Illustration of the Stone-Wales defect (55-77) and its origin. In a) a perfect crystalline silica film is shown, which consists only of 6-member rings, b) shows the rotation of silica tetrahedra units and c) the Stone-Wales defect with two 5- and two 7-member rings. The silicon atoms are shown as green spheres, the oxygen atoms are red spheres. b) shows only the principle of the transformation (final rotation by 30°), it is not known if this transition state exists. The film with the Stone-Wales defect in c) is shown without any relaxation.

9.6 Controlling the oxygen amount at the Ru(0001)-surface by thermal annealing or oxygen intercalation

Studies done in the department show that it is possible to decrease the oxygen amount beneath a vitreous silica bilayer film [10, 18, 20], and to intercalate oxygen again or CO, for example. The silica bilayer appears to act as a mesh or molecular sieve above the ruthenium surface and may open the possibility to probe chemical reactions in the confined space between ruthenium and the silica bilayer sheet. The temperature dependence in the range of 1030 K to 1150 K for the desorption of oxygen in UHV from the silica-covered ruthenium surface has been investigated in detail by XPS in [10]. In that paper, it has also been shown that it is possible to intercalate oxygen and adsorb it on the ruthenium surface by annealing with 2.0×10^{-6} mbar oxygen at 1140 K for 10 min. The Si 2p and Si-O components in the O 1s line show a dependency of the adsorbed oxygen at the ruthenium interface. For decreasing oxygen content at the interface, both core level lines shift to higher binding energies (max. 0.8 eV). Through re-oxidation the lines shift back to their initial position. In [148] the thermal desorption of oxygen was investigated by XPS in more detail again in the range of 900 K to 1200 K (however, no annealing times are

given) and the re-oxidation was done at 820 K in 2.0×10^{-4} mbar oxygen. Similar shifts for the binding energies of the Si 2p and of the Si-O peak in the O 1s line and of the work function were found, too [10]. Both papers explain the found binding energy and work function shifts, using theoretical calculations, by a dipole, induced by electron transfer from ruthenium to the oxygen atoms at the interface; the strength of the dipole should depend on the oxygen amount adsorbed on ruthenium below the silica bilayer. The experiments done so far describe the desorption and intercalation of oxygen only as a function of temperature, with the time dependency not yet being investigated.

In this work controlling the oxygen amount at the ruthenium interface by UHV annealing and exposure to oxygen was studied as well. In contrast to the described publications, the time dependence for a fixed annealing temperature and the intercalation at lower temperature was probed. Figure 9.19 shows the XPS results of these experiments. After annealing the silica bilayer at 1125 K for 1h in UHV, the Si 2p line is shifted about 0.7 eV to higher binding energies (103.1 eV, figure 9.19 a)). The ruthenium line shape resembles quite well the shape found for the 1O termination figure 9.19 b). The Si-O peak in the O 1s line is shifted about 0.6 eV also to higher binding energies and the (not shifted) Ru-O component in the O 1s line is weakly visible. Prolonged annealing for 1.7 h at 1125 K shifts the Si-O peak even further by about 0.8 eV and the Ru-O peak is slightly further decreased. The energy shifts are comparable to the ones found in [10, 148]. A small remaining intensity is found at about 530 eV in the O 1s line, maybe connected to Ru-O-Si bindings on the surface. They could have already been present after the preparation of the vitreous phase, or occurred during the annealing. The films annealed for 1.7 h in UHV were then exposed to oxygen at 375 K. In figure 9.19 d) the results of an in-situ XPS measurement of the O 1s line are shown as a function of oxygen dosing. The image stack illustrates the shift of the Si-O component of O 1s line in dependency of the intercalated oxygen amount. First, the oxygen pressure was increased to 1.0×10^{-7} mbar and then kept constant over time. While increasing the oxygen pressure no change in the Si-O component position is found, however when 1.0×10^{-7} mbar is reached it starts to shift linearly with time by about 0.5 eV to lower binding energies until about 50 L are reached, then no shift occurs anymore. The intensity of the Ru-O component starts to increase earlier, when 2.0×10^{-8} mbar are reached and a linear intensity increase for the whole experiment is found. The change of the O 1s line before and after the first intercalation experiment is shown in graph c). The Si-O component shifted to lower binding energies and the Ru-O component reoccurred.

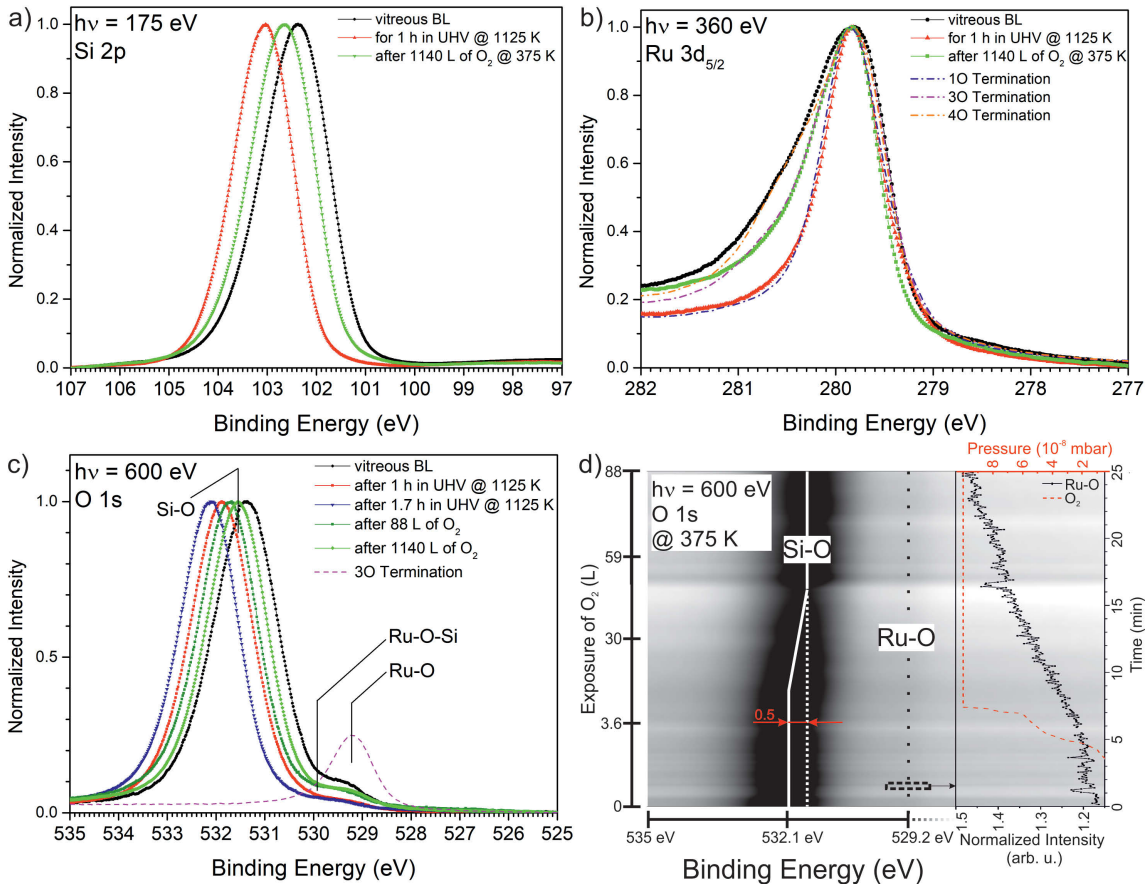


Figure 9.19: XPS spectra of the vitreous silica bilayer after UHV annealings and subsequent oxygen exposures of the Si 2p in a), the Ru 3d_{5/2} in b) and the O 1s line in c). The experimental conditions are given in the insets. In d) the region of O 1s line was measured in-situ and in real time during an oxygen exposure up to 1.0×10^{-7} mbar at 375 K. The cross section of the O 1s line is shown as image stack with an inverted grey scale over time. The dose of oxygen is the left y axis (scaling not linear at the beginning, but becomes linear after about 4 L) and the inset shows the pressure and the intensity of the Ru-O line over time. (For details see text).

The oxygen pressure was then increased to 5.0×10^{-6} mbar to increase the intercalation rate and the film exposed to 1140 L of oxygen overall. An in-situ XPS measurement under these pressures is not possible with the spectro-microscope, because of technical reasons: the interlock system of the beamline activates above pressures of 2.0×10^{-7} mbar. However, the Si 2p, Ru 3d_{5/2} and the O 1s lines were measured after the oxygen exposure and the results are shown in a), b) and c). The Si 2p line shifted about 0.5 eV and the Ru 3d_{5/2} line resembles a 3O termination. The Si-O component in the O 1s line shifted further to lower binding energies and the Ru-O component slightly increased its intensity.

Figure 9.20 shows LEEM(IV) curves, LEEM and LEED images done after the annealing in UHV and after the exposures to oxygen described for the previous measurement. The kinetic energy axis of the LEEM(IV) curves is relative to the value of

the MEM to LEEM transition of each curve, that means to the vacuum level of each surface. All curves have similar features in comparison to the as prepared vitreous silica bilayer, which differ slightly in their intensity, but the peak energy relative to the vacuum level is the same. Below the graph of the curves LEEM and LEED images of the surface obtained after each treatment are shown. The first LEEM image I shows atomic steps, step bunches and the terraces, which have a homogenous contrast with only small changes. In the LEED image the ring pattern originating from the vitreous silica bilayer is found. After the first UHV annealing the step bunches have gained in contrast and holes in the film are found, which are located above atomic steps or step bunches (see LEEM image II). Except for these features the film looks very homogeneous. The LEED image showed the ring structures of silica and additionally a faint (1x1) pattern. After continuing the UHV annealing, the holes in the film grew in size, and their density at step bunches has increased (see LEEM image III), while the contrast of the atomic steps decreased. The LEED image shows again the ring structure of the vitreous bilayer, however a weak p(2x2) pattern is visible now. After oxygen exposure of 88 L the contrast of the steps and step bunches has increased and the holes remain unchanged (see the LEEM image IV). In the LEED image the contrast of the vitreous silica ring pattern has increased and a p(2x2) pattern is slightly visible. After an overall oxygen exposure of 1140 L only slight differences between the LEEM and LEED images to the previous oxygen exposure are found (compare LEEM and LEEM images IV and V).

From these results it can be concluded that the oxygen desorption is a continuous, temperature-dependent process. Moreover, for the future one could follow the Ru $3d_{5/2}$ change over time while holding a freshly prepared film at different temperatures. For each temperature, the time needed to reach a certain oxygen termination could be measured and the temperature dependence of this time analysed via an Arrhenius plot. From the slope one might determine an activation energy for each desorption step. However, it should not be neglected that the annealing of the film in UHV leads to the formation of mesoscopic holes in the film. So, it cannot easily be concluded whether the oxygen adsorption occurs through the larger rings formed by the silica tetrahedra in the vitreous silica bilayer, or through these mesoscopic holes to which the oxygen diffuses below the bilayer. A similar experimental series like that suggested for desorption could be done in LEEM following the formation of these holes over time. With their distribution, number or size an Arrhenius plot could be done as well to determine an activation energy for the formation of mesoscopic holes in the film. The combination of the results of both experiments could

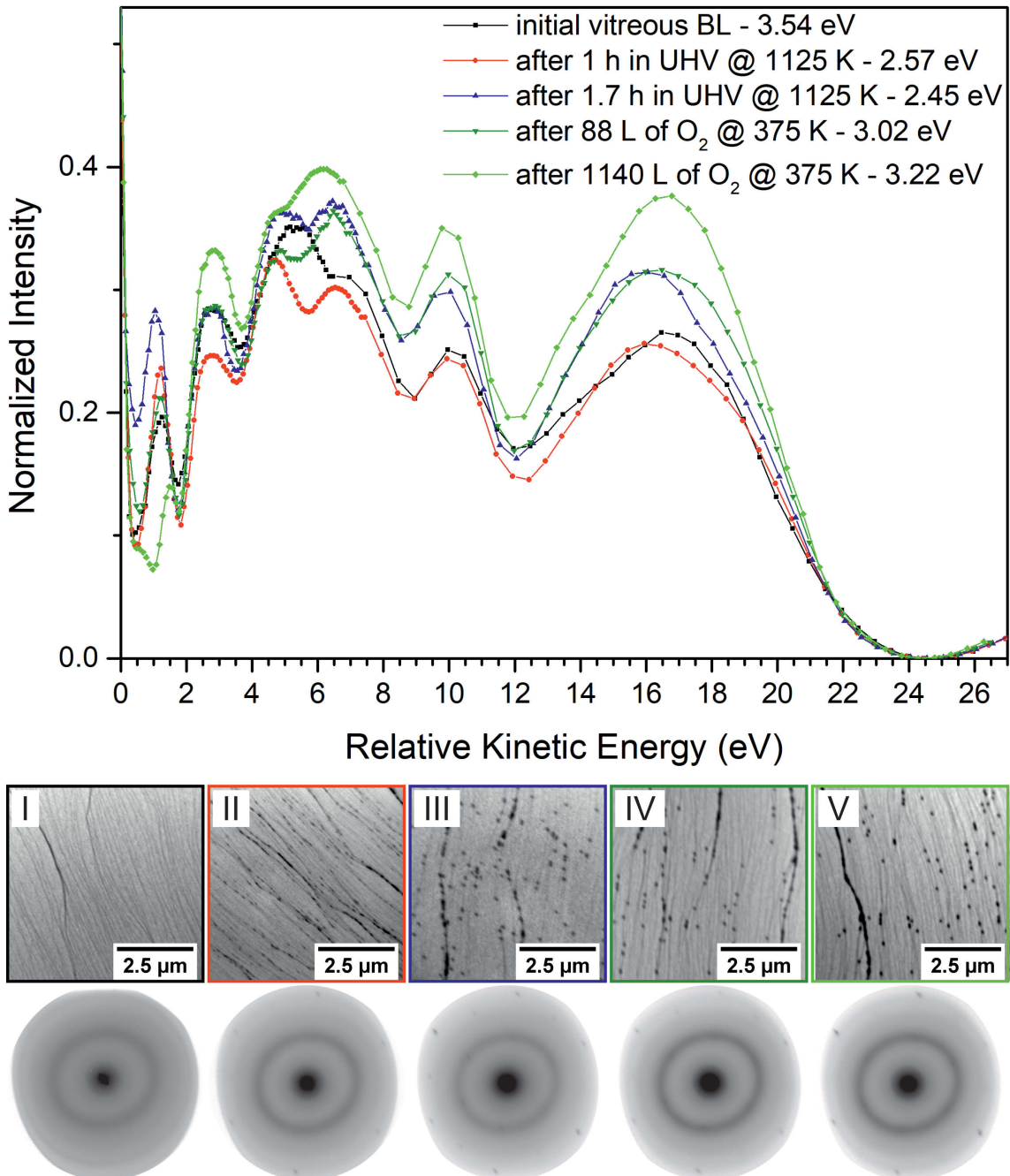


Figure 9.20: LEEM(IV) curves, LEEM and LEED images of a vitreous silica bilayer after high temperature annealings in UHV and after oxygen exposures. The used parameters and value of the MEM to LEEM transitions are given in the inset of graph. The kinetic energies of each curve are relative to their MEM to LEEM transition. Below the graph LEEM and LEED images made after each annealing step are shown. For them a kinetic energy of 42 eV was used. (for details see text)

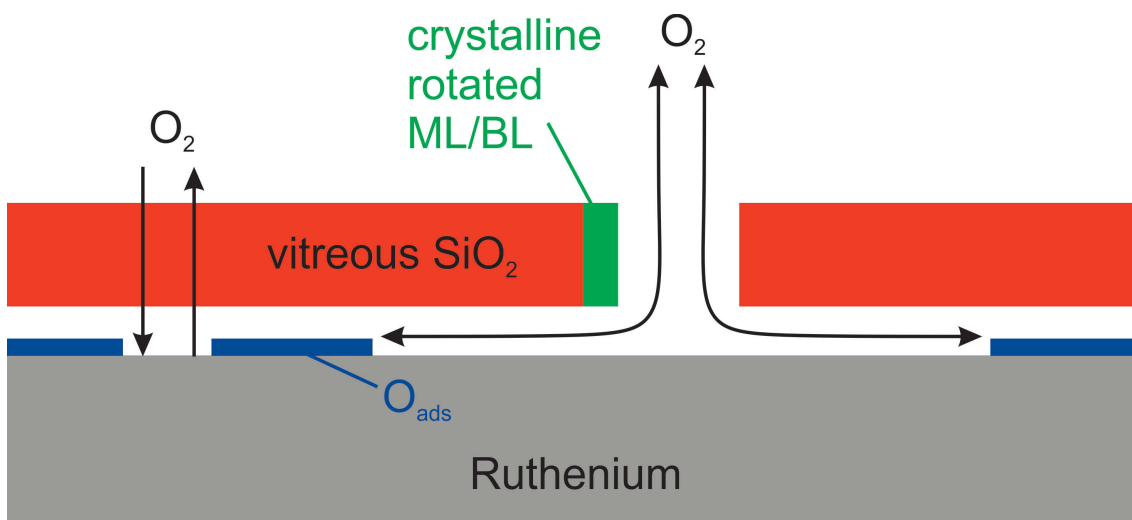


Figure 9.21: Sketch of the possible desorption and intercalation routes of oxygen below a silica bilayer on ruthenium.

then give a first glimpse which desorption process (oxygen desorption through the film or the mesoscopic holes) is dominant. The observed occurrence of the p(2x2) pattern in LEED is highly likely connected to mesoscopic holes, as it was already shown in figure 9.11 that the holes are reaching down to the ruthenium surface and that their bottom can be covered with oxygen.

For the intercalation, it can be concluded that the oxygen adsorption below the silica film at the ruthenium surface is a continuous process at 375 K. Again, following the Ru 3d line during intercalation at different temperatures could be used to determine the activation energy for this process. However, also for this the mesoscopic holes could play a role as entry point for oxygen below the bilayer. The two processes, oxygen desorption and intercalation, are sketched in figure 9.21. To prepare oxygen poor samples like after the UHV annealing for an intercalation experiment, it is preferred to use a H₂ treatment instead as already mentioned in [148] to exclude the formation of mesoscopic holes.

Summary and outlook

Here the results of this work will be summarized and a short outlook about possible additional results will be given. For details see the corresponding subchapters.

In this work all steps of the preparation of silica ML and BL on a single crystal metal substrate (Ru(0001)) were investigated in detail by LEEM, LEED and XPS. The possibility to measure in-situ and in real-time brought new insights into the preparation procedures and the properties of the resulting silica phases.

First, four oxygen terminations of Ru(0001) were investigated in detail to create a trustworthy reference data base measured in the same experimental setup (see chapter 4). They are referred to as 1O, 2O, 3O and 4O terminations. The first three terminations cannot be distinguished by the spot positions of their LEED patterns, so it was necessary to establish their differences by LEEM(IV), DF-LEEM(IV), LEED(IV) and XPS. At this stage, the XPS of the Ru $3d_{5/2}$ line and dark field LEEM measurements were very important, which enabled a direct comparison with the silica covered surface.

As next step, the various deposition procedures were investigated (see chapter 5). First a silicon over layer grown in UHV was used to characterize the stability of the deposition depending on the evaporator parameters. With this knowledge, various amounts of silicon were deposited on the surface and oxidized to form silica. The so prepared samples were transferred to the FHI campus and were characterized by IRRAS to determine the deposited amounts. With these results, it was possible to establish a method, using the intensity decay in LEED, to determine the deposited silicon amount in-situ. This represents an important milestone of this work, because it opened up the possibility to investigate a data base of more than 400 previously prepared films, to compare them with each other and to deposit well-defined amounts of silicon.

Then the deposition of silicon amounts corresponding to ML and BL silica were investigated in detail at room temperature under an oxygen atmosphere on an oxygen pre-covered Ru(0001) surface. It has been found that under the used conditions ruthenium acts as a catalyst by supplying atomic oxygen for the oxidation of silicon. So, the ML silicon is already fully oxidized after deposition, while the BL amount needs an additional low temperature annealing step to 600 K in $p_{\text{O}_2} = 5.0 \times 10^{-6}$ mbar oxygen to become fully oxidized. Both films are poorly ordered at this stage.

This result enabled new routes for the preparation of silica on Ru(0001) (see chapters 6, 7, 8, 9). The influence of the parameters such as oxygen pressure, annealing temperature, holding time, and heating rate were probed for both silica amounts. For instance, the silica ML shows two phases depending on the oxygen background pressure during annealing, namely, a $(2 \times 2)R30^\circ$ phase in UHV and a $p(2 \times 2)$ phase in $p_{\text{O}_2} = 5.0 \times 10^{-6}$ mbar oxygen. The silica BL has three phases, one with a complex LEED pattern denoted as Xmas star BL phase, a crystalline $p(2 \times 2)$ phase, and a vitreous phase. The occurrence of the phases has a complex dependency on the oxygen pressure, the holding temperature and the heating rate. For instance, the Xmas star BL phase can be produced via annealing in UHV with a low heating rate or via annealing in oxygen with a high heating rate. On the other hand, the $p(2 \times 2)$ phase is formed by annealing in oxygen with a low heating rate. It is transformed into the vitreous phase by increasing the holding temperature in oxygen or by annealing in UHV at slightly lower temperatures.

The transformation of the $p(2 \times 2)$ silica phase into the vitreous phase was investigated in detail. It was found that it is a continuous process that happens everywhere on the surface at the same time and is below the resolution limit in LEEM under the used conditions. An activation energy of 4.2 eV was determined for the crystalline to vitreous transformation from an Arrhenius plot of the transition times for different temperatures. The value of 4.2 eV is in good agreement with theoretical calculations for the activation energy to form a Stone-Wales-defect in a hexagonal silica bilayer. Furthermore, the vitreous bilayer was used to investigate the desorption and intercalation of oxygen below the layer. It was found that the silica BL starts to form mesoscopic holes (diameter of a few tens of nanometer) during the UHV annealing and that the O 1s line undergoes a linear shift to lower binding energies during intercalation.

For the different phases of the ML and the BL the preparation conditions, LEED pattern, and XPS results are summarized in table 10.1.

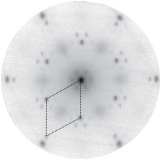
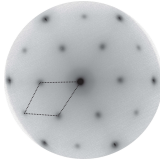
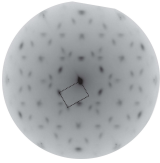
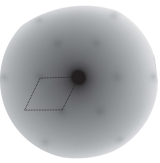
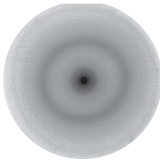
amount of silica\ para- meters	ML		BL				
	Phase	(2x2)R30°	p(2x2)	Xmas star	p(2x2)	vitreous	
Oxygen pressure (mbar)	$< 5.0 \times 10^{-9}$	5.0×10^{-6}	$< 5.0 \times 10^{-9**}$	5.0×10^{-6}		$< 5.0 \times 10^{-9**}$	
Final annealing temperature T (K)	1075	1045	1080		1050	>1075	>1025
Heating rate (K/s)	7	1	1	7.5	1		
Holding time (min)	1.25	10	5	2	10	$\sim \exp(-T)$	
Final LEED pattern with 42 eV at RT							
Comparison to Ru 3d _{5/2} oxygen reference	10	30	10		30	40	10
E _{bin} for Si-O (Si 2p, eV)	102.8	102.3	102.8	102.6	102.5	102.4	102.9
E _{bin} for Si-O (O 1s, eV)	531.7	531.2	531.7	531.4	531.0	529.9	532.0

Table 10.1: Preparation conditions, LEED patterns and XPS results of the different phases of the silica ML and BL. (* Before the annealing a fully oxidized, disordered silica template was prepared. ** A crystalline phase was prepared in oxygen before annealing and served as a template.)

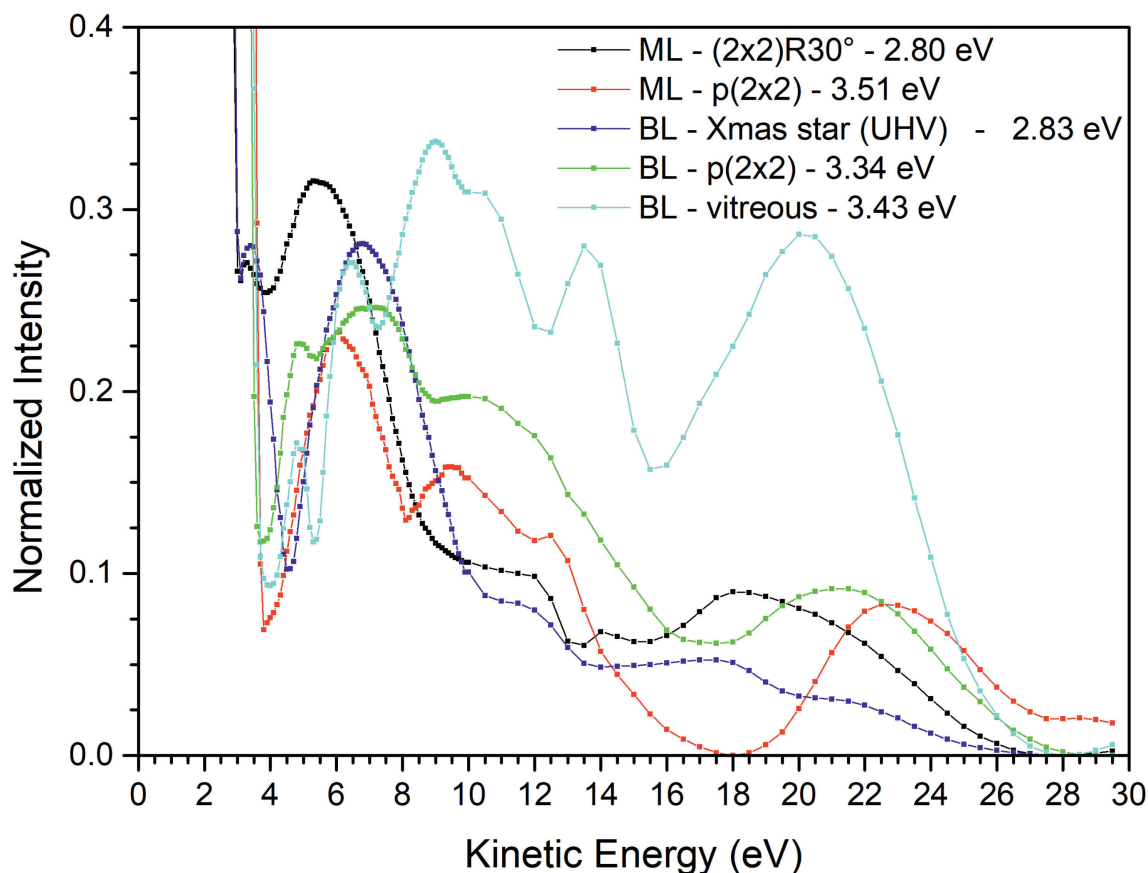


Figure 10.1: LEEM(IV) curves of the ML- and BL-phases of silica on ruthenium. The kinetic energy of MEM to LEEM transitions are given in the inset.

Figure 10.1 shows the LEEM(IV) curves for the ML- and BL-phases after preparation. Only the vitreous phase shows very large differences in comparison to the other ML- and BL-phases. The $(2 \times 2)R30^\circ$ phase of the ML and the Xmas star BL phase of the BL have a similar value for the MEM to LEEM transition of about 2.8 eV, the phases prepared in oxygen have a value larger than 3.3 eV.

The phase transition of the $(2 \times 2)R30^\circ$ to the $p(2 \times 2)$ phase starts in $p_{O_2} = 5.0 \times 10^{-6}$ mbar oxygen at 925 K. It had been shown before that this phase transformation is reversible [16] by heating in UHV. A LEED image of the intermediate state of the transformation is shown in Figure 10.2. The LEED spots of the $(2 \times 2)R30^\circ$ and the $p(2 \times 2)$ phases are clearly visible, so both phases co-exist during the transition next to each other at the surface. In contrast to the preparation of the $(2 \times 2)R30^\circ$ phase in UHV no ring appears.

For the Xmas star BL phase it was found that at about 1100 K and $p_{O_2} = 5.0 \times 10^{-8}$ mbar oxygen pressure a transformation to the $p(2 \times 2)$ phase starts over time. With increasing temperature to 1125 K and the oxygen pressure to 5.0×10^{-6} mbar, a ring appears in LEED suggesting the formation of a vitreous

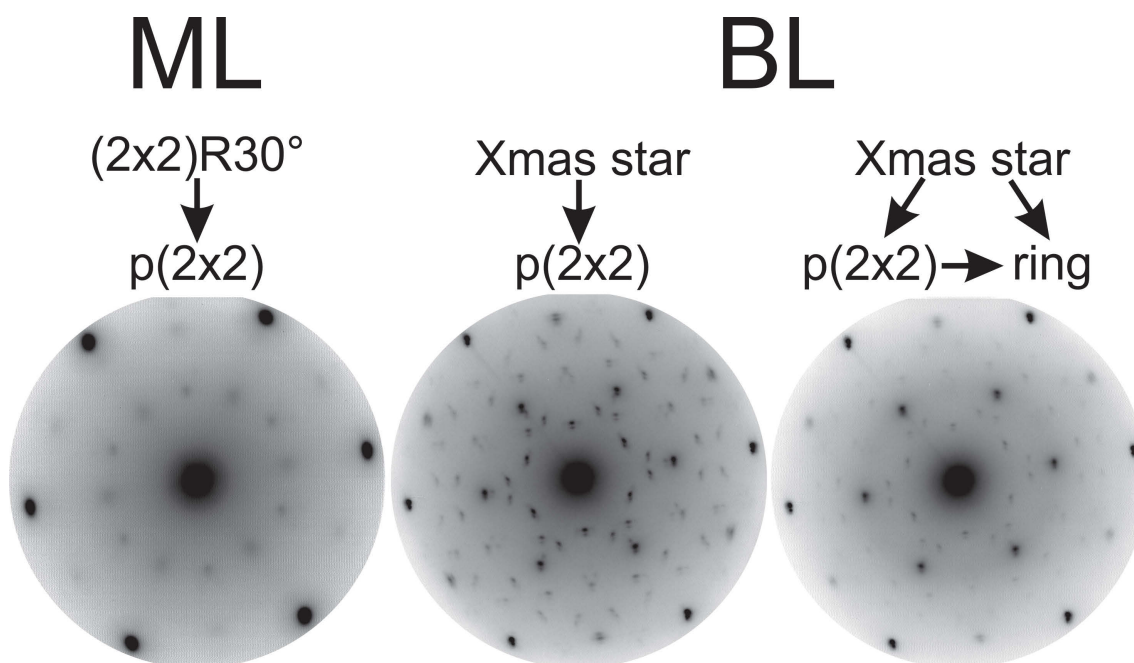


Figure 10.2: Intermediate states of the phase transitions. Left that of the $(2 \times 2)R30^\circ$ to the $p(2 \times 2)$ phase, and in the middle and the right, the transitions of the Xmas star to the $p(2 \times 2)$ and ring. The used kinetic energy was 42 eV.

phase. At this point three phases co-exist on the surface at the same time. The two intermediate states are shown in Figure 10.2.

The phase transition to the vitreous phase is irreversible. Prolonged annealing above 700 K in UHV or in oxygen showed no evidence of a structural change of the silica bilayer, only the formation of holes was found. Also, slower heating and cooling rates, with < 1 K/s, and faster heating and cooling rates of about 15 K/s have no effect on the formation of the vitreous phase.

The bilayer starts to de-wet at temperatures of above 1200 K. The process starts especially at step bunches, the evaporation of the silica layer on top is faster than the evaporation of the second layer closer to the ruthenium surface. This leaves behind exposed areas of the ruthenium surface, close to the step bunches, surrounded by islands of the $(2 \times 2)R30^\circ$ ML-phase and a vitreous phase in the distant areas (see images in [141]).

For amounts lower than 1 ML the $(2 \times 2)R30^\circ$ or $p(2 \times 2)$ structure appear by annealing in UHV or oxygen at temperatures found for 1 ML. Amounts between 1 and 2 ML have shown a mixture of the $(2 \times 2)R30^\circ$ and Xmas star patterns in LEED after UHV annealing, while in oxygen only a $p(2 \times 2)$ pattern is found. Amounts above 2.5 ML after preparation in $p_{O_2} = 5.0 \times 10^{-6}$ mbar oxygen show no $p(2 \times 2)$ phase and only a vitreous one appears. On the other hand, for thicker amounts (> 4 ML),

an evaporation front of silica is found at about 1150 K in $p_{\text{O}_2} = 5.0 \times 10^{-6}$ mbar oxygen, see figure 10.3. In the initial state, the film consists of fully oxidized and incompletely oxidized silicon. After the evaporation front, an intermediate state is found, the amounts of silica and incompletely oxidized silicon are reduced. At the final state, nearly all the incompletely oxidized silicon is gone and an oxygen intercalation is found (right side in figure 10.3).

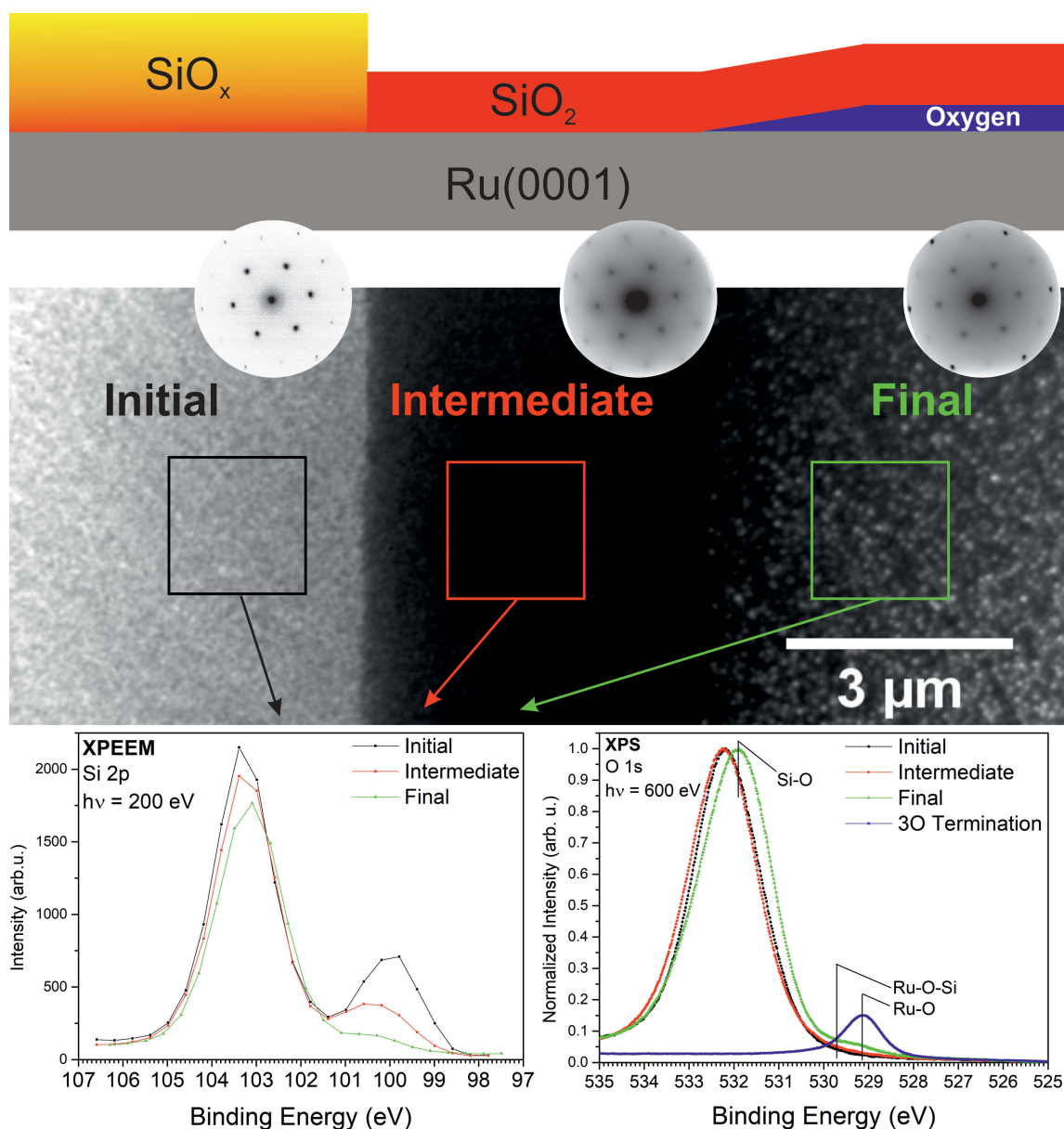


Figure 10.3: A quenched evaporation front of a film with more than 4 ML silicon at room temperature. In the upper part, a suggested model of the front is shown. In the middle, a LEEM image with a kinetic energy of 30 eV and as inset the LEED images for each area taken with 42 eV. In the lower part, the results of a XPEEM and XPS analysis of the three different areas.

As an outlook the following experiments are suggested for the future:

The LEED analysis used for the transformation of the p(2x2) to vitreous phase of the BL could be applied for several other phase formations and transitions of the silica to determine their activation energies. For example, to the formation of the (2x2)R30° phase of the ML and its transition to the p(2x2) phase or the transitions of the Xmas star BL phase in oxygen. Also, the influence of the oxygen pressure during the preparation could be investigated in greater detail. In this work only two extremes (UHV or $p_{\text{O}_2} = 5.0 \times 10^{-6}$ mbar of oxygen) were probed, however, investigating at the minimal oxygen pressures needed for the formations and transitions of the phases in oxygen could lead to new insights of these processes.

As shown for the intercalation of oxygen, the process is time-dependent at a fixed temperature. A XPS study with various oxygen pressures and temperatures could lead to a better understanding of the process. Moreover, the intercalation and desorption of other species like hydrogen or carbon-monoxide can be probed. For this the first successful experiments were done recently, that open the route to explore the chemistry in the confined space between silica and ruthenium.

The results of this work could be used as a reference for doping of the silica with other elements like iron, aluminium, and chromium, to probe the formation of the corresponding mixed phases and their properties. On the other hand, also Pt(111) or Pd(111) could be used as different substrates to investigate the role of the interaction of the substrate with the oxygen pressure for the phase formation of silica .

Bibliography

- [1] C. Meade and R. Jeanloz. Effect of a Coordination Change on the Strength of Amorphous SiO₂. *Science*, 241(4869):1072–1074, aug 1988.
- [2] Charles Meade and Raymond Jeanloz. The strength of mantle silicates at high pressures and room temperature: implications for the viscosity of the mantle. *Nature*, 348(6301):533–535, dec 1990.
- [3] E. C. T. Chao, J. J. Fahey, Janet Littler, and D. J. Milton. Stishovite, SiO₂, a very high pressure new mineral from Meteor Crater, Arizona. *Journal of Geophysical Research*, 67(1):419–421, jan 1962.
- [4] S. M. Sze and K. K. Ng. *Physics of Semiconductor Devices*. Wiley, Hoboken, 3 edition, 2007.
- [5] H. J. Freund, M. Heyde, N. Nilius, S. Schauer mann, S. Shaikhutdinov, and M. Sterrer. Model studies on heterogeneous catalysts at the atomic scale: From supported metal particles to two-dimensional zeolites. *Journal of Catalysis*, 308(0):154 – 167, 2013. 50th Anniversary Special Issue.
- [6] Friedrich Liebeu. *Structural Chemistry of Silicates: Structure, Bonding, and Classification*. Springer-Verlag, 1985.
- [7] W. H. Zachariasen. THE ATOMIC ARRANGEMENT IN GLASS. *Journal of the American Chemical Society*, 54(10):3841–3851, 1932.
- [8] L. Lichtenstein, C. Büchner, B. Yang, S. Shaikhutdinov, M. Heyde, M. Sierka, R. Włodarczyk, J. Sauer, and H.-J. Freund. The Atomic Structure of a Metal-Supported Vitreous Thin Silica Film. *Angewandte Chemie International Edition*, 51(2):404 – 407, 2012.
- [9] D. Löffler, J. J. Uhlrich, M. Baron, B. Yang, X. Yu, L. Lichtenstein, L. Heinke, C. Büchner, M. Heyde, S. Shaikhutdinov, H.-J. Freund, R. Włodarczyk, M. Sierka, and J. Sauer. Growth and Structure of Crystalline Silica Sheet on Ru(0001). *Phys. Rev. Lett.*, 105:146104, Sep 2010.
- [10] R. Włodarczyk, M. Sierka, J. Sauer, D. Löffler, J. J. Uhlrich, X. Yu, B. Yang, I. M. N. Groot, S. Shaikhutdinov, and H.-J. Freund. Tuning the electronic

- structure of ultrathin crystalline silica films on Ru(0001). *Phys. Rev. B*, 85:085403, Feb 2012.
- [11] B. Yang, W. E. Kaden, X. Yu, J. A. Boscoboinik, Y. Martynova, L. Lichtenstein, M. Heyde, M. Sterrer, R. Włodarczyk, M. Sierka, J. Sauer, S. Shaikhutdinov, and H.-J. Freund. Thin silica films on Ru(0001): monolayer, bilayer and three-dimensional networks of $[\text{SiO}_4]$ tetrahedra. *Phys. Chem. Chem. Phys.*, 14:11344 – 11351, 2012.
- [12] X. Yu, B. Yang, J. A. Boscoboinik, S. Shaikhutdinov, and H.-J. Freund. Support effects on the atomic structure of ultrathin silica films on metals. *Applied Physics Letters*, 100(15):151608, 2012.
- [13] Leonid Lichtenstein, Markus Heyde, and Hans-Joachim Freund. Crystalline-Vitreous Interface in Two Dimensional Silica. *Phys. Rev. Lett.*, 109:106101, Sep 2012.
- [14] Pinshane Y. Huang, Simon Kurasch, Jonathan S. Alden, Ashivni Shekhawat, Alexander A. Alemi, Paul L. McEuen, James P. Sethna, Ute Kaiser, and David A. Muller. Imaging Atomic Rearrangements in Two-Dimensional Silica Glass: Watching Silica’s Dance. *Science*, 342(6155):224–227, 2013.
- [15] S. Shaikhutdinov and H.-J. Freund. Ultrathin Silica Films on Metals: The Long and Winding Road to Understanding the Atomic Structure. *Advanced Materials*, 25(1):49 – 67, 2013.
- [16] B. Yang, J. A. Boscoboinik, X. Yu, S. Shaikhutdinov, and H. J. Freund. Patterned Defect Structures Predicted for Graphene Are Observed on Single-Layer Silica Films. *Nano Letters*, 13(9):4422 – 4427, 2013. PMID: 23937399.
- [17] B. Yang, E. Emmez, W. E. Kaden, X. Yu, J. A. Boscoboinik, M. Sterrer, S. Shaikhutdinov, and H.-J. Freund. Hydroxylation of Metal-Supported Sheet-Like Silica Films. *The Journal of Physical Chemistry C*, 117(16):8336 – 8344, 2013.
- [18] Emre Emmez, J. Anibal Boscoboinik, Samuel Tenney, Peter Sutter, Shamil Shaikhutdinov, and Hans-Joachim Freund. Oxidation of the Ru(0001) surface covered by weakly bound, ultrathin silicate films. *Surface Science*, 646:19 – 25, 2016. Surface science for heterogeneous catalysis, a special issue in Honour of Richard Lambert.
- [19] Hans-Joachim Freund. Controlling Silica in Its Crystalline and Amorphous States: A Problem in Surface Science. *Accounts of Chemical Research*, 50(3):446–449, 2017.
- [20] E. Emmez, B. Yang, S. Shaikhutdinov, and H. J. Freund. Permeation of a Single-Layer SiO_2 Membrane and Chemistry in Confined Space. *The Journal of Physical Chemistry C*, 118(50):29034 – 29042, 2014.

- [21] C. Büchner, Z.-J. Wang, K. M. Burson, M.-G. Willinger, M. Heyde, R. Schlögl, and H.-J. Freund. A Large-Area Transferable Wide Band Gap 2D Silicon Dioxide Layer. *ACS Nano*, 10(8):7982–7989, 2016. PMID: 27421042.
- [22] R. Fink, M.R. Weiss, E. Umbach, D. Preikszas, H. Rose, R. Spehr, P. Hartel, W. Engel, R. Degenhardt, R. Wichtendahl, H. Kuhlenbeck, W. Erlebach, K. Ihmann, R. Schlögl, H.-J. Freund, A.M. Bradshaw, G. Lilienkamp, Th. Schmidt, E. Bauer, and G. Benner. SMART: a planned ultrahigh-resolution spectromicroscope for BESSY II. *Journal of Electron Spectroscopy and Related Phenomena*, 84(1):231 – 250, 1997.
- [23] T. Schmidt, U. Groh, R. Fink, E. Umbach, O. Schaff, W. Engel, B. Richter, H. Kuhlenbeck, R. Schlögl, H.-J. Freund, A. M. Bradshaw, D. Preikszas, P. Hartel, R. Spehr, H. Rose, G. Lilienkamp, E. Bauer, and G. Benner. XPEEM WITH ENERGY-FILTERING: ADVANTAGES AND FIRST RESULTS FROM THE SMART PROJECT. *Surface Review and Letters*, 09(01):223–232, 2002.
- [24] T. Schmidt, H. Marchetto, P. L. Lévesque, U. Groh, F. Maier, D. Preikszas, P. Hartel, R. Spehr, G. Lilienkamp, W. Engel, R. Fink, E. Bauer, H. Rose, E. Umbach, and H.-J. Freund. Double aberration correction in a low-energy electron microscope. *Ultramicroscopy*, 110(11):1358 – 1361, 2010.
- [25] T. Schmidt, A. Sala, H. Marchetto, E. Umbach, and H.-J. Freund. First experimental proof for aberration correction in XPEEM: Resolution, transmission enhancement, and limitation by space charge effects. *Ultramicroscopy*, 126:23 – 32, 2013.
- [26] E. Jäschke. BESSY II in Betrieb genommen. Brillantes Licht in Berlin-Adlershof. *Physik in unserer Zeit*, 29(6):261–261, 1998.
- [27] J. Kirschner, H. Engelhard, and D. Hartung. An evaporation source for ion beam assisted deposition in ultrahigh vacuum. *Review of Scientific Instruments*, 73(11):3853 – 3860, 2002.
- [28] Helder Marchetto. *High-resolution spectro-microscopic investigations of organic thin film growth*. PhD thesis, 2010.
- [29] Alessandro Sala. *Characterization of iron oxide thin films as a support for catalytically active nanoparticles*. PhD thesis, 2013.
- [30] H. Müller, D. Preikszas, and H. Rose. A beam separator with small aberrations. *Journal of Electron Microscopy*, 48(3):191–204, 1999.
- [31] E. Hess. Beitrag zur Kenntnis der elektronenoptischen Immersionslinse. *Zeitschrift für Physik*, 92(3):274–282, Mar 1934.

- [32] D. Preikszas and H. Rose. Correction properties of electron mirrors. *Journal of Electron Microscopy*, 46(1):1–9, 1997.
- [33] H. Rose. *Advances in Electron Optics*, pages 189–270. Springer Berlin Heidelberg, Berlin, Heidelberg, 2003.
- [34] H. H. Rose. Optics of high-performance electron microscopes. *Science and Technology of Advanced Materials*, 9(1):014107, 2008.
- [35] H. Rose and D. Krahl. *Electron Optics of Imaging Energy Filters*, pages 43–149. Springer Berlin Heidelberg, Berlin, Heidelberg, 1995.
- [36] Ernst Bauer. *Surface Microscopy with Low Energy Electrons*. Springer New York Heidelberg Dordrecht London, 2014.
- [37] M. A. Van Hove, W. H. Weinberg, and C.-M. Chan. *Low-Energy Electron Diffraction*, volume 6 of *Surface Sciences*. Springer Verlag, Berlin, 2 edition, 1986.
- [38] G. Wedler and H.-J. Freund. *Lehrbuch der Physikalischen Chemie*. Wiley-VCH, Weinheim, 6 edition, 2012.
- [39] Louis de Broglie. The reinterpretation of wave mechanics. *Foundations of Physics*, 1(1):5–15, Mar 1970.
- [40] H. Marchetto, T. Schmidt, U. Groh, F. C. Maier, P. L. Levesque, R. H. Fink, H.-J. Freund, and E. Umbach. Direct observation of epitaxial organic film growth: temperature-dependent growth mechanisms and metastability. *Phys. Chem. Chem. Phys.*, 17:29150–29160, 2015.
- [41] R. Henderson, J.M. Baldwin, T.A. Ceska, F. Zemlin, E. Beckmann, and K.H. Downing. Model for the structure of bacteriorhodopsin based on high-resolution electron cryo-microscopy. *Journal of Molecular Biology*, 213(4):899 – 929, 1990.
- [42] S. Hüfner. *Photoelectron Spectroscopy*. Springer, Berlin / Heidelberg, 3rd edition, 2003.
- [43] H. Hertz. Ueber einen Einfluss des ultravioletten Lichtes auf die elektrische Entladung. *Ann. Phys.*, 267:983 – 1000, 1887.
- [44] W. Hallwachs. Ueber den Einfluss des Lichtes auf electrostatisch geladene Körper. *Ann. Phys.*, 269:301 – 312, 1888.
- [45] P. Lenard. Erzeugung von Kathodenstrahlen durch ultraviolettes Licht. *Ann. Phys.*, 307:359 – 375, 1900.
- [46] A. Einstein. Über einen die Erzeugung und Verwandlung des Lichtes betreffenden heuristischen Gesichtspunkt. *Ann. Phys.*, 17:132 – 148, 1905.

- [47] K. Siegbahn. Energy calibration of Instruments. *Physica*, 18:1043 – 1062, 1952.
- [48] K. Siegbahn and K. Edvarson. β -ray spectroscopy in the precision range of $1 : 10^5$. *Nucl. Phys.*, 1:137 – 159, 1956.
- [49] P. J. Feibelman and D. E. Eastman. Photoemission spectroscopy - Correspondence between quantum theory and experimental phenomenology. *Phys. Rev. B*, 10:4932 – 4947, 1974.
- [50] C. N. Berglund and W. E. Spicer. Photoemission Studies of Copper and Silver: Theory. *Phys. Rev.*, 136:A1030 – A1044, 1964.
- [51] M. P. Seah and W. A. Dench. Quantitative electron spectroscopy of surfaces: A standard data base for electron inelastic mean free paths in solids. *Surface and Interface Analysis*, 1(1):2 – 11, 1979.
- [52] J. Meija, T. B. Coplen, M. Berglund, W. A. Brand, P. De Bièvre, M. Gröning, N. E. Holden, J. Irrgeher, R. D. Loss, T. Walczyk, and T. Prohaska. Atomic weights of the elements 2013 (IUPAC Technical Report). *Pure and Applied Chemistry*, 88(3):265 – 291, November 2016.
- [53] J. W. Arblaster. Crystallographic Properties of Ruthenium. *Platinum Metals Review*, 57(2):127 – 136, 2013.
- [54] Ken ichi Aika, Humio Hori, and Atsumu Ozaki. Activation of nitrogen by alkali metal promoted transition metal I. Ammonia synthesis over ruthenium promoted by alkali metal. *Journal of Catalysis*, 27(3):424 – 431, 1972.
- [55] A.I. Foster, P.G. James, J.J. McCarroll, and S.R. Tennison. Process for the synthesis of ammonia using catalysts supported on graphite containing carbon, August 7 1979. US Patent 4,163,775.
- [56] A.I. Foster, P.G. James, J.J. McCarroll, and S.R. Tennison. Process for producing a catalyst comprising a graphite containing carbon, a transitional metal and a modifying metal ion, February 10 1981. US Patent 4,250,057.
- [57] I. Palacio and O. Rodríguez de la Fuente. Methanol decomposition on Ru(0001) during continuous exposure at room temperature. *Surface Science*, 606(15):1152 – 1159, 2012.
- [58] J. Zhang and H. Liu. *Electrocatalysis of Direct Methanol Fuel Cells: From Fundamentals to Applications*. Green chemistry. Wiley, 2009.
- [59] P. H. Dixneuf and C. Bruneau. *Ruthenium in Catalysis*, volume 48 of *Topics in Organometallic Chemistry*. Springer International Publishing, Gewerbestrasse 11 CH-6330 Cham (ZG), Switzerland, topics in organometallic chemistry edition, 2014.

- [60] J. Z. Shi, S. N. Piramanayagam, C. S. Mah, H. B. Zhao, J. M. Zhao, Y. S. Kay, and C. K. Pock. Influence of dual-Ru intermediate layers on magnetic properties and recording performance of *CoCrPt – SiO₂* perpendicular recording media. *Applied Physics Letters*, 87(22):222503, 2005.
- [61] E.E. Marinero, N.F. Supper, and B.R. York. Intermediate tri-layer structure for perpendicular recording media, November 16 2010. US Patent 7,833,640.
- [62] J. Assmann, V. Narkhede, N. A. Breuer, M. Muhler, A. P. Seitsonen, M. Knapp, D. Crihan, A. Farkas, G. Mellau, and H. Over. Heterogeneous oxidation catalysis on ruthenium: bridging the pressure and materials gaps and beyond. *Journal of Physics: Condensed Matter*, 20(18):184017, 2008.
- [63] T. E. Madey, H. A. Engelhardt, and D. Menzel. Adsorption of oxygen and oxidation of CO on the ruthenium (001) surface. *Surface Science*, 48(2):304 – 328, 1975.
- [64] J. De la Figuera, J. M. Puerta, J. I. Cerda, F. El Gabaly, and K. F. McCarty. Determining the structure of Ru(0001) from low-energy electron diffraction of a single terrace. *Surface Science*, 600(9):L105 – L109, 2006.
- [65] M. Lindroos, H. Pfnür, and D. Menzel. Theoretical and experimental study of the unoccupied electronic band structure of Ru(001) by electron reflection. *Phys. Rev. B*, 33:6684–6693, May 1986.
- [66] E. E. Krasovskii, J. Höcker, J. Falta, and J. I. Flege. Surface resonances in electron reflection from overlayers. *Journal of Physics: Condensed Matter*, 27(3):035501, 2015.
- [67] G. Held, S. Uremović, and D. Menzel. Rearrangement of stepped Ru(001) surfaces upon oxygen adsorption. *Surface Science*, 331:1122 – 1128, 1995.
- [68] A. Baraldi, S. Lizzit, G. Comelli, A. Goldoni, P. Hofmann, and G. Paolucci. Core-level subsurface shifted component in a 4d transition metal: Ru (10 $\bar{1}0$). *Phys. Rev. B*, 61:4534–4537, Feb 2000.
- [69] S. Lizzit, A. Baraldi, A. Groso, K. Reuter, M. V. Ganduglia-Pirovano, C. Stampfl, M. Scheffler, M. Stichler, C. Keller, W. Wurth, and D. Menzel. Surface core-level shifts of clean and oxygen-covered Ru(0001). *Phys. Rev. B*, 63:205419, May 2001.
- [70] M. Lindroos, H. Pfnür, G. Held, and D. Menzel. Adsorbate induced reconstruction by strong chemisorption: Ru(001)p(2x2)-O. *Surface Science*, 222(2-3):451 – 463, 1989.
- [71] H. Pfnür, G. Held, M. Lindroos, and D. Menzel. Oxygen induced reconstruction of a close-packed surface: A LEED IV study on Ru(001)-p(2x1)O. *Surface Science*, 220(1):43 – 58, 1989.

- [72] M. Gsell, M. Stichler, P. Jakob, and D. Menzel. Formation and Geometry of a High-Coverage Oxygen Adlayer on Ru(001), the p(2x2)-3O Phase. *Israel Journal of Chemistry*, 38(4):339 – 348, 1998.
- [73] K. L. Kostov, M. Gsell, P. Jakob, T. Moritz, W. Widdra, and D. Menzel. Observation of a novel high density 3O(2x2) structure on Ru(001). *Surface Science*, 394(1-3):L138 – L144, 1997.
- [74] C. Stampfl, S. Schwegmann, H. Over, M. Scheffler, and G. Ertl. Structure and Stability of a High-Coverage (1x1) Oxygen Phase on Ru(0001). *Phys. Rev. Lett.*, 77:3371 – 3374, Oct 1996.
- [75] W. E. Bell and M. Tagami. High-temperature chemistry of the ruthenium-oxygen system. *The Journal of Physical Chemistry*, 67(11):2432 – 2436, nov 1963.
- [76] J. I. Flege, J. Hrbek, and P. Sutter. Structural imaging of surface oxidation and oxidation catalysis on Ru(0001). *Phys. Rev. B*, 78:165407, Oct 2008.
- [77] J. I. Flege and P. Sutter. Nanoscale analysis of Ru(0001) oxidation using low-energy and photoemission electron microscopy. *Journal of Physics: Condensed Matter*, 21(31):314018, 2009.
- [78] W. J. Mitchell and W. H. Weinberg. Interaction of NO_2 with Ru(001): Formation and decomposition of RuO_x layers. *The Journal of Chemical Physics*, 104(22):9127–9136, 1996.
- [79] K. Reuter and M. Scheffler. Composition, structure, and stability of $RuO_2(110)$ as a function of oxygen pressure. *Phys. Rev. B*, 65:035406, Dec 2001.
- [80] K Meinel, H Wolter, Ch Ammer, A Beckmann, and H Neddermeyer. Adsorption stages of O on Ru(0001) studied by means of scanning tunnelling microscopy. *Journal of Physics: Condensed Matter*, 9(22):4611, 1997.
- [81] M. Gsell. *Chemisorption von O mit verschiedenen Koadsorbaten auf Ru(001): Strukturbestimmung mittels LEED und STM*. PhD thesis, 2002.
- [82] H. Pfnür, M. Lindroos, and D. Menzel. Investigation of adsorbates with low energy electron diffraction at very low energies (VLEED). *Surface Science*, 248(1-2):1 – 10, 1991.
- [83] S. Lizzit, Y. Zhang, K. L. Kostov, L. Petaccia, A. Baraldi, D. Menzel, and K. Reuter. O- and H-induced surface core level shifts on Ru(0001): prevalence of the additivity rule. *Journal of Physics: Condensed Matter*, 21(13):134009, 2009.
- [84] R. Domnick, G. Held, P. Witte, and H.-P. Steinrück. The transition from oxygen chemisorption to oxidation of ultra-thin Ni layers on Cu(111). *The Journal of Chemical Physics*, 115(4):1902–1908, 2001.

- [85] Y. D. Kim, A. P. Seitsonen, and H. Over. The atomic geometry of oxygen-rich Ru(0001) surfaces: coexistence of (1x1)O and RuO₂(110) domains. *Surface Science*, 465(1-2):1 – 8, 2000.
- [86] M. Sokolowski and H. Pfnür. Influence of steps on the critical behavior of a two-dimensional system: $p(2 \times 2)$ oxygen on a stepped Ru(0001) surface. *Phys. Rev. Lett.*, 63:183 – 186, Jul 1989.
- [87] M. Sokolowski, H. Pfnür, and M. Lindroos. Structural correlations of a chemisorbate across monatomic steps: $p(2 \times 2)$ -ordered oxygen on stepped Ru(001) surfaces. *Surface Science*, 278(1):87 – 98, 1992.
- [88] S. L. Parrott, G. Praline, B. E. Koel, J. M. White, and T. N. Taylor. Oxygen chemisorption on a stepped Ru ($\tilde{0}01$) crystal. *The Journal of Chemical Physics*, 71(8):3352–3354, 1979.
- [89] J. Winterlin, J. Trost, S. Renisch, R. Schuster, T. Zambelli, and G. Ertl. Real-time STM observations of atomic equilibrium fluctuations in an adsorbate system: O/Ru(0001). *Surface Science*, 394(1):159 – 169, 1997.
- [90] H. Pfnür and P. Piercy. Oxygen on Ru(001): Critical behavior of $p(2 \times 1)$ order-disorder transition. *Phys. Rev. B*, 41:582–589, Jan 1990.
- [91] P. Debye. Zerstreung von Röntgenstrahlen. *Annalen der Physik*, 351(6):809–823, 1915.
- [92] Y. D. Kim, S. Wendt, S. Schwegmann, H. Over, and G. Ertl. Structural analyses of the pure and cesiated Ru(0001)-(2x2)-3O phase. *Surface Science*, 418(1):267 – 272, 1998.
- [93] C. Léandri, H. Saifi, O. Guillermet, and B. Aufray. Silicon thin films deposited on Ag(001): growth and temperature behavior. *Applied Surface Science*, 177(4):303 – 306, 2001. Surface science approach to stress and strain in epitaxy.
- [94] B. Aufray, A. Kara, S. Vizzini, H. Oughaddou, C. Lándri, B. Ealet, and G. Le Lay. Graphene-like silicon nanoribbons on Ag(110): A possible formation of silicene. *Applied Physics Letters*, 96(18):183102, 2010.
- [95] B. Lalmi, H. Oughaddou, H. Enriquez, A. Kara, S. Vizzini, B. Ealet, and B. Aufray. Epitaxial growth of a silicene sheet. *Applied Physics Letters*, 97(22):223109, 2010.
- [96] A. Acun. Growth of silicene on Ag(111) studied with low energy electron microscopy. Master’s thesis, 2013.
- [97] C.-L. Lin, R. Arafune, K. Kawahara, N. Tsukahara, E. Minamitani, Y. Kim, N. Takagi, and M. Kawai. Structure of Silicene Grown on Ag(111). *Applied Physics Express*, 5(4):045802, 2012.

- [98] G. Hollinger and F. J. Himpsel. Oxygen chemisorption and oxide formation on Si(111) and Si(100) surfaces. *Journal of Vacuum Science & Technology A: Vacuum, Surfaces, and Films*, 1(2):640–645, apr 1983.
- [99] F. J. Himpsel, F. R. McFeely, A. Taleb-Ibrahimi, J. A. Yarmoff, and G. Hollinger. Microscopic structure of the SiO₂/Si interface. *Physical Review B*, 38(9):6084–6096, sep 1988.
- [100] W. Braun and H. Kuhlenbeck. Chemical structure of ultrathin thermally grown oxides on a Si(100)-wafer using core level photoemission. *Surface Science*, 180(1):279 – 288, 1987.
- [101] I. Abbati, G. Rossi, L. Calliari, L. Braicovich, I. Lindau, and W. E. Spicer. Interaction of oxygen with silicon d-metal interfaces: A photoemission investigation. *Journal of Vacuum Science and Technology*, 21(2):409–412, jul 1982.
- [102] A. Cros, R. A. Pollak, and K. N. Tu. Room-temperature oxidation of Ni, Pd, and Pt silicides. *Journal of Applied Physics*, 57(6):2253–2257, mar 1985.
- [103] S. Lizzit, R. Larciprete, P. Lacovig, M. Dalmiglio, F. Orlando, A. Baraldi, L. Gammelgaard, L. Barreto, M. Bianchi, E. Perkins, and P. Hofmann. Transfer-Free Electrical Insulation of Epitaxial Graphene from its Metal Substrate. *Nano Letters*, 12(9):4503 – 4507, 2012.
- [104] S. R. Das, J. B. Webb, S. C. de Castro, and V. S. Sundaram. Photoelectron spectra of amorphous Si_xH_y alloy films: The effect of microstructure on the Si-2p level shift. *Journal of Applied Physics*, 60(7):2530–2535, oct 1986.
- [105] Ana G. Silva, Kjeld Pedersen, Zheshen S. Li, and Per Morgen. Oxidation of the surface of a thin amorphous silicon film. *Thin Solid Films*, 520(2):697–699, nov 2011.
- [106] Z. H. Lu, T. K. Sham, P. R. Norton, and K. H. Tan. Photoemission studies of silicon on the Ru(001) surface. *Applied Physics Letters*, 58(2):161 – 163, 1991.
- [107] L. Pasquali, N. Mahne, M. Montecchi, V. Mattarello, and S. Nannarone. Formation and distribution of compounds at the Ru–Si(001) ultrathin film interface. *Journal of Applied Physics*, 105(4):044304, 2009.
- [108] M. A. Chesters and A. B. Horn. The deposition of silicon on metal single-crystal surfaces, studied by RAIRS, LEED and AES. *Journal of Physics: Condensed Matter*, 3(S):S251 – S256, 1991.
- [109] Li Huang, Yan-Fang Zhang, Yu-Yang Zhang, Wenyan Xu, Yande Que, En Li, Jin-Bo Pan, Ye-Liang Wang, Yunqi Liu, Shi-Xuan Du, Sokrates T. Pantelides, and Hong-Jun Gao. Sequence of Silicon Monolayer Structures Grown on a Ru Surface: from a Herringbone Structure to Silicene. *Nano Letters*, 17(2):1161–1166, jan 2017.

- [110] Dietrich Menzel. personal email communication, 2017.
- [111] M. Henzler. Quantitative evaluation of random distributed steps at interfaces and surfaces. *Surface Science*, 73:240 – 251, 1978.
- [112] P. Hahn, J. Clabes, and M. Henzler. LEED-investigations and work-function measurements of the first stages of epitaxy of tungsten on tungsten (110). *Journal of Applied Physics*, 51(4):2079–2084, 1980.
- [113] H. Ibach, H. D. Bruchmann, and H. Wagner. Vibrational study of the initial stages of the oxidation of Si(111) and Si(100) surfaces. *Applied Physics A*, 29(3):113–124, 1982.
- [114] G. Mende, J. Finster, D. Flamm, and D. Schulze. Oxidation of etched silicon in air at room temperature; Measurements with ultrasoft X-ray photoelectron spectroscopy (ESCA) and neutron activation analysis. *Surface Science*, 128(2–3):169 – 175, 1983.
- [115] J. Westermann, H. Nienhaus, and W. Mönch. Oxidation stages of clean and H-terminated Si(001) surfaces at room temperature. *Surface Science*, 311(1-2):101–106, may 1994.
- [116] S. Helveg, J. V. Lauritsen, E. Lægsgaard, I. Stensgaard, J. K. Nørskov, B. S. Clausen, H. Topsøe, and F. Besenbacher. Atomic-Scale Structure of Single-Layer MoS₂ Nanoclusters. *Physical Review Letters*, 84(5):951–954, jan 2000.
- [117] Jeppe V. Lauritsen, Jakob Kibsgaard, Stig Helveg, Henrik Topsoe, Bjerne S. Clausen, Erik Laegsgaard, and Flemming Besenbacher. Size-dependent structure of MoS₂ nanocrystals. *Nat Nano*, 2(1):53–58, January 2007.
- [118] Xiao Lin, Niklas Nilius, Martin Sterrer, Pekka Koskinen, Hannu Häkkinen, and Hans-Joachim Freund. Characterizing low-coordinated atoms at the periphery of MgO-supported Au islands using scanning tunneling microscopy and electronic structure calculations. *Physical Review B*, 81(15), apr 2010.
- [119] Christian Stiehler, Florencia Calaza, Wolf-Dieter Schneider, Niklas Nilius, and Hans-Joachim Freund. Molecular Adsorption Changes the Quantum Structure of Oxide-Supported Gold Nanoparticles: Chemisorption versus Physisorption. *Physical Review Letters*, 115(3), jul 2015.
- [120] T. Schmidt. *Strukturelle Untersuchungen zur Homoepitaxie auf Pt(111)*. PhD thesis, 1994.
- [121] S. Mathur, S. Vlaic, E. Machado-Charry, A.-D. Vu, V. Guisset, P. David, E. Hadji, P. Pochet, and J. Coraux. Degenerate epitaxy-driven defects in monolayer silicon oxide on ruthenium. *Phys. Rev. B*, 92:161410, Oct 2015.

- [122] C. Büchner, P. Schlexer, L. Lichtenstein, S. Stuckenholtz, M. Heyde, and H. J. Freund. Topological Investigation of Two-Dimensional Amorphous Materials. *Zeitschrift für Physikalische Chemie*, 228:587 – 607, 2014.
- [123] C. Büchner, L. Lichtenstein, X. Yu, J. A. Boscoboinik, B. Yang, W. E. Kaden, M. Heyde, S. K. Shaikhutdinov, R. Włodarczyk, M. Sierka, J. Sauer, and H.-J. Freund. Ultrathin Silica Films: The Atomic Structure of Two-Dimensional Crystals and Glasses. *Chemistry – A European Journal*, 20(30):9176–9183, 2014.
- [124] K. M. Burson, P. Schlexer, C. Büchner, L. Lichtenstein, M. Heyde, and H.-J. Freund. Characterizing Crystalline-Vitreous Structures: From Atomically Resolved Silica to Macroscopic Bubble Rafts. *Journal of Chemical Education*, 92(11):1896–1902, 2015.
- [125] K. M. Burson, C. Büchner, M. Heyde, and H.-J. Freund. Assessing the amorphousness and periodicity of common domain boundaries in silica bilayers on Ru(0001). *Journal of Physics: Condensed Matter*, 29(3):035002, 2017.
- [126] C. Büchner, L. Liu, S. Stuckenholtz, K. M. Burson, L. Lichtenstein, M. Heyde, H.-J. Gao, and H. J. Freund. Building block analysis of 2D amorphous networks reveals medium range correlation. *Journal of Non-Crystalline Solids*, 435:40 – 47, 2016.
- [127] LEEDpat, Version 4.1, utility by K.E. Hermann (FHI) and M.A. Van Hove (HKBU), Berlin / Hong Kong, 2014; see also <http://www.fhi-berlin.mpg.de/KHsoftware/LEEDpat/index.html>, 2014.
- [128] X. Xu and D. W. Goodman. New approach to the preparation of ultrathin silicon dioxide films at low temperatures. *Applied Physics Letters*, 61(7):774 – 776, 1992.
- [129] X. Xu and D. W. Goodman. The preparation and characterization of ultrathin silicon dioxide films on a Mo(110) surface. *Surface Science*, 282(3):323 – 332, 1993.
- [130] L. Giordano, D. Ricci, G. Pacchioni, and P. Ugliengo. Structure and vibrational spectra of crystalline SiO_2 ultra-thin films on Mo(112). *Surface Science*, 584(2-3):225 – 236, 2005.
- [131] J. Weissenrieder, S. Kaya, J.-L. Lu, H.-J. Gao, S. Shaikhutdinov, H.-J. Freund, M. Sierka, T. K. Todorova, and J. Sauer. Atomic Structure of a Thin Silica Film on a Mo(112) Substrate: A Two-Dimensional Network of SiO_4 Tetrahedra. *Phys. Rev. Lett.*, 95:076103, Aug 2005.
- [132] S. Wendt, E. Ozensoy, T. Wei, M. Frerichs, Y. Cai, M. S. Chen, and D. W. Goodman. Electronic and vibrational properties of ultrathin SiO_2 films grown on Mo(112). *Phys. Rev. B*, 72(11):115409, Sep 2005.

- [133] M. Chen and D. W. Goodman. The structure of monolayer SiO_2 on Mo(112): A 2-D [S-O-Si] network or isolated $[SiO_4]$ units? *Surface Science*, 600(19):L255 – L259, 2006.
- [134] T. K. Todorova, M. Sierka, J. Sauer, S. Kaya, J. Weissenrieder, J.-L. Lu, H.-J. Gao, S. Shaikhutdinov, and H.-J. Freund. Atomic structure of a thin silica film on a Mo(112) substrate: A combined experimental and theoretical study. *Phys. Rev. B*, 73:165414, Apr 2006.
- [135] S. Kaya, M. Baron, D. Stacchiola, J. Weissenrieder, S. Shaikhutdinov, T. K. Todorova, M. Sierka, J. Sauer, and H. J. Freund. On the geometrical and electronic structure of an ultra-thin crystalline silica film grown on Mo(112). *Surface Science*, 601(21):4849 – 4861, 2007.
- [136] F. Ben Romdhane, T. Björkman, J. A. Rodríguez-Manzo, O. Cretu, A. V. Krasheninnikov, and F. Banhart. In Situ Growth of Cellular Two-Dimensional Silicon Oxide on Metal Substrates. *ACS Nano*, 7(6):5175 – 5180, 2013.
- [137] H. Ohsaki, K. Miura, and Y. Tatsumi. Oxidation mechanism of amorphous silicon in air. *Journal of Non-Crystalline Solids*, 93(2-3):395–406, sep 1987.
- [138] A. Szekeres and P. Danesh. Oxidation of amorphous and crystalline silicon. *Journal of Non-Crystalline Solids*, 187:45–48, jul 1995.
- [139] J. P. Perdew, K. Burke, and M. Ernzerhof. Generalized Gradient Approximation Made Simple. *Phys. Rev. Lett.*, 77:3865–3868, Oct 1996.
- [140] F. B. Romdhane, T. Björkman, A. V. Krasheninnikov, and F. Banhart. Solid-State Growth of One- and Two-Dimensional Silica Structures on Metal Surfaces. *The Journal of Physical Chemistry C*, 118(36):21001–21005, 2014.
- [141] H. W. Klemm, G. Peschel, E. Madej, A. Fuhrich, M. Timm, D. Menzel, T. Schmidt, and H.-J. Freund. Preparation of silica films on Ru(0001): A LEEM/PEEM study. *Surface Science*, 643:45 – 51, 2016. Present challenges in surface science, a special issue in honour of Dietrich Menzel.
- [142] Heloise Tissot, Linfei Li, Shamil Shaikhutdinov, and Hans-Joachim Freund. Preparation and structure of Fe-containing aluminosilicate thin films. *Phys. Chem. Chem. Phys.*, 18:25027–25035, 2016.
- [143] Linfei Li, Heloise Tissot, Shamil Shaikhutdinov, and Hans-Joachim Freund. Transition Metal Induced Crystallization of Ultrathin Silica Films. *Chemistry of Materials*, 29(3):931–934, 2017.
- [144] Torbjörn Björkman, Simon Kurasch, Ossi Lehtinen, Jani Kotakoski, Oleg V. Yazyev, Anchal Srivastava, Viera Skakalova, Jurgen H. Smet, and Ute Kaiser and Arkady V. Krasheninnikov. Defects in bilayer silica and graphene: common trends in diverse hexagonal two-dimensional systems. *Scientific Reports*, 3:3482, 2013.

- [145] A.J. Stone and D.J. Wales. Theoretical studies of icosahedral C₆₀ and some related species. *Chemical Physics Letters*, 128(5):501 – 503, 1986.
- [146] Jannik C. Meyer, C. Kisielowski, R. Erni, Marta D. Rossell, M. F. Crommie, and A. Zettl. Direct Imaging of Lattice Atoms and Topological Defects in Graphene Membranes. *Nano Letters*, 8(11):3582–3586, 2008. PMID: 18563938.
- [147] J. Kotakoski, J. C. Meyer, S. Kurasch, D. Santos-Cottin, U. Kaiser, and A. V. Krasheninnikov. Stone-Wales-type transformations in carbon nanostructures driven by electron irradiation. *Phys. Rev. B*, 83:245420, Jun 2011.
- [148] J. A. Boscoboinik, X. Yu, E. Emmez, B. Yang, S. Shaikhutdinov, F. D. Fischer, J. Sauer, and H.-J. Freund. Interaction of Probe Molecules with Bridging Hydroxyls of Two-Dimensional Zeolites: A Surface Science Approach. *The Journal of Physical Chemistry C*, 117(26):13547 – 13556, 2013.

ISBN 978-3-945682-66-1